

AD-A077 805

SCIENCE APPLICATIONS INC EL SEGUNDO CALIF

F/G 17/9

HARDENED RADAR COMPONENT MATERIALS DEVELOPMENT STUDY. (U)

MAY 79 I OSOFSKY , R SEMELSBERGER , T DUNCAN

DAAG46-78-C-0052

UNCLASSIFIED

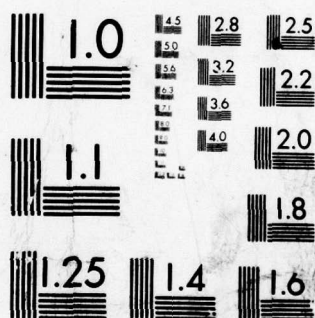
AMMRC-TR-79-34

NL

1 OF 3

AD
A077805





MICROCOPY RESOLUTION TEST CHART
NATIONAL BUREAU OF STANDARDS-1963-A

AD A 077805



AMMRC TR 79-34

HARDENED RADAR COMPONENT MATERIALS DEVELOPMENT STUDY

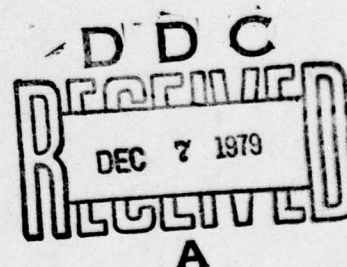
MAY 1979

SCIENCE APPLICATIONS, INC.
101 CONTINENTAL BLVD., SUITE 310
EL SEGUNDO, CA 90245

FINAL REPORT

CONTRACT NUMBER DAAG46-78-C-0052

Approved for public release; distribution unlimited.



Prepared for

ARMY MATERIALS AND MECHANICS RESEARCH CENTER
Watertown, Massachusetts 02172

79 12 7 062

DDC FILE COPY

The findings in this report are not to be construed as an official Department of the Army position, unless so designated by other authorized documents.

Mention of any trade names or manufacturers in this report shall not be construed as advertising nor as an official indorsement or approval of such products or companies by the United States Government.

DISPOSITION INSTRUCTIONS

Destroy this report when it is no longer needed.
Do not return it to the originator.

UNCLASSIFIED

SECURITY CLASSIFICATION OF THIS PAGE (When Data Entered)

19 REPORT DOCUMENTATION PAGE		READ INSTRUCTIONS BEFORE COMPLETING FORM
1. REPORT NUMBER AMMRC TR-79-34	2. GOVT ACCESSION NO.	3. RECIPIENT'S CATALOG NUMBER
4. TITLE (and Subtitle) Hardened Radar Component Materials Development Study.	5. TYPE OF REPORT & PERIOD COVERED Final Report, 28 May 78 -	6. PERFORMING ORG. REPORT NUMBER 24 Jan 79
7. AUTHOR(s) Irving, Robert, Thomas Osofsky, Semelsberger, Duncan	8. CONTRACT OR GRANT NUMBER(s) DAAG46-78-C-0052	9. PERFORMING ORGANIZATION NAME AND ADDRESS Science Applications, Inc. 101 Continental Blvd., Suite 310 El Segundo, CA 90245
10. CONTROLLING OFFICE NAME AND ADDRESS Army Materials and Mechanics Research Center Watertown, Massachusetts 02172	11. REPORT DATE May 1979	12. PROGRAM ELEMENT, PROJECT, TASK AREA & WORK UNIT NUMBERS D/A Project: 8X363304D215 AMCMS Code: 633304.21500.07 Agency Accession:
13. MONITORING AGENCY NAME & ADDRESS (if different from Controlling Office) 1254	14. SECURITY CLASS. (of this report) Unclassified	15a. DECLASSIFICATION/DOWNGRADING SCHEDULE ---
16. DISTRIBUTION STATEMENT (of this Report) Approved for public release; distribution unlimited.		
17. DISTRIBUTION STATEMENT (of the abstract entered in Block 20, if different from Report)		
18. SUPPLEMENTARY NOTES		
19. KEY WORDS (Continue on reverse side if necessary and identify by block number) Radar materials Thermal Radiation Simulation Porous Ceramics Silicone rubber Nuclear hardened materials Radar French solar furnace		
20. ABSTRACT (Continue on reverse side if necessary and identify by block number) A combined analytical and experimental study was conducted to identify and evaluate materials for protecting Ballistic Missile Defense system ground radar components from nuclear thermal radiation damage. This program included thermal testing using the French Solar Furnace and the SAI Thermal Radiation Simulator; electrical property tests at the Georgia Institute of Technology, Engineering Experiment Station; and planning of mechanical property tests to be conducted in the BMD Materials Test facility at AMMRC.		

UNCLASSIFIED

SECURITY CLASSIFICATION OF THIS PAGE(When Data Entered)

Block No. 20

ABSTRACT

Materials included bulk ceramics, ceramic coatings and bulk ablators. The results indicated promise for the use of a silicone rubber ablator and uninfiltreated porous ceramic coatings for radar component thermal hardening. Further tests and analyses are recommended for these classes of materials in order to evaluate the effect on radar performance.

Accession For	
NTIS GRA&I	
DDC TAB	
Unannounced	
Justification	
By	
Distribution/	
Availability Codes	
Dist.	Avail and/or special
A	I

UNCLASSIFIED

SECURITY CLASSIFICATION OF THIS PAGE(When Data Entered)

TABLE OF CONTENTS

	<u>Page</u>
1.0 INTRODUCTION AND SUMMARY.	1
2.0 HARDENING REQUIREMENTS.	4
2.1 Nuclear Environment	4
2.2 Phased Array Radar Design Require- ments	4
3.0 CANDIDATE HARDENING MATERIALS	15
3.1 Ceramic Coating	15
3.2 Bulk Window Materials	19
3.3 Bulk Ablative Materials	20
4.0 THERMAL PROPERTIES ANALYSIS AND TEST.	23
4.1 Thermal Analysis.	23
4.1.1 Ceramic Coating Thermal Analysis	23
4.1.2 Silicone Rubber Ablation Model	28
4.1.3 Bulk "Window" Material Thermal Modeling	28
4.2 Comparison of Thermal Simulators Facil- ities Capabilities.	33
4.2.1 Solar Furnace.	33
4.2.2 Plasma Jet	34
4.2.3 Glow Heaters	35
4.2.4 SAI Thermal Radiation Simulator.	36
4.3 Thermal Radiation Simulator Tests	39
4.3.1 Description of the TRS Facility.	39
4.3.2 Pre-Test Analysis.	41
4.3.3 Test Procedures.	43
4.3.4 TRS Test Results	44

	<u>Page</u>
4.4 French Solar Furnace Test Program.	51
4.4.1 Facility Description.	51
4.4.2 Test Procedure and Approach	52
4.4.3 Pre-Test Analysis	52
4.4.4 Test Results.	54
4.5 Conclusions.	63
5.0 ELECTRICAL PROPERTIES TEST AND ANALYSES.	66
5.1 Introduction and Summary	66
5.1.1 Plasma-Sprayed Ceramic Coatings	66
5.1.2 Bulk Materials.	70
5.1.3 Material-Array Interactions	73
5.2 Electrical Properties Test Program	74
5.2.1 Test Facility Description (Resonant Cavity Measurements	74
5.2.2 Test Procedure.	78
5.2.3 Pre-Test Analysis	94
5.3 Array-Hardening Materials Interaction Analysis	106
5.3.1 Mechanisms of Array Performance Degradations.	106
5.3.2 Reflection and Dissipative Losses.	108
5.3.3 Array Blindness	108
5.4 Conclusions.	115
6.0 MECHANICAL PROPERTIES TEST	117
6.1 Mechanical Properties Requirements	117
6.2 Mechanical Properties Test Program Plan	119

	<u>Page</u>
7.0 CONCLUSIONS AND RECOMMENDATIONS.	123
8.0 REFERENCES	127
APPENDIX A - MATERIAL THERMAL PROPERTIES.	129
APPENDIX B - SUMMARY OF CAVITY RESULTS FOR ALL TEST RUNS	139
APPENDIX C - ANALYSIS OF A CYLINDRICAL CAVITY MEASURE- MENT PROCEDURE FOR THE DETERMINATION OF THE DIELECTRIC CONSTANT AND THE LOSS TANGENT OF A THIN DIELECTRIC SLAB MOUNTED ON A METAL DISC.	147
APPENDIX D - ANALYSIS OF HARDENING MATERIAL-ARRAY INTERACTIONS FOR A DIELECTRIC COVERED PHASED ARRAY ANTENNA	191
APPENDIX E - MECHANICAL PROPERTIES OF HARDENED RADAR CANDIDATE MATERIALS.	201
APPENDIX F - THERMAL ANALYSIS RESULTS	215
APPENDIX G - FRENCH SOLAR TEST DATA	227

LIST OF FIGURES

		<u>Page</u>
Figure 2.1	Overpressure History	5
2.2	Dynamic Pressure History	6
2.3	Air Temperature History.	7
2.4	Air Particle Velocity History.	8
2.5	Air Density History.	9
2.6	Thermal Radiation Flux	10
2.7	Thermal Radiation Fluence.	11
2.8	Effective Blackbody Temperature.	12
3.1	Infiltrated Ceramic Coating Backface Temperature From Arc Jet Tests	17
4.1	Ceramic Coating Thermal Model.	24
4.2	Alumina Coated Steel Exposed to One Nuclear Blast.	29
4.3	0.125 In. Alumina Coating on 1.0 In. Steel in Nuclear Environment ($\alpha=0.2$)	30
4.4	Absorptivity Effect on Ceramic Coating in Nuclear Environment (1 Burst)	31
4.5	Silicone Rubber Thermal Model.	32
4.6	SAI Thermal Radiation Simulator.	37
4.7	TRS Test Layout.	38
4.8	Expected TRS Heat Output Used in Predictions.	40
4.9	Predicted 24 Bag TRS Heat Flux	42
4.10	Three Inch Diameter Ceramic Coatings Test Fixture	45
4.11	Four Inch Square Ceramic Coating Test Fixture	46
4.12	Test Sample Installation	47
4.13	Calorimeter Output	49
4.14	Predicted Thermal Response of Alumina Coating With Silicone Infiltrant in Solar Furnace.	55
4.15	Effect of Absorptivity on Predicted Aluminum Temperatures.	56

LIST OF FIGURES (CONT'D)

	<u>Page</u>
Figure 4.16 Effect of Absorptivity on Predicted Aluminum Coating Ablation	57
4.17 AS-3DX Front Face Temperature	61
5.1A Sectional View of the Resonant Cavity Sample Holder to be Used for Testing Thin Coatings	75
5.1B Photograph of Disassembled Cavity	76
5.1C Photograph of Assembled Cavity.	77
5.2A Block Diagram of the Electromagnetic Test System for Thin Coatings	80
5.2B Photograph of Cavity Measurement Equipment	81
5.3 Sample Holder Made from a Shortened Section of Waveguide (or Coaxial Line.	89
5.4 Circular Resonator With Dielectric Sample Filling Region 1 ($0 < z \leq b$).	96
5.5 Normalized Frequency Shift vs. Dielectric Constant.	98
5.6 Dielectric Constant Error Bounds Caused by Uncertainty in Resonant Frequency Shift	100
5.7 LOADED Q VERSUS LOSS TANGENT, $\alpha = 0.5$ Brass	102
5.8 Loss Tangent Error Bounds Caused by Uncertainty in Q Measurement.	104
5.9 Schematic of Array Performance Degradations Mechanisms for a Dielectrically Covered Array	107
5.10 Radome Efficiency for a Flat Array Covered By a Slab With a Dielectric Constant of 2.8	109
5.11 Radome Efficiency for a Flat Array Covered by a Slab With a Dielectric Constant of 7.0	110
5.12 Covered Array Model	111

LIST OF FIGURES (CONT'D)

	<u>Page</u>
Figure 5.13 Max Slab Thickness vs. Dielectric Constant for Blindspot Angles Greater than Specified Scan Angle	113
A.1 Thermal Conductivity	137
B.1 A Cross-Section of the Ceramic-Coated Endplate	146
C.1 Circular Resonator with Dielectric Sample Filling Region 1 ($0 < z \leq b$) . . .	150
C.2 Relative Cutoff Frequencies of Waves in a Cylindrical Resonator	154
C.3 Normalized Resonant Frequency Change as a Function of Dielectric Constant for TE_{011} Cavity	158
C.4 Fill Factor as a Function of Cavity Radius for TE_{011} Mode and Material Thickness of 0.050 Inches	160
C.5 Fill Factor as a Function of Cavity Radius for TE_{011} Mode and Material Thickness of 0.125 Inches	161
C.6 Normalized Frequency Shift vs. Dielectric Constant	173
C.7 Loaded Q Versus Loss Tangent, α = Brass .	175
C.8 Loaded Q Versus Loss Tangent, α = 0.5 Brass	176
C.9 Loaded Q Versus Loss Tangent, α = 0.25 Brass	177
C.10 Dielectric Constant Error Bounds Caused by Uncertainty in Resonant Frequency Shift	181

LIST OF FIGURES (CONT'D)

		<u>Page</u>
Figure C.11	Loss Tangent Error Bounds Caused by Uncertainty in the Dielectric Constant	184
C.12	Loss Tangent Error Bounds Caused by Uncertain in Q Measurement	188
D.1	Dielectric Slab on a Ground Plane.	193
D.2	Excitation of TM Slab Modes.	195
D.3	Slab Thickness vs Dielectric Constant.	198
D.4	Slab Thickness vs. Scan Angle.	199
E.1	Linear Thermal Expansion Coefficient From 70°F For Bulk Materials	205
E.2	Modulus of Elasticity for Various Bulk Materials.	206
E.3	Tensile Strength for Various Bulk Materials.	207
E.4	Compressive Strength for Various Bulk Materials.	208
E.5	Linear Thermal Expansion Coefficients for Metals	209
E.6	Modulus of Elasticity for Various Metals	210
E.7	Tensile Strength for Various Metals.	211
E.8	Linear Thermal Expansion Coefficient for Plasma Sprayed Ceramics.	212
E.9	Modulus of Elasticity for Plasma Sprayed Materials.	213
F.1	TRS Heat Flux Environment.	216
F.2	TRS vs Nuclear Burst Thermal Flux as Received by a Material with an Absorptivity of 0.2	218
F.3	Thermal Model Schematic.	219
F.4	0.060 Inch Alumina on 0.1875 Inch Stainless Steel Exposed to TRS Fireball	220
F.5	0.090 Inch Alumina on 0.1875 Inch Stainless Steel Exposed to the TRS Fireball	221

LIST OF FIGURES (CONT'D)

		<u>Page</u>
Figure F.6	0.060 Inch Zirconia on 0.1875 Inch Stainless Steel Exposed to TRS Fireball	222
G.1	Alumina Coating/Silicone Infiltrant, Sample F2.	229
G.2	0.25 Inch Silastic E, Sample F3.	230
G.3	0.5 Inch Silastic E, Sample F4	231
G.4	Boron Nitride (HBR), Sample F8	232
G.5	AS-3DX, Sample F9.	233
G.6	Magnesia-Spinel Coating/Silicone Infil- trant, Sample F16.	234
G.7	Alumina Coating/Silicone Infiltrant, Sample F2, Temperature Response.	235
G.8	0.25 Inch Silastic E/Steel, Sample F3, Temperature Response	236
G.9	0.5 Inch Silastic E/0.125 Inch Steel, Sample F4, Temperature Response.	237
G.10	Boron Nitride, Sample F8, Temperature Response	238
G.11	AS-3DX Sample F9, Temperature Response .	239
G.12	Magnesia Spinel Coating/Silicone Infil- trant, Sample F16, Temperature Response.	240

LIST OF TABLES

		<u>Page</u>
Table 3.1	Ceramic Coating	21
3.2	Bulk Window Materials	21
3.3	Ablator/Insulator Materials	22
4.1	TRS Test Calorimeter Measurements	48
4.2	French Solar Test Materials	53
4.3	Material Visual Response.	58
5.1	Dielectric Properties of Ceramic Coatings at S-Band	67
5.2	Dielectric Properties of Ceramic Coatings at X-Band	68
5.3	Dielectric Properties of Bulk Materials at S-Band (3 GHz)	71
5.4	Dielectric Properties of Bulk Materials at X-Band (9 GHz)	72
5.5	Nominal Cavity Dimensions	79
5.6	Test Equipment for Cavity Measurements. .	82
5.7	Nominal Dielectric Parameters of Known Materials	88
5.8	Nominal Dielectric Parameters of Known Materials	95
5.9	Maximum Slab Thickness for Which Scan Re- quirements May be Met Without Any Array Design Modifications.	114
6.1	Structural Test Coupon Matrix	120
A.1	Plasma Sprayed Alumina Thermal Properties	130
A.2	Plasma Sprayed Zirconia Thermal Proper- ties.	131
A.3	Stainless Steel and Nichrome Bond Thermal Properties.	132
A.4	Silicone Rubber Thermal Properties.	134
A.5	Bulk Materials Thermal Properties	136
B.1	Tabulation of All S-Band Cavity Measure- ments for SAI Materials	141

LIST OF TABLES (CONT'D)

		<u>Page</u>
Table B.3	Ceramic Sample Thicknesses	145
E.1	General Material Properties.	204
F.1	Non-Infiltrated Ceramic Coatings Thermal Response	223
F.2	Comparison of Performance With and Without Resin.	225
G.1	Sample Dimension and Weight Data	228

FOREWORD

This document is the final report for the Hardened Radar Component Materials Development Study. This work was performed by Science Applications, Inc. (SAI) for the Army Materials and Mechanics Research Center (AMMRC) under Contract DAAG60-78-C-0052. The period of technical performance was May 28, 1978 through January 20, 1979. The AMMRC program manager was Mr. John Dignam. The SAI Program Team included the following key participants:

Mr. Irving Osofsky	- Principal Investigator, Materials and Requirements
Mr. Thomas Duncan	- Thermal Analysis and Test Planning
Dr. Robert Semelsberger	- Electrical Property Test Planning and Analysis
Dr. Donald Dudley	- Electrical Property Test Planning
Mr. Leonard Porcello	- Electrical Property Test Planning
Mr. John Dishon	- Thermal Radiation Simulator Test Conduct
Mr. Kenneth Sites	- Instrumentation

Thermal testing was performed at the French Solar Furnace in Odeillo, France and at the SAI Thermal Radiation Simulator Facility at the Nuclear test site in Nevada. The electrical properties tests were conducted at the Georgia Institute of Technology, Engineering Experiment Station, with Dr. J. Fuller as principal Investigator.

1.0 INTRODUCTION AND SUMMARY

The multiple nuclear burst environment resulting from an attack on ground based US ICBMs provides a severe environment for the nearby ground-based phased array radars which are part of a ballistic missile defense system. The phased array radars must survive the nuclear blast overpressure and resulting thermal environment with minimal performance degradation prior-to as well as post-attack.

The severity of the nuclear burst generated thermal radiation environment requires identification of resistant materials which satisfy the thermal, structural and electrical requirements with minimal phased array radar performance degradation. The objective of the present study was to identify and evaluate materials for nuclear thermal radiation and blast hardening of BMD phased array radar components.

The scope of the present study included identification of candidate materials, compilation of existing structural and thermal property data, design and fabrication of test specimens for thermal, electrical and mechanical property tests, designing, planning, and conducting thermal and electrical property tests, and simulating the performance of candidate materials in nuclear environments. A wide range of candidate materials for both radiating and non-radiating phased array radar components was identified. Emphasis was placed on the use of uninfiltrated and infiltrated porous ceramic coatings and low-carbonaceous char ablative materials. However, the materials list includes metals, bulk and composite ceramics as well. Limited thermal radiation tests were conducted at the French

Solar Furnace Facility in France and at the SAI Thermal Radiation Test Facility at the Nevada Nuclear Test Site. Electrical property tests at both S-band and X-band were conducted at the Georgia Institute of Technology Engineering Experiment Station in Atlanta, Georgia.

The results of this study showed that uninfiltreated ceramic coatings and a silicone rubber ablatiave material had promise for thermal protection of radiating phased array radar components. The use of an infiltrant in the porous ceramic coating resulted in high surface thermal absorptivity as the infiltrant decomposed and charred on heating. Analyses show that the absorptivity must be approximately 0.2 in order for the thin ceramic coating to provide the necessary thermal protection for the required nuclear criteria environment. Emissivity values of 0.2 have been obtained in previous program tests of aluminum oxide and zirconia ceramic coatings. Measurements of the electrical properties (dielectric constant and loss tangent) showed the ceramics to have adequate properties for possible radar applications, e.g., loss tangent less than 0.03. A major concern for the ceramics is a potential thermal stress failure problem. However, analyses suggest the possible solution of pre-heating during processing to minimize tensile stresses during exposure to the high heat flux environment from nuclear bursts.

The silicone ablator shows much promise for protecting radar components. This material forms a low carbon content char which is reasonably strong. The excellent insulative properties and high temperature char characteristics result in good thermal resistance. Measurements of electrical properties showed low loss tangents and dielectric constants for the virgin materials. Although the char properties are not as good as the virgin properties, analyses show that the material could be used as a coating in integral phased array radar designs.

The following sections present the results of test and analysis work performed during this study. Section 2.0 describes the phased array radar hardening requirements including a definition of the nuclear environment, contractor phased array radar design studies and material hardness requirements. Section 3.0 describes the candidate materials selected for evaluation in this study. In Section 4.0, the thermal analysis and test results are presented. The electrical properties test approach and results are presented in Section 5.0. Mechanical properties tests and analyses are described in Section 6.0 and the conclusions and recommendations resulting from this study are presented in Section 7.0. Detailed test and analysis results are presented in Appendices A-G.

2.0 HARDENING REQUIREMENTS

2.1 Nuclear Environment

The hardened radar will be designed to withstand the nuclear weapon environments associated with three successive nuclear bursts with a time spacing sufficient for radar cool down between bursts. The free field peak design overpressure hypothesized is 150 psi. The nuclear environments are based on IDEA code calculations documented in References 1 and 2. Figures 2.1 through 2.5 present the overpressure, dynamic pressure, local air temperature, particle velocity and density for each burst. Note that the nuclear fireball sweeps over the radar at about 0.7 seconds after burst. The thermal radiation flux is given in Figure 2.6 and the fluence is given in Figure 2.7. The shock arrival time is 0.48 seconds after burst, and approximately 250 cal/cm^2 (~10 percent of total fluence) precedes the shock. The thermal flux at shock arrival is about $1500 \text{ cal/cm}^2\text{-sec}$. Figure 2.8 presents the fireball equivalent blackbody temperature useful for spectral analysis.

2.2 Phased Array Radar Design Requirements

The phased array radar must survive the nuclear thermal and blast environment and remain operational. The system must still be capable to electromagnetically function in an undegraded manner after exposure to the three consecutive nuclear events. The damage after a single nuclear burst must not detract from the capability of the radar to function or survive a second or third burst.

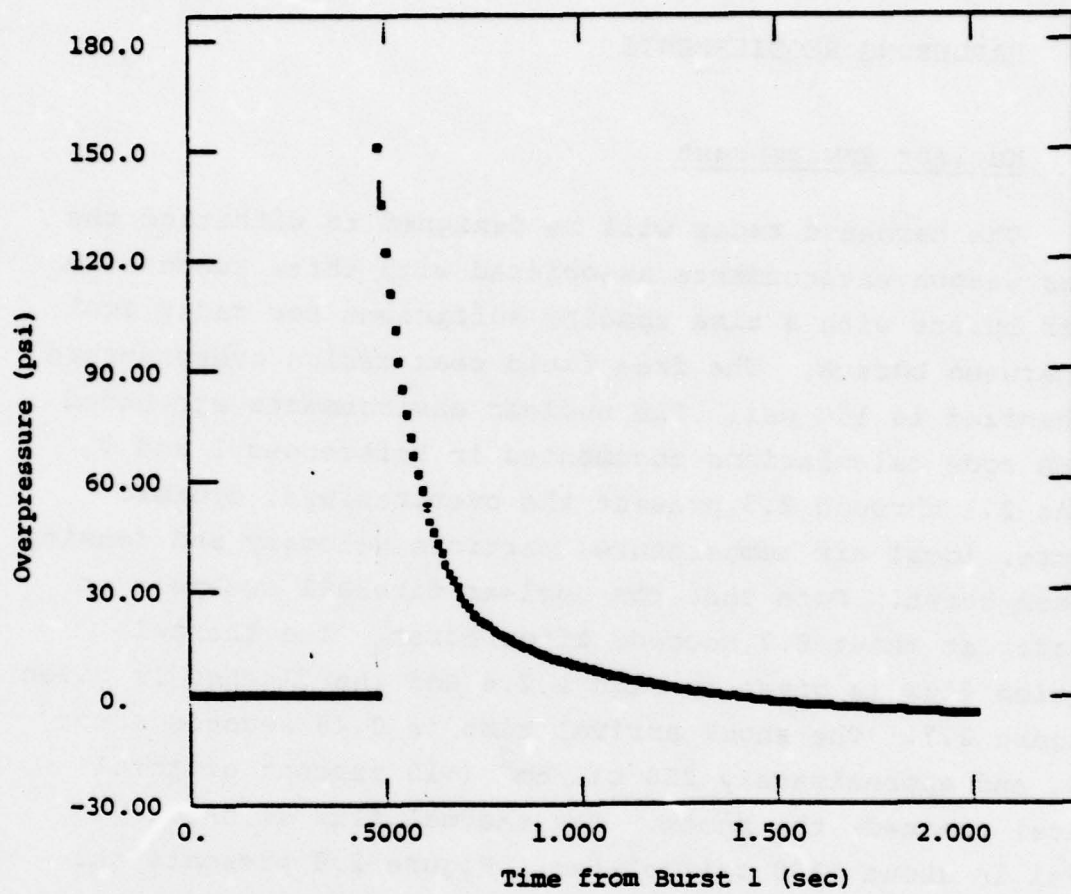


FIGURE 2.1. OVERPRESSURE HISTORY

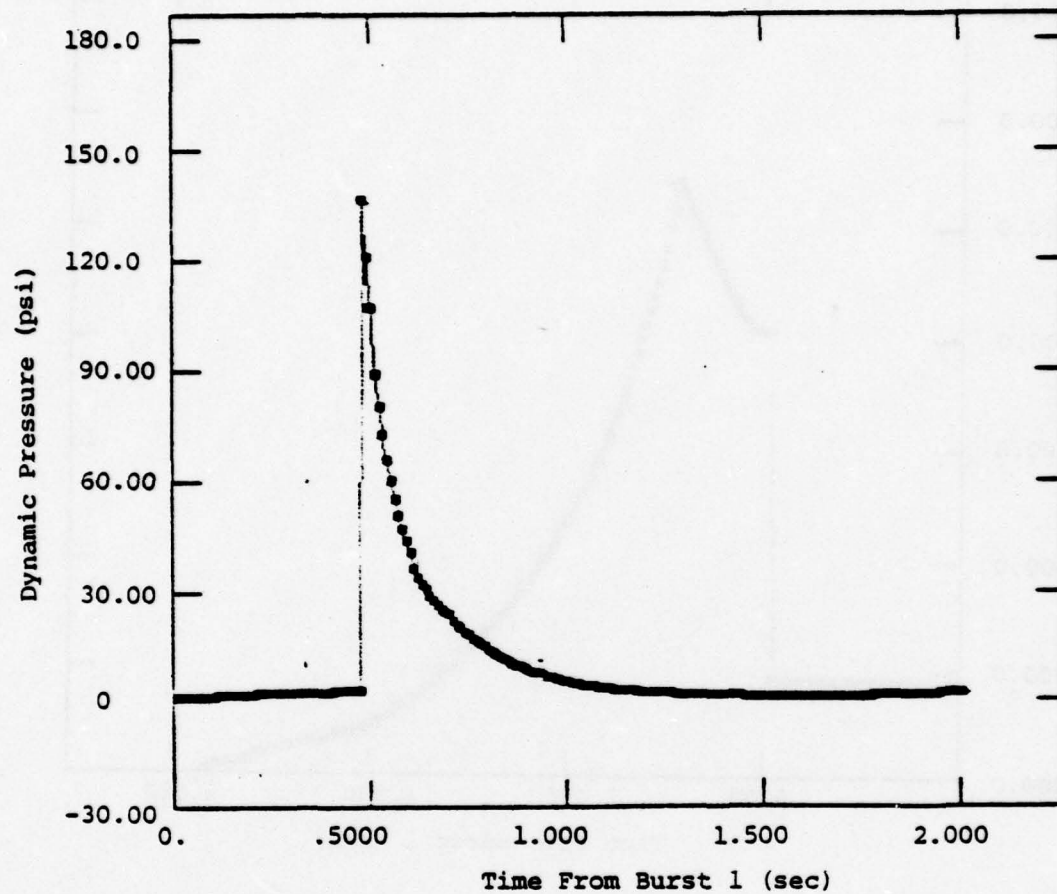


FIGURE 2.2. DYNAMIC PRESSURE HISTORY

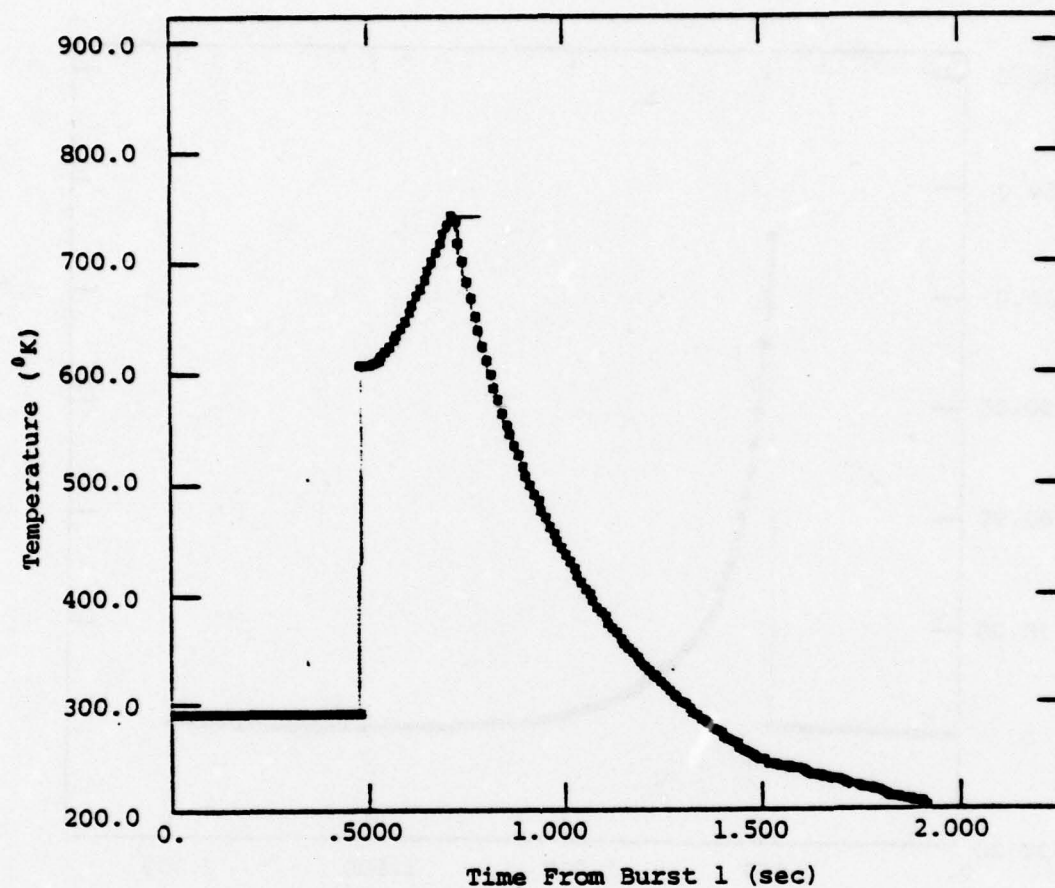


FIGURE 2.3. AIR TEMPERATURE HISTORY

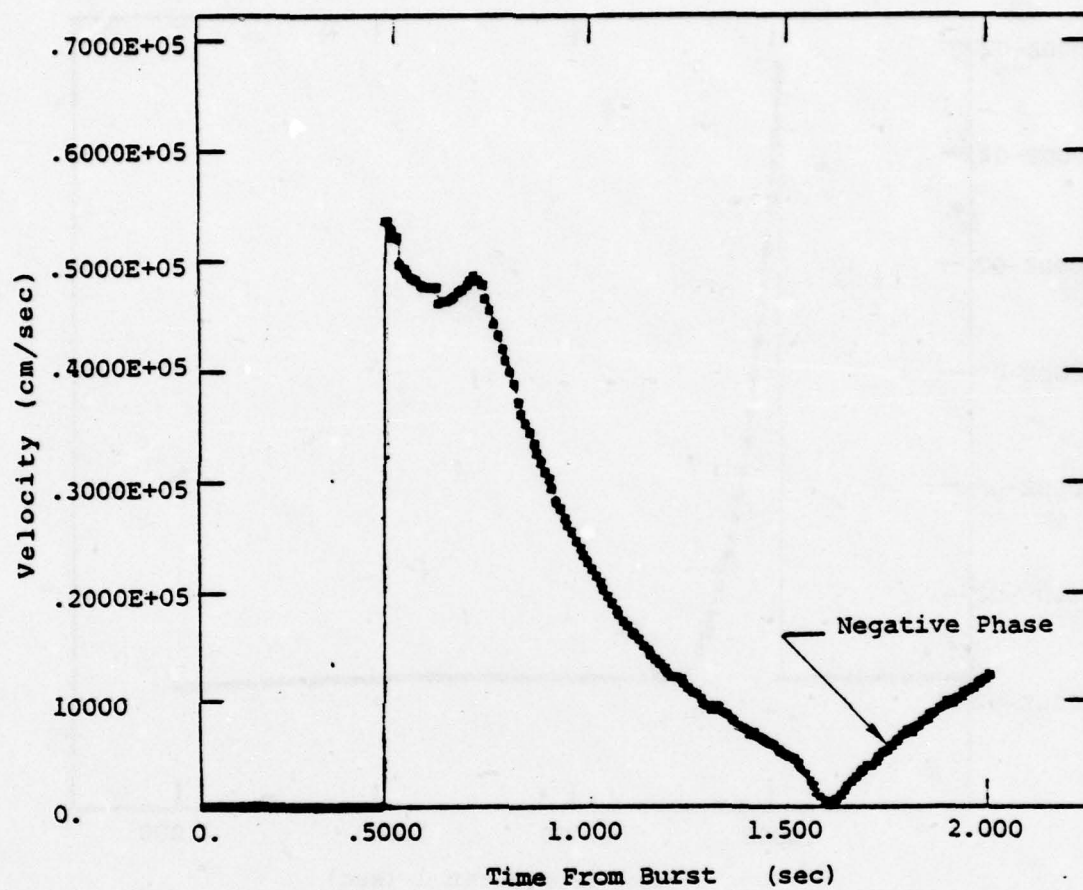


FIGURE 2.4. AIR PARTICLE VELOCITY HISTORY

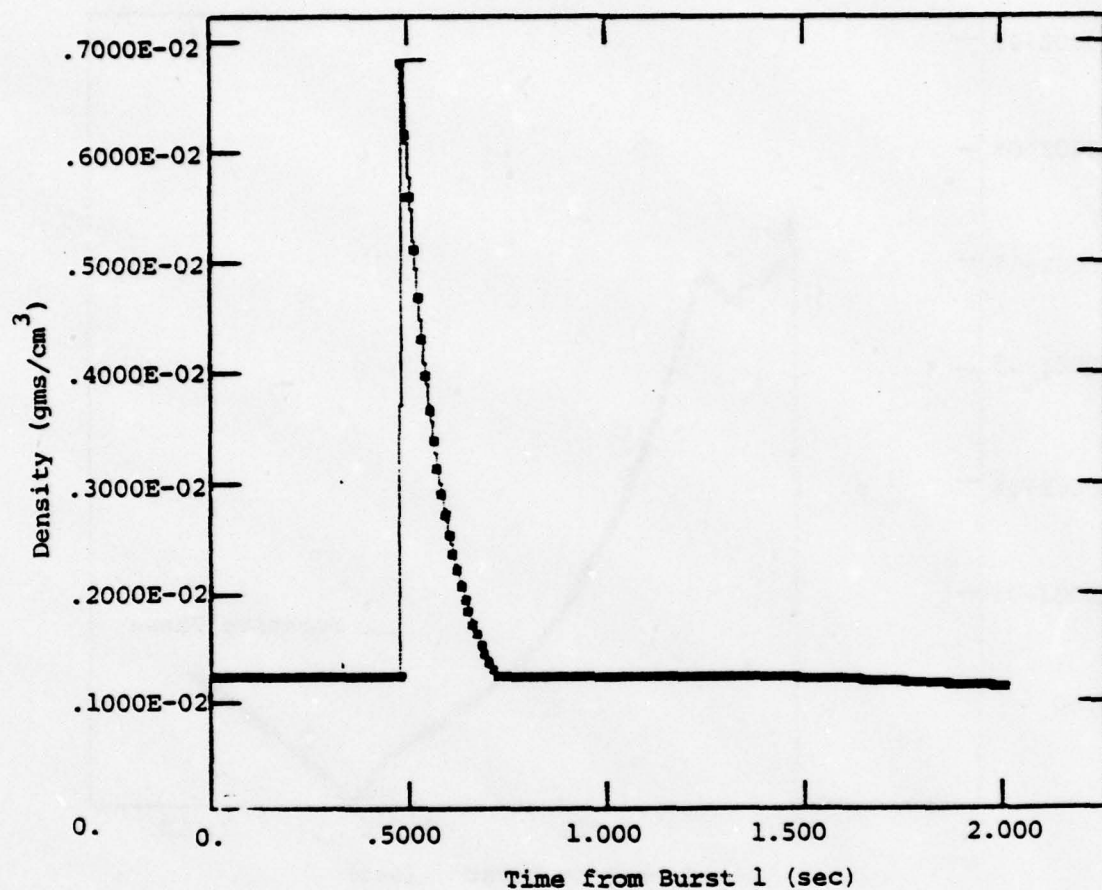


FIGURE 2.5. AIR DENSITY HISTORY

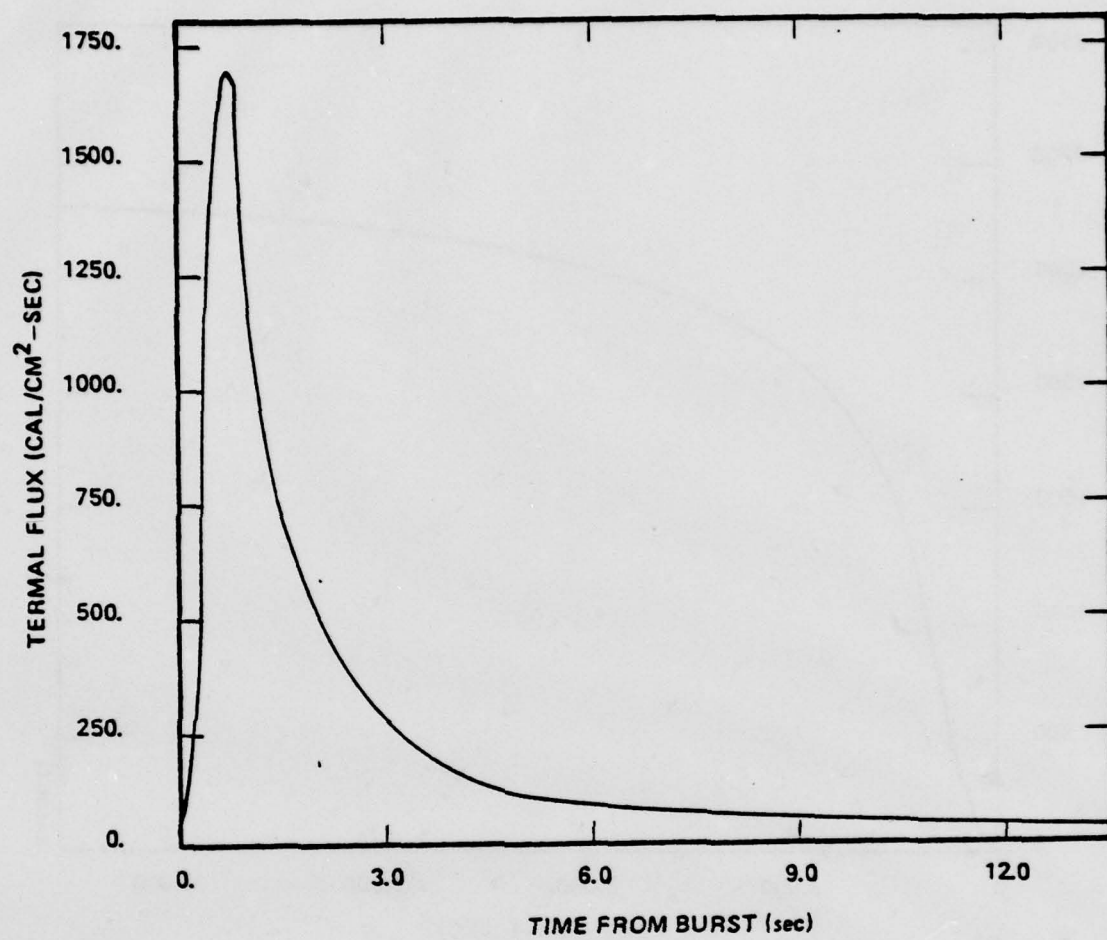


FIGURE 2.6. THERMAL RADIATION FLUX

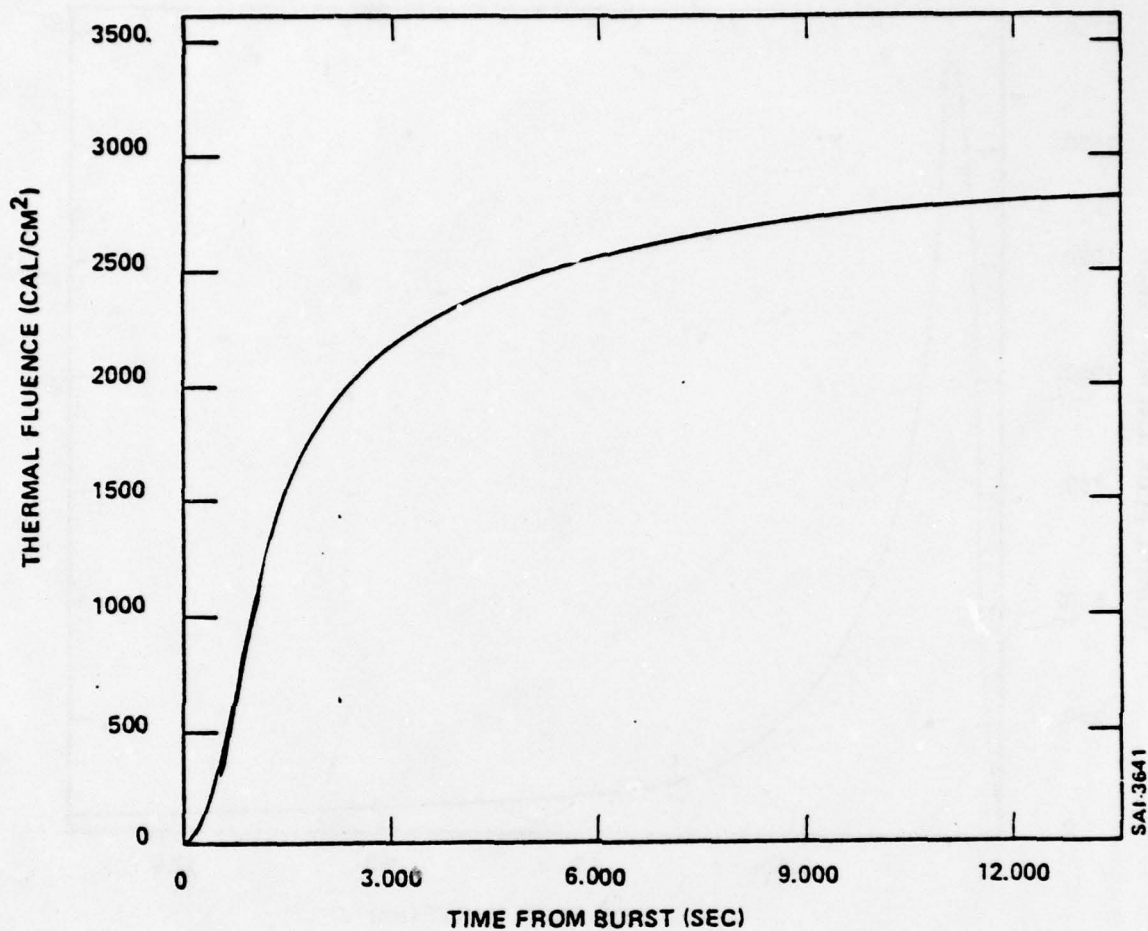


FIGURE 2.7. THERMAL RADIATION FLUENCE

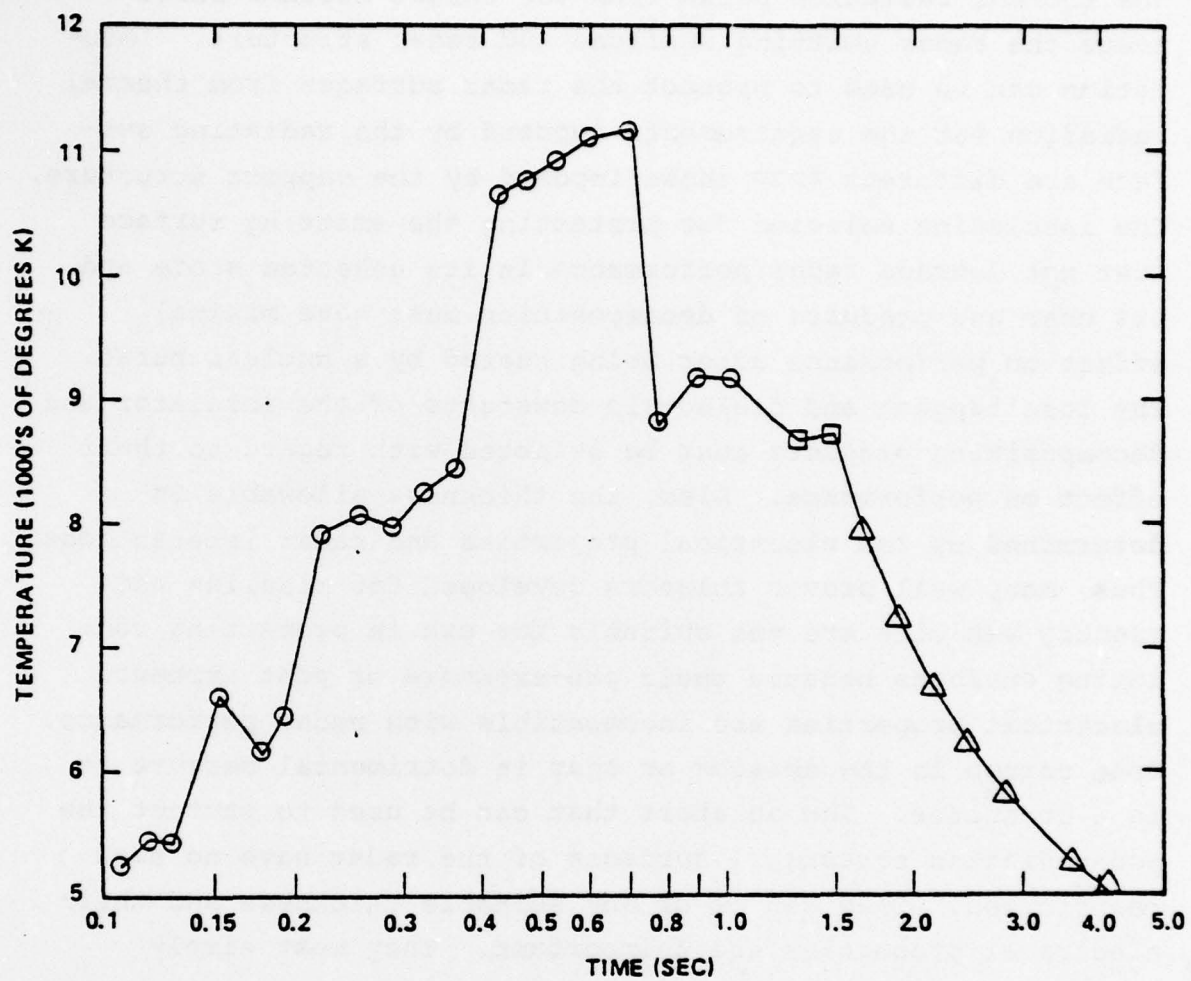


FIGURE 2.8. EFFECTIVE BLACKBODY TEMPERATURE

The thermal radiation pulse from the threat nuclear burst heats the radar emitting surfaces and radar structure. Insulation can be used to protect the radar surfaces from thermal radiation but the requirements imposed by the radiating surface are different from those imposed by the support structure. The insulation selected for protecting the emitting surface must not degrade radar performance in its unheated state and its char and products of decomposition must have minimal effect on performance after being heated by a nuclear burst. The loss tangent and dielectric constants of the insulator and decomposition products must be selected with regard to their effect on performance. Also, the thickness allowable is determined by the electrical properties and radar interactions. Thus, many well proven ablators developed for missiles and reentry vehicles are not suitable for use in protecting radiating surfaces because their pre-exposure or post exposure electrical properties are incompatible with radar performance. Free carbon in the ablator or char is detrimental because it is a conductor. The ablators that can be used to protect the non-radiating structural surfaces of the radar have no such restriction. They can be of any suitable thickness and their electrical properties are unimportant. They must simply survive and remain weather resistant.

The insulators or ablators chosen to protect the radar radiating surfaces and structural surfaces must be able to withstand the environment (rain, snow and ice) without deteriorating and they must be capable of withstanding the airblast pressures which will tend to deform them. They must be capable of transmitting the pressure to a load carrying member. Furthermore, the ablator should not absorb water to any depth because the steam formed by the heat from a nuclear burst may destroy the ablator or if it collects in the bond area, it may blow the ablator from the protected structure. Furthermore

trapped or absorbed water will freeze and tend to breakup the insulator when ice is formed.

Thermally, the ablator must be adequate to prevent wrapping of the structure due to differential thermal expansion. Of course, it should prevent melting, cracking, or electrical property and mechanical property changes in the protected structures. For example, although most steels could withstand heating to 400°F for a short time, the thermal stresses introduced by suddenly heating the surface to 400°F even for a short time could cause wrapping or failure of a structure.

Thus, the establishment of thermal performance requirements and electrical performance requirements for materials to protect radars from nuclear thermal radiation and blast environments is not a simple task. The requirements can only be determined after establishing selected materials performance levels and evaluating the impact of these materials on the radar performance. This analysis was performed during this program and is reported in Section 5 of this report.

3.0 CANDIDATE HARDENING MATERIALS

3.1 Ceramic Coating

During previous studies* for BMDATC, SAI has investigated the use of thin ceramic coatings for thermal protection under severe environments. The mission for the ceramics was to protect a metal missile structure from atmospheric heating in the lower atmosphere while flying through the air at velocities as high as 16,000 fps. Heating rates experienced by the ceramic coating would be as high as 3500 BTU/Sec.Ft². (949 cal/cm²sec.) Numerous tests were conducted in the SAI arcjet heater facility in which thin layers of various ceramics attached to thin metal substructures were heated at rates of 2000 BTU/Sec.Ft² (542 cal/cm²Sec). The specimens were representative of missile structures in which the substructure was a MAR-M200 superalloy or TZM molybdenum alloy. Plasma spray and flame spray processes were used to spray molten ceramic droplets onto the surface of the base metal for thermal protection. The thickness of ceramic varied between 0.005 to .090 inches and metal thickness was .090 inches for the MAR-M200 and .125 inches for the TZM. Ceramics evaluated in the thermal test program included:

- Chromium oxide
- Aluminum oxide
- Zirconium oxide
- Zirconium oxide plus yttrium oxide
- Zirconium oxide plus magnesium oxide
- Aluminum oxide plus calcium oxide
- Aluminum oxide plus magnesium oxide

The thermal tests conducted in the SAI arcjet successfully demonstrated the thermal performance predicted for the ceramic coatings. Some ceramics were infiltrated with epoxy which acted as an ablator and reduced the back surface temperature of the metal in a very effective

* See References 3 and 4

manner. This is illustrated in Figure 3.1 which shows that the back surface temperature of the $\text{ZrO}_2 - \text{Y}_2\text{O}_3$ ceramic protected specimen is 1500°F lower at the end of test (1.8 seconds at $2000 \text{ BTU/sec. Ft}^2$) when it is infiltrated with epoxy than when it is uninfiltrated. The figure also shows that at 0.8 seconds the ceramic protected specimens are heated to approximately 300°F whereas a bare unprotected specimen is at 2000°F .

An optical pyrometer was used to obtain front surface temperature of the specimens during heating. The alumina and zirconia specimens all exhibited an emissivity of approximately 0.2. Thus, when the ceramic coatings were postulated for use as radar protection, the heating results were compared to radar environments.

Because the $2000 \text{ BTU/Sec.Ft}^2$ ($542 \text{ cal/cm}^2\text{Sec.}$) is a measure of actual input flux it must be compared to the actual input from thermal radiation with emissivity of 0.2. The test conditions corresponded to nuclear thermal equivalent radiations as shown below:

$$\text{Absorbed Flux} \approx 2700 \text{ Cal/cm}^2\text{Sec.}$$

$$\text{Absorbed Fluence} > 300 \text{ Cal/cm}^2$$

Actual nuclear radiation threat

$$\text{Absorbed Flux} \approx 1650 \text{ cal/cm}^2\text{Sec} \times 0.2 = 3330 \text{ cal/cm}^2\text{Sec.}$$

Because the flame and plasma sprayed ceramic coatings had successfully withstood heat fluxes greater than those expected for the radar environment and because they were a dielectric, they were proposed as candidate radar hardening materials. Also, because infiltrants were so effective in protecting the structure in the arc jet tests, it was proposed to use them for radar protection with the additional constraint of using

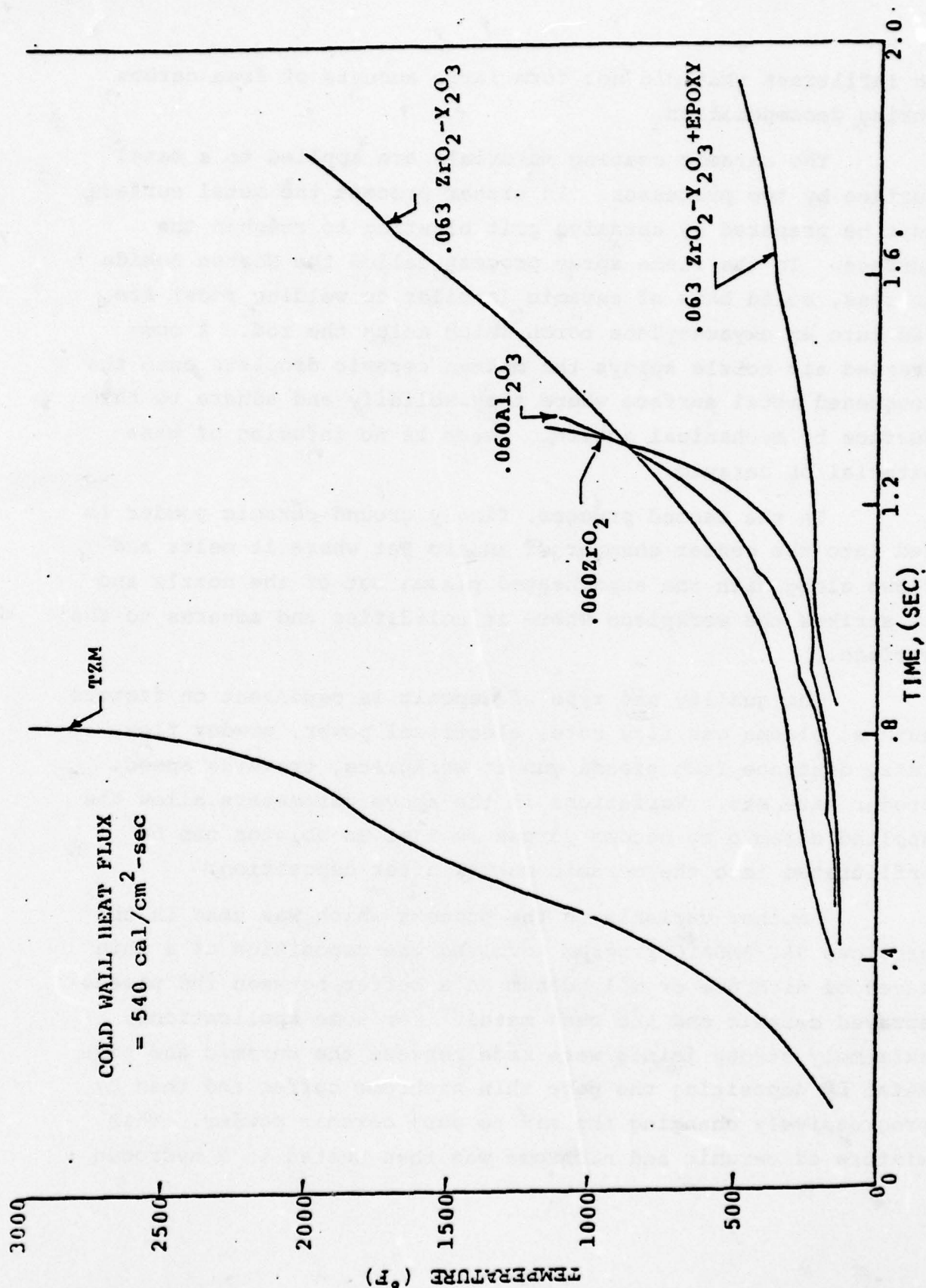


FIGURE 3.1. INFILTRATED CERAMIC COATING BACKFACE TEMPERATURE
FROM ARC JET TESTS

an infiltrant that did not form large amounts of free carbon during decomposition.

The ceramic coating materials are applied to a metal surface by two processes. In either process the metal surface must be prepared by abrasive grit blasting to roughen the surface. In the flame spray process called the Norton Rokide process, solid bars of ceramic (similar to welding rods) are fed into an oxyacetylene torch which melts the rod. A compressed air nozzle sprays the molten ceramic droplets onto the roughened metal surface where they solidify and adhere to the surface by mechanical action. There is no infusion of base material or ceramic.

In the second process, finely ground ceramic powder is fed into the center chamber of an arc jet where it melts and flows along with the superheated plasma out of the nozzle and it strikes the workpiece where it solidifies and adheres to the surface.

The quality and type of deposit is dependent on factors such as plasma gas flow rate, electrical power, powder flow rate, distance from plasma gun to workpiece, traverse speed, powder size, etc. Variations in the above parameters allow the applied ceramic to become porous so that an ablator can be infiltrated into the ceramic matrix after deposition.

Another variable in the process which was used in the previous SAI/BMDATC program involved the deposition of a thin layer of nichrome or molybdenum as a buffer between the plasma sprayed ceramic and the base metal. For some applications, extremely strong joints were made between the ceramic and base metal by depositing the pure thin nichrome buffer and then by progressively changing the mix to pure ceramic powder. This mixture of ceramic and nichrome was then heated in a hydrogen

furnace to diffuse the nichrome into the base metal and ceramic to form a cermet layer approximately .008 inches thick. For the radar experiment described in this report, the use of the cermet process was not investigated because preliminary investigated showed it to be bad from a radar transmission standpoint. Whether this initial assumption is still valid can not be answered at this time. No thermal bond failures were observed with this type of process. The ceramic coatings investigated are presented in Table 3.1.

3.2 Bulk Window Materials

As a part of this program, SAI investigated materials that could be used for windows or plugs for several BMDATC radar concepts. The material had to be strong enough to take the overpressure and had to be able to resist the thermal exposure without significant change in thickness or change in radar signal propagation properties. Investigation of the available window materials and tests previously conducted in the French Solar Furnace showed that most of the available candidates failed by thermal shock. As a result, the literature and manufacturers were consulted to see if there were new developments which could be useful for BMDATC radars. A number of candidate materials were obtained. These are listed in Table 3.2.

3.3 Bulk Ablative Materials

Unlike the bulk window materials, the bulk ablative materials need have no special electrical properties. They are to be used to protect structural portions of the radar from thermal radiation. They should be effective ablators and should be relatively inexpensive. Some may be very poor ablators but may have excellent insulation properties and resistance to thermal shock. They must be weather resistant and moisture proof. Structurally, the bulk ablators must be capable of transmitting, by compression and shear, the blast load imparted by the shock wave. This will be less than 1000psi and most materials are capable of doing this. Some of the candidate bulk ablators were rubbers, silicone rubbers, firebrick and commercial insulators. Table 3.3 lists the bulk ablators.

TABLE 3.1. CERAMIC COATINGS

Coating Materials

Al_2O_3

$\text{Al}_2\text{O}_3 \cdot \text{TiO}_2$

$\text{ZrO}_2 \cdot \text{CaO}$

$\text{ZrO}_2 \cdot \text{MgO}$

$\text{ZrO}_2 \cdot \text{Y}_2\text{O}_3$

Spinel

Infiltrant

Sylgard 184 (Silicone Resin)

TABLE 3.2. BULK WINDOW MATERIALS

Boron Nitride (NBR)

Boron Nitride (HP)

Boron Nitride (M)

Alumina (AD-995)

Alumina (AD-995) with porous alumina coating

Alumina (Durafrax)

Alumina (M)

Alumina (A)

Beryllia

Fused Silica 7941

AS-3DX

TABLE 3.3 ABLATOR/INSULATOR MATERIALS

Silicone Rubber (Down Corning Silastic E)

Alumina Firebrick

Zirconia Firebrick

Silfrax Firebrick

Teflon

4.0 THERMAL PROPERTIES ANALYSIS AND TEST

Thermal models were developed for the ceramic coatings, with and without infiltrant, and for the bulk "window" materials without ablation. The bulk silicone rubber model has been formulated; however, it must be updated with experimental data before it will give satisfactory results. The models were used to predict the performance of the ceramic coatings in the nuclear environment, to predict the material sample's response in the thermal tests and hence to size the samples and define instrumentation requirements, and to parametrically investigate the influence of various thermophysical properties.

All of the materials investigated were tested in the Thermal Radiation Simulator (TRS) and a limited number of materials were tested in the French Solar Furnace (FSF). The following paragraphs discuss the thermal modeling, the thermal tests and the results obtained.

4.1 Thermal Analysis

An analytical model was used to predict the transient thermal response of ablating ceramic coatings and silicone rubber. The method used and the models developed are as follows:

4.1.1 Ceramic Coating Thermal Analysis

The ceramic coating being modeled consists of a porous ceramic bonded to a steel substrate. The porous ceramic can either contain or not contain a silicone rubber infiltrant. The basic model to be described contains the infiltrant. If the infiltrant is not included, the model is simplified accordingly by removing the infiltrant's contribution to the thermal response.

A physical description of the material and the thermal model is shown in Figure 4.1. The primary heat input in the nuclear environment is time dependant radiation and it is the only heat input considered. The infiltrated ceramic coating acts as a thermally protective material through the following heat transfer mechanisms:

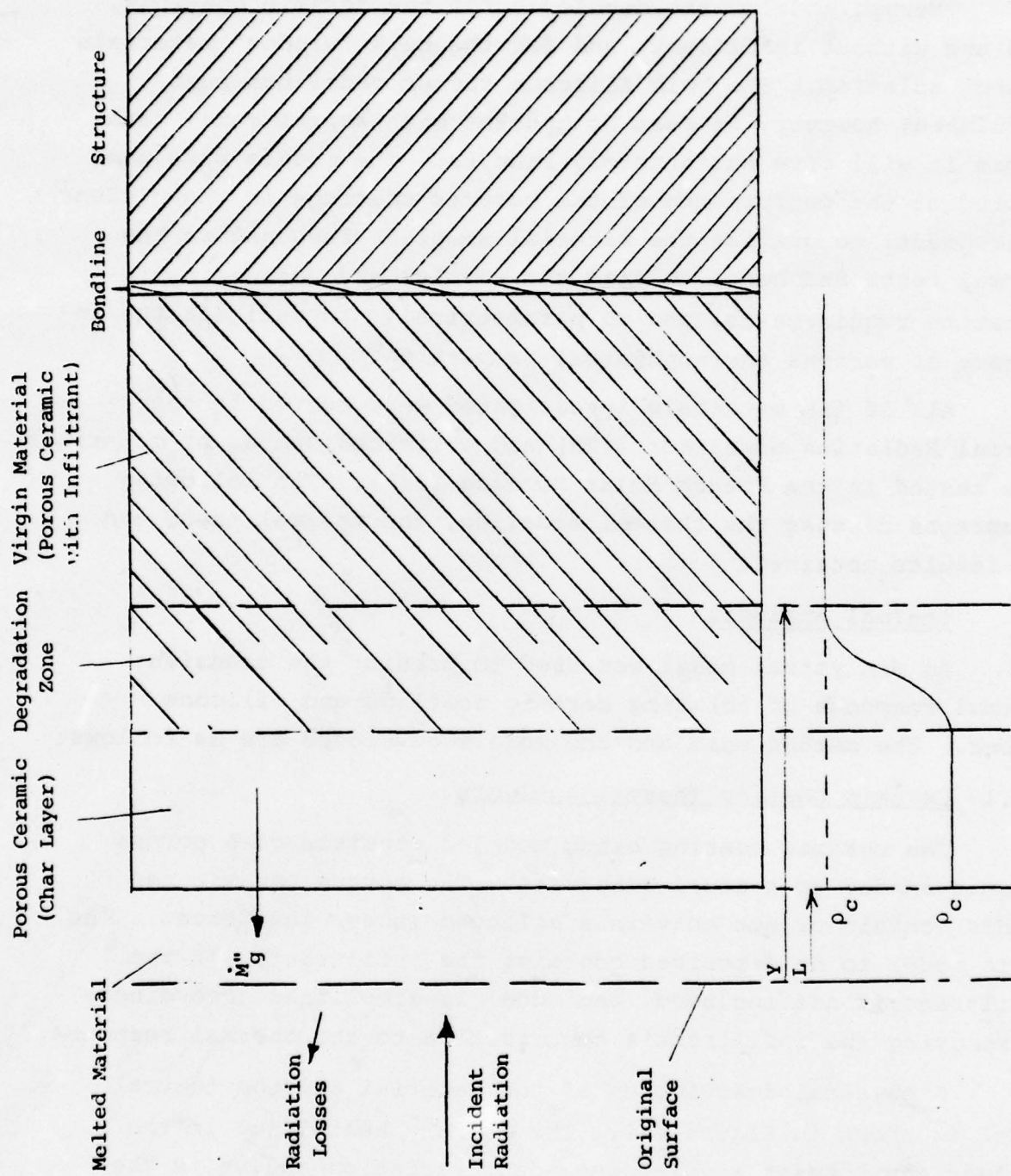


FIGURE 4.1. CERAMIC COATING THERMAL MODEL

1. The majority of the incoming heat is reflected due to a low surface absorptivity.
2. The surface reradiates at a high temperature.
3. Heat is conducted into the coating and absorbed.
4. The infiltrant decomposes to its product gases, absorbing its heat of decomposition and also absorbing heat from the ceramic as it escapes to the surface.
5. The ceramic melts, absorbing its change of phase heat.

In the current model, the melt layer of ceramic is assumed to be removed from the surface immediately due to the nuclear environment air flow. This is a conservative model, because if the melt layer did remain, it would offer additional thermal protection due to its thermal resistance, thermal mass, and possible vaporization.

Another parameter not included is possible radiation blockage due to a vapor cloud formed by the reactant gases. If this cloud were able to remain in front of the venting surface during a portion of the heating, it could absorb some of the incident radiation.

The analytical model was developed using the MRCAPER computer code, of which the basic theory is presented in Reference 5. A schematic of the model is shown in Figure 4.1. As the outer surface of the ceramic is heated, heat is conducted inward and the infiltrant decomposes as its temperature of decomposition is reached. The decomposing infiltrant evolves gases which percolate to the ceramic surface through the pores. Thus, the infiltrant is in a steady state condition of decomposition below the surface of the ceramic. As the ceramic surface itself reaches its melt temperature, it is removed, thus causing recession of the surface.

The governing equations for energy conservation, infiltrant decomposition rate, and pyrolysis gas mass flux are

$$\rho_c \frac{\partial T}{\partial t} = \frac{\partial}{\partial y} \left(k \frac{\partial T}{\partial y} \right) + (h_g - h_s) \frac{\partial \rho}{\partial t} + \dot{m}_g \frac{\partial h_g}{\partial y} \quad (4-1)$$

$$\frac{\partial \rho}{\partial t} = - \sum_{i=1}^N \frac{(\rho - \rho_c)^{n_i}}{\rho_v} A_i e^{-E_i/RT} \quad (4.2)$$

$$\dot{m}_g = - \int_y^{\infty} \frac{\partial \rho}{\partial t} dy \quad (4.3)$$

where A_i = frequency factor for i^{th} pyrolyzing reaction

- c = specific heat
- E_i = activation energy for the i^{th} pyrolyzing state
- h = enthalpy
- k = thermal conductivity
- L = surface recession
- m = mass flux
- n_i = reaction order for i^{th} pyrolyzing reaction state
- R = universal gas constant
- t = time
- y = coordinate normal to surface
- ρ = density

Subscripts

- c = of ceramic without infiltrant or of char
- g = of gas
- s = of solid
- v = virgin material

The heat removed by the melting of the ceramic is handled as a boundary condition and removed from the incoming heat.

These equations then form the basis of the theoretical model that is solved by the MRCAPER computer code. The model has been developed for porous alumina and zirconia coatings with and without the silicon resin infiltrant, Dow Corning Sylgard 184. The material thermal properties are given in appendix A. The model has been used to predict the performance of alumina with infiltrant in the nuclear environment, Section 4.1.1.2, to predict the performance and size the samples and instrumentation in the thermal tests, Section 4.3.2 and 4.4.3, and used in a parametric investigation of the effects of infiltrant and various thermal/physical parameters, Section 4.1.1.1 and Appendix F.

4.1.1.1 Ceramic Coating Thermal Analysis

A parametric analysis was made of porous alumina and zirconia coatings, with and without silicone resin infiltrant bonded on a stainless steel substrate. The purpose of the analysis was to size the material specimen for the thermal tests, to provide temperature profiles for the structural analysis, and to investigate the effect of various material property and design variables. The heat flux utilized was the TRS expected maximum heating environment. This environment is similar to the nuclear environment for a material with surface absorptivity of 0.2.

The thermal environment description and the analysis results are presented in Appendix F. The results of the parametric investigation of variables are summarized as follows:

1. The ceramic acts as an insulator and its surface heats to its melting temperature almost immediately.
2. The alumina and zirconia perform similarly thermally except that the zirconia has a higher melt temperature.
3. A thicker coating exhibits more ablation than a thin one; however, the thicker coating also has more material remaining after the exposure.
4. Decreasing the porosity of a non-infiltrated ceramic increases its conductivity and thermal mass, resulting in a lower ceramic temperature.
5. A silicone resin infiltrant in the porous ceramic reduces the amount of ablation of the ceramic, as long as it doesn't increase the ceramic absorptivity.

4.1.1.2 Ceramic Coating Predicted Performance In The Nuclear Environment

The porous ceramic coating model was used with the design nuclear radiant flux profile to predict the performance of 15 percent porous alumina coating on 1.0 inch steel. An absorptivity

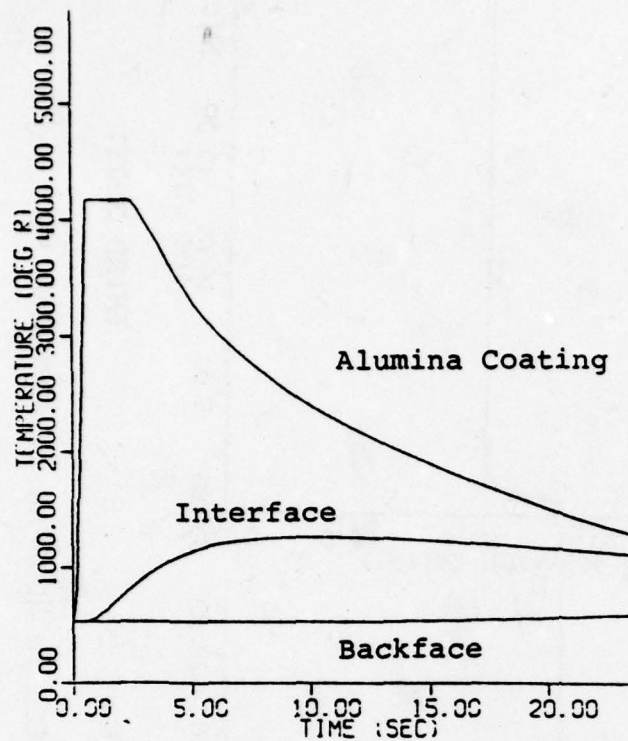
of 0.2 was used. The resulting surface recession, surface temperatures, and indepth temperature profiles are shown for a single burst in Figure 4.2. The resulting surface recession is approximately 0.02 inches for the 0.125 inch sample. Figure 4.3 shows the surface temperature profile and cumulative surface recession for an exposure to 3 bursts, with sufficient time between bursts to return to ambient temperature. This coating would be able to withstand 3 nuclear bursts.

A low surface absorptivity is critical. Figure 4.4 compares the results of the 0.2 absorptivity ceramic with a 0.5 absorptivity ceramic. The ceramic with an absorptivity of 0.5 has a single burst recession of 0.09 inches. Thus, it could not withstand exposure to multiple bursts.

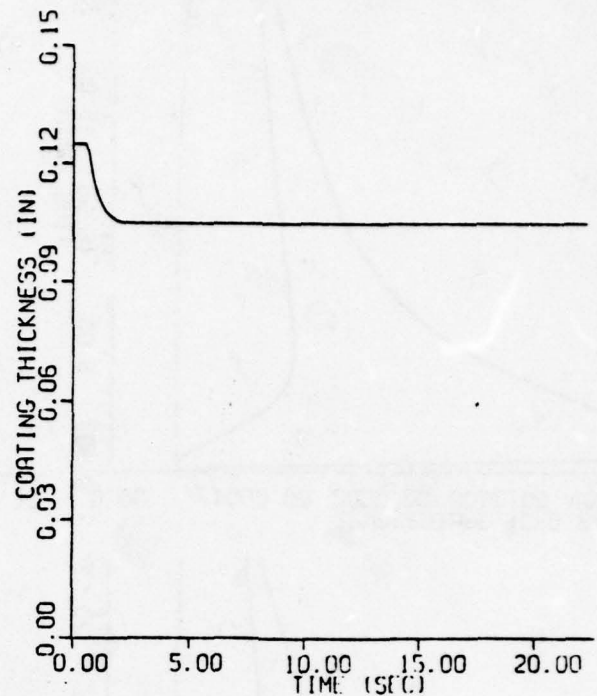
4.1.2 Silicone Rubber Ablation Model

The physical description of the silicone rubber coating in the nuclear environment is shown in Figure 4.5. The incoming heat decomposes the silicone rubber and forms a char layer. If this char layer stays intact, it forms a low conductivity layer that protects the remaining virgin silicone rubber, which is still decomposing, but at a much slower rate. The char layer has a high absorptivity so that it absorbs most of the incoming energy; but likewise, it has a high emissivity and high surface temperature such that a large amount of the absorbed energy is reradiated away.

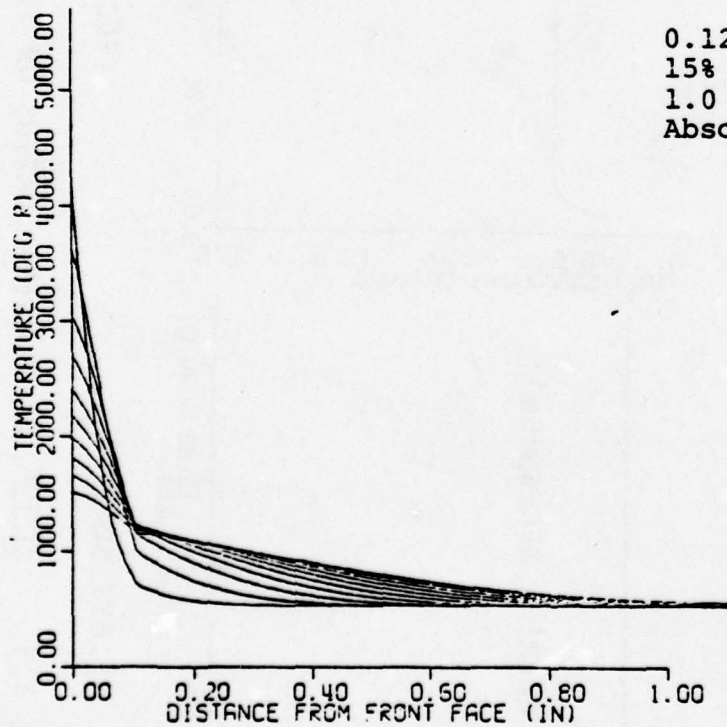
The thermal model again uses the MRCAPER code and the theory of Section 4.1.1. The portion of the material at the lower density, ρ_c , is now the char layer (Figure 4.1). The necessary material thermal and kinetics data were evaluated and are presented in Appendix A. The model has not yet been checked out and made operational, although preliminary investigations indicated that the char layer which would develop in the thermal tests would remain relatively thin with the remainder of the silicone rubber remaining in its virgin state.



Temperature Profiles



Surface Recession



In-Depth Temperature Profiles

0.125 Inch Alumina
15% Porosity
1.0 Inch Steel Substrate
Absorptivity - 0.2

FIGURE 4.2. ALUMINA COATED STEEL EXPOSED TO ONE NUCLEAR BURST

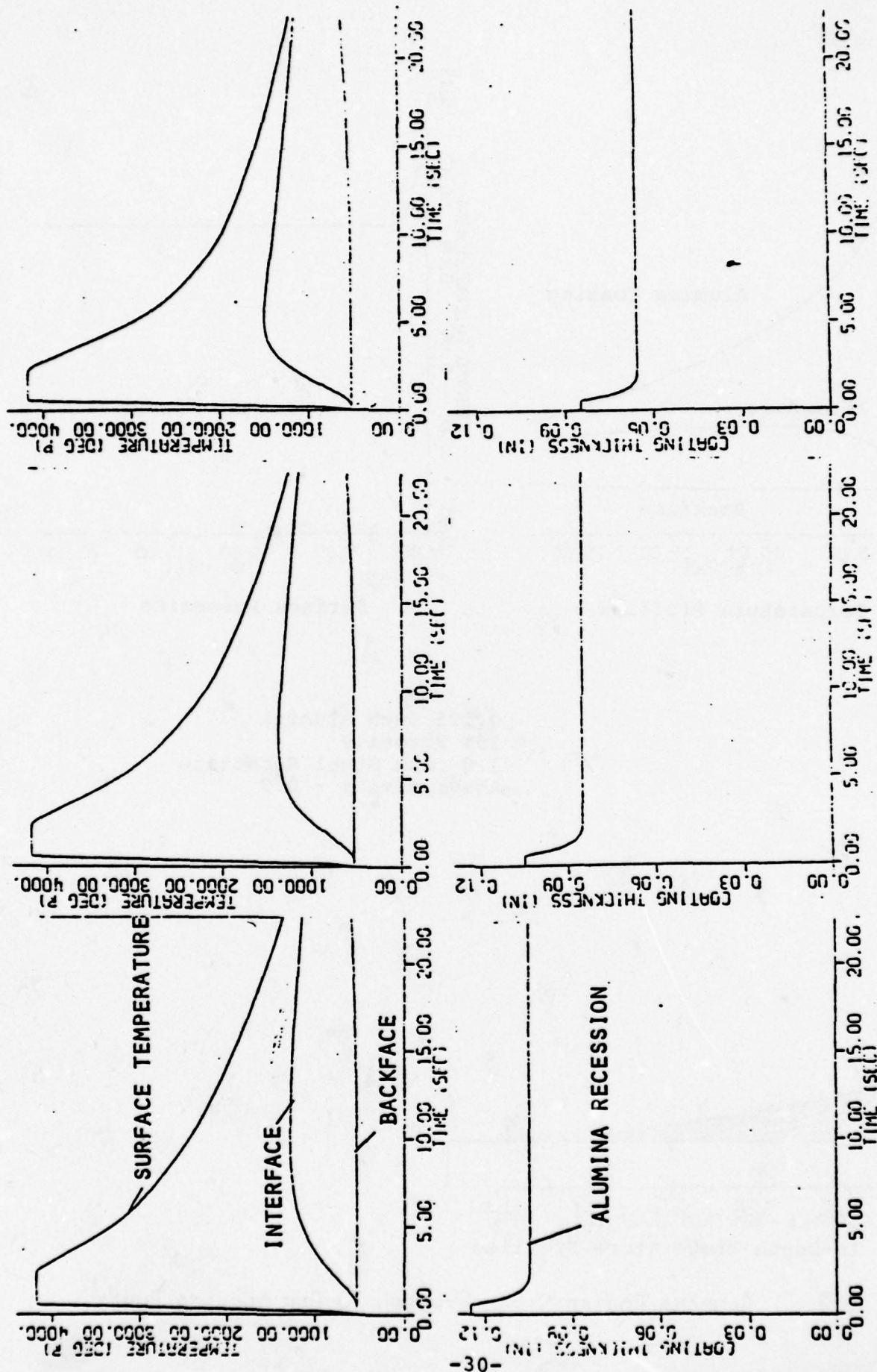


FIGURE 4.3. 0.125 IN. ALUMINA COATING ON 1.0 IN. STEEL IN NUCLEAR ENVIRONMENT ($\alpha = 0.2$)

0.125 IN ALUMINA COATING
1.0 IN STEEL SUBSTRATE

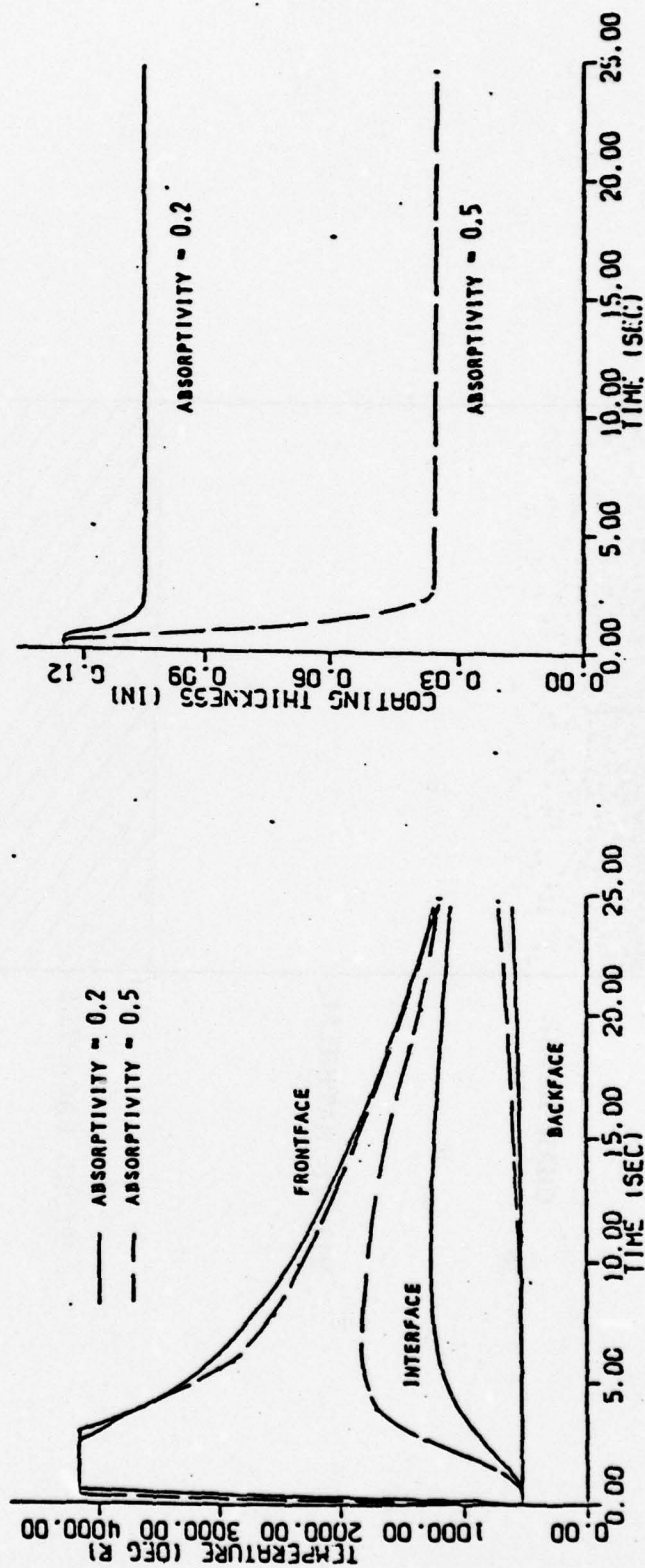


FIGURE 4.4 ABSORPTIVITY EFFECT ON CERAMIC COATING IN NUCLEAR ENVIRONMENT (1 BURST)

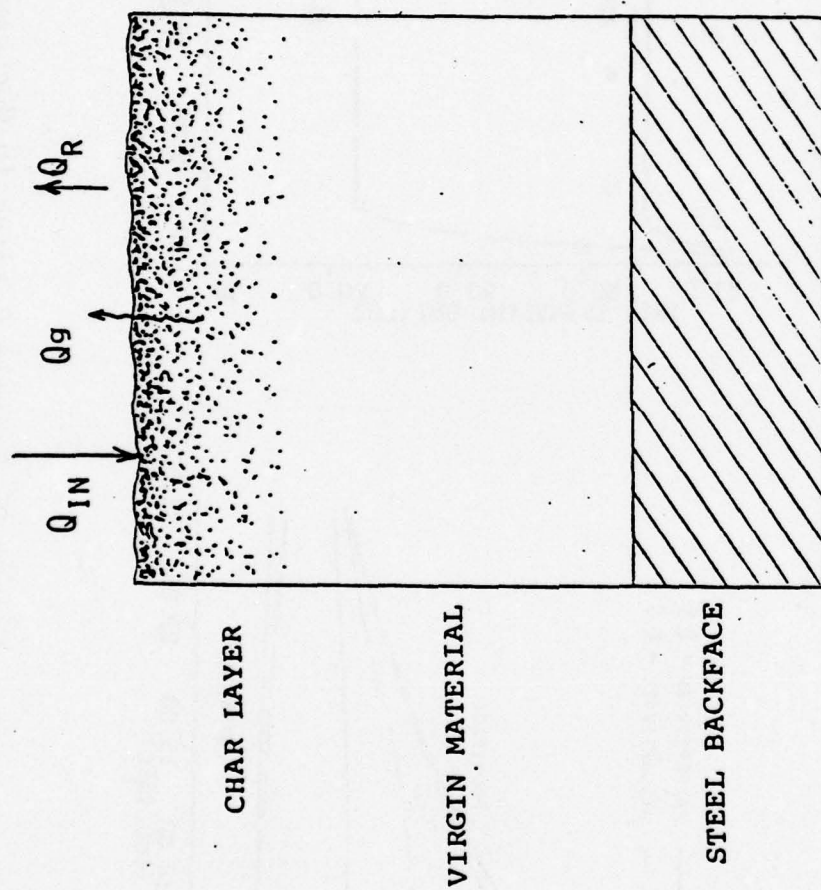


FIGURE 4.5. SILICONE RUBBER THERMAL MODEL

4.1.3 Bulk "Window" Material Thermal Modeling

The thermal response of the bulk materials in the TRS tests was predicted to (1) indicate the backface temperatures expected in order to specify the temperature indicating paint ranges required, and (2) indicate the type of thermal response expected, i.e., surface melting or interior absorption of all of the heat. The response was calculated using a transient conduction code which does not take surface decomposition into account. This code is described in Reference 6.

4.2 Comparison Of Thermal Simulators Facilities Capabilities

In materials research, there are a number of different types of heating schemes in use. These types are briefly discussed to show their characteristics.

4.2.1 Solar Furnace

The solar furnace uses radiant energy from the sun. It collects the radiation in the form of visible light, infra red and ultra violet on a large area covered by mirrors. The mirrors are then focussed onto the target by curved mirrors acting as a lens. Some of these systems use first surface mirrors which reflect all of the energy to the target but most of them use second surface mirrors which internally absorb ultra violet and other radiation wavelengths depending on the glass characteristics. These simulators are useful but their performance and characteristics depend on time and aging.

The French Solar Furnace facility at Odeillo, France is the most powerful thermal radiation source available. It has a second surface mirror system which means that the aluminized reflecting surface is behind the glass as in a common household mirror. Thus the rays of the sun must pass through the glass to strike the rear reflecting surface and then pass out of the glass to exit. This causes ultra violet to be absorbed in the glass and also refracts the light rays to some degree. In addition, as the mirror system ages, its glass cover becomes

less transparent due to sandblasting by wind driven particles and deterioration. Therefore, although the French solar furnace had a maximum flux capability of $400 \text{ cal/cm}^2 \text{ sec}$ on a bright sunny day, it has deteriorated to approximately 50% of that value; however, it is being refurbished. Fluence available depends on the quality and time exposure of sunlight.

Testing is accomplished by focussing the hot spot to a diameter in the order of three inches. The radiation is blocked from the specimens by shutters that can open or close upon demand. For precise timing, the specimen (generally 2 inches in diameter) is exposed to the hot spot by rotating a disk holding the specimen past a water cooled iris by means of a geneva mechanism. It is possible to instrument the specimens with thermocouples and to observe the specimens with cameras and optical pyrometers.

A second solar furnace designed for materials research is located at the White Sands Missile Range. It has a flux capability on the order of $80 \text{ cal/cm}^2 \text{ sec}$. It is similar to the French facility but is smaller and in a poor state of repair. A visit was made to WSMR to inspect the facility and its instrumentation. A $400 \text{ cal/cm}^2 \text{ sec}$ facility is in the design stage at WSMR and is scheduled for construction in 1979. It consists of a large parabolic radar dish lined with mirrors which is capable of tracking the sun directly.

4.2.2 Plasma Jet

Much materials heating research is conducted in a plasma

jet or arc jet heating facility. Heat is generated by striking an arc between an internal and external electrode and passing a gas between the electrodes. The gas is heated by the electrical discharge and becomes a plasma which exits the nozzle and impinges on the test specimen. Very high heating rates can be generated in these arc jet facilities, but the heating action does not simulate radiation heating from a nuclear burst.

The plasma jet has sufficient kinetic energy to sweep away melt as soon as it is formed. Thus, the heat absorbing capacity of the melt on the surface is lost in that no account is taken of the heat required to raise the melt to boiling temperature and the heat required to actually boil the melt. Also, the effect of effluent gases and vaporized material in screening radiation is not measurable because the gases are driven away by the plasma and there is no radiation heating. Furthermore, because many materials of interest may be or are transparent to radiation to a degree, heating in depth cannot be simulated. Therefore, the plasma jet facilities were not recommended for the tests in this study. However, the plasma jet may be a useful way to screen materials for susceptibility or resistance to thermal shock.

4.2.3 Glow-Bar Heaters

Considerable radiation heating can be obtained by electrically heating bars or plates of tungsten or graphite near a specimen. The heating must be in a vacuum to prevent oxidation of the radiator. This type of facility was not considered because the radiating surfaces evaporate large quantities of graphite or tungsten which will contaminate the specimen being irradiated and change its absorptivity and electrical properties. The radiation heaters generally work in a vacuum to reduce oxidation of the radiating element. Maximum temperatures are limited to values well below the melting point of the radiator because evaporation or sublimation near the melting point becomes very severe. Generally, tungsten radiators may operate below 5000°F and graphite radiators below 6000°F. This makes the sources marginal

(even if deposits of radiator vapor are no problem) because the ceramics melt and boil at high temperatures. Alumina, Al_2O_3 , melts at 3700°F and boils at 5396°F while zirconia, ZrO_2 melts at 4800°F and boils at 5890°F . Unless emissivity and absorbtivity approach one, these temperatures will never be reached in a glow heater type of facility. Other variations of the glow heater facilities are banks of quartz lamps with radiating filaments all focussed on the test specimen. Their maximum temperature is approximately 3000°F which is too low to melt and ablate many of the materials of interest in this program, hence, this limits the usefulness of such a facility.

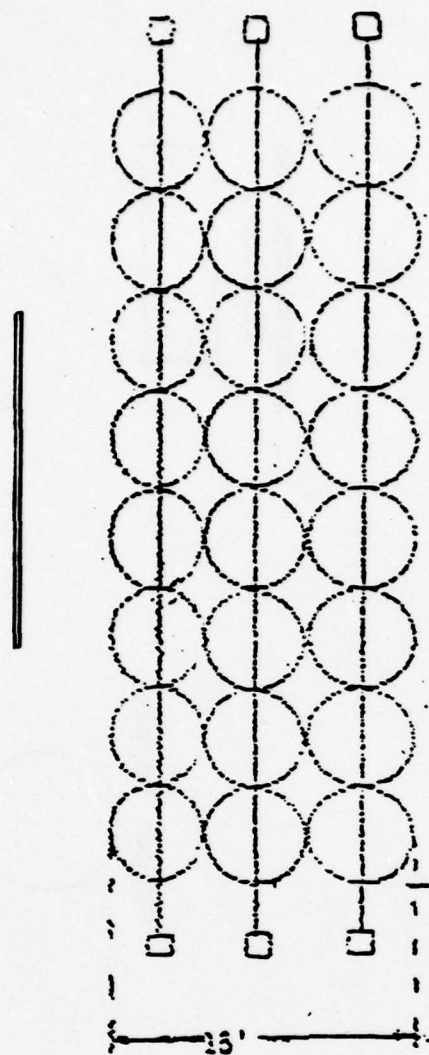
4.2.4 SAI Thermal Radiation Simulator

Under contract to DNA, SAI has developed and tested a thermal radiation simulator based on the flashbulb principal. Thin plastic bags are filled with gaseous oxygen. Fine aluminum powder is dispersed throughout the interior of the oxygen filled bag and is ignited by an electrically initiated pyrotechnic. The combustion of aluminum in oxygen generates a high temperature gas which glows and radiates. A large fireball is formed which expands and cools down as time progresses. The fireball rises and leaves the ground within a few seconds.

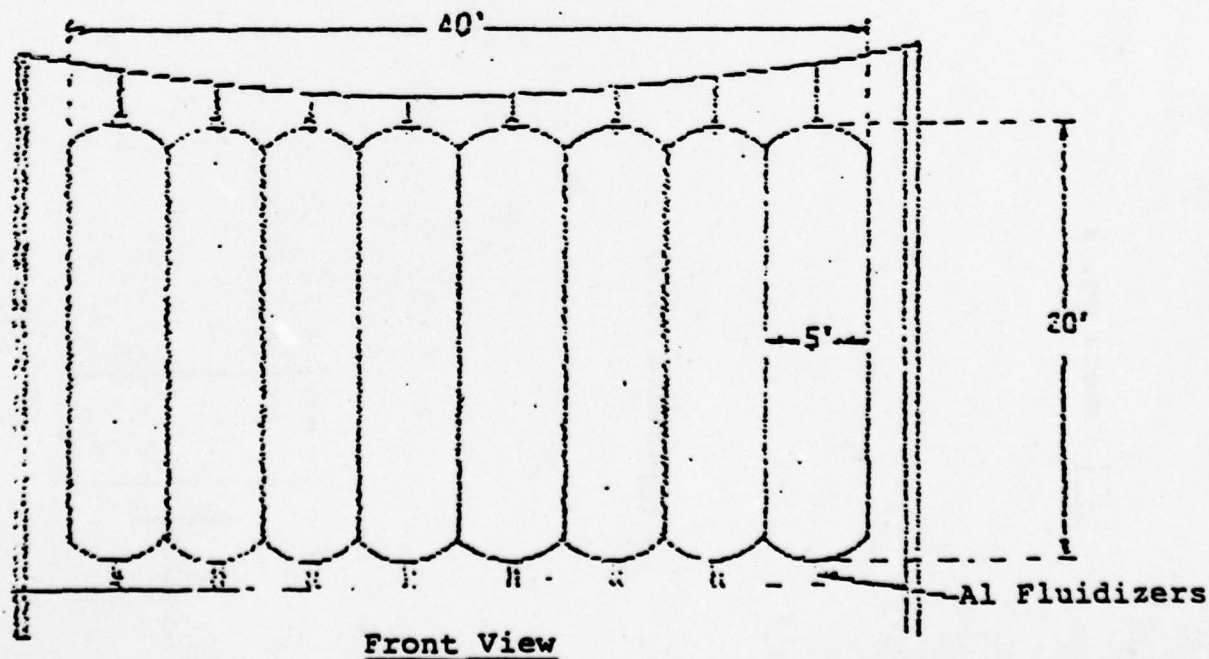
Although the aluminum powder combustion type of thermal simulator was fully developed for DNA in small sizes, a large 24 bag array was designed and fabricated for this project. Figure 4.6 schematically illustrates the bag array. The framework was fabricated from heavy steel structural members. The array consisted of three rows of 8 bags each as shown in the figure.

Oxygen was supplied in liquid form and was stored in a reservoir as illustrated in figure 4.7. An air-liquid heat exchanger was used to convert the liquid oxygen to gaseous oxygen. It was piped from the storage and converter area to the test area. Instrumentation consisting of calorimeters and thermocouples were located on the specimen mount and in several points outside of the fireball.

Samples
and
Calorimeters



Plan View of Array



Front View

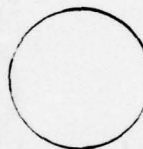
FIGURE 4.6. SAI THERMAL RADIATION SIMULATOR

☐ Camera No. 2

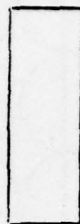
☐ Camera No. 1

Samples
Plastic Bags

Oxygen Supply



Instrumentation
Trailer



☐ Camera #3

FIGURE 4.7. TRS TEST LAYOUT

Based on previous tests with smaller arrays (fewer bags), the predicted total maximum flux was 400-1000 cal/cm²-sec within the fireball, of which 350 cal/cm²-sec is due to radiation. Fluence was predicted to be 403 cal/cm² outside the fireball. Actual performance was lower than expected and is described in Section 4.3.

The primary advantages attributed to the flashbulb type thermal radiation simulator are its very high heat flux, its large available area for testing, and its ability to radiate over the desired frequency band.

4.3 Thermal Radiation Simulator Tests

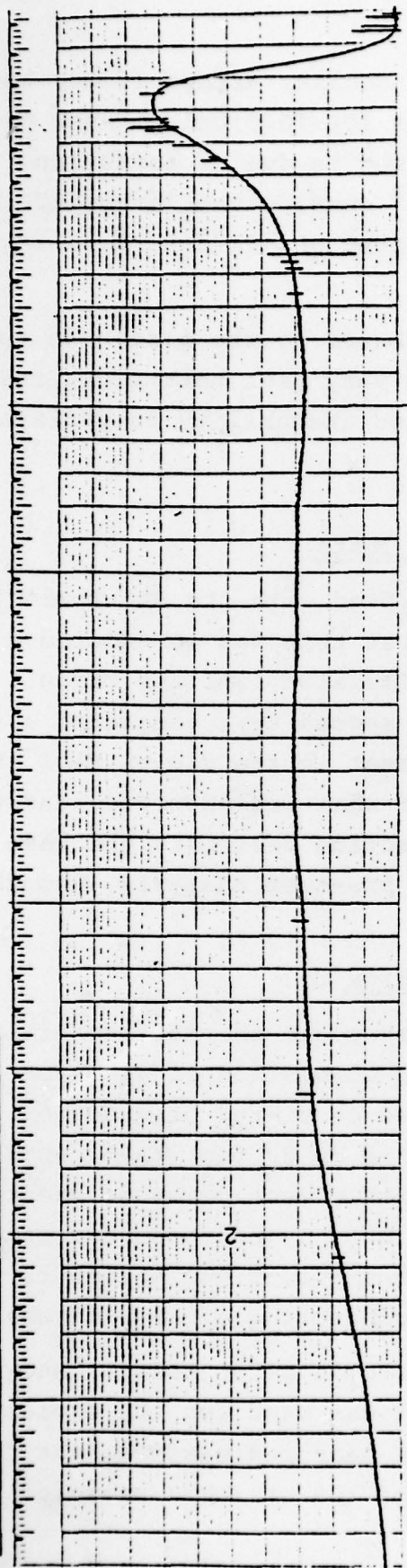
Two thermal tests were attempted with the SAI Thermal Radiation Simulator (TRS). The first test was considered a no-test because of a failure in the simulator ignition circuit which resulted in very low heating. The second test generated a successful fireball; however, the heat in the vicinity of the sampler was less than 10 percent of what was expected, and the results are quite limited. This section describes the test facility, the test procedures, the pre-test analysis, and the results.

4.3.1 Description Of The TRS Facility

The TRS simulates the nuclear event thermal radiation by generating a large fireball through combustion of aluminum powder in oxygen. The facility used consisted of a set of 24 plastic bags, each 5 feet in diameter by 20 feet tall, shown in Figure 4.6. The bags are filled with oxygen prior to the test. Aluminum is then injected into the bags by nitrogen gas prior to ignition. At the time required for the aluminum powder to fill the bags, the mixture is ignited, generating a large fireball.

A TRS calorimeter printout from a prior test is shown in Figure 4.8. This is the model that was used for the expected TRS heat output. The largest prior measured maximum heat flux was 225 cal/cm² sec and a fluence of 109 cal/cm², measured 5 feet from a 4 bag array.

Typical TRS Calorimeter Printout



-40-

Expected Output

Radiation Only

Fireball Heating

Maximum Flux, $\text{Cal/cm}^2\text{sec}$
Fluence, cal/cm^2

350
400

400-1000
460-1150

FIGURE 4.8. EXPECTED TRS HEAT OUTPUT USED IN PREDICTIONS

In order to obtain a more severe heating environment, a 24 bag array was selected. The mechanics of this fireball are unknown and the facility should be considered very exploratory. The resulting fireball heat output is a function of the fuel-oxidation mixture, the array layout, the calorimeter/sample location, the ignition timing, and other factors as yet unknown. For the 24 bag array, the TRS facility operator predicted a flux of $350 \text{ cal/cm}^2 \text{ sec}$ and a fluence of $400 \text{ cal/cm}^2 \text{ sec}$ due to radiation alone (no fireball convective heating). Within the fireball, the total flux was predicted to be 400 to $1000 \text{ cal/cm}^2 \text{ sec}$ and a fluence of 460 to 1150 cal/cm^2 . This very large heating within the fireball was assumed to partially be due to condensation of aluminum oxide vapor. This expected flux was applied to the heat profile of Figure 4.8 with the resulting predicted heat profiles shown in Figure 4.9.

4.3.2 Pre-Test Analysis

Pre-test analyses were run on the materials for the purpose of sizing the samples, specifying the instrumentation, and to predict the expected material thermal response. Radiation only heating utilized the lower curve of Figure 4.9 giving a peak flux of $350 \text{ cal/cm}^2 \text{ sec}$. For samples within the fireball, the upper curve with a peak flux of $1000 \text{ cal/cm}^2 \text{ sec}$ was used. Of this $1000 \text{ cal/cm}^2 \text{ sec}$, $350 \text{ cal/cm}^2 \text{ sec}$ was treated as radiation and $650 \text{ cal/cm}^2 \text{ sec}$ as convection or condensation (all $650 \text{ cal/cm}^2 \text{ sec}$ is absorbed, which is the maximum possible heating).

The radiation only heating, with the sample behind a pyrex glass cover was used so that the effective absorptivity of the samples could be obtained. The full fireball heat flux, $1000 \text{ cal/cm}^2 \text{ sec}$, represents the maximum heat the samples could receive. The actual heat received would be somewhat less depending on the sample surface temperature and that part of the flux due to convection or condensation. However, this maximum flux was used for sizing the samples; and, it also more nearly represents the nuclear flux for the parametric study in Appendix F.

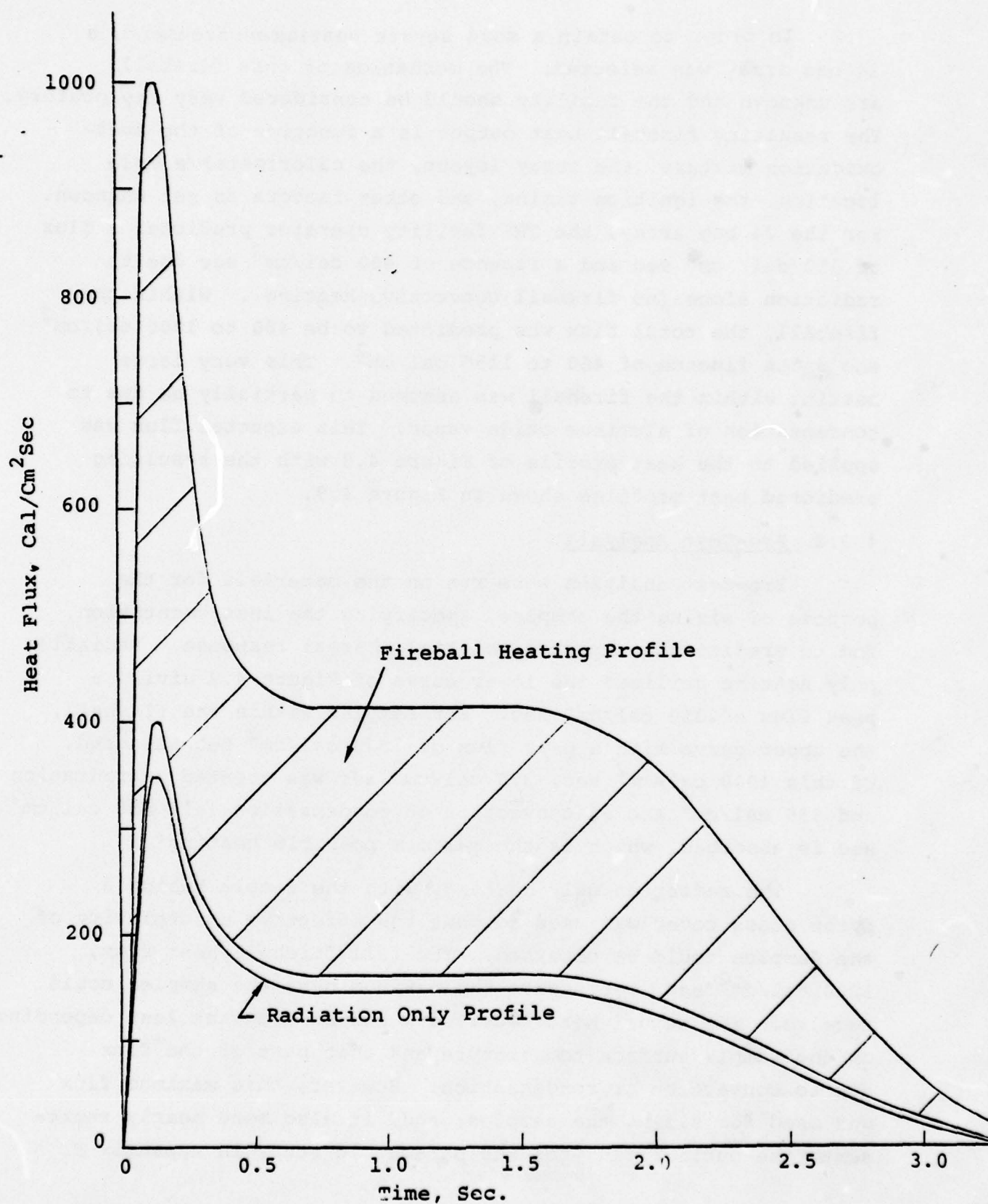


FIGURE 4.9. PREDICTED 24 BAG TRS HEAT FLUX

The results of the pre-test analysis on alumina and zirconia coatings are presented in Appendix F. Based on these results, plus a minimum thickness requirement for the plasma spraying process, a 0.125 inch thick stainless steel substrate was selected for the radiation environment only samples, and 0.25 inch thick stainless steel substrate for the fireball exposure samples. At maximum heating, the radiation only samples would attain a surface temperature of about 1500°R (below melting), and a backface temperature rise of about 300°F. Those exposed to the full fireball flux of 1000 cal/cm² sec would have melting at the surface, and backface temperature rises of about 500 to 1000°F.

The thermal model discussed in Section 4.1.2 is not yet capable of predicting the true thermal response of the silicone rubber samples. However, from the chemical kinetics and heat of decomposition data developed and presented in Appendix A, it was estimated that 0.25 inch silicone rubber on a 0.125 inch thick stainless steel substrate would develop a thin char layer, with most of the silicone rubber remaining in its virgin state. A very small temperature rise is expected for the steel backface.

4.3.3 Test Procedures

All of the materials discussed in Section 3.0 were tested in the TRS test. The specimens consisted of six basic types:

1. 3 inch diameter plasma coated ceramic discs with stainless steel backing plates and thermocouples on the rear metal face. (S Band)
2. 4 inch square plasma coated ceramic plates with steel backing plates (X band)
3. 1 inch diameter plasma coated ceramic discs with steel backing plates (X band)
4. 2 and 3 inch diameter and 2 inch square bulk material samples
5. 2 inch square tantalum, columbium, aluminum, and stainless steel samples

6. 2 inch diameter teflon cylinder with thermocouples imbedded at 1/8, 1/4, 3/4, and 1 inch from the heated surface.

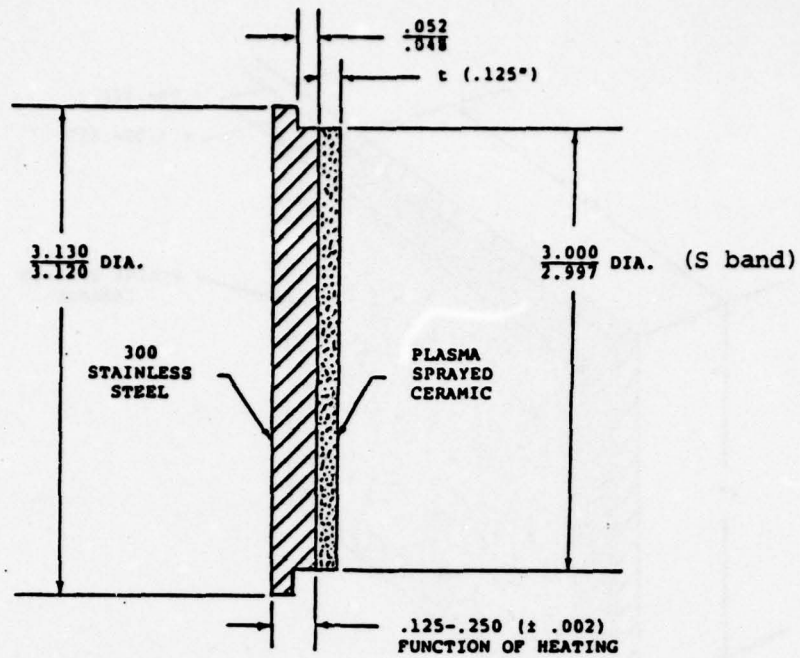
The samples were all mounted in transite holders. These mountings are shown in Figures 4.10 and 4.11 for the 3 inch diameter and 4 inch square ceramic coated steel substrate. Similar holders were used for the bulk material samples. The holders were designed to restrict heat conduction out of the samples as much as possible.

The test plan was to expose 4 samples of each material during the first test, with two of the samples mounted behind pyrex glass. This is shown in Figure 4.12. In the second test, one of the samples behind the pyrex glass would be removed as well as one of the unprotected samples. Thus, one sample would be exposed to the fireball of one test as well as one sample exposed to radiation only, and one sample exposed to the fireball of 2 tests, and similarly for one sample exposed to radiation only in 2 tests. Because the first test was considered a no test, only the second test setup was used, and one sample was exposed to the fireball of one effective test, and one sample was exposed to the radiation of this test.

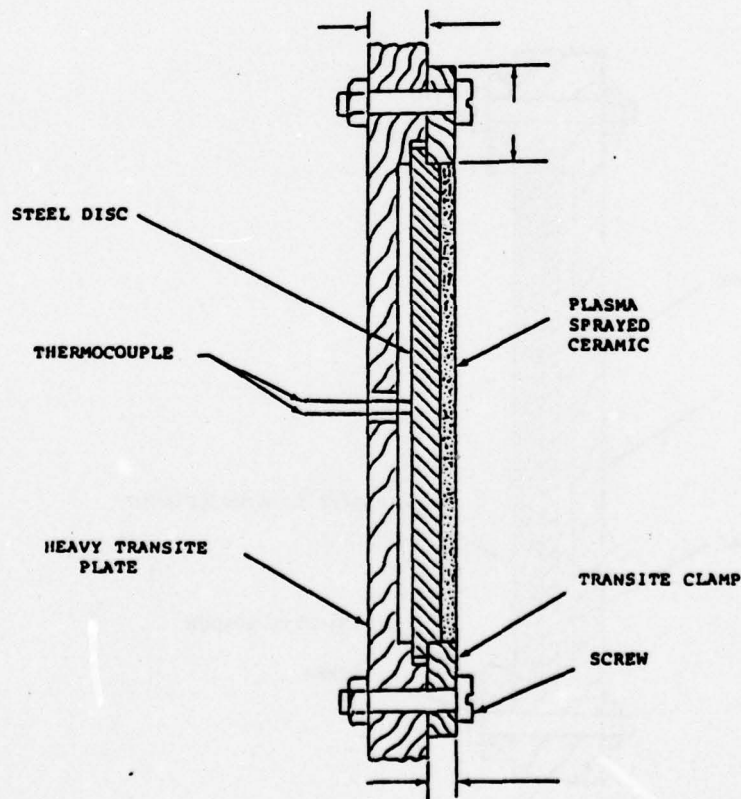
The samples, in their transite holders, were mounted on a steel frame 5 feet from the TRS bags at a height of 10 feet. (See Figure 4.6.) Three calorimeters were also mounted in this frame. Instrumentation included chromel-alumel thermocouples on the backface of all the 3 inch diameter ceramic coated disks, and temperature indicating paint on the backface of all samples. Standard and high speed cameras were used to take motion pictures of the samples and fireball.

4.3.4 TRS Test Results

As discussed, the first test was considered a no-test and only the second test is considered in these results. Although better than the first test, the second test gave much less heat than expected. The peak flux and fluence measured by 4 calorimeters



S band Radar Test Disc



TYPICAL TRANSITE TRS SPECIMEN MOUNT

FIGURE 4.10. THREE INCH DIAMETER CERAMIC COATINGS TEST FIXTURE

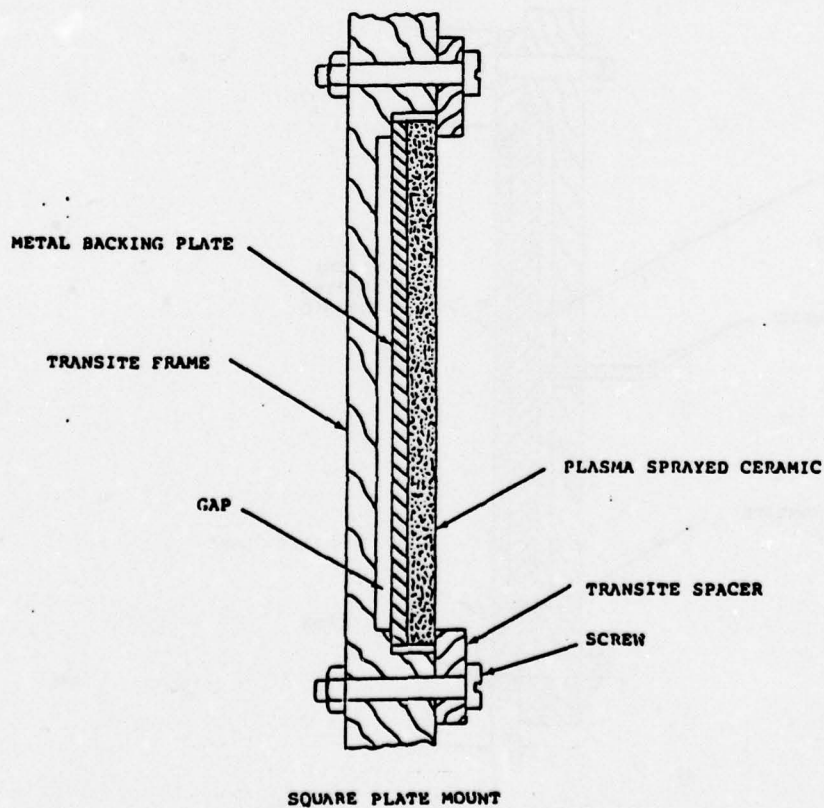
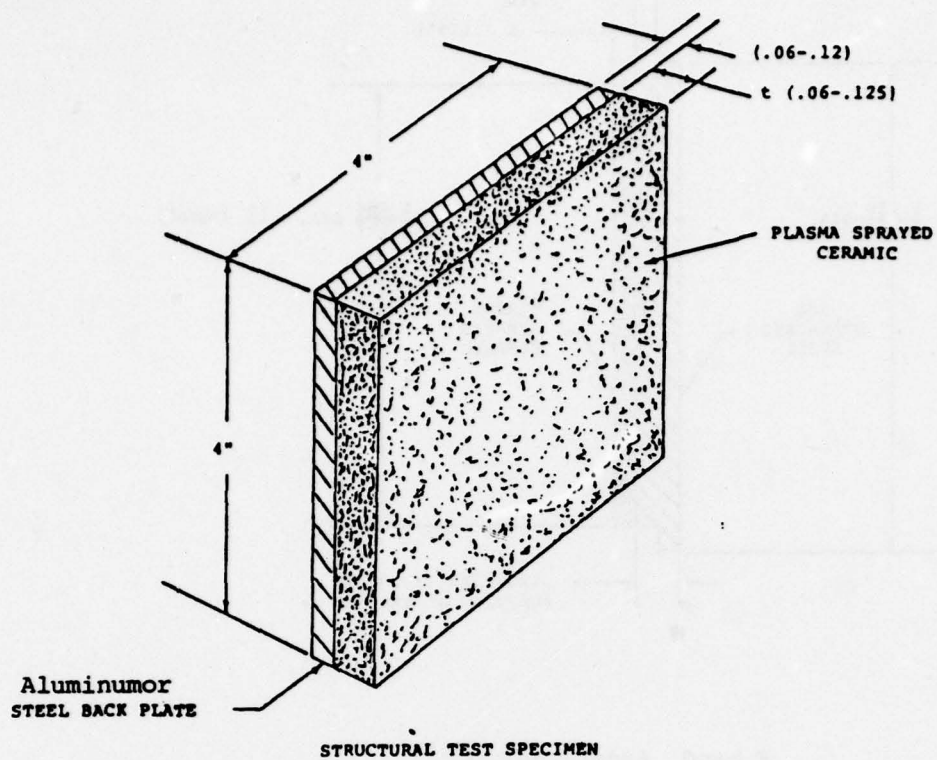
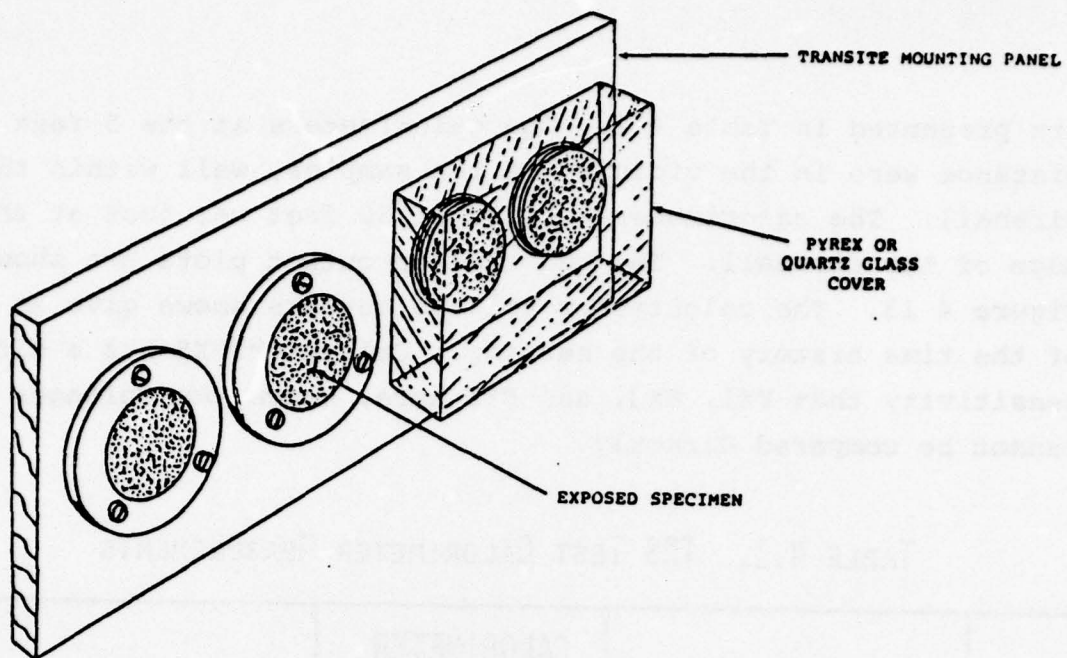
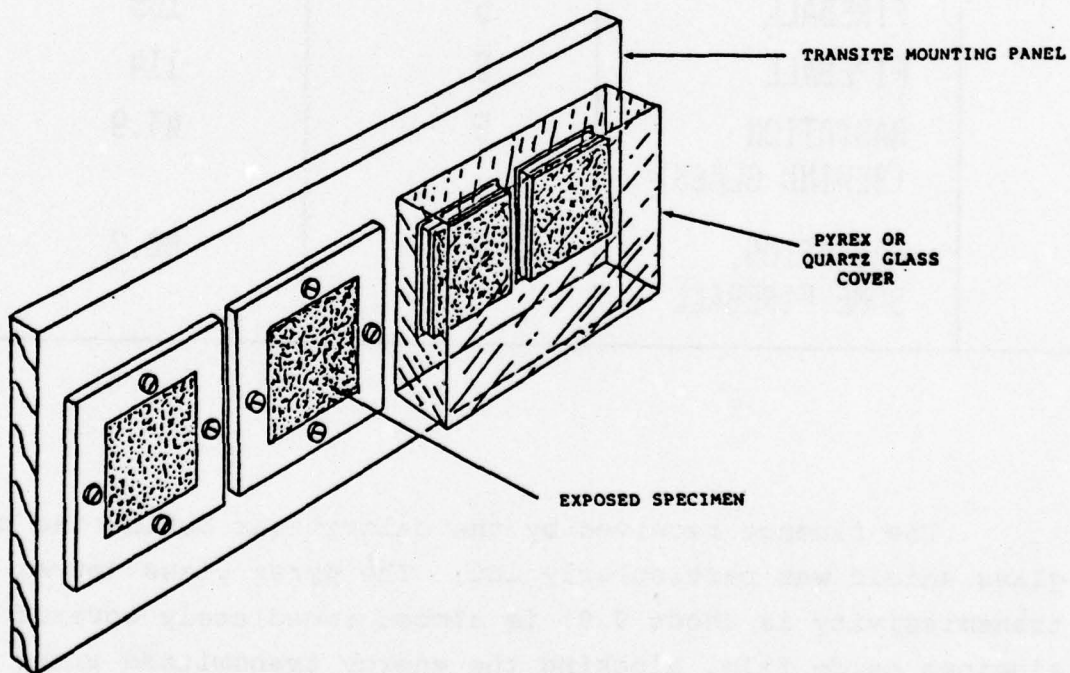


FIGURE 4-11. FOUR INCH SQUARE CERAMIC COATING TEST FIXTURE



TYPICAL TRS INSTALLATION - ROUND SPECIMEN



TYPICAL TRS INSTALLATION - SQUARE SPECIMEN

FIGURE 4.12. TEST SAMPLE INSTALLATION

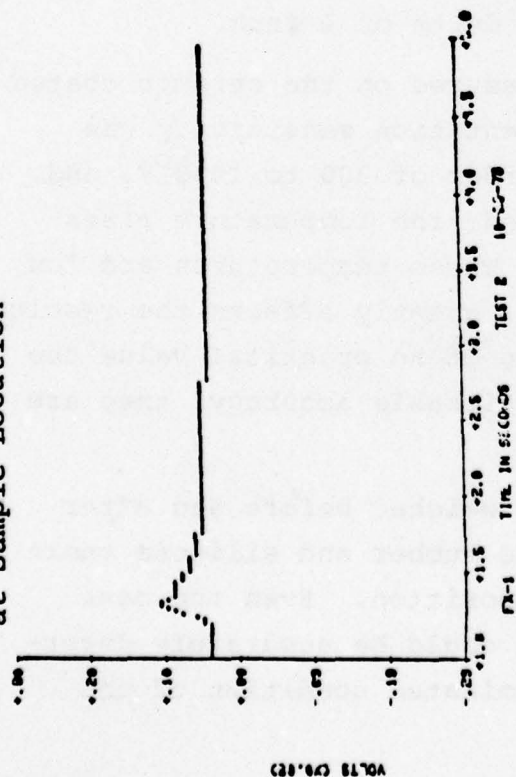
are presented in Table 4.1. The calorimeters at the 5 feet distance were in the vicinity of the samples, well within the fireball. The calorimeter located at 30 feet was just at the edge of the fireball. The calorimeter output plots are shown in Figure 4.13. The calorimeter voltage outputs shown give an idea of the time history of the heating. Calimeter FX5 has a different sensitivity than FX1, FX2, and FX3 have, hence the voltages cannot be compared directly.

TABLE 4.1. TRS TEST CALORIMETER MEASUREMENTS

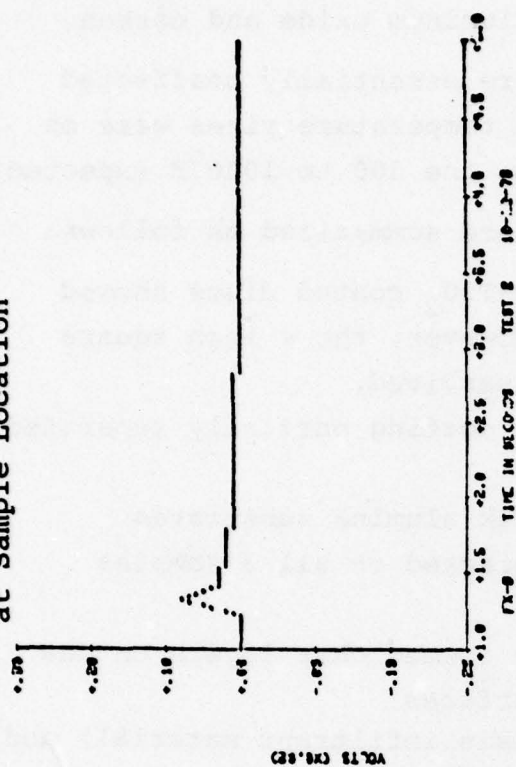
CALORIMETER NUMBER	ENVIRONMENT	CALORIMETER DISTANCE (FT)	MAXIMUM FLUX (CAL/CM ² -SEC)	FLUENCE (CAL/CM ²)
FX1	FIREBALL	5	105	45.6
FX3	FIREBALL	5	114	41.3
FX2	RADIATION (BEHIND GLASS)	5	43.9	3.0
FX5	RADIATION, SOME FIREBALL	30	68.2	82.7

The fluence received by the calorimeter behind the pyrex glass shield was particularly low. The pyrex glass (pyrex transmissivity is about 0.9) is almost immediately covered by an aluminum oxide film, blocking the energy transmitted after about 0.15 seconds. Thus, the glass shield proved not to be a good way to prevent the samples from being heated by convection/condensation mechanisms. Similarly, the samples exposed to the fireball

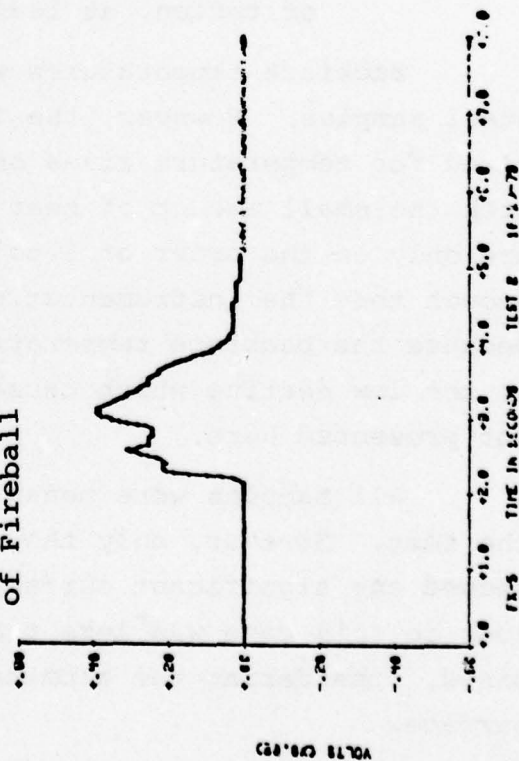
Calorimeter FX1. Located in Fireball
at Sample Location



Calorimeter FX3. Located in Fireball
at Sample Location



Calorimeter FX5. Located in Far Edge
of Fireball



Calorimeter FX2. Located Behind Pyrex
Glass at Sample Location

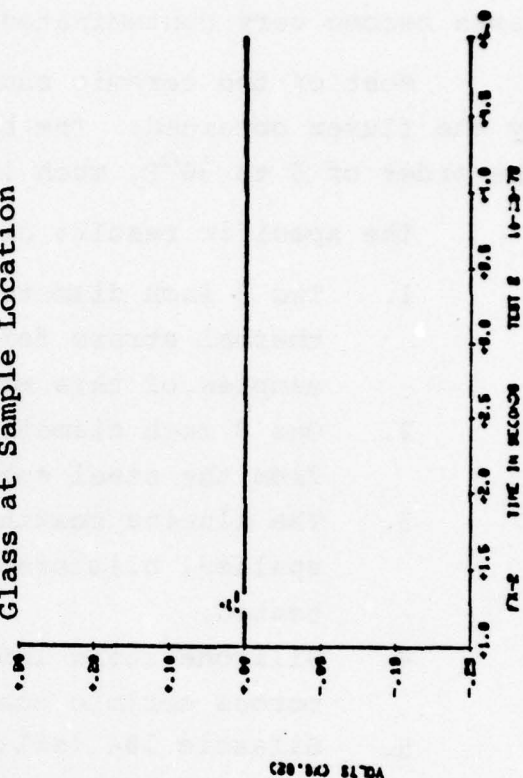


FIGURE 4.13. CALORIMETER OUTPUT

gases become very contaminated with aluminum oxide and carbon.

Most of the ceramic samples were essentially unaffected by the fluxes obtained. The backface temperature rises were on the order of 5 to 80°F, much less than the 300 to 1000°F expected.

The specific results obtained are summarized as follows:

1. Two 3 inch diameter Al_2O_3 - TiO_2 coated discs showed thermal stress failure; however, the 4 inch square samples of this material survived.
2. One 3 inch diameter Al_2O_3 coating partially separated from the steel substrate.
3. The alumina coating on bulk alumina substrates spalled, blistered, and cracked on all 3 samples tested.
4. Silicone resin infiltrant formed char layers on the porous ceramic coating surfaces.
5. Silastic 184 (silicone resin infiltrant material) and Sylgard E (silicone rubber) bulk samples developed char layers on their surfaces.
6. Indepth thermocouples indicated radiation transparency of teflon, at least to a depth of 1 inch.

Backface temperatures were measured on the ceramic coated steel samples. However, the instrumentation sensitivity was sized for temperature rises on the order of 300 to 1000°F, and, with the small amount of heat received, the temperature rises are only on the order of 5 to 80°F. These temperatures are low enough that the instrumentation drift greatly affects the results. Because the backface temperatures are of no practical value due to the low heating which caused questionable accuracy, they are not presented here.

All samples were measured and weighed before and after the test. However, only the silicone rubber and silicone resin showed any significant surface decomposition. Even the mass loss in this case was less than what could be accurately determined, considering the alumina contaminated condition of the surface.

4.4 French Solar Furnace Test Program

A series of tests were conducted on selected material candidates in the French Solar Furnace at Odeillo-Font-Romeu, France. A description of this test program is provided on the following pages.

4.4.1 Facility Description

The solar furnace has a parabolic reflector with a focal length of 59 feet, is 130 feet high and 175 feet wide, and is composed of 9500 mirrors, each 127 by 127 inches. Because the parabolic reflector is too large to track the sun, 63 smaller mirrors (heliostats) set in eight tiers, follow the sun and reflect its rays in parallel beams onto the parabola. The heliostats are each 24.6 by 19.7 feet.

The solar energy incident on an area of about 23000 square feet is concentrated by the parabolic reflector into an area about 2 feet in diameter. The diameter of the image of the sun at the focal point is 6.61 inches and 27 percent of the thermal energy is concentrated in this area. Reference 7 contains a complete description of the distribution of energy at this point.

The SAI samples were 2 inch diameter. For an area defined by a 2 inch diameter at the focal point, the minimum design heat flux, with all mirrors operating, is $365 \pm 15 \text{ cal/cm}^2 \text{ sec}$ for an incident radiation of 950 watts/cm^2 , at an effective radiation temperature of 6840°F . The flux is supposed to vary less than ± 2.5 percent over the 2 inch diameter area.

In this test, because of the condition of the mirrors, the flux obtained was about $180 \text{ to } 200 \text{ cal/cm}^2 \text{ sec}$ and varied less than ± 5 percent over the 2 inch diameter. Exposure times on the order of 16 seconds were used in order to match the total fluence for the nuclear burst model, approximately 3100 cal/cm^2 .

4.4.2 Test Procedure and Approach

4.4.2.1 Samples Tested

A series of 14 test specimens, consisting of 8 different materials, were submitted. These samples are listed in Table 4.2. Six of the samples were tested, as noted in Table 4.2. All samples were 2 inch diameter disks.

4.4.2.2 Instrumentation

Samples were instrumented with chromel-alumel thermocouples on the backface. Savereisen cement was used to fasten thermocouples to the non metallic specimens and in some cases the bond failed due to insufficient cure time before shipping to France. Metal substrates had thermocouples spot welded to the rear face. Front face temperatures were obtained using an optical pyrometer, which operated at a wavelength at which the surface emissivity is approximately 1, according to Reference 8. The pyrometer field of view covered a 1 inch diameter area in the center of the 2.0 inch diameter sample face.

Motion pictures were taken of the specimen front surface during the test with a 20 frame/second camera. All samples were measured, weighed, and photographed before and after the test.

4.4.3 Pre-Test Analysis

The thermal response of the alumina coating with the silicone infiltrant exposed to the heat flux of the solar furnace was predicted using the thermal model described in Section 4.1. The physical parameters are as follows:

Flux = $350 \text{ cal/cm}^2 \text{ sec}$
Exposure Time = 9 seconds
Fluence = 3150 cal/cm^2
Alumina Thickness = 0.125 in
Steel Thickness = 0.25 in.
Porosity = 15%
Alumina Absorptivity = 0.2

TABLE 4.2. FRENCH SOLAR TEST MATERIALS

<u>No.</u>	<u>Samples Submitted to Test for one Exposure</u>	<u>Sample Tested</u>
F2	Alumina coating/silicone infiltrant/steel substrate	yes
F16	Magnesia - spinel coating/silicone infiltrant/steel	yes
F19	0.5 inch Sylgard 184/Steel	no
F3	0.25 inch Silastic E/Steel	yes
F4	0.5 inch Silastic E/Steel	yes
F5	0.25 inch Boron Nitride, Grade M	no
F6	0.25 inch Boron Nitride, Grade HP	no
F7	0.25 inch Boron Nitride, Grade HBR	no
F8	0.50 inch Boron Nitride, Grade HBR	yes
F9	0.25 inch AS-3DX	yes

SAMPLES SUBMITTED TO TEST FOR TWO EXPOSURES

F11	Alumina coating/silicone infiltrant/steel	no
F12	0.5 inch Silastic E/Steel	no
F13	0.25 inch Boron Nitride, Grade HBR	no
F14	0.25 inch Silastic E/Steel	no

The resulting temperature and recession predictions are shown in Figure 4.14. Melting of the surface begins at 6.7 seconds and the total predicted recession is only .007 inches.

In the actual tests, discussed in the following paragraphs, the flux was $195 \text{ cal/cm}^2 \text{ sec}$ for 16 seconds. Also, the absorptivity appeared to be much larger, so that 3 to 4 times as much heat would be absorbed as used in the above prediction. Therefore, the prediction model was updated using these data. Absorptivities of 0.2 and 0.5 were used. Even an absorptivity of 0.5 is probably less than what it actually was in the test.

The resulting temperature predictions are shown in Figure 4.15 and the recession predictions are presented in Figure 4.16. With an absorptivity of 0.2, the melt temperature is not obtained and there is no recession. However, with an absorptivity of 0.5, the melt temperature is obtained at the surface in 4 seconds, and at 16 seconds the total recession is .068 inches, which is more than half of the material.

4.4.4 Test Results

A description of the material surface effects seen on the film are shown in Table 4.3. The measured front face and back face temperatures, pre-test and post-test pictures and sample dimension and mass data are presented in Appendix H. A description of the response of each material is given in the following paragraphs.

4.4.4.1 Alumina/Silicone Infiltrant/Steel

A dark brown char layer, caused by the silicone resin charring, develops immediately, increasing the surface absorptivity. Also, the alumina coating was contaminated (dirty appearance) due to the processing. These factors caused the heat absorbed to probably be 3 to 4 times that anticipated for the expected absorptivity of 0.2. Melting began at 3.5 seconds and spalling of the coating begins at 4.5 seconds. Very high surface temperatures were measured (Appendix H) about 2500 to

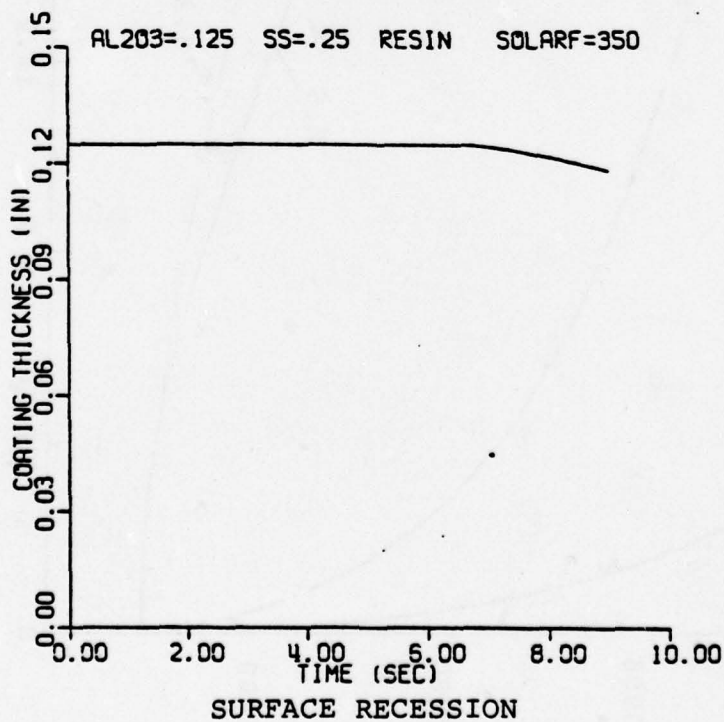
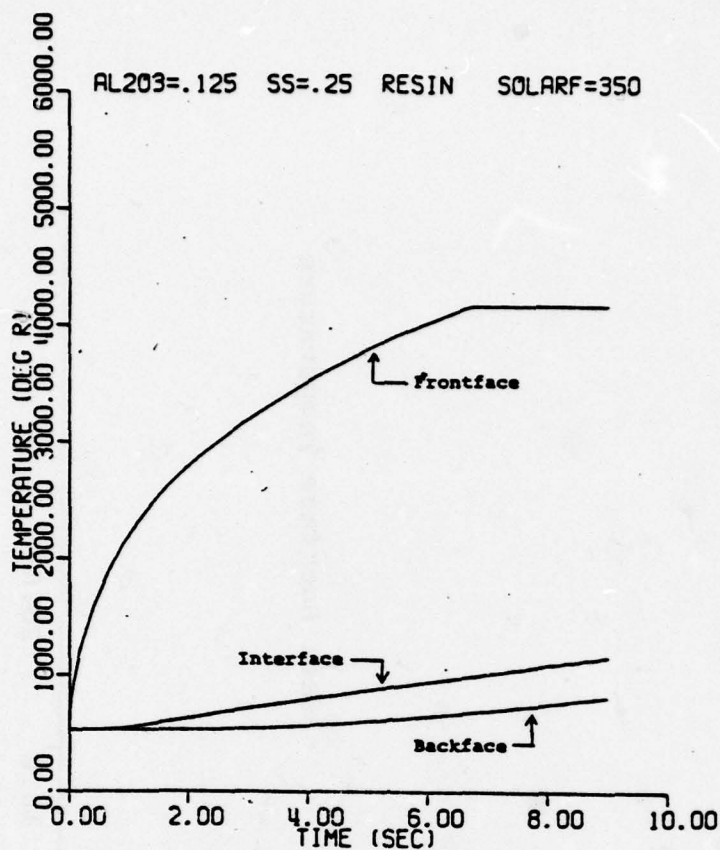


FIGURE 4.14. PREDICTED THERMAL RESPONSE OF ALUMINA COATING WITH SILICONE INFILTRANT IN SOLAR FURNACE

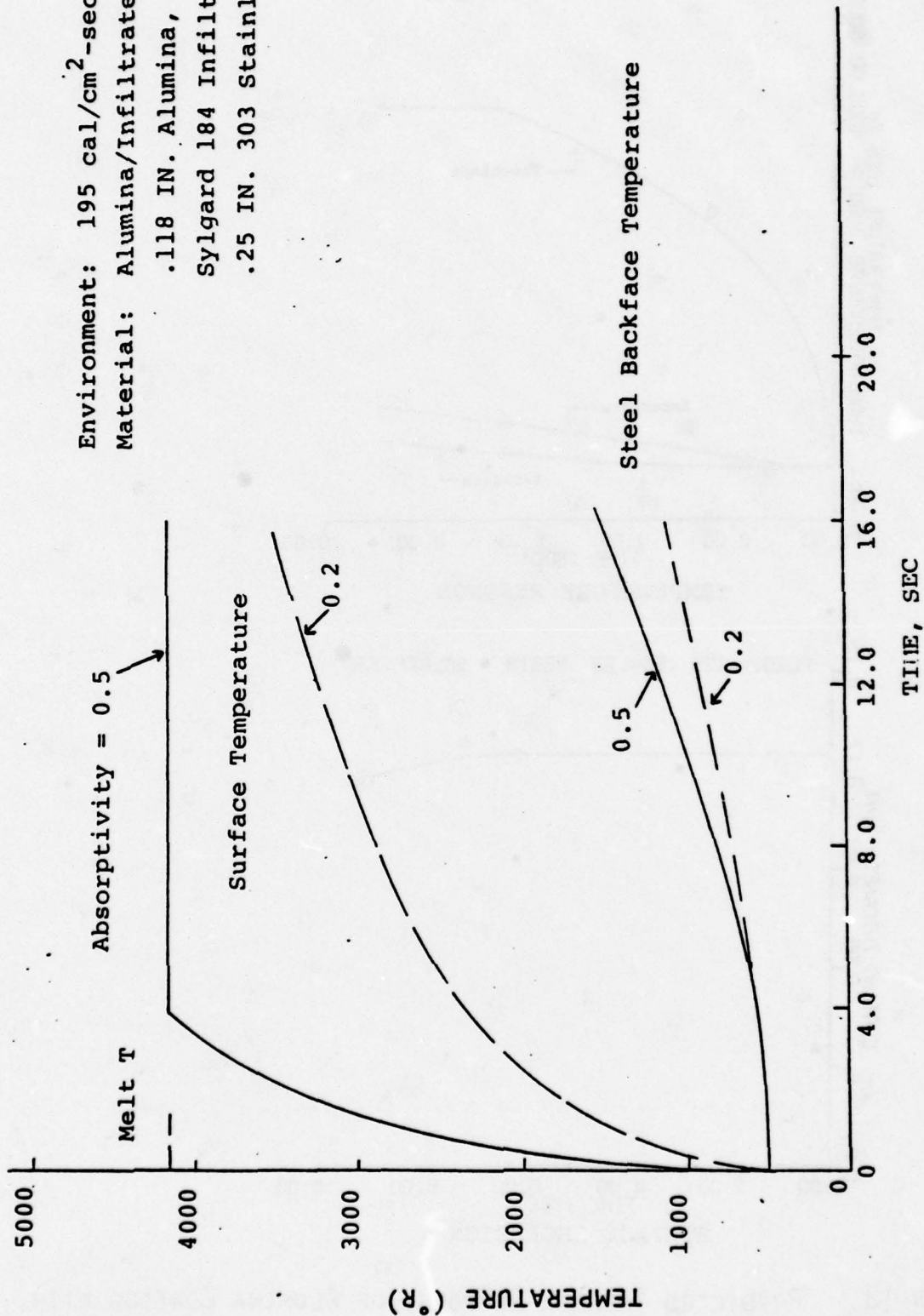


FIGURE 4.15. EFFECT OF ABSORPTIVITY ON PREDICTED ALUMINUM TEMPERATURES

Environment: 195 cal/cm²-sec FLUX
 Material: Alumina/Infiltrate/Steel
 .118 IN. Alumina, 15% Porous
 Sylgard 184 Infiltrate
 .25 IN. 303 Stainless Steel

Absorptivity = 0.2

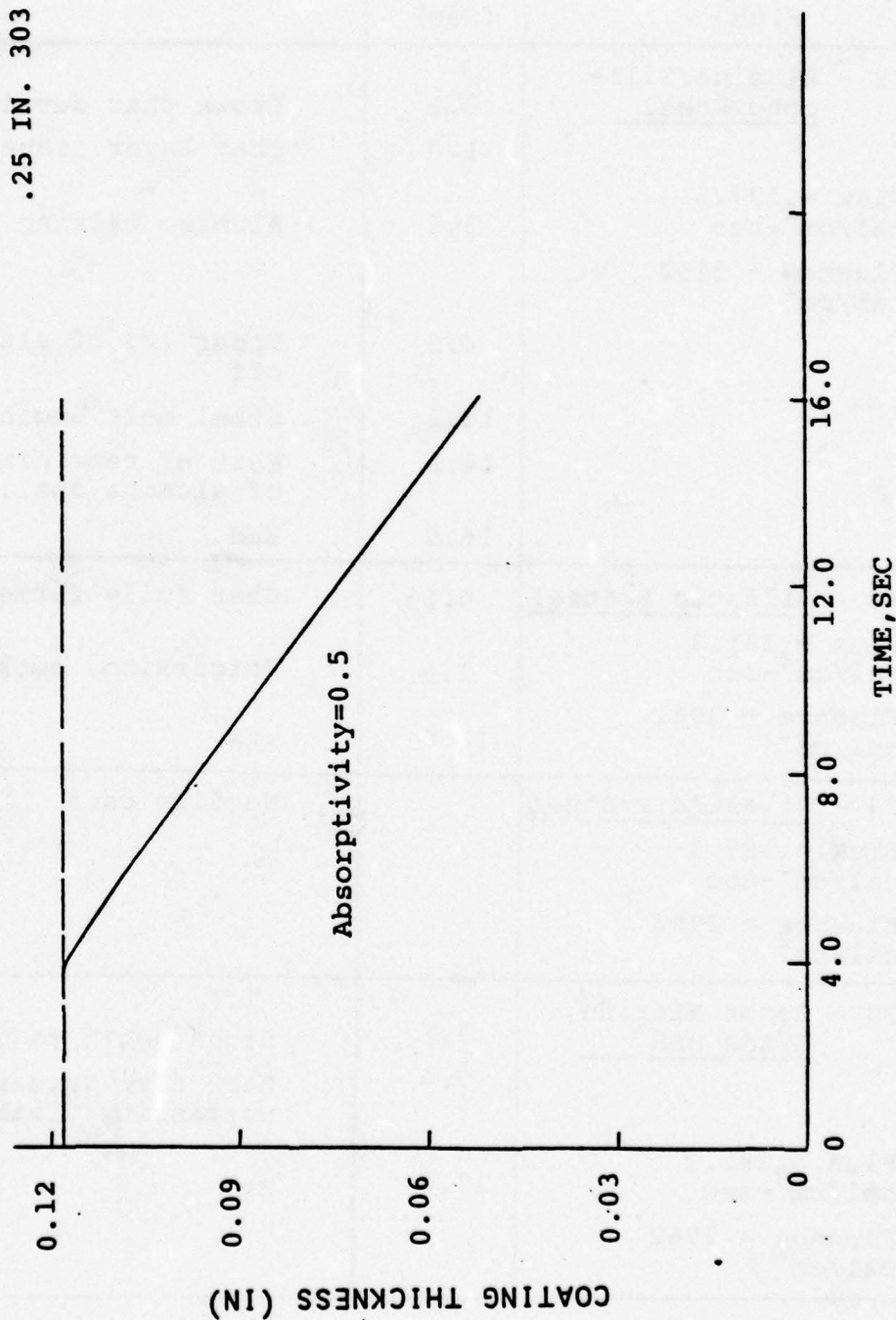


FIGURE 4.16. EFFECT OF ABSORPTIVITY ON PREDICTED ALUMINUM COATING ABLATION

TABLE 4.3. MATERIAL VISUAL RESPONSE

Sample and Flux	Exposure Time (Sec)	Sample Response
F2 - <u>Alumina/Silicone/Steel</u> Flux = $197.5 \text{ cal/cm}^2\text{-sec}$ Fluence = 3152 cal/cm^2	0.1	Brown char develops, smokes
	1.0	Char layer lightens
	3.5	Alumina melting begins
	4.5	Upper 1/3 of alumina spalls off
	13.1	Steel melt begins
	14.5	Most of remaining lower part of alumina spalls off
	16.0	End
F3 - <u>Silastic E/Steel</u> Flux = $191.3 \text{ cal/cm}^2\text{-sec}$ Fluence = 3061 cal/cm^2	0.15	Char fully formed
	2.2	Outgassing, smoking visible
	16.0	End
F4 - <u>Silastic E/Steel</u> Flux = $187.3 \text{ cal/cm}^2\text{-sec}$ Fluence = 2992 cal/cm^2	-	No film data
F8 - <u>Boron Nitride, Grade HBR</u> Flux = $182.9 \text{ cal/cm}^2\text{-sec}$ Fluence = 2962 cal/cm^2	9.1	Sides begin to spall
	9.6	Dark flaw appears in center, outgassing visible
	17.0	End

TABLE 4.3. MATERIAL VISUAL RESPONSE (CONT'D)

Sample and Flux	Exposure Time (Sec)	Sample Response
F9 - <u>AS-3DX</u> Flux = 184.8 cal/cm ² -sec Fluence = 2957 cal/cm ²	1.0	Outgassing begins
	10.5	Small bubble forms
	15.2	Large bubbles, discoloration
	16.0	End
F16 - Spinel/Sili- cone/Steel Flux = 193.6 cal/cm ² -sec Fluence = 3098 cal/cm ²	0.1	Brown char layer develops, smokes
	0.8	~ 1/8 of coating spalls off
	1.0	Char lightens
	1.2	~ 1/3 of coating spalls off
	1.8	Remaining coating is clean looking
	2.9	Coating melting in center
	4.0	~ 1/4 of coating melts, falls, exposes center
	4.9	3/4 of coating gone
	8.6	Steel begins to melt
	16.0	End

2800°C, which is above the alumina melt temperature (2100°C). This may be the silicone char temperature. Backface temperatures were not measured on this sample.

4.4.4.2 Silastic E on Steel

The silicone rubber Silastic E samples performed very well during the test. A char layer forms immediately and protects the remaining material by both insulating the virgin material and reradiating at a high temperature (3000°C, see Appendix G). The decomposing hydrocarbons in the silicone rubber and the pyrolysis gases passing through the char layer remove additional heat. As a result, a .07 to .09 inch thick char layer formed and the steel backface temperature increases were only 180°C and 50°C for the 0.25 inch and 0.5 inch thick samples respectively. There was some dark brown smoke emitted which left a small deposit on the holder, and a considerable amount of whitish gas was emitted. A chemical analysis of the post-test sample showed that the char layer was 7.0 percent carbon.

4.4.4.3 Boron Nitride, Grade HBR

The boron nitride began to spall at 7.1 seconds and had severe cracks at the end of exposure. The frontface temperature profile is shown in Appendix G. The temperature profile is quite non-uniform which can be due to either changing emissivity in the pyrometer wavelength, changing absorptivity, and/or conductivity decreasing with temperature. Backface temperature data was not available.

4.4.4.4 AS-3DX

The AS-3DX exhibited outgassing immediately; however, the surface did not exhibit deterioration until after 10 seconds of exposure. The surface temperature is shown in Appendix G. The surface temperature rise rate indicates a very low absorptivity. A non-decomposing material thermal model was made of the AS-3DX and the results are shown in Figure 4.17. A surface absorptivity of 0.1 matches the experimental surface temperatures quite well. An absorptivity of 0.2 was also considered, and the melt temper-

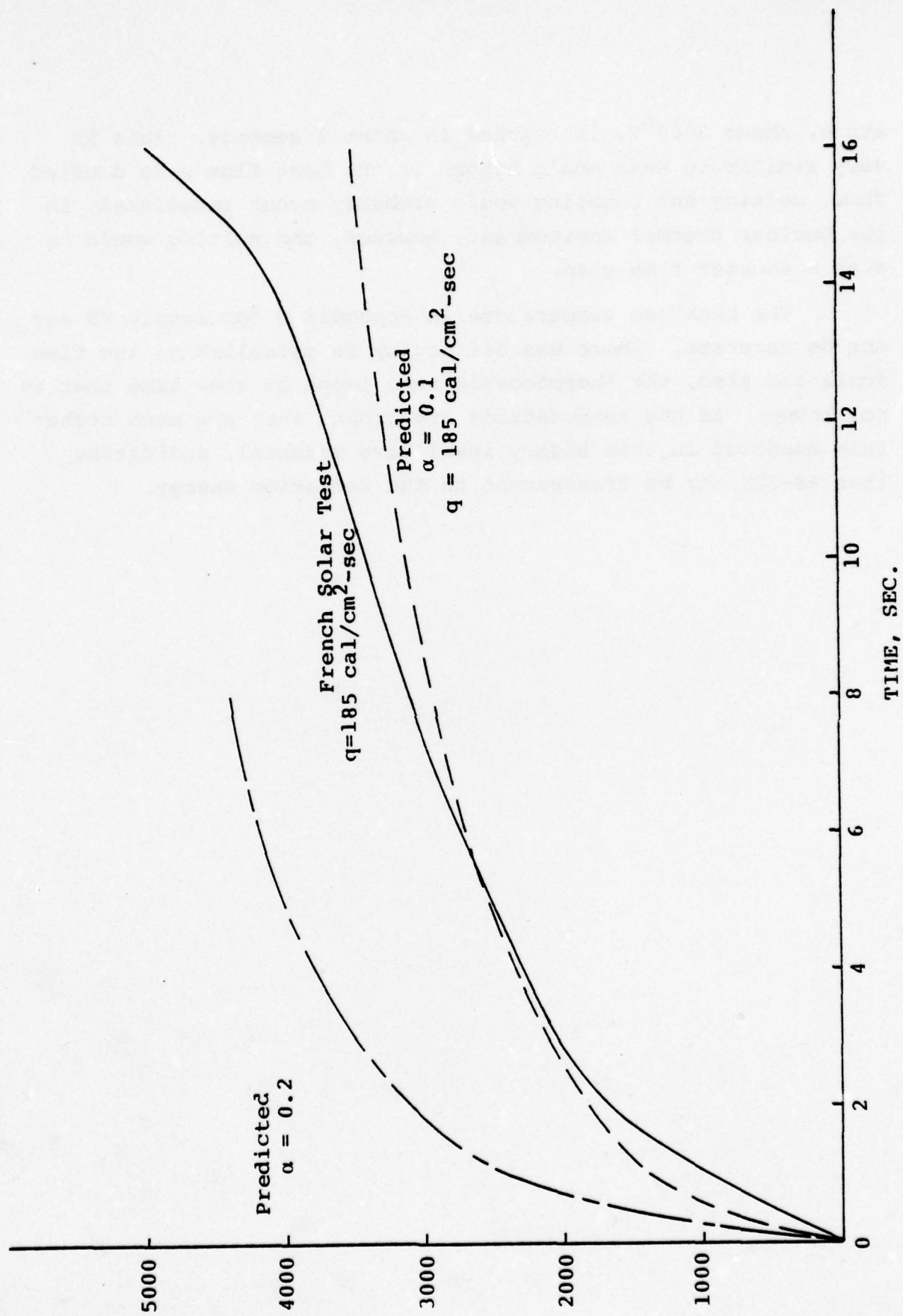


FIGURE 4.17. AS-3DX FRONT FACE TEMPERATURE

ature, about 3000°F, is reached in about 2 seconds. This is very similar to what would happen if the heat flux were doubled. Thus, melting and bubbling would probably occur immediately in the nuclear thermal environment; however, the melting would be over a shorter time span.

The backface temperature in Appendix G for sample F9 may not be accurate. There was difficulty in establishing the time scale and also, the thermocouple came loose at some time that is not known. If the temperatures are right, they are much higher than expected in this highly insulative material, indicating that AS-3DX may be transparent to the radiation energy.

4.4.4.1 Spinel/Silicone Infiltrate/Steel

This material behaves similarly to the alumina/infiltrate sample. The infiltrate charred and increased the absorptivity immediately. Also, spalling began at an exposure of less than 0.8 seconds. Melting is evident at 2.9 seconds, and three-fourths of the coating has spalled off at 4.9 seconds.

4.5 Conclusions

Material response thermal models of the porous ceramic coatings, with and without silicone resin infiltrant, were developed. Similar models for silicone rubber were partially developed. All of the materials considered were subjected to the Thermal Radiation Simulator tests, and a limited number of materials were subjected to the French Solar Furnace test. The conclusions obtained are as follows:

1. Test Facilities

The large scale TRS test facility did not produce the flux and fluence needed. For even moderately high heating rates, the sample must be in the fireball, which contaminates the surface with aluminum oxide and carbon residue. Further calibration of the TRS fireball heat flux is needed as well as a better understanding of the kinetics and dynamics of the fireball. It currently could be used for testing at lower fluxes modeling lesser nuclear environments; but, it apparently does not have the capability to give the environment conditions required in this study.

The FSF does supply sufficient flux and fluence to severely test the materials. However, since its flux is much less than the nuclear environment being modeled and long heating time durations are required, the material re-

sponse is different than what would be expected in a nuclear environment. However, it is the best testing method available.

2. Porous Ceramic Coatings

Based on the thermal tests, primarily the FSF test, the porous ceramic coatings conclusions are:

- a) The silicone resin infiltrant forms a thin char layer which increases the absorptivity of the ceramic coating. A low absorptivity of about 0.2 is required, hence, the infiltrant should not be used.
- b) Process methods must be carefully controlled to insure a non-contaminated, low absorptivity coating.
- c) Ceramic coatings are very susceptible to thermal stress. Pre-stress during processing, material expansion compatibility, etc. should be investigated to alleviate this problem.

The thermal modeling gave the following significant conclusions:

- a) Alumina coating, 0.125 inches thick, can survive three nuclear bursts, if it has an absorptivity on the order of 0.2. The other ceramics may have similar performance, but only the alumina was investigated. This is based on material loss due to melting only, thermal stress is not considered.
- b) A thick coating exhibits more ablation than a thin one; however, the thicker coating also has more material remaining after the exposure.

3. Silicone Rubber

The conclusions obtained about using silicone rubber as an ablative thermal protection coating in the nuclear environment are as follows:

- a) A highly insulative, low carbon content char layer develops and protects the remaining virgin material and structure from severe heating. This material survived the 3150 cal/cm^2 fluence of the FSF test with very little material loss and low backface temperature rise. Different types of silicone rubber have different types of chars, ranging from very fragile to very tough.
- b) The thermal protection capability is independent of contaminated surface conditions.
- c) It is a very practical material, in that it is inexpensive, easy to apply, adheres well, resists weathering, and acts as a moisture barrier.

4. Miscellaneous Bulk Materials

Results of the thermal tests produced the following pertinent results on a few of the materials tested:

- a) Teflon is semi-transparent to thermal radiation in the short IR wavelengths being investigated.
- b) AS-3DX exhibited very low absorptivity and held up well at the test flux of $185 \text{ cal/cm}^2 \text{ sec}$.
- c) Union Carbide boron nitride HBR showed severe spalling and cracking in the FSF tests.

5.0 ELECTRICAL PROPERTIES TEST AND ANALYSIS

5.1 Introduction And Summary

This chapter presents the electromagnetic aspects of the array hardening problem. The electrical properties of the materials are tabulated and discussed, while the array implications of the use of these materials are briefly considered.

The electrical property values of the candidate materials were determined by the Engineering Experiment Station at the Georgia Institute of Technology and are presented later in this section.⁽⁹⁾ The complete data base from which these average values were calculated are given in Appendix B. A brief discussion of the theoretical basis for the cavity measurement procedure used for the plasma-sprayed ceramic materials is included later in this chapter. The complete analysis which supports this discussion is given in Appendix C. The conclusions of the array-material interaction question are summarized in Section 5.1, while the third section of this chapter considers the problem in somewhat more detail. The theoretical analysis associated with the interaction question can be found in Appendix D.

5.1.1 Plasma-Sprayed Ceramic Coatings

The dielectric properties of the ceramic coatings are summarized in Tables 5.1 and 5.2. These two tables present the results of S-band and X-band measurements, respectively. For each material, an average (Avg.) and a standard deviation (σ) are shown for the dielectric constant (ϵ_r) and loss tangent ($\tan \delta$). The statistics are based on repeated test runs for each sample, with the cavity completely disassembled between runs. The S-band tests were repeated at least six times, and the X-band tests of unburned samples were repeated four times.

TABLE 5.1. DIELECTRIC PROPERTIES OF CERAMIC COATINGS AT S-BAND

SAI Sample #	Material	Dielectric Constant ($\epsilon_r/\sigma \epsilon_r$)	Loss Tangent ($\tan \delta/\sigma \tan \delta$)
2	ZrO ₂ - MgO stabilized	18.13/2.02	0.042/0.02
3	ZrO ₂ - 12% Y ₂ O ₃ stabilized	26.14/1.39	0.027/0.016
4	Al ₂ O ₃	7.65/0.34	0.024/0.015
5	ZrO ₂ - 2% CaO ₂ stabilized	14.21/0.078	0.039/0.015
6	Spinel (Al ₂ O ₃ + MgO)	6.29/0.37	0.028/0.008
201 [†]	ZrO ₂ - CaO ₂	19.58/1.44	0.025/0.008
210 [†]	ZrO ₂ - MgO	6.65/0.78	0.051/0.040
356 [†]	Spinel (Al ₂ O ₃ + MgO)	3.65/0.19	0.023/0.008

[†]These samples are believed to more porous than the other samples.

TABLE 5.2. DIELECTRIC PROPERTIES OF CERAMIC COATINGS AT X-BAND

SAI Sample #	Material	Dielectric Constant ($\overline{\epsilon_r}/\sigma_{\epsilon_r}$)	Loss Tangent ($\tan \delta/\sigma_{\tan \delta}$)
201	ZrO ₂ - CaO ₂	20.44/1.3	0.0156/ 0.003
202	ZrO ₂ - Y ₂ O ₃	13.53/1.92	0.03/0.04
210	ZrO ₂ - MgO	16.00/0.97	0.0163/0.007
333*	Al ₂ O ₃ - TiO ₂	12.48	0.15
356	Spinel (Al ₂ O ₃ + MgO)	5.66/0.09	0.023/0.018
202 Burned	ZrO ₂ - Y ₂ O ₃	28.10	0.116
333 Burned	Al ₂ O ₃ - TiO ₂	24.85	0.17

* Averages based on 2 runs completed before sample was chipped

Note that these runs are all for the same sample. Thus the statistics reflect the consistency of the measurement process rather than the material variability from sample to sample. A complete tabulation of the results of individual tests is provided in Appendix B. The statistical averages are developed after discarding the highest and lowest values of ϵ_r and $\tan \delta$. The reason for repeated tests and for discarding extreme data is that the particular (TM) cavity mode excited in these tests is known to be sensitive to the electrical contact at the assembly joint in the cavity wall. An alternative (TE) mode would have been less sensitive to the conduction properties of the joint, but it may not have provided adequate measurement sensitivity for these electrically thin coatings.

Three samples of burned coatings were provided for X-band measurements. The burns were produced with an arc jet. The burned samples had apparently expanded and were difficult to insert in the cavity. One sample, #356, shattered on the first attempt to fit it into the cavity, and the other two samples, #202 and #333, cracked when they were being pressed out of the cavity after second test runs. Therefore, the variance of the data cannot be assessed.

The unburned ceramics generally have a speckled appearance. Contamination by metallic particles would contribute an "artificial dielectric" mechanism and could explain the relatively high dielectric constants that were measured for some ceramics. Samples #2 through #6 are known to be less porous than the others, and this fact is reflected in their higher dielectric constants. For the two materials that were tested before and after burning, the burn increased the dielectric constant and the loss tangent significantly. The surfaces of the burned samples were glazed, and it seems likely that some change of state occurred. Because the burned samples

were not perfectly homogeneous, it is possible that the theoretical model used for data analysis may have been inadequate, but the results are believed to be reasonably accurate.

5.1.2 Bulk Materials

The dielectric properties of the bulk materials are summarized in Tables 5.3 and 5.4, which present the results of S-band and X-band measurements, respectively. The solid, silicone-based materials were molded to fill short lengths of rectangular waveguide, and shorted waveguide sections were used as sample holders. For the ash materials, the sample holder was a female SMA coaxial connector, from which the dielectric plug had been removed.

The two basic solid materials that were tested are distinguished by color (i.e., clear RTV and white RTV). Two sample lengths, denoted -1 and -2, were tested at each of the two nominal frequencies, 3 GHz and 9 GHz. The white material was retested, after one end of the samples had been burned. The X-band samples were burned with an arc jet, while the S-band samples were burned with an oxyacetylene torch. The jet produced smooth, hardened surfaces, with a fine, black, ash residue. The torch produced rough, hardened surfaces, covered with a black-speckled, loose, granular ash. The arc jet ash was mostly lost during the burning process. The loose ash from the oxyacetylene torch was brushed away and saved before tests were run on the burned solids. The burned surfaces were not uniform, so measurement of the effective sample thicknesses involved some exercise of judgment.

The sample holders used for the bulk tests did not have mechanical joints that seriously affected the electrical repeatability of the measurements. Therefore, the tabulated values are the results of single measurements, rather than

TABLE 5.3. DIELECTRIC PROPERTIES OF BULK MATERIALS AT S-BAND (3 GHz)

Sample	Length (in)	Dielectric Constant (ϵ_r)	Loss Tangent ($\tan \delta$)
White RTV-1	2.562	2.96	0.011
White RTV-2	2.200	2.98	0.011
Clear RTV-1	2.465	2.78	0.012
Clear RTV-2	2.085	2.77	0.011
White RTV-1*	2.520	2.98	0.016
White RTV-2*	2.170	2.93	0.015
Ash (White RTV-1)*	0.260	7.16	0.191
Ash (White RTV-2)*	0.260	5.20	0.180
Ash (White RTV) ⁺	0.260	5.86	0.330

* After burning with an oxyacetylene torch

+ After burning in a solar furnace

NOTE:

1. All values are for single run
2. White RTV is DOW Silastic E
3. Clear RTV is DOW Sylgard 184

TABLE 5.4. DIELECTRIC PROPERTIES OF BULK MATERIALS AT X-BAND (9 GHz)

Sample	Length (in)	Dielectric Constant	Loss Tangent
White RTV-1	1.070	2.96	0.029
White RTV-2	0.995	2.98	0.028
Clear RTV-1	0.970	2.69	0.020
Clear RTV-2	0.728	2.68	0.029
White RTV-1*	0.835	2.86	0.030
White RTV-2*	0.825	2.93	0.023
Ash (White RTV-1)*	0.260	5.86	0.104
Ash (White RTV-2)*	0.260	2.04	0.100
Ash (AS3DX) [†]	0.260	4.13	0.383

* After burning with an arc-jet

† After burning in a solar furnace

Note:

1. All values are for a single run
2. White RTV is DOW Silastic E
3. Clear RTV is Dow Sylgard 184

statistical averages of repeated measurements. The solid materials were supplied in two sample lengths for each waveguide band. The nearly equal values obtained for the two sample lengths are a good indication of the repeatability of the measurements.

Three types of ash were tested. The granular ash that resulted from the torch burn on the white, S-band samples was tested at S-band. The fine black ash that resulted from the arc jet burn on the white, X-band samples was tested at X-band. Ash from a sample of white RTV that was burned in the French solar furnace was tested in both frequency bands. In all cases, the ash was packed as tightly as possible into a short (0.260 in.) length of short-circuited, coaxial transmission line. The electrical properties of powders vary substantially with density, although empirical evidence⁽¹⁰⁾ indicates that the dielectric constant is more sensitive to density than is the loss tangent. The packing density could not be carefully controlled in these tests.

5.1.3 Material-Array Interactions

The hardening concepts under consideration here involve the use of waveguide plugs and/or slabs which cover the antenna array. The effects of these structures on array performance are well known to be deleterious, and involve the issues of (1) reflections, (2) losses and (3) blind spots. For hardening applications (or any other that requires covering slabs or waveguide plugs), it is desirable that any material have as low a dielectric constant and loss tangent as possible. Further, in order to reduce the incidence of array blindness, it is exceedingly desirable that the material be as thin as possible. From the interaction point of view, the array blindness is perhaps the most significant problem for either the plasma-sprayed ceramic materials or the silicone rubber (RTV) materials.

In general, the most significant conclusion of the interaction analysis is that the hardening of the array must be treated as an integral part of the array design process. Given an integral design, there is reasonable hope that the silicone rubber materials as well as some of the plasma-sprayed materials may have some applicability to the array hardening problem. In particular, Al_2O_3 and Spinel are the most likely ceramic candidates from the electrical point of view. Although the silicone rubber materials produce a char, the loss associated with the char appears to be tolerable provided that the char is not too thick. For most of the char values in the tables, this means less than 0.125 inches.

5.2 Electrical Properties Test Program

This section describes the electrical properties test program. It consists of three parts: (1) Test Facility Description, (2) Test Procedures and Approach, and (3) Pre-Test Analysis. The first two parts deal primarily with the resonant cavity measurement procedure. The bulk sample measurement technique is conventional, and is not discussed in detail.

5.2.1 Test Facility Description (Resonant Cavity Measurements)

The dielectric properties of the thin ceramic coatings were measured using a resonant cavity. The cavity was a right-circular cylinder of radius a and height d , with $d \ll a$. The coatings were applied to cover the surface of one end of the cavity, and the electrical coupling was made via a short coaxial probe inserted through the opposite end of the cavity.

A cross-section of the cavity is shown in Figure 5.1A. A photograph of the disassembled cavity is shown in Figure 5.1B and a photograph of the assembled cavity provided as Figure 5.1C. The main box (the upper section in Figure 5.1A is brass, and the interchangeable, ceramic-coated endplates are stainless steel. The endplate is held tightly in the cavity by a clamping plate,

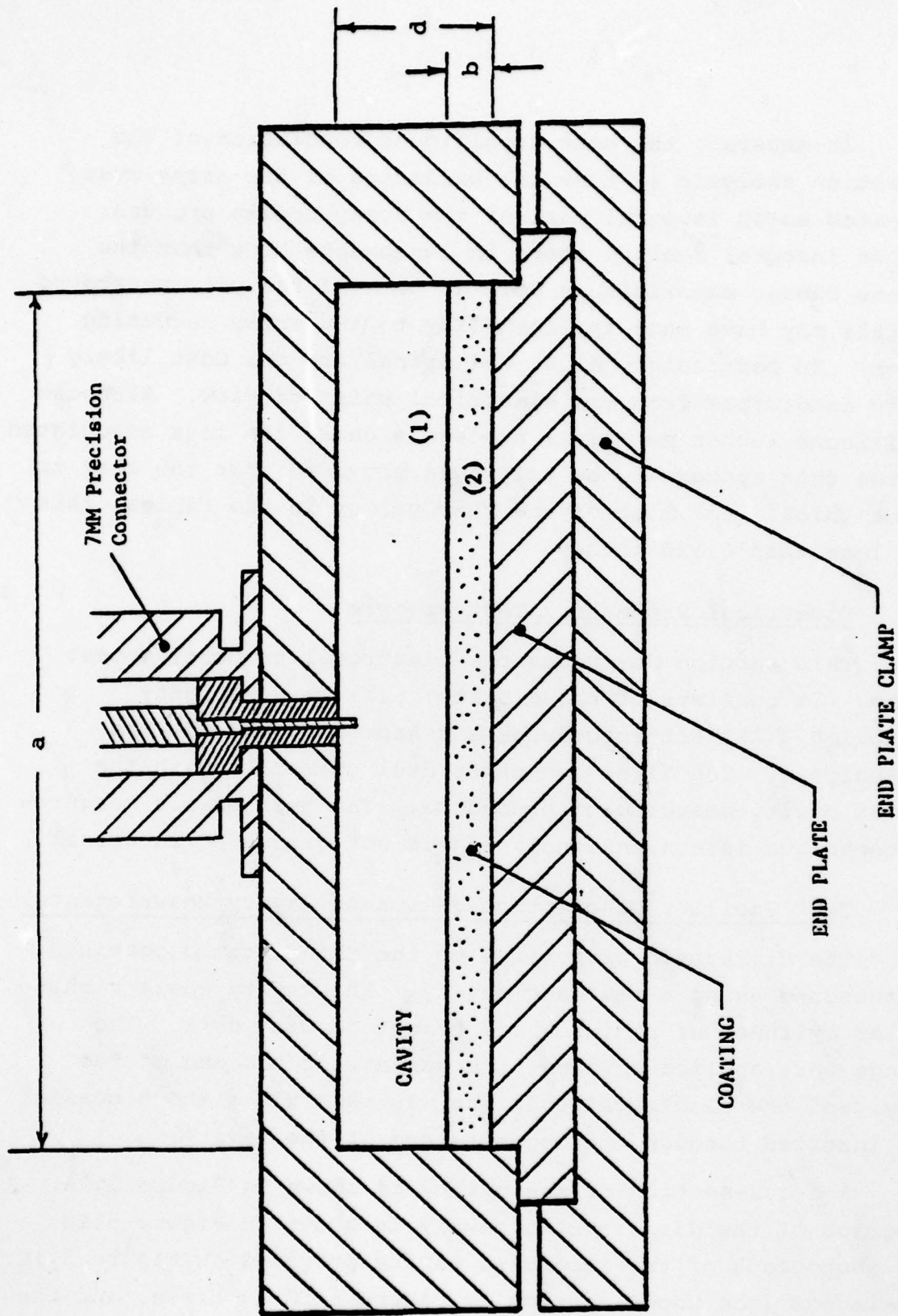


FIGURE 5.1A. SECTIONAL VIEW OF THE RESONANT CAVITY SAMPLE HOLDER TO BE USED FOR TESTING THIN COATINGS

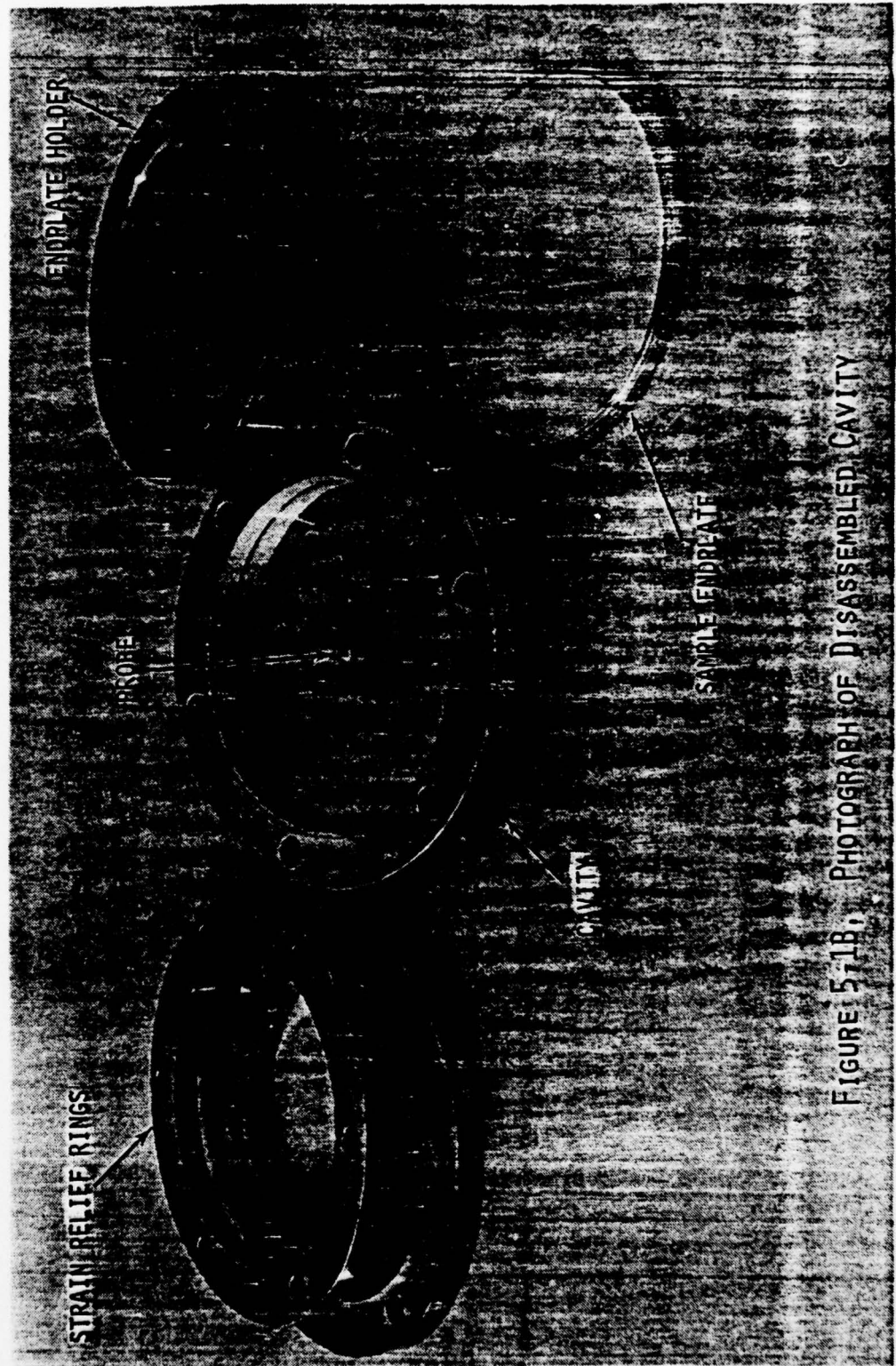


FIGURE 5-1B. PHOTOGRAPH OF DISASSEMBLED CAVITY

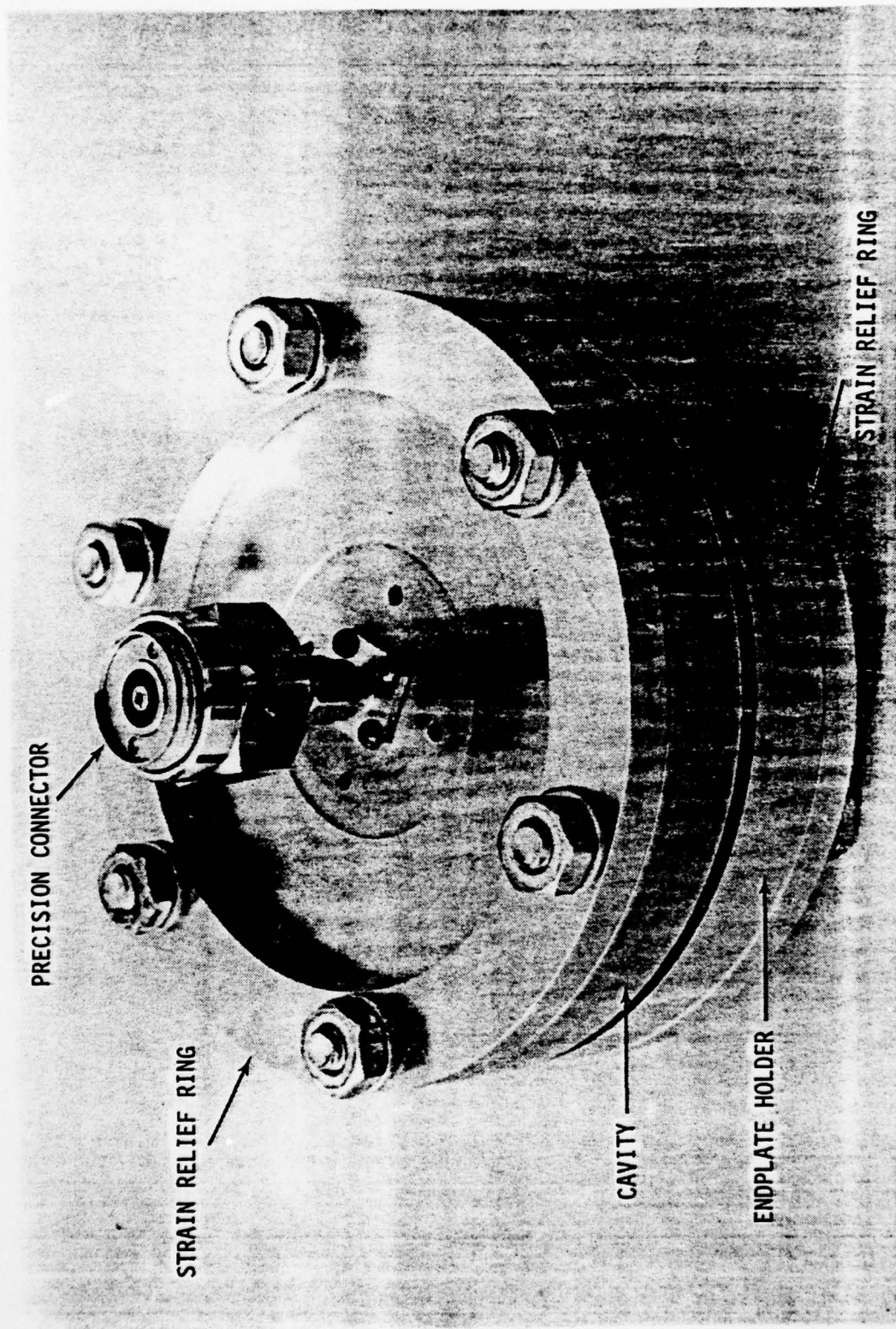


FIGURE 5.1C. PHOTOGRAPH OF ASSEMBLED CAVITY

which is bolted through the main body. The nominal dimensions of the three cavities that were used for these tests are shown in Table 5.5. The nominal coating thicknesses were in the range 0.050 to 0.100 in.

The coupling probe was the center contact extension of a flange-mounted, 7mm precision connector. This configuration minimized transmission line discontinuities between the cavity port and the instrumentation. The probe penetration was 0.060 in. for S-band measurements and 0.040 in. for X-band measurements. The probe diameter was 0.050 in.

The basic instrumentation used in this measurement is diagrammed in Figure 5.2A and photographically illustrated in Figure 5.2B. A list of equipment is given in Table 5.6. The Network Analyzer and the Reflection/Transmission Test Set provide the capability for swept-frequency measurements of complex reflection coefficients. Amplitude and phase are plotted vs. frequency on an X-Y recorder. The system is calibrated by recording the reflection coefficients of several (at least three) known loads^(11,12). For these measurements, calibration loads included a matched termination, an open circuit, and short circuits placed at three different positions relative to the connector reference plane.

5.2.2 Test Procedure

5.2.1.1 Resonant Cavity Measurements

Before each experiment, the equipment is allowed to warm up for one hour. The sample to be tested and the brass cavity are cleaned with methanol and dried with laboratory tissues. The sample and end-plate are placed in position and the cavity body is assembled. Caution must be taken at this point to torque the bolts holding the cavity to a uniform tightness since the TM_{010} cavity mode is known to be sensitive to the electrical conductivity of the mechanical joint between the end-plate and the cylinder. A problem of this type would

TABLE 5.5. NOMINAL CAVITY DIMENSIONS

Cavity Designation	S-1	S-2	S-3
TM ₀₁₀ Frequency (GHz)	3.011	3.011	8.604
Diameter (in)	3.000	3.000	1.050
Height (in)	0.200	1.000	0.450
Probe Penetration (in)	0.060	0.060	0.040

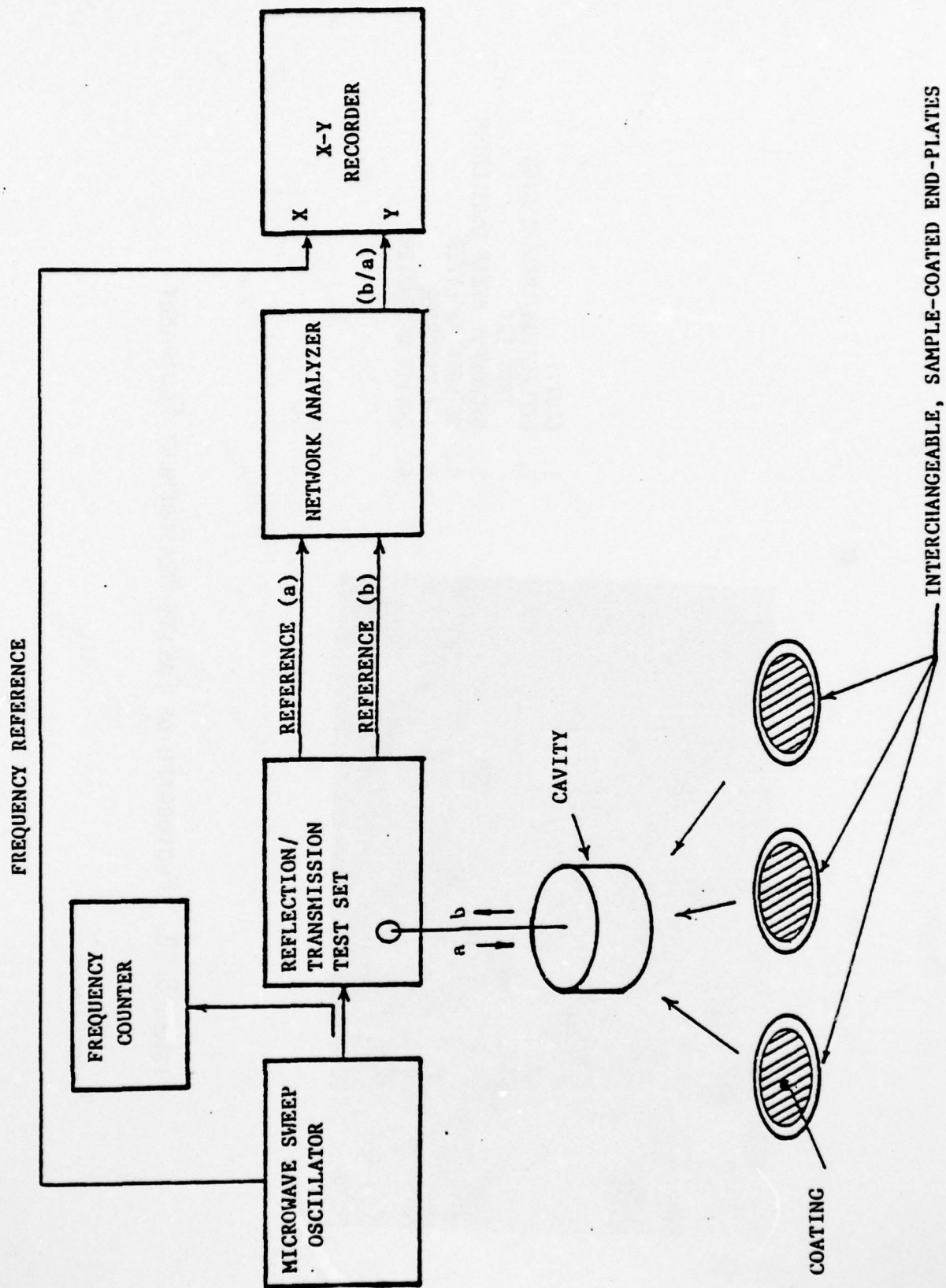
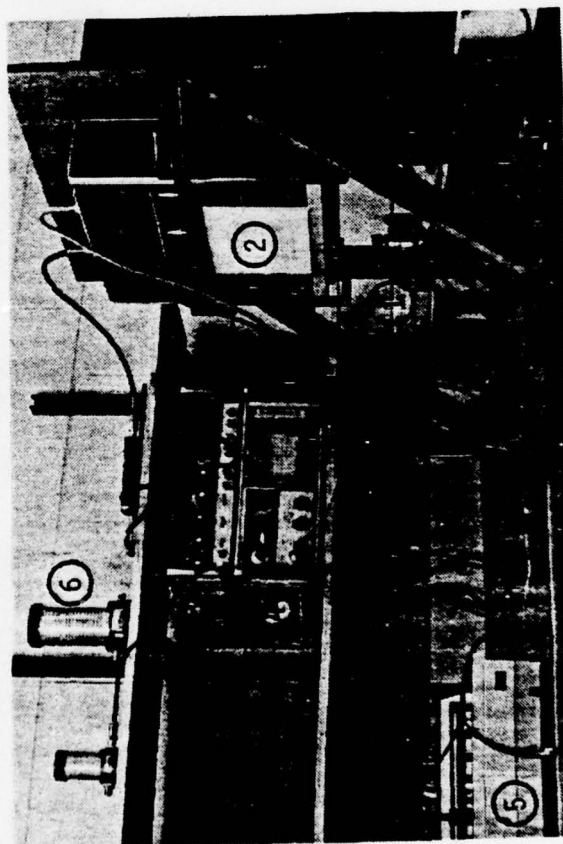


FIGURE 5.2A. BLOCK DIAGRAM OF THE ELECTROMAGNETIC TEST SYSTEM FOR THIN COATINGS



1. CAVITY
2. REFLECTION/TRANSMISSION
TEST SET
3. MICROWAVE SWEEP OSCILLATOR
4. NETWORK ANALYZER
5. X-Y RECORDER
6. CAVITY WAVEMETER

FIGURE 5.2B. PHOTOGRAPH OF CAVITY MEASUREMENT EQUIPMENT

AD-A077 805

SCIENCE APPLICATIONS INC EL SEGUNDO CALIF

F/G 17/9

HARDENED RADAR COMPONENT MATERIALS DEVELOPMENT STUDY. (U)

MAY 79 I OSOFSKY , R SEMELSBERGER , T DUNCAN

DAAG46-78-C-0052

UNCLASSIFIED

AMMRC-TR-79-34

NL

2 OF 3

AD
A077805



TABLE 5,6. TEST EQUIPMENT FOR CAVITY MEASUREMENTS

Item	Manufacturer/Model
Sweep Oscillator	Hewlett Packard/HP-8620C *Weinschel/430-A
Frequency Meter: Counter Wavemeter	Hewlett Packard/HP-5245 *Hewlett Packard/HP-537A
Reflection/Transmission Test Set	Hewlett Packard/HP-8743A
Network Analyzer	Hewlett Packard/HP-8410B
Phase/Amplitude Display	Hewlett Packard/HP-8412A
Recorder	Hewlett Packard/HP-7044A

* Alternate Equipment

be evidenced by poor repeatability of the test. To minimize this problem, each sample was tested several times, and extreme (high and low) values were discarded.

A Reflection/Transmission Test Set is used to separate incident and reflected signals at the cavity excitation port, and a Network Analyzer is used to measure the ratio of reflected-to-incident signals. The "Gain" and "Phase Offset" controls of the Network Analyzer provide the basic amplitude and phase calibration information. The Test Set can be viewed as an imperfect two-port network that is placed between the Network Analyzer and the load under test. The system calibration can be improved by determining the scattering parameters of the two-port. Such a calibration is accomplished routinely with a computerized "Automatic Network Analyzer", and the same procedures have been adapted for these cavity measurements with the manual Network Analyzer.^(11,12) Basically, the scattering parameters of the two-port are determined by recording reflection coefficients for several known loads. Typically, a matched termination, a short, and an open are used. Offset shorts may be used instead of the open. The procedure adopted for these tests uses a matched termination, three shorts, and one open. The three shorts are designated S-0 (Offset=0.000 in), S-1 (Offset=0.289 in), and S-2 (Offset=0.983 in). The open circuit was represented mathematically by the capacitance of an open-circuited 7mm connector. This calibration procedure requires manual transcription (digitization) of a large quantity of recorded data, but a substantial improvement in measurement accuracy is achieved.

A Frequency counter is used to measure frequencies at discrete points in the sweep range for each test recording. For the relatively narrow sweep ranges used here, the microwave frequency varies linearly with the dc "Sweep Output" signal from

the Sweep Oscillator. Therefore, the counter is used to measure the frequency at the start of the sweep and at the resonance peak, and intermediate frequencies are determined by linear interpolation.

The Network Analyzer measures the cavity reflection coefficient at the 7mm connector interface on the Test Set. The data is digitized, and a computer program is used to locate the reference plane that corresponds to the plane of the detuned open. At the detuned open position, the impedance varies like that of a series RLC circuit,

$$Z = R + j(\omega L - \frac{1}{\omega C}) \quad (5-1)$$

where ω is the source frequency. For real frequencies, the impedance locus is a straight line that is parallel to the imaginary axis. At other reference planes, the locus is not parallel to the imaginary axis. The computer program adjusts the reference plane to minimize the standard deviation of the resistance,

$$\sigma_R = \frac{1}{N-1} \left[\sum_{n=1}^N (R_{av} - R_n)^2 \right]^{1/2} \quad (5-2)$$

where R_n is the resistance at the n-th frequency, and R_{av} is the average resistance. When a minimum is obtained, the detuned open position is located. The plane of the detuned open will nearly coincide with the wall where the probe enters the cavity.

At the resonant frequency

$$\omega_1 = (LC)^{-1/2} \quad (5-3)$$

the locus intersects the real axis at $Z=R$. At the half-power frequencies $\omega_{1\pm}$, the impedances are

$$Z(\omega_{1\pm}) = R(1 \pm j) \quad (5-4)$$

Therefore, when the cavity impedance is referred to the plane of the detuned open, the resonant frequency and the half-power bandwidth may be easily recognized. Near resonance, the reactance varies almost linearly with frequency,

$$X(\omega) = s(\omega - \omega_1) \quad (5-5)$$

where s is the slope of the curve at resonance. The slope is determined by a least-squares fit of a linear function to the measured data. The half-power frequencies are calculated in terms of the resistance at resonance and the slope,

$$\omega_{1\pm} = \omega_1 \pm R/s \quad (5-6)$$

The factor Q_1 is a measure of the cavity resonance quality, with effects of the coupling network removed. In general, Q_1 includes losses in the cavity walls and losses in any dielectric material in the cavity. If a factor Q_W is associated with wall losses, and a factor Q_O is associated with dielectric losses, the unloaded factor is given by⁽⁵⁾,

$$Q_1^{-1} = Q_W^{-1} + Q_O^{-1} \quad (5-7)$$

If a factor Q_W' is determined from measurements of an empty cavity, Q_W in Equation (5-7) is related to Q_W' by the ratio of resonant frequencies,

$$Q_W = Q_W' (\omega_1 / \omega_1') \quad (5-8)$$

where ω_1' is the resonant frequency of the empty cavity. When low-loss dielectrics are measured, wall losses are a significant contribution to the unloaded Q , and the measurement of an empty cavity is necessary for an accurate calculation of Q_0 . Because this procedure incorporates all of the recorded data, it is presumably less subject to errors than one based on a simple observation or interpolation of the half-power points. However, the assumption that $X(\omega)$ is linearly varying does imply that the half-power bandwidth must be relatively narrow and, therefore, that the losses must be small. This assumption is not restrictive for the materials tested here.

In these tests, the walls of the main body of the brass cavity were polished to reduce surface losses. However, the ceramics were sprayed on relatively rough, molybdenum-coated end-plates. To determine Q_W' , empty cavity measurements were made using a molybdenum-coated end-plate with no ceramic coating.

The objective of the measurement is to determine the complex wave number k_0 . In the complex frequency plane, $\omega_c = \omega + jv$, and the resonance occurs at

$$\omega_0 = k_0 (\mu_0 \epsilon_0)^{-1/2} \quad (5-9)$$

It can be shown that ω_0 can be expressed in terms of a real frequency ω and the quality factor Q_1 at ω_1 , as follows:

$$\omega_0 = \omega_1 \left[\sqrt{1 - \frac{1}{4Q_1^2} + \frac{j}{2Q_1}} \right] \quad (5-10)$$

The cavity reactance is zero at ω_1 , and Q_1 is simply related to the half-power bandwidth. Therefore, ω_1 , Q_1 , ω_0 , and k_0 may be determined from a swept-frequency impedance measurement.

Table 5.7 shows dielectric properties for some known materials. The measured values were obtained using the measurement and data analysis procedures that were developed for these tests. The results agree reasonably well with the published values.

5.2.2.2 Shorted Waveguide Measurements

The dielectric parameters of a solid dielectric can be determined from a measurement of the input impedance of a sample-filled section of shorted transmission line. The measurement is convenient because special sample holders are not necessarily required and because the measurement itself can be accomplished by conventional microwave impedance measurement techniques (e.g., with slotted lines, reflectometers, or microwave network analyzers). The basic procedures are outlined here and measurement results for some known dielectrics are given in Table 5.3.

A sample holder for this measurement can be fabricated from standard, uniform transmission line (e.g., rectangular waveguide or coaxial line). As shown in Figure 5.3, a section of the line is shorted at one end, and the end adjacent to the short is completely filled with the dielectric to be tested. The thickness t of the dielectric sample should be measured with an accuracy better than one percent of the wavelength in the sample. The standard transmission line is usually air-filled, but in general it may be filled with a non-magnetic, low-loss dielectric having permittivity ϵ_m . The free space permeability and permittivity are μ_0 and ϵ_0 , respectively,

TABLE 5.7. NOMINAL DIELECTRIC PARAMETERS OF KNOWN MATERIALS

Material	Source*	Frequency (GHz)	Dielectric Constant :	Loss Tangent
Teflon	1a	3.000	2.10	0.0001
	2	2.728	2.21	0.0006
	1a	10.000	2.08	0.0006
	2	8.250	2.33	0.0110
Polyolefin	1b	0.001	2.36	0.0002
	1b	1.300	2.36	-
	2	2.715	2.38	0.0011
	2	8.227	2.75	0.0009

* 1a: Published tables: Dielectric Materials and Applications,
A.R. Von Hippel, ed., MIT Press, 1954.

1b: Manufacturer's literature: "Polyguide", Electronized
Chemical Corp.

2: Cavity Measurements

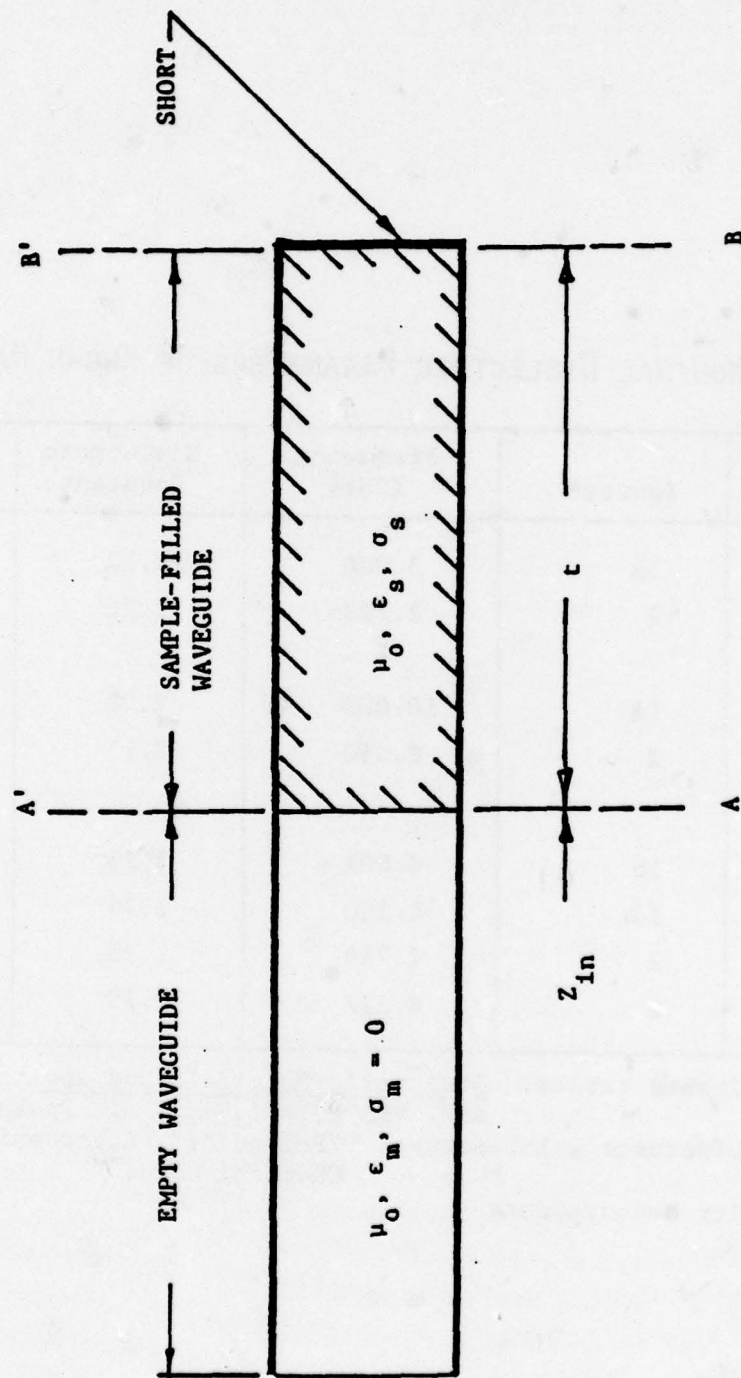


FIGURE 5.3. SAMPLE HOLDER MADE FROM A SHORTENED SECTION OF WAVEGUIDE (OR COAXIAL LINE)

and the (relative) dielectric constant is defined as $\epsilon_r = \epsilon_m / \epsilon_0$. The material under test (MUT) has dielectric constant $\epsilon_r = \epsilon_s / \epsilon_0$, and the conductivity σ_s .

The dielectric parameters of the sample can be expressed in terms of propagation constants and impedances. With an assumed time dependence $\exp(j\omega t)$, the transmission line propagation constant is

$$\gamma_g = j(k_m^2 - k_c^2)^{1/2} \quad (5-11)$$

where k_m is the wavenumber in the dielectric,

$$k_m = \omega(\mu_0 \epsilon_m)^{1/2} \quad (5-12)$$

and k_c is the cutoff wavenumber for the dominant mode in the line. For coax, $k_c = 0$, and for rectangular waveguide of width a , $k_c = \pi/a$. If losses are significant, the propagation constant may be measured and expressed in the form $\gamma_g = \alpha + j\beta$, where α is an attenuation constant. For both TE and TEM modes, the characteristic impedance of a transmission line can be defined as

$$Z_g = \frac{j\omega\mu_0}{\gamma_g} \quad (5-13)$$

which for TEM modes ($k_c=0$) reduces to the intrinsic wave impedance of the medium,

$$Z_m = (\mu_0 / \epsilon_m)^{1/2} \quad (5-14)$$

In the sample-filled section of the transmission line, the propagation constant is given by

$$\gamma_s = j(k_s^2 - k_c^2)^{1/2} \quad (5-15)$$

with

$$\begin{aligned} k_s^2 &= \omega^2 \mu_o \epsilon_s - j\omega \mu_o \sigma_s \\ &= \omega^2 \mu_o \epsilon_s (1 - j \tan \delta) \end{aligned} \quad (5-16)$$

where the loss tangent of the sample is

$$\tan \delta = \frac{\sigma_s}{\omega \epsilon_s} \quad (5-17)$$

For most microwave dielectrics, the conductivity is much more nearly constant with frequency than is the loss tangent. The useful aspect of the loss tangent parameter is that, for low-loss dielectrics, the power of a TEM wave is attenuated by a factor $\exp(-2\pi \tan \delta)$ in a distance of one wavelength. The characteristic impedance of the sample-filled section of line is

$$Z_s = \frac{j\omega \mu_o}{\gamma_s} \quad (5-18)$$

The input impedance Z_{in} at the sample interface (the plane A-A') in Figure 5.8 is given by the familiar formula for a shorted line,

$$Z_{in} = Z_s \tanh \gamma_s t \quad (5-19)$$

By normalizing impedances with respect to Z_g , and utilizing Equations (5-13), (5-18), and (5-19), the following transcendental equation for the unknown propagation constant γ_s is obtained:

$$\frac{Z_{in}}{Z_g} = \frac{\gamma_g t}{\gamma_s t} \tanh \gamma_s t \quad (5-20)$$

The quantities t , γ_g , and Z_{in}/Z_g can be determined from measured data.

The impedance ratio is related to the reflection coefficient Γ at the interface by

$$\frac{Z_{in}}{Z_g} = \frac{1 - \Gamma}{1 + \Gamma} \quad (5-21)$$

The impedance ratio or the reflection coefficient may be determined with a slotted line, a reflectometer, or a microwave network analyzer.

When transmission line losses are negligible, γ_g may be calculated from a measured frequency, using Equation (5-11). Otherwise, the input impedance ratio Z_{in}/Z_g for the empty sample holder may be measured; then, the propagation constant is given by

$$\gamma_g = t^{-1} \operatorname{arc} \tanh (Z_{in}/Z_g) \quad (5-22)$$

The transcendental equation (5-21) can be solved for γ_s by numerical iteration using Newton's method. Let

$$\omega = \gamma_s t \quad (5-23a)$$

$$z = z_{in}/(z_g \gamma_g t) \quad (5-23b)$$

and

$$f(\omega) = \omega^{-1} \tanh \omega - z \quad (5-24)$$

Then the roots of $f(\omega) = 0$ are required. By Newton's method, successive iterations of ω_n , $n=1,2,\dots$, are generated according to

$$\omega_{n+1} = \omega_n - \frac{f(\omega_n)}{f'(\omega_n)} \quad (5-25)$$

and it may be shown that

$$\frac{f(\omega)}{f'(\omega)} = \frac{\sinh \omega - z \omega \cosh \omega}{\omega - \cosh \omega \sinh \omega} \omega \cosh \omega \quad (5-26)$$

Equation (5-25) has been found to converge rapidly and accurately. Multiple roots may be resolved by inspection or by taking measurements with more than one sample thickness.

The dielectric constant and loss tangent are determined from the solution γ_s , using Equations (5-11) and (5-12) as follows

$$K_s = (1 - j \tan \delta) = \frac{k_c^2 - \gamma_s^2}{k_o^2} \quad (5-27)$$

where $k_o = \sqrt{\mu_o \epsilon_o}$ is the free space wavenumber.

Table 5-8 presents results of dielectric measurements for a number of low-loss materials. Impedances were measured by slotted-line techniques. For low-loss materials, the most significant error is in the measurement of voltage standing wave ratio (VSWR) or, equivalently, in the measurement of the magnitude of the reflection coefficient. The VSWR is very large (typically, greater than 50dB), and the magnitude of the reflection coefficient is very nearly unity.

A standing wave pattern is caused by interference between incident and reflected waves, and the null depths are very sensitive to slight differences in the wave amplitudes. However, for nearly equal wave amplitudes, the nulls are deep, and they may be hidden in noise. With laboratory sources, it is not practical to increase the power level enough to raise the nulls above the noise level. To overcome this problem, a procedure has been developed to fit a standing-wave interference curve (i.e., a curve of the form $A+B \cos^2 kz$) to a large number of measured data points. A least-squares curve-fitting routine is used. Typically, the positions and relative power levels of four points on each side of a null are recorded. Data is recorded at two successive nulls, to permit line losses to be measured and taken into account. Using this procedure, it has been found that severely mismatched impedances can be measured more accurately with a slotted line than with a Network Analyzer.

5.2.3 Pre-Test Analysis

As the resonant cavity measurement procedure has not been used extensively in the same form as that employed in this program, analysis was undertaken to ensure the accuracy and applicability of the technique. This part of Section 5.2 briefly highlights the analysis of the TM_{010} cavity case. A more complete treatment is provided in Appendix C.

TABLE 5.8. NOMINAL DIELECTRIC PARAMETERS OF KNOWN MATERIALS

Material	Source *	Frequency (GHz)	Dielectric Constant	Loss Tangent
Nylon 66	1a	3.0	3.03	0.0128
	2	9.0	2.94	0.0175
Rexolite 2200	1b	10.0	2.62	0.0014
	2	9.0	2.68	0.0012
Plexiglass	1a	10.0	2.59	0.0067
	2	9.0	2.68	0.0120
Polystyrene	1a	10.0	2.54	0.0004
	2	3.0	2.52	0.0008
	2	9.0	2.54	0.0003
Teflon	1a	10.0	2.08	0.0006
	2	3.0	2.06	0.0010
	2	9.0	2.04	0.0004

* 1a: Published tables: Dielectric Materials and Applications,
A.R. Von Hippel, ed., MIT Press, 1954.

1b: Manufacturer's literature

2 : Slotted line measurements

The geometry of this problem is illustrated by Figure 5.4. A right circular cylinder of radius "a" and height "d" is partially filled from the bottom to a height "b" with a material having a permittivity $\epsilon = \epsilon_r \epsilon_0$ and a conductivity σ . The dielectric-filled portion of the cylinder is called region 1, while the remaining free space portion is called region 2. The coordinate system is oriented so that the z - axis is coincident with the longitudinal axis of the cylinder.

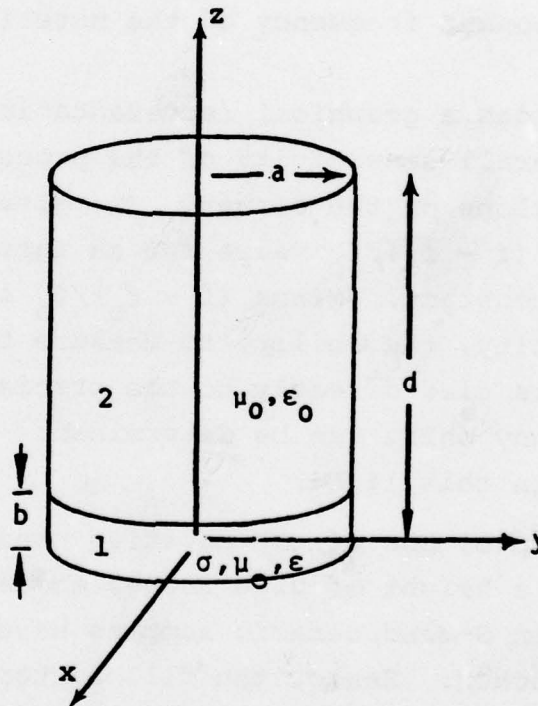


FIGURE 5.4. CIRCULAR RESONATOR WITH DIELECTRIC SAMPLE FILLING REGION 1 ($0 < z \leq b$)

For this geometry, the dielectric constant determination can be shown to be a function only of the shift in the resonant frequency of the cavity, viz:

$$\frac{f - f_o}{f_o} = \left[1 - b/d \left(\frac{\epsilon_r - 1}{\epsilon_r} \right) \right]^{1/2} - 1 \quad (5-28)$$

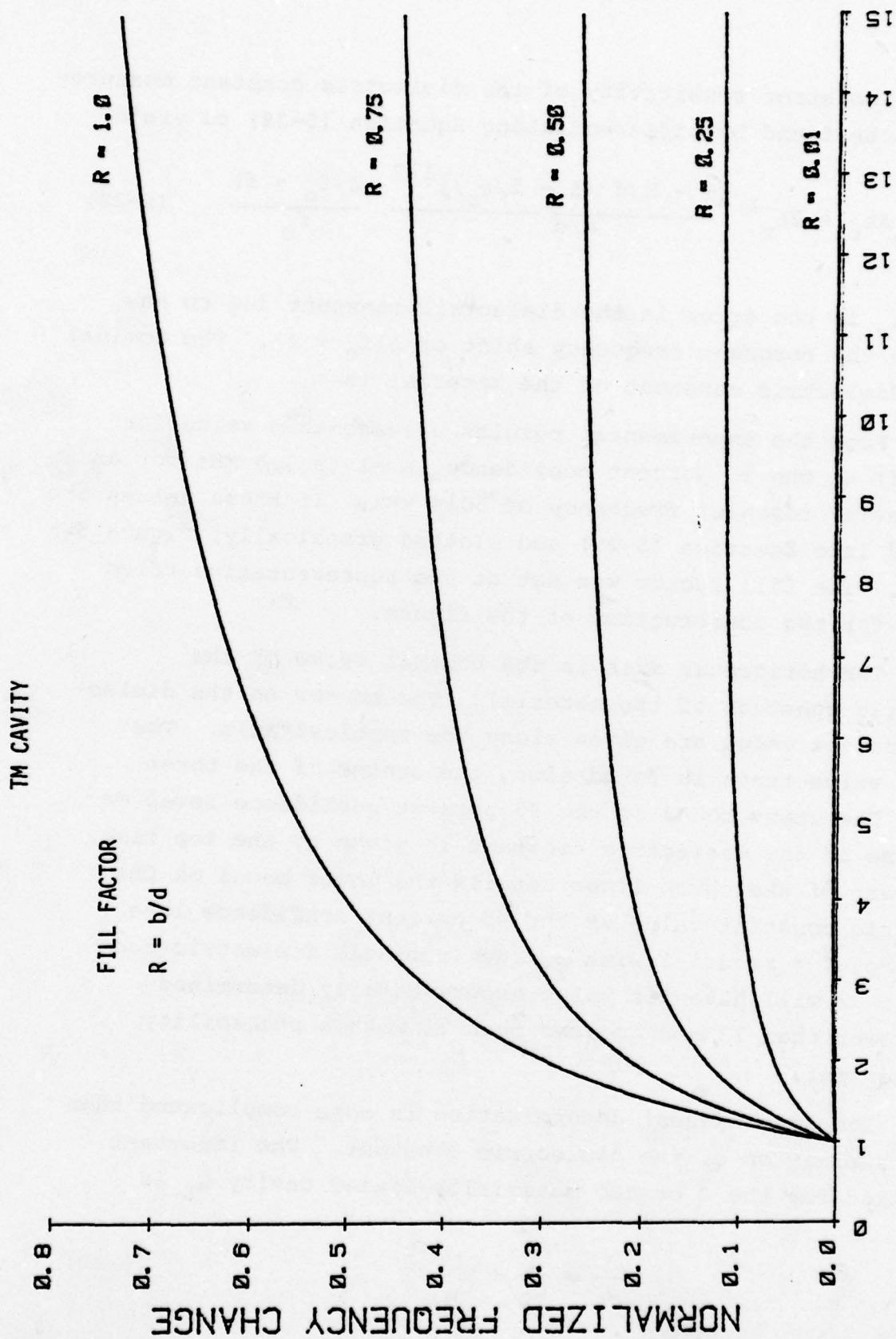
where

f_o = resonant frequency of the empty cavity

f = resonant frequency of the materially-loaded cavity

Figure 5.5 provides a graphical representation of Equation (5-28). The overall sensitivity of the procedure can be estimated from the slope of the curves. The greater the slope, the greater the $(f - f_o)/f_o$ value for an incremental change in the dielectric constant. Since $(f - f_o)/f_o$ is an experimentally measurable quantity, the ability to measure the dielectric constant value is tied directly to the precision with which the resonant frequency shift can be determined. The figure should be interpreted in this light.

For example, one of the cavities used in the experimental program had a height of 0.20 inches and a radius of 1.50 inches. The thin, S-band, ceramic samples have a nominal thickness of 0.050 inches. Hence, the fill factor is 0.25 for this example, and from Figure 5-5 it can be seen that the sensitivity of the measurement procedure degrades markedly as the nominal value of the dielectric constant increases.



DIELECTRIC CONSTANT

FIGURE 5.5. NORMALIZED FREQUENCY SHIFT VS. DIELECTRIC CONSTANT

The error sensitivity of the dielectric constant measurement can be found by differentiating Equation (5-28) to yield

$$\Delta\epsilon_r = 2\epsilon_r^2 \frac{[1 - b/d (1 - 1/\epsilon_r)]^{1/2}}{b/d} \frac{\Delta(f_o - f)}{f_o} \quad (5-29)$$

where $\Delta\epsilon_r$ is the error in the dielectric constant due to an error in the resonant frequency shift of $\Delta(f_o - f)$. The nominal (true) dielectric constant of the material is ϵ_r .

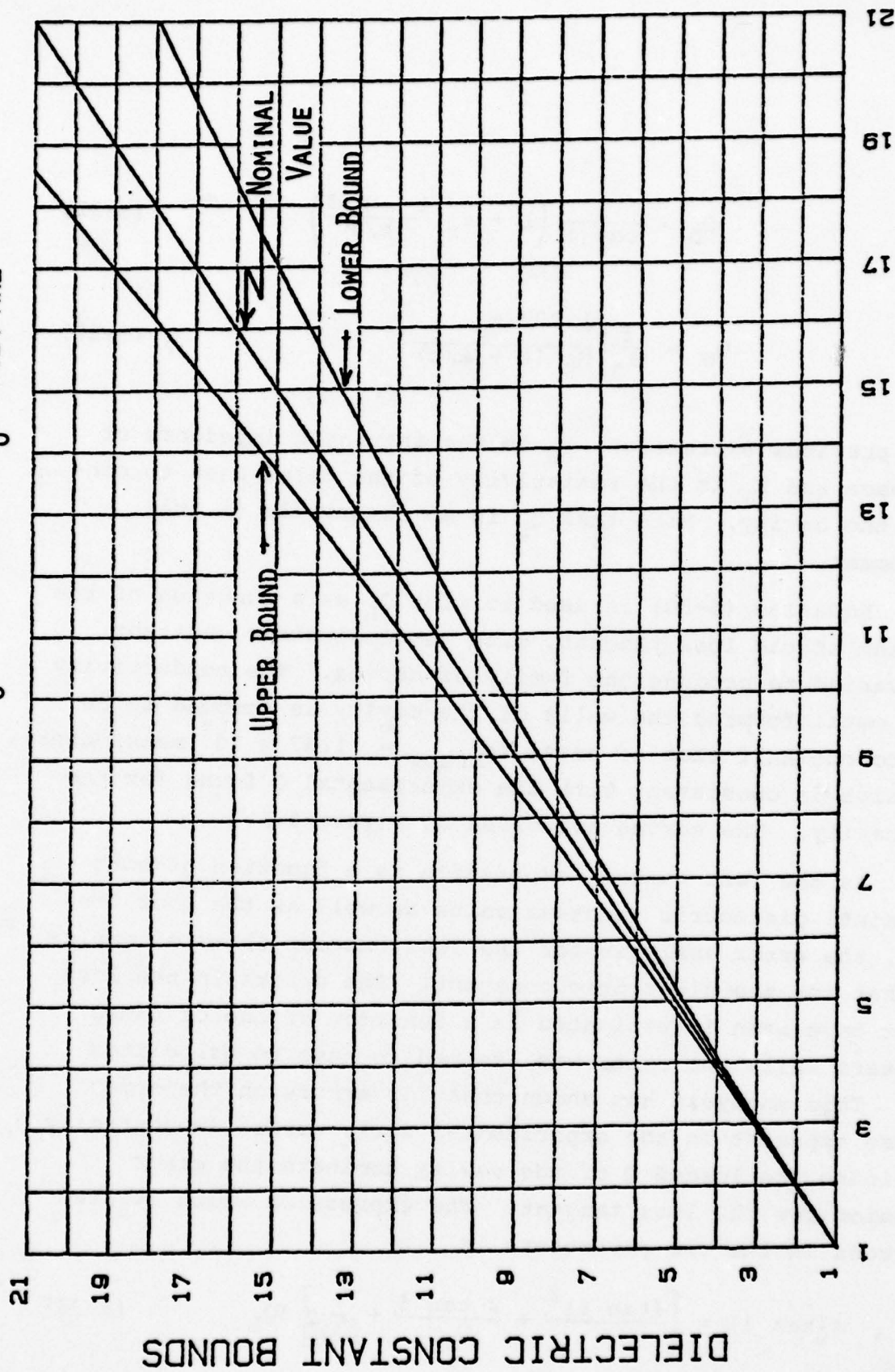
From the experimental results, a reasonable value for $\Delta(f_o - f)$ at the 95 percent confidence level is 3.0 MHz for an empty-cavity resonant frequency of 3014 MHz. If these values are inserted into Equation (5-29) and plotted graphically, Figure 5.6 results. The fill factor was set at the representative value of 0.25 for the construction of the figure.

The horizontal axis is the nominal value of the dielectric constant of the material. The bounds on the dielectric constant value are given along the vertical axis. The nominal value trace is found along the center of the three lines. The upper bound at the 95 percent confidence level on the value of the dielectric constant is given by the top line. The lowest of the three lines details the lower bound on the dielectric constant value at the 95 percent confidence level. For example, a material with a true (nominal) dielectric constant of 12 will have its value experimentally determined to be lower than 13 and greater than 11 with a probability of 95 percent.

The loss tangent determination is more complicated than the determination of the dielectric constant. The important expression for the Q of the materially-loaded cavity Q_L is

$$\frac{1}{Q_L} = \frac{1}{Q_D} + \frac{1}{Q_W} \quad (5-30)$$

TM CAVITY WITH $B/D = 0.25$ $\Delta(F - F_0) \approx 3.0$ MHZ $F_0 = 3014$ MHZ



NOMINAL DIELECTRIC CONTANT

FIGURE 5.6. DIELECTRIC CONSTANT ERROR BOUNDS CAUSED BY UNCERTAINTY IN RESONANT FREQUENCY SHIFT

where

$$Q_D \approx \frac{1}{\tan \delta} \left(1 + \epsilon_r \frac{1 - b/d}{b/d} \right) \quad (5-31)$$

$$Q_W = \frac{f}{f_0} \left[\frac{1.202 \eta_0}{R_S (1 + a/b)} \right] \quad (5-32)$$

In the previous expression, η_0 is the intrinsic impedance of free space and R_S is the resistivity of the metal used to construct the cavity. Note that Q_L is an observable in the measurement.

Equation (5-30) is used to plot Q_L as a function of the logarithm of the loss tangent, with the dielectric constant value varied to produce the family of curves. The conductivity of the metal forming the walls of the cavity is assumed to be equal to one-half that of brass ($\sigma_{\text{brass}} = 1.57 \times 10^7$ mhos/meter). This value is consistent with the experimental Q found for the empty cavity. The curves are given as Figure 5.7.

As the loss tangent expression is a function of both the nominal dielectric constant value as well as the Q of the cavity, the error analysis for the loss tangent is more complex than that for the dielectric constant. The errors in the loss tangent have been investigated as a function of one of these parameters while the other was assumed to have no associated error. This analysis has shown that for errors on the order of those apparent in the experimental work, errors in correctly determining the loaded Q of the cavity dominate the error expression for the loss tangent. The expression which relates the errors in the two parameters is

$$\Delta(\tan \delta) = \left[\frac{(\tan \delta)^2}{\tau} + \frac{2 \tan \delta}{Q_W} + \frac{\tau}{(Q_W)^2} \right] \Delta Q_L \quad (5-33)$$

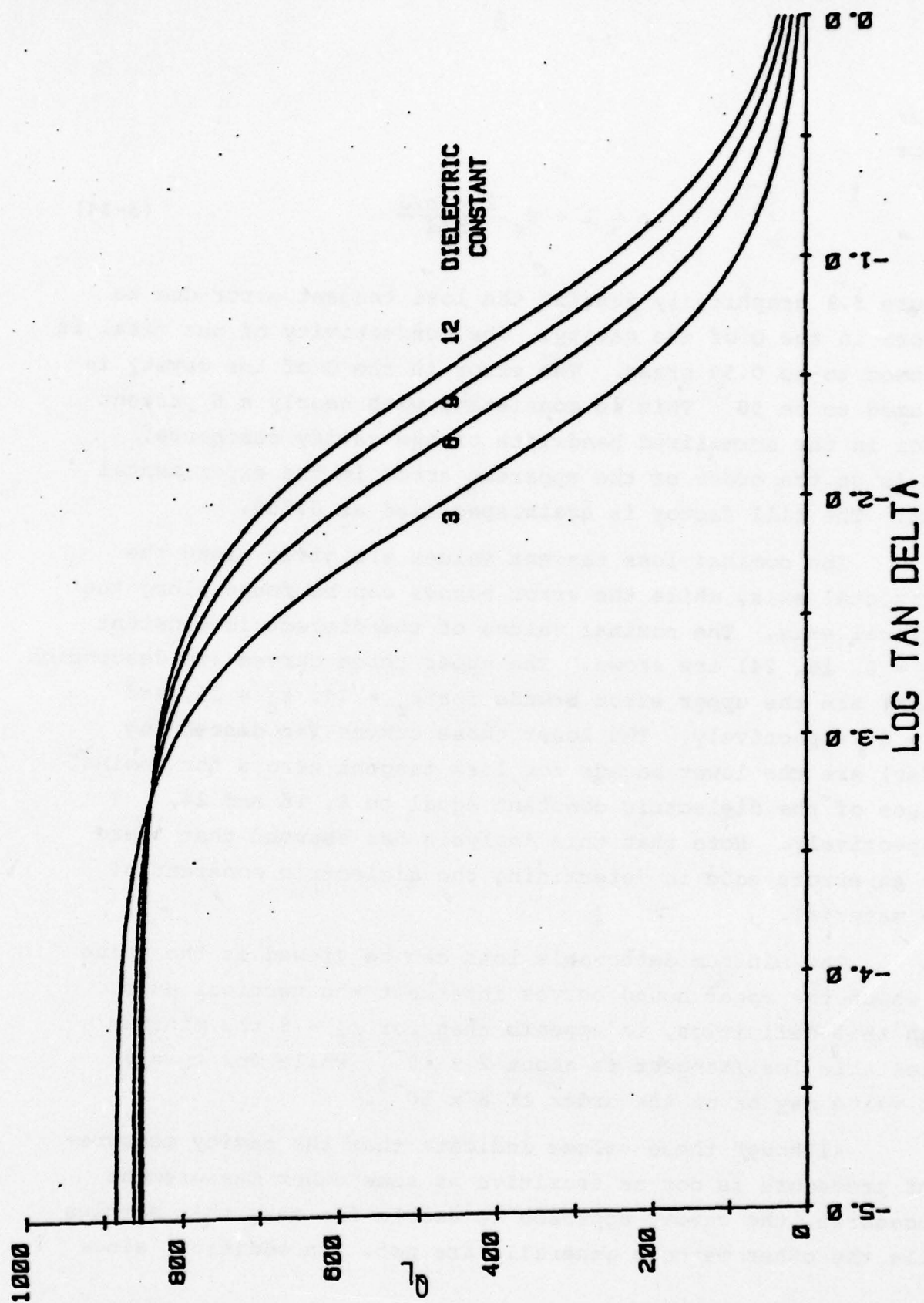


FIGURE 5.7. LOADED Q VERSUS LOSS TANGENT, $\sigma = 0.5$ BRASS

where

$$\tau = 1 + \epsilon_r \frac{1 - b/d}{b/d} \quad (5-34)$$

Figure 5.8 graphically details the loss tangent error due to errors in the Q of the cavity. The conductivity of the metal is assumed to be 0.50 brass. The error in the Q of the cavity is assumed to be 50. This is consistent with nearly a 6 percent error in the normalized bandwidth of the cavity resonance, and is on the order of the apparent error in the experimental work. The fill factor is again specified as 0.250.

The nominal loss tangent values are given along the horizontal axis, while the error bounds can be found along the vertical axis. The nominal values of the dielectric constant ($\epsilon_r = 8, 16, 24$) are shown. The upper three curves (in descending order) are the upper error bounds for $\epsilon_r = 24$, $\epsilon_r = 16$, and $\epsilon_r = 8$ respectively. The lower three curves (in descending order) are the lower bounds for loss tangent errors for nominal values of the dielectric constant equal to 8, 16 and 24, respectively. Note that this analysis has assumed that there are no errors made in determining the dielectric constant of the material.

The minimum detectable loss can be viewed as the value at which the upper bound curves intersect the vertical axis. With this definition, it appears that for $\epsilon_r = 8$ the minimum detectable loss tangent is about 2×10^{-3} , while for $\epsilon_r = 24$ the value may be on the order of 6×10^{-3} .

Although these values indicate that the cavity measurement procedure is not as sensitive as some other measurement procedures, the cavity approach is usable for very thin samples while the other methods generally are not. In addition, since

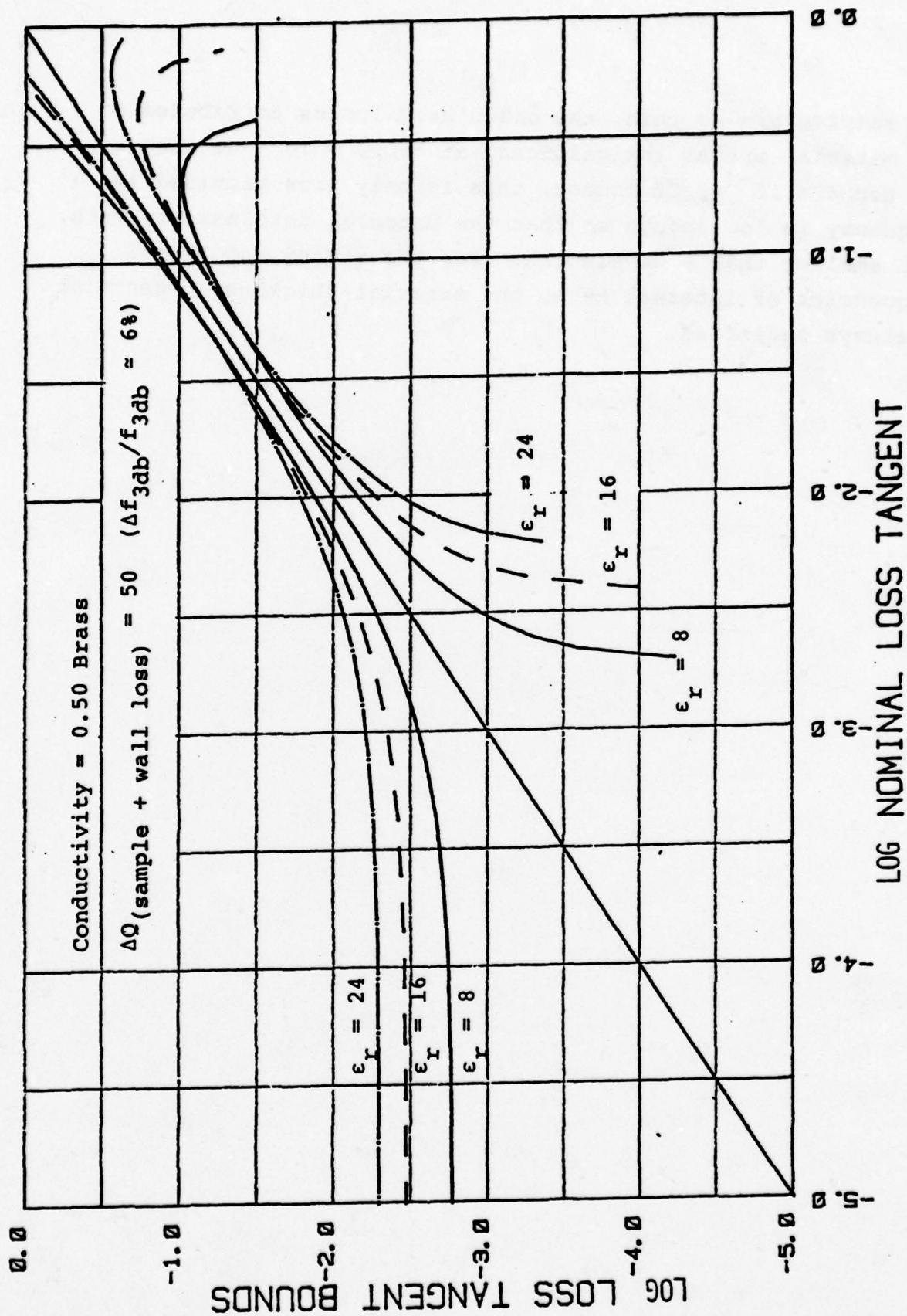


FIGURE 5.8. LOSS TANGENT ERROR BOUNDS CAUSED BY UNCERTAINTY IN Q MEASUREMENT

the samples are so thin, the calculated losses attributed to the material are as insignificant at $\tan \delta = 10^{-3}$ as they are for $\tan \delta < 10^{-4}$. Of course, this is only true provided the frequency is low enough so that the material thickness is much, much smaller than a wavelength. For the S-Band and X-Band frequencies of interest here, the material thickness constraint is always satisfied.

5.3 Array-Hardening Materials Interaction Analysis

The materials under consideration in this study would primarily be used in either of two ways: (1) dielectric waveguide plugs or (2) dielectric slabs covering an array. It is well known in the array design field that the application of any material in either of these ways has important implications regarding the performance of an array. In this section, the interactions between the hardening material and array performance parameters are considered. The issues of reflection losses and dissipative losses is addressed briefly, while somewhat greater emphasis is placed on the issue of array blindness. The theoretical analysis of the array blindness question is presented in Appendix D and only the implications of that analysis are presented.

5.3.1 Mechanisms of Array Performance Degradations

As a first order approximation, there are three phenomena which contribute to the degradation of array performance when that array has either a covering dielectric slab or dielectric waveguide plugs. These are (1) reflection losses, (2) dissipative losses and (3) array blindness. A schematic representation of the degradation mechanisms is given by Figure 5-9 for a dielectric covered array. The phenomena are essentially the same for an array with waveguide plugs.

The figure portrays an array of apertures containing incident energy. A portion of that energy is reflected at the slab interface, while the remaining energy passes into the slab. In the slab, some of the incident energy is consumed in material losses while the rest of the energy is, in general divided between the desired main antenna beam and perhaps a "leaky wave" in the slab structure. If the leaky wave is launched, the energy in that wave propagates out of the slab along its entire extent and interferes in a vector sense with the main beam. At those

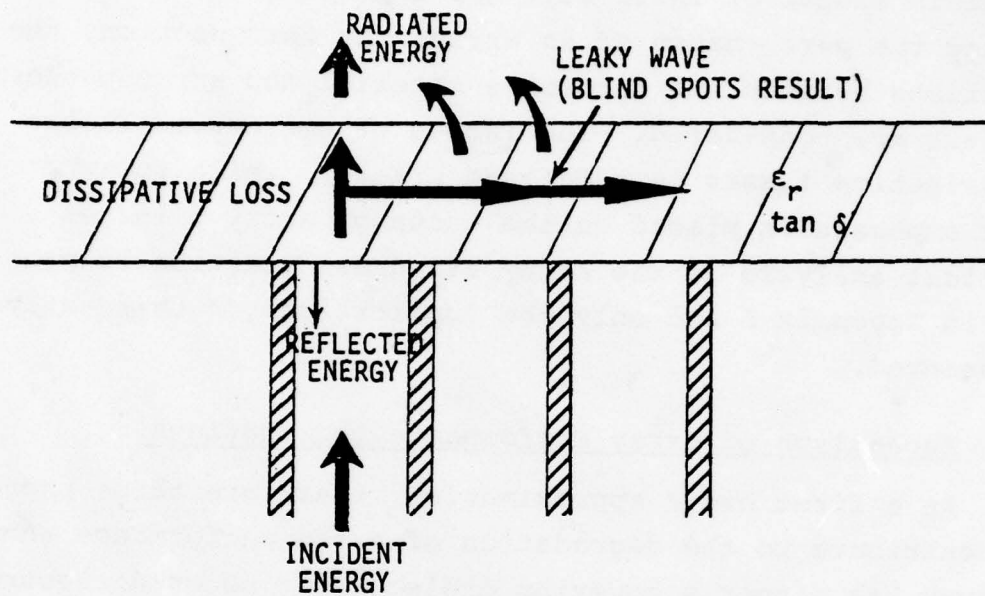


FIGURE 5.9. SCHEMATIC OF ARRAY PERFORMANCE DEGREDEDATIONS MECHANISMS FOR A DIELECTRICALLY COVERED ARRAY

array scan angles at which the leaky wave exactly cancels the main beam, the array is said to have a blind spot; the array will neither transmit nor receive energy in that direction.

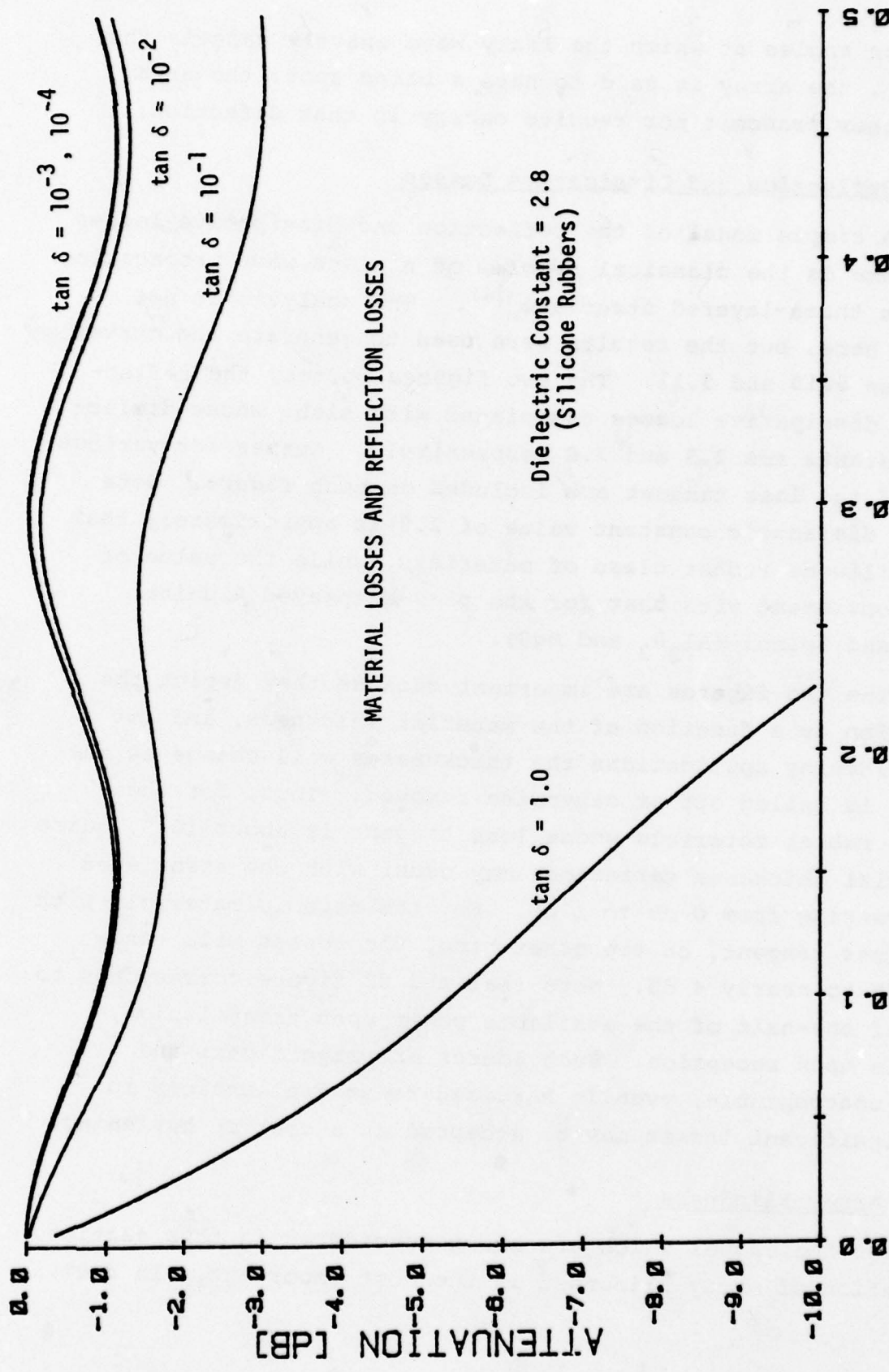
5.3.2 Reflection and Dissipative Losses

A simple model of the reflection and dissipative losses in a radome is the classical problem of a plane wave propagating through a three-layered structure⁽¹⁴⁾. The analysis is not repeated here, but the results were used to generate the curves of Figures 5.10 and 5.11. The two figures portray the reflection and dissipative losses associated with slabs whose dielectric constants are 2.8 and 7.0 respectively. Curves for various values of the loss tangent are included on each figure. Note that the dielectric constant value of 2.8 is approximately that of the silicone rubber class of materials, while the value of 7.0 is consistent with that for the plasma-sprayed Alumina (Al_2O_3) and Spinel (Al_2O_3 and MgO).

The two figures are important because they depict the attenuation as a function of the material thickness, and for these hardening applications the thicknesses will change as the material is boiled off or otherwise removed. Thus, for the silicone rubber materials whose loss tangent is about 10^{-2} , quite substantial thickness variations may occur with the associated losses ranging from 0 dB to 1 dB. For the ceramic materials with a 10^{-2} loss tangent, on the other hand, the losses will range from 0 dB to nearly 4 dB. Note that a 3 dB figure corresponds to a loss of one-half of the available power upon transmission, and again upon reception. Such losses are significant and perhaps unacceptable, even in hardened radar applications in which significant losses may be accepted as a cost of hardening.

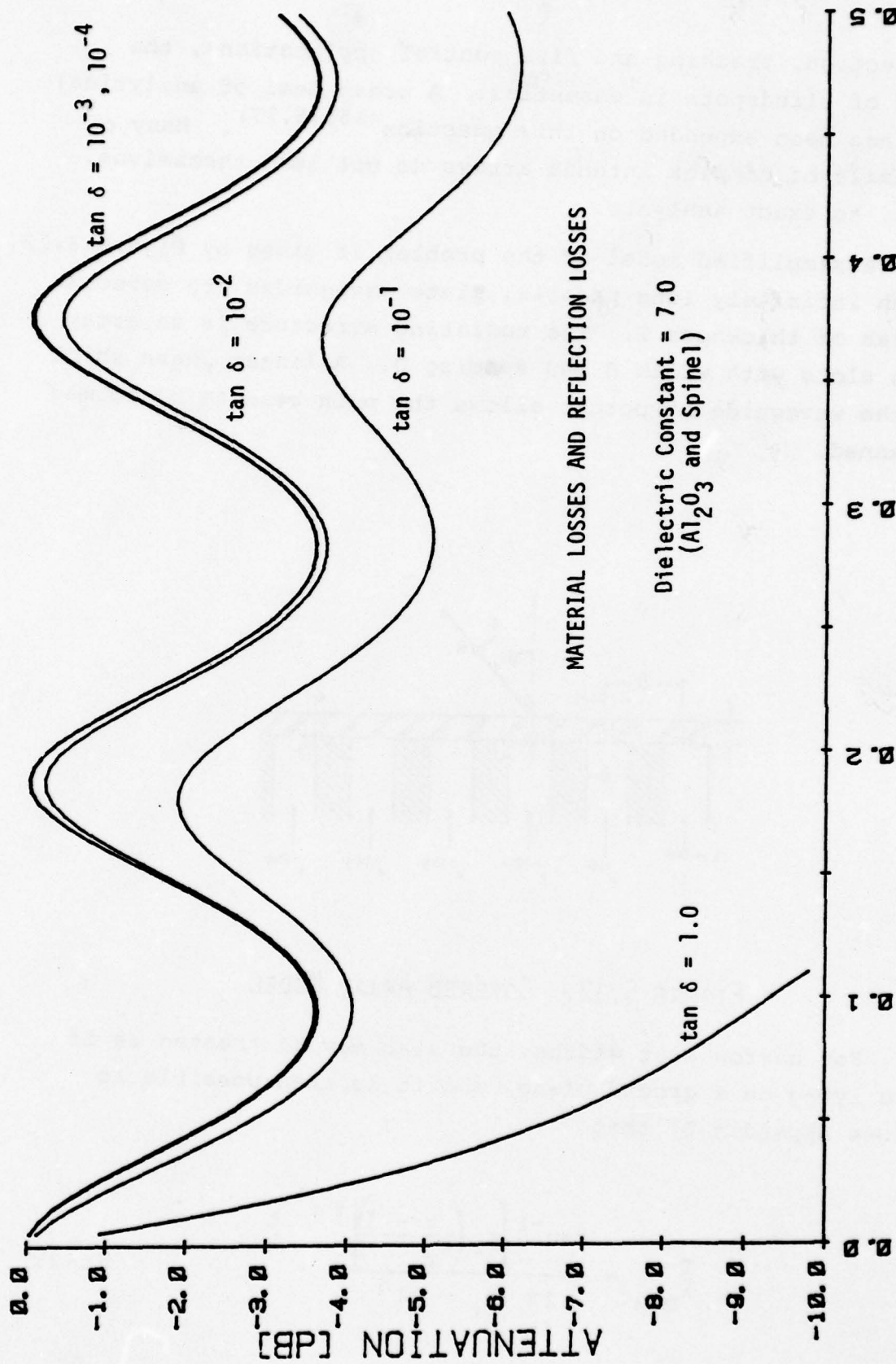
5.3.3 Array Blindness

Of the issues which are being considered in this section, the question of array blindness is the most important. In fact,



THICKNESS [freespace wavelengths]

FIGURE 5.10. RADOME EFFICIENCY FOR A FLAT ARRAY COVERED
BY A SLAB WITH A DIELECTRIC CONSTANT OF 2.8



THICKNESS [freespace wavelengths]

FIGURE 5.11. RADOME EFFICIENCY FOR A FLAT ARRAY COVERED BY A SLAB WITH A DIELECTRIC CONSTANT OF 7.0

for detection, tracking and fire control applications, the absence of blindspots is essential. A great deal of analytical effort has been expended on this question^(15,16,17). Many of the details of complex antenna arrays do not lend themselves, however, to exact analysis.

A simplified model of the problem is given by Figure 5.12, in which infinitely long parallel plate waveguides are covered by a slab of thickness T . The radiating structure is an array of thin slots with width B and spacing D . A linear phase shift along the waveguide structure allows the main beam to be formed and scanned.

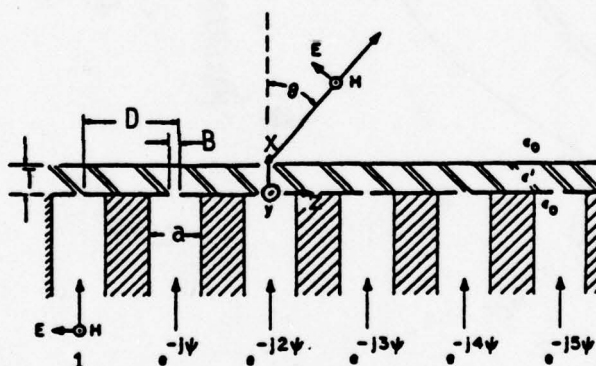


FIGURE 5.12. COVERED ARRAY MODEL

For narrow slot widths, the slab may be treated as if it were lying on a ground plane, and it is then possible to show (see Appendix D) that

$$\frac{T}{\lambda_{\max}} = \frac{\tan^{-1} \left[\epsilon_r \left(\frac{\tau - 1}{\epsilon_r - \tau} \right) \right]^{\frac{1}{2}}}{2\pi (\epsilon_r - \tau)^{\frac{1}{2}}} \quad (5-35)$$

where

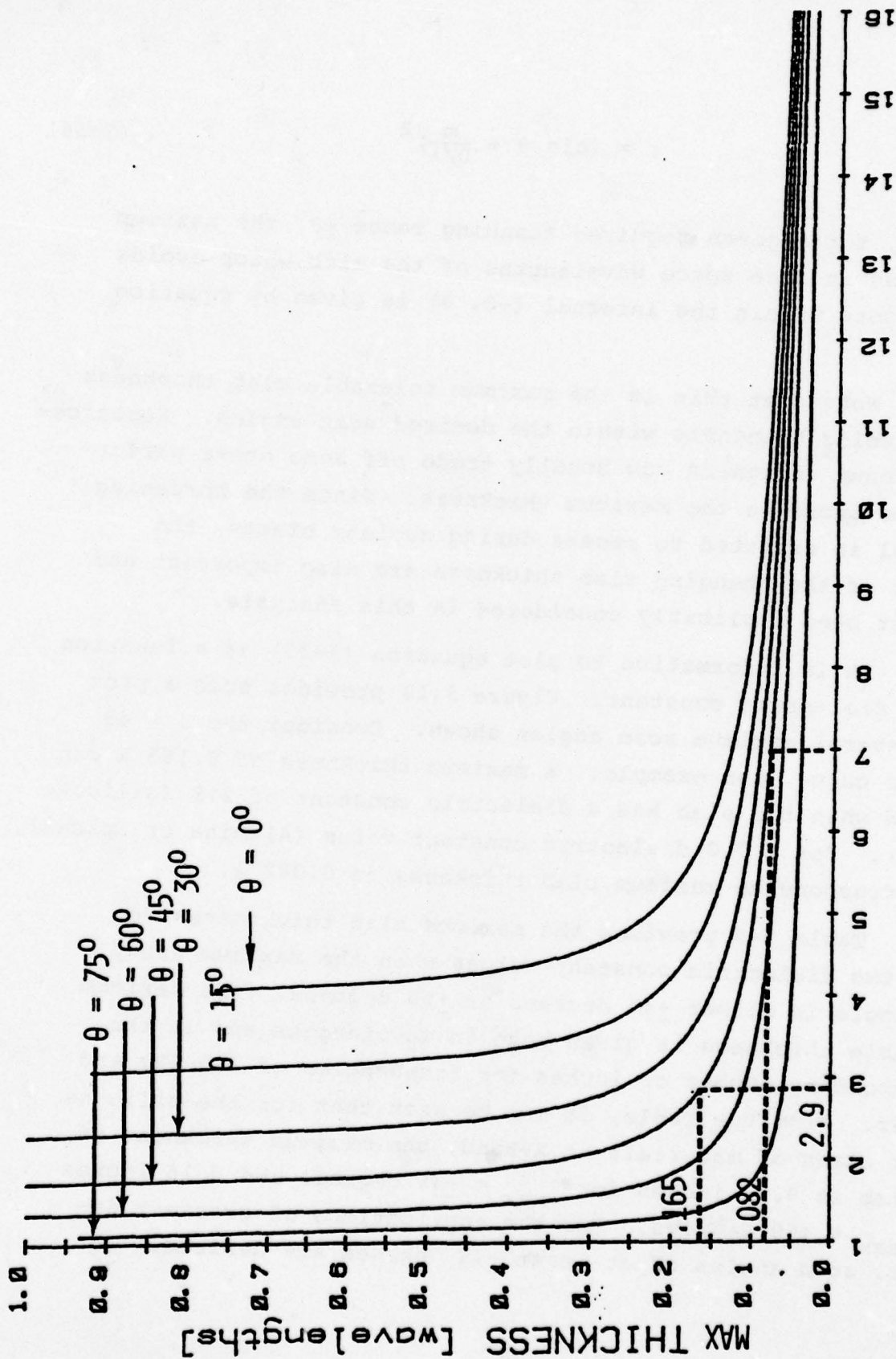
$$\tau = \left(\sin \theta + \frac{m}{D/\lambda} \right)^2 \quad (5-36)$$

That is, for a given required scanning range $\pm\theta$, the maximum thickness in free space wavelengths of the slab which avoids blind spots within the interval $(-\theta, \theta)$ is given by equation (5-35).

Note that this is the maximum tolerable slab thickness which avoids blindness within the desired scan angles. Resourceful antenna designers can usually trade off some other performance to increase the maximum thickness. Since the hardening material is expected to recess during nuclear blasts, the effects of the changing slab thickness are also important and have not been explicitly considered in this analysis.

It is informative to plot equation (5-35) as a function of the dielectric constant. Figure 5.13 provides such a plot with several maximum scan angles shown. Consider the $\theta = 45$ degrees curve, for example: a maximum thickness of 0.165λ can be used when the slab has a dielectric constant of 2.9 (silicone rubber). For a 7.0 dielectric constant value (Alumina or Spinel), the corresponding maximum slab thickness is 0.082λ .

Table 5.9 provides the maximum slab thicknesses for these two dielectric constant values when the maximum array scan angle is either ± 45 degrees or ± 60 degrees. The maximum allowable thickness is given both in wavelengths and in the corresponding number of inches for frequencies of 3.0 GHz and 9.0 GHz. From the Table, it can be seen that for the silicone rubber class of materials at X-Band, the maximum thickness of the slab is 0.22 inches for $\theta_{\max} = \pm 45$ degrees and 0.16 inches for $\theta_{\max} = \pm 60$ degrees. For the applications of greatest interest, scan angles of at least ± 45 degrees are desired. For



DIELECTRIC CONSTANT

FIGURE 5.13. MAX SLAB THICKNESS VS. DIELECTRIC CONSTANT FOR BLINDSPOT ANGLES GREATER THAN SPECIFIED SCAN ANGLE θ

TABLE 5.9. MAXIMUM SLAB THICKNESS FOR WHICH SCAN REQUIREMENTS
MAY BE MET WITHOUT ANY ARRAY DESIGN MODIFICATIONS

DIELECTRIC CONSTANT	MAX THICKNESS (WAVELENGTHS)		FREQUENCY	MAX THICKNESS (INCHES)	
	$\theta_{\text{MAX}} = 45$	$\theta_{\text{MAX}} = 60^\circ$		$\theta_{\text{MAX}} = 45$	$\theta_{\text{MAX}} = 60^\circ$
2.9 (SILICONE RUBBER)	0.165 λ	0.111 λ	S-BAND (3.0 GHZ)	0.656	0.469
			X-BAND (9.0 GHZ)	0.219	0.156
7.0 (ALUMINA, SPINEL)	0.082 λ	0.067 λ	S-BAND (3.0 GHZ)	0.344	0.266
			X-BAND (9.0 GHZ)	0.115	0.089

the ceramics at X-Band, the maximum thickness is 0.12 inches for $\theta_{\max} = \pm 45$ degrees and 0.09 inches for $\theta_{\max} = \pm 60$ degrees. Of the ceramic materials which were subjected to the electrical tests, no samples were found with a thickness greater than 0.09 inches. Thus, for either type of material, there is good reason to believe that these materials may be useful for array hardening from an electrical point of view, provided that the thicknesses which have been discussed are adequate for the thermal protection of the array. If greater thicknesses are required, then the array must be "tuned" to tolerate the greater thickness. However, recession of the layer due to thermal exposure would tend to affect the performance of such an array.

5.4 Conclusion

The major accomplishments and conclusions of the electrical properties test and analysis task are as follows:

1. A cavity measurement procedure for plasma-sprayed ceramic materials has been developed and refined.
2. Electrical properties have been measured for plasma-sprayed ceramics at S-Band and at X-Band.
3. Electrical properties have been measured for silicone rubber materials (including their chars) at S-Band and at X-Band.
4. For the material thicknesses considered in this study, the silicone rubber materials appear promising from an electrical point of view. Of the plasma-sprayed ceramics, the Alumina (Al_2O_3) and Spinel appear to be the most promising, again from an electrical perspective.
5. The hardening material/array interaction question must be considered as an integral part of the array design process.

While the results to date show promise, a significant amount of work remains to be undertaken before the usefulness of these materials may be adequately assessed. In particular:

1. Larger numbers of samples of each promising material must be evaluated.

2. The char structure of the silicone rubber materials must be quantitatively investigated.
3. The array interaction questions must be treated in greater depth. This can be accomplished only by considering specific array configurations in detail.
4. The electrical variations in the materials must be found for such large structures as arrays.
5. The thickness variations in the materials must be found for such large structures as arrays.
6. The implications of (4) and (5) on the array performance must be determined in an analytical manner.
7. A proof-of-principle model would be instructive in assessing the viability of specific hardening concepts.

6.0 MECHANICAL PROPERTIES TEST

6.1 Mechanical Properties Requirements

In the structural analysis of structures with thermal protection, it is necessary to calculate and predict how the structure will survive the thermal pulse and the shock wave pulse caused by a nuclear burst. The primary type of construction under investigation consists of a metal surface coated with a plasma sprayed ceramic. Typically, the ceramic is thin, in the order of 0.125 inches or less and the metal substrate is at least .125 inches thick. It may even be on the order of one inch thick on parts of the radar assembly.

During the thermal pulse, the ceramic heats up rapidly, especially near its outer surface, but the metal substrate heats relatively slowly below the ceramic. During heating, the ceramic and metal expand or try to expand according to the relationship

$$\delta = \alpha l \Delta t$$

δ = total expansion, inches

α = expansion coefficient, inches/inch $^{\circ}\text{F}$

Δt = temperature rise, $^{\circ}\text{F}$

Because the outer layer of ceramic is very hot, on the order of its melting point, $t \approx 5000^{\circ}\text{F}$ for ZrO_2 , and the inner layers next to the steel are relatively cool, initially a differential expansion exists across the ceramic layer. This is restrained by shear forces in the ceramic and metal-ceramic bond. Thus compressive stresses are generated in the outer layer and tensile stresses in the inner layer as well as shear stresses in the lamanae.

The elongation due to such stress at constant uniform temperature is given by the relationship $\delta = \frac{s l}{E}$

δ = elongation, inches

s = unit stress (compressive or tensile), psi

E = modulus of elasticity, (psi) at specific temperature

The relationship shown is for a simple one-dimensional case. Poisson's ratio is used to calculate the effect of two and three-dimensional stress and strain.

The values of α , E, S_t , S_c , S_s and ν are used to calculate thermal stress and failure criteria in the structures. Therefore, as a minimum, it is necessary to have the following data for the ceramics:

1. Modulus of Elasticity
2. Tensile Strength
3. Compressive Strength
4. Shear Strength (Parallel to Substrate)
5. Bond Strength (Shear and Tension)
6. Poisson's Ratio
7. Linear Coefficient of Expansion (Three Axes)

It is desirable to obtain the following properties for the plasma-sprayed ceramic as a function of at least three temperatures: Room temperature, 1500°F and 3000°F.

Desired Data

1. Modulus of elasticity
 - a. Tensile (parallel to layer)
 - b. Compressive (parallel to layer)
 - c. Tensile (normal to layer)
2. Ultimate strength
 - a. Tensile (parallel to layer)
 - b. Compressive (parallel to layer)
 - c. Tensile (normal to layer)

3. Bond shear strength (parallel to layers)
4. Adhesive strength (normal to layers)
5. Linear thermal expansion coefficient
6. Poisson's Ratio
7. Open and closed porosity sizes and ratios
8. Density
9. Shear strength

Most of these values must be determined as a function of temperature from room temperature to as close to the melting point as is practical. Because the above mentioned properties are functions of the processing, it is important to determine their values for specimens manufactured by the same process that would be used to coat the radar surfaces.

6.2 Mechanical Properties Test Program Plan

Mechanical properties testing will be conducted by the BMD Materials Program test facility at AMMRC. SAI has fabricated the bulk specimens, exposed them to a predetermined thermal environment, and suggested required properties and temperatures to be obtained. A standard plasma spray structural test specimen was designed and fabricated by SAI. It was a thin metal plate four inches square coated with plasma sprayed ceramic approximately 0.125 inches thick. Figure 4.11 illustrates a typical specimen.

This specimen was designed to be cut into smaller shapes for actual test by means of a diamond coated abrasive wheel. The actual shape and size of each sub specimen to be determined by AMMRC. Forty of these specimens were fabricated and were to be exposed to thermal environments as described in Table 6.1

TABLE 6.1
Structural Test Coupon Matrix
All Specimens 4" Square

<u>Spec. No.</u>	<u>Test Type</u>	<u>No. of Exposures</u>	<u>Coating Material</u>	<u>Infiltrant</u>
52	No Exposure	0	Al ₂ O ₃	Silicone
53	Radiation	1	"	"
54	"	2	"	"
55	Fireball	1	"	"
56	"	2	"	"
58	No Exposure	0	"	0
59	Radiation	1	"	0
60	"	2	"	0
61	Fireball	1	"	0
62	"	2	"	0
64	No Exposure	0	Spinel	Silicone
65	Radiation	1	"	"
66	"	2	"	"
67	Fireball	1	"	"
68	"	2	"	"
70	No Exposure	0	"	0
71	Radiation	1	"	0
72	"	2	"	0
73	Fireball	1	"	0

Table 6.1 (Cont'd)

<u>Spec. No.</u>	<u>Test Type</u>	<u>No. of Exposures</u>	<u>Coating Material</u>	<u>Infiltrant</u>
74	Fireball	2	Spinel	0
76	No Exposure	0	ZrO ₂	Silicone
77	Radiation	1	"	"
78	"	2	"	"
79	Fireball		"	"
80	"	2	"	"
82	No Exposure	0	"	0
83	Radiation	1	"	0
84	"	2	"	0
85	Fireball	1	"	0
86	"	2	"	0
88	No Exposure	0	ZrO ₂ MgO	Silicone
89	Radiation	1	"	"
90	"	2	"	"
91	Fireball	1	"	"
92	"	2	"	"
94	No Exposure	0	"	0
95	Radiation	1	"	0
96	"	2	"	0
97	Fireball	1	"	0
98	"	2	"	0
100	No Exposure	0	ZrO ₂ ·Y ₂ O ₃	Silicone
101	Radiation	1	"	"
102	"	2	"	"
103	Fireball	1	"	"
104	"	2	"	"
106	No Exposure	0	"	0
107	Radiation	1	"	0
108	"	2	"	0
109	Fireball	1	"	0
110	"	2	"	0

Some of the specimens were to be tested before heating in the TRS facility to obtain results on virgin material. Similar structural tests were to be performed on once heated and twice heated ceramic to see what if any property damages were caused by the radiation and convective heating. The temperature cycling will also be done at AMMRC by cyclic heating the specimens.

7.0 CONCLUSIONS AND RECOMMENDATIONS

The conclusions derived from this study are presented under the categories of (1) test techniques, (2) material performance, and (3) radar hardening implications.

Test Techniques

The nuclear thermal radiation environment design criteria is so severe that no currently available test facility can simulate the combined flux and fluence level. The Solar Furnace is a proven technique for obtaining the desired fluence level but is limited in flux level and size of components which can be tested. The SAI Pulse Type Thermal Radiation Simulator shows promise for simulating the higher flux levels and for testing larger components but is limited in total fluence. This facility is also in the development stage and requires extensive calibration before it can be used for routine testing with high confidence. A continuous burning TRS with high fluence capability is in development.

A cavity measurement procedure was designed for electrical properties tests for thin specimens at s-band and x-band frequencies. Analyses confirmed that adequate measurement sensitivity was available for obtaining dielectric constant and loss tangent values for the materials under evaluation.

Material Performance

The infiltrated (silicone) porous ceramic coatings had poor thermal performance. The silicone forms a low carbon char when it decomposes under thermal radiation heating. This residual char raises the absorptivity of the surface to high values which result in excessive material heating and melting. Uninfiltrated porous ceramic coatings are expected

to provide adequate thermal performance if the absorptivity can be maintained at 0.2 or less. This level has been obtained for Al_2O_3 and ZrO_2 coatings in previous program tests.

The ceramics experienced some thermal stress failures during heating. This remains a major concern; however, analyses suggest that pre-heating the base metal during plasma spraying of the coating may reduce tensile failures during subsequent thermal exposure. The electrical property test results showed loss tangent values less than 0.03 but reasonably large values of dielectric constant (6-20) for the ceramic coating materials.

The silicone ablator showed excellent thermal performance. The thick char allows a high surface temperature and thus high re-radiation of incident heat flux while the insulative properties of the char and virgin material protect the underlying structure. The char was found to contain a low fraction ($\sim 7\%$) of carbon which degraded the electrical properties to some extent. The virgin electrical properties tests showed low loss tangent and dielectric constants.

Other materials were tested thermally with the following results. An AS-3DX composite partially melted but survived the solar furnace test environment. The BN (HBR Grade) experienced thermal stress cracking in the solar furnace tests. The teflon specimens were observed to absorb significant radiation in-depth and free carbon forms on the surface during heating. Insufficient thermal data was obtained on a number of bulk ceramic and uninfiltrated porous ceramic coating materials due to the lack of adequate heating during the Thermal Radiation Simulator tests and the limited number of specimens which could be tested in the French Solar Furnace during the designated test period.

Radar Hardening Implications

The uninfiltreated ceramic coatings are viable candidates for protection of radar components. Analyses show that absorptivities of 0.2 or less must be maintained in order to survive the thermal design criteria for typical coating thicknesses. The electrical properties of the ceramic are not as good as desired but appear adequate if an integral hardened radar were designed. A remaining problem which must be addressed is the potential thermal stress failure due to multiple cycle heating. Pre-heating during processing may solve this potential problem.

The silicone rubber ablative material looks very promising for radar hardening. The electrical properties of the virgin material are very good. The low carbon-content char shows some degraded electrical characteristics but not significant enough to preclude use of this material. Materials similar to this have been used for radome applications and combustion chamber wall ablative materials. In addition, the material appears practical because it is inexpensive, easy to apply, adheres well, resists weathering and would provide a moisture barrier. It also would be less affected by surface contaminants especially due to the expected dust environment during a nuclear attack.

It is recommended that further work be performed to evaluate uninfiltreated ceramic coatings and the silicone rubber class of materials. Improved process techniques must be developed for the plasma sprayed ceramic coating to obtain desired porosity, surface absorptivity and to minimize thermal stress problems. Alternative silicone rubber materials with varying degrees of char strength, thermal characteristics and electrical characteristic should be evaluated. Preliminary thermal screening test are recommended during the material

process development and material selection phase. Larger scale thermal tests which would use the French Solar Furnace or updated WSMR Solar Furnace are recommended for evaluation of the subset of materials which passes the screening test phase. Electrical property tests at x-band frequencies should be performed on these materials. In concert with these tests, analyses of these material concepts should be performed for a hardened integral array preliminary design because it does not appear possible to simply identify materials to harden existing DAR designs without significant performance degradation. By incorporating hardening materials into the initial preliminary design, performance degradation can be minimized.

8.0 REFERENCES

1. Byrn, N., "Selected Blast and Thermal Environments on a Hardened Facility (U)", SAI-78-222-HU, January 16, 1978 (SRD).
2. Byrn, N., "Nuclear Analysis and Technology Assessment - Quarterly Progress Report," SAI-79-644-HU, June 16, 1978 (U).
3. Osofsky, I.B., "Lightweight Heatsink Concept Development Study - Final Report," SAI-78-202-LA, June 30, 1977 (U).
4. Osofsky, I.B., "Leightweight Heatsink Concept Development Study - Final Report," SAI-78-204-LA, January 25, 1978 (C).
5. Clevel, R.M. and Denny, V.E., "Response of Charring Ablators to Severe Aerodynamic and Erosion Environments", J. of Spacecraft and Rockets, V12, No. 9, Sept. 1975.
6. O'Neill, R.F. and Brawn, B.S., "Variable-Boundary Transient Heat Conduction Program", General Dynamics/Astronautics Report No. AY63-0065, June 1963.
7. Walton, J.D., et.al., "Evaluation of Materials in a High Heat Flux Radiant Thermal Energy Environment", AMMRC CTR 73-16, May 1973.
8. Conversation with Sam Mercurio, Sperry, November 16, 1978.
9. Fuller, J.A., R.L. Moore and R.T. Foscue, "Dielectric Test Results: Plasma Sprayed Ceramic Coatings and Bulk Silicone Materials," Final Report Project A-2178, Engineering Experiment Station, Georgia Institute of Technology, Atlanta, Georgia, January 1979.
10. Lichteneker, K. and K. Rother, "Complex Permittivity of Powders," Phys. Z, Volume 32, 1931, p. 255.
11. Hewlett Packard, "Semi-Automatic Measurements Using the 8410B Microwave Network Analyzer and the 9825A Desk Top Computer," Application Note 221.
12. Fitzpatrick, Jim, "Error Models for Systems Measurement," Microwave Journal, Vol. 21, May 1978, pp. 63-66.

13. Harrington, R.F., Time Harmonic Electromagnetic Fields, McGraw-Hill, New York, 1961.
14. Ramo, S., J.R. Whinnery, and T. VanDuzer, Fields and Waves in Communications Electronics, Wiley, New York, 1965, pp. 346-355.
15. Wu, C.P. and V. Galindo, "Surface-Wave Effects on Dielectric Sheathed Phased Arrays of Rectangular Waveguides," BSTJ, January 1968, pp. 117-142.
16. Knittel, G.H., A. Hessel, and A.A. Oliner, "Element Pattern Nulls in Phased Arrays and Their Relation to Guided Waves," Proc. IEEE, V. 56, Nov., 1968, pp. 1822-1836.
17. Ametay, N. and V. Galindo, "Characteristics of Dielectric Loaded and Covered Circular Waveguide Phased Arrays," IEEE Trans. Antenna Propagation, Vol. AP-14, pp. 722-729, November 1967.

APPENDIX A - Material Thermal Properties

This appendix presents the thermal data used for all analyses of the materials.

A1. Ceramic Coatings and Steel Substrates

Table A1 presents the alumina coating thermal data. For porous alumina, the thermal conductivity was found to be a strong function of the material structure (Reference A1). For example, according to Reference A1, plasma sprayed alumina with 15% porosity has a thermal conductivity only 10 to 25% that of bulk alumina. This indicates that the conductivity of porous alumina cannot accurately be expressed as:

$$k_p = (1 - \eta_p)k_b \quad (A1)$$

where k_p = conductivity of a porous layer of material
 k_b = conductivity of non-porous bulk material
 η_p = porosity

Reference A1 also showed that the conductivity of a plasma sprayed Al_2O_3 layer increases by heating it to near the melt temperature and then cooling it to room temperature. After five such cycles, the conductivity was just 20% less than that of non-porous bulk alumina.

The zirconia thermal data are presented in Table A2. The conductivity of porous zirconia was not known and so equation A1 was used to establish it.

Table A3 presents the stainless steel substrate and the nichrome bond thermal properties.

TABLE A1. PLASMA SPRAYED ALUMINA THERMAL PROPERTIES

Density: 230 lb/ft³ (non-porous)

Heat of Fusion: 461 Btu/lb

Melt Temperature: 4173 °R

Thermal Conductivity and Specific Heat

Temperature °R	Non-Porous Conductivity (BTU/ft-hr-°R)	15% Porous Conductivity (BTU/ft-hr-°R)	Specific Heat (BTU/lb-°R)
400	24.1	2.5	0.18
800	12.6	2.5	0.23
1200	7.2	1.8	0.26
1600	4.7	1.6	0.29
2400	3.1	1.6	0.33
4177	3.1	1.6	0.42

Data From Reference A1.

TABLE A2. PLASMA SPRAYED ZIRCONIA THERMAL PROPERTIES

Density: 359 lb/ft³ (non-porous)

Heat of Fusion: 303.8 BTU/lb

Melt Temperature: 5310[°]R

Thermal Conductivity and Specific Heat

Temperature ([°] R)	Non-Porous Conductivity (BTU/ft-hr- [°] R)	Specific Heat (BTU/lb- [°] R)
400	0.88	0.1
800	0.97	0.13
1600	1.12	0.15
2400	1.30	0.16
3200	1.48	0.15
4000	1.82	0.15

TABLE A3. STAINLESS STEEL AND NICHROME BOND THERMAL PROPERTIES

	303 Stainless	Nichrome Bond
Density (lb/ft ³):	494	525
Melt Temperature (°R):	3010	3012

Temperature (°R)	Conductivity (BTU/ft-hr-°R)	
400	8.5	4.7
1000	10.9	6.8
2000	13.6	10.1
3000	13.6	19.4

Temperature (°R)	Specific Heat (BTU/lb-°R)	
400	.12	.11
1000	.13	.11
2000	.16	.11
3000	.16	.11

A2. Silicone Rubber

The thermal properties for the Sylgard 184 silicone resin used as the infiltrant and Silastic E silicone rubber used as an ablator are presented in Table A4. The decomposition of the silicone resin was modeled, using a heat of decomposition determined from Dow Corning data based on plasma torch tests. The kinetics scheme was approximated using the decomposition rate data for natural rubber, three reinforced polymeric materials, and carbon phenolic, as shown in Table A4. Based on this comparison, it was decided that the three-legged carbon phenolic decomposition scheme would be an adequate representation of silicone resin infiltrant. The frequency factors, A_i , and the activation energy, E_i , needed in equation 4-2 of Section 4.1.1, were evaluated from this data. A_1 was determined to be $5.1 \times 10^4 \text{ sec}^{-1}$, however, this resulted in decomposition at room temperature. This behavior is unrealistic and a result of an empirical smoothing of actual kinetics data at low temperatures. To avoid this problem, A_1 was set equal to $5.1 \times 10^6 \text{ sec}^{-1}$, which essentially eliminates the low temperature reaction.

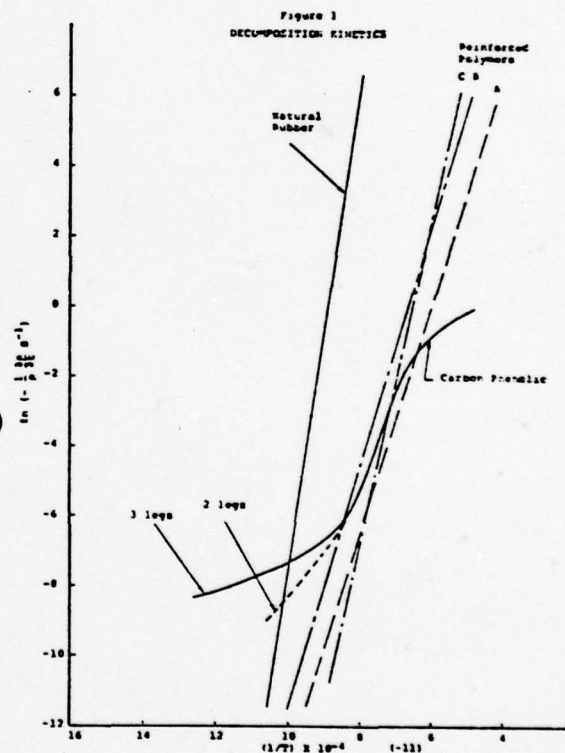
TABLE A4. SILICONE RUBBER THERMAL PROPERTIES

<u>Property*</u>	<u>Sylgard 184 Silicone Resin</u>	<u>Silastic E Silicone Rubber</u>
Density (lb/ft ²)	65.5	69.3
Specific Heat @ 77°F (BTU/lb-°F)	0.34	0.34
Thermal Conductivity (BTU/ft-hr-°F)	0.09	0.12
Heat of Decomposition (BTU/lb)	4500	----

Reaction Kinetics **

Frequency Factor, A_i (Sec⁻¹)
 5.1×10^{-6} , 85.4, 1.01125×10^6

Activation Energy, E_i (BTU/lb-mole)
 1208, 25200, 56041



* Properties from Dow Corning data sheets

** Modified three-legged carbon phenolic decomposition scheme

A3. Bulk Materials Thermal Properties

A series of bulk materials intended to serve as RF window materials, structural materials, or thermal protection materials were investigated. Their thermal properties are presented in Table A5 and Figure A1.

TABLE A5. BULK MATERIALS THERMAL PROPERTIES

Material	Density (lb/ft ³)	Specific Heat (BTU/lb-°R)	Melt Temperature (°F)	Thermal Conductivity (BTU/ft-hr-°F)	Data Source
Boron Nitride-HBR	119	0.44	5400	Fig. A1	Union Carbide
Boron Nitride-HP	119	0.44	5400	Fig. A1	Carborundum
Boron Nitride-M	132	0.3*	3000	Fig. A1	Carborundum
Alumina-AD995	243	0.21	3680	Fig. A1	Coors
Alumina-Fused Cast	213	0.21	3680	Fig. A1	Carborundum
Beryllia	188	0.21 @ 500°R 0.5 @ 1900°R	4680	Fig. A1	Bush Welman
Fused Silica	125	0.223	2700	Fig. A1	Corning
AS-3DX	109	0.185 @ 520°R 0.3 @ 2260°R	2700*	Fig. A1	Aeronutronics
Tantalum	1010	.033 @ 500°R .041 @ 3450°R	5420	33 @ 500°R 49.7 @ 5000°R	**
Columbium	537	.072	4380	40	**
Alumina-Firebrick 90% Al ₂ O ₃	185	.2*	3680		Chicago Wellsville Co.
Zircon-Firebrick	230	.25*	4850		Taylor Refractories
Silfrax-Firebrick	32	.25*	2700	0.11	Harbison-Walker

* Assumed Value

* Report EM-3644 RI, JHU Applied Physics Laboratory, 1963

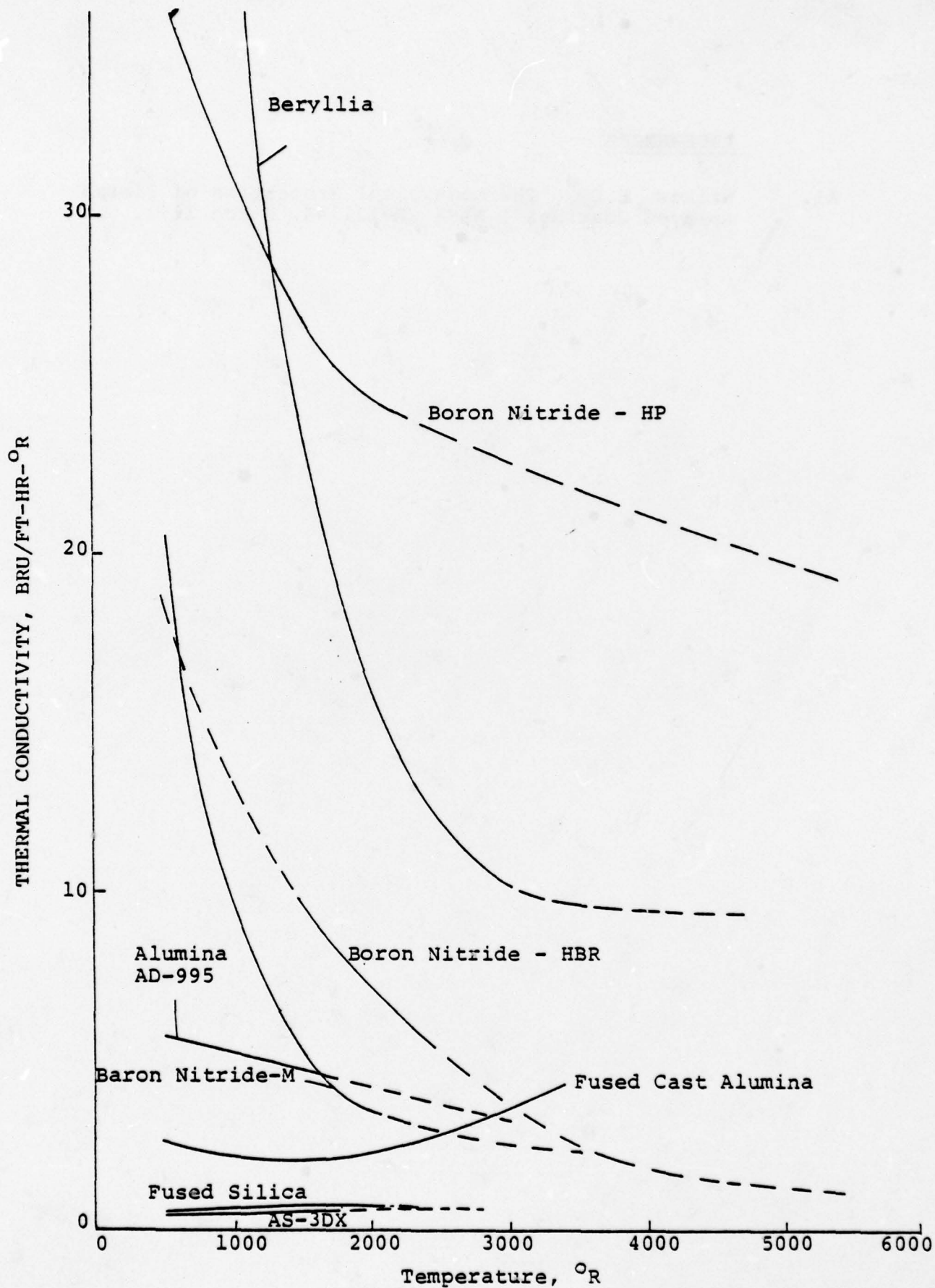


FIGURE A1. THERMAL CONDUCTIVITY
-137-

REFERENCES

- A1. Wilkes, K.E., "Thermophysical Properties of Plasma sprayed Coatings", NASA CR-121144, March 1973.

APPENDIX B

SUMMARY OF CAVITY RESULTS
FOR ALL TEST RUNS

This appendix gives the results of each test run completed for each sample. Table B.1 gives the results of S-band tests, and Table B.2 gives the X-band results. Where four or more runs are indicated, an average (Avg.) and standard deviation (S.D.) are provided. In computing these statistics, the high and low values of ϵ_r and $\tan\sigma$ have been discarded. Where only two runs are shown, the results are averaged. A total of seventy-eight runs are tabulated.

The thickness of each sample is given in Table B.3. In the table, the thickness value is listed in the D_1 column. The height of the end-plate shoulder is denoted as D_2 . Figure B-1 provides the cross-section of a specimen end-plate showing the location of these parameters.

Two cavity heights were used for the S-band tests, while only one was used at X-band. The nominal heights at S-band were 0.200 inch and 1.00 inches. The run numbers that correspond to the larger S-band cavity are preceded by an asterisk(*)

TABLE B.1. TABULATION OF ALL S-BAND CAVITY MEASUREMENTS
FOR SAI MATERIALS

SAI Sample #	Material Identification	Run #	Dielectric Constant (ϵ_r)	Loss Tangent ($\tan\delta$)	Dielectric Constant ($\epsilon_r/\sigma_{\epsilon_r}$)	Loss Tangent ($\tan\delta/\sigma_{\tan\delta}$)
2	ZrO_2 -MgO	CD10092	15.05	0.027	18.13/2.02	0.042/0.02
		* CD10112	16.89	0.026		
		* CD10132	18.67	0.050		
		CD10202	17.11	0.040		
		CD10208	21.05	0.030		
		* CD11132	18.00	0.042		
		CD11222	20.02	0.078		
3	ZrO_2 -12% Y_2O_3	CD10093	23.86	0.021	26.14/1.39	0.027/0.016
		CA10093	24.21	0.030		
		* CD10113	26.72	0.018		
		* CD10133	26.67	0.017		
		CD10203	27.77	0.010		
		CD10209	26.64	0.032		
		* CD11133	26.10	0.020		
		CD11223	27.14	0.059		
		CD10094	6.95	0.023		
		* CD10114	7.72	0.016		
4	Al_2O_3	* CD10134	7.72	0.014	7.65/0.34	0.024/0.015
		CD10204	7.83	0.010		
		CD10200	8.06	0.021		
		* CD11134	7.67	0.049		
		CD11224	7.61	0.033		
		CD10095	12.69	0.020		
		* CD10115	14.43	0.033		
5	ZrO_2 - 2% CaO_2	* CD10135	14.50	0.031	14.21/1.078	0.039/0.015
		CD10205	14.57	0.027		
		CA10201	15.17	0.039		
		* CD11135	14.31	0.058		
		CD11225	13.87	0.059		

TABLE B.1. TABULATION OF ALL S-BAND CAVITY MEASUREMENTS
FOR SAI MATERIALS (CONTINUED)

SAI Sample #	Material Identification	Run #	Dielectric Constant (ϵ_r)	Loss Tangent ($\tan\delta$)	Dielectric Constant ($\bar{\epsilon}_r/\sigma\epsilon_r$)	Loss Tangent ($\tan\delta/\sigma\tan\delta$)
6	Spinel	CD10096	5.81	0.027	6.29/0.37	0.028/.008
		* CD10116	6.47	0.029		
		* CD10136	6.48	0.037		
		CD10206	6.15	0.018		
		CA10202	6.20	0.019		
		* CD11136	6.94	0.038		
201	ZrO ₂ - CaO ₂	CD11226	6.00	0.030	19.58/1.44	0.025/0.008
		CD11227	19.65	0.023		
		CD11272	17.39	0.026		
		CD11275	18.32	0.039		
		* CD12012	20.99	0.020		
		* CD12015	20.60	0.019		
210	ZrO ₂ - MgO	* CD12018	20.58	0.020	6.65/0.78	0.051/0.040
		CD11228	7.23	0.095		
		CD11273	7.11	0.023		
		CD11276	7.19	0.028		
		* CD12013	6.71	0.016		
		* CD12016	5.17	0.095		
356	Spinel	* CD12019	6.53	0.050	3.65/0.19	0.023/0.008
		CD11229	3.70	0.032		
		CD11274	3.79	0.034		
		CD11277	3.76	0.022		
		* CD12014	3.62	0.031		
		* CD12017	3.82	0.014		
		* CD12010	3.60	0.021		
		* CD12127	3.22	0.024		
		* CD12128	3.72	0.014		

TABLE B.1. TABULATION OF ALL S-BAND CAVITY MEASUREMENTS
FOR SAI MATERIALS (CONTINUED)

SAI Sample #	Material Identification	Run #	Dielectric Constant (ϵ_r)	Loss Tangent ($\tan\delta$)	Dielectric Constant ($\frac{\epsilon_r}{\sigma/\epsilon_r}$)	Loss Tangent ($\frac{\tan\delta}{\sigma/\epsilon_r}$)
201	$ZrO_2 - CaO_2$	CD12081	21.56	0.016	20.44/1.30	0.0156/0.003
		CD12094	21.17	0.018		
		CD12122	20.41	0.012		
		CD01034	18.62	0.007		
202	$ZrO_2 - Y_2O_3$	CD12082	21.56	0.016 (excluded)	13.53/1.92	0.03/0.04
		CD12092	12.42	0.075		
		CD12123	15.74	0.003		
		CD01035	12.42	0.017		
210	$ZrO_2 - MgO$	CD12083	16.04	0.011	16.00/0.97	0.0163/0.007
		CD12095	15.36	0.014		
		CD12121	15.25	0.014		
		CD01052	17.35	0.008		
333	$Al_2O_3 - TiO_2$	CD12085	12.45	0.148	12.48 Damaged	0.150 Damaged
		CD12096 Damaged	12.50	0.152		
356	Spinel	CD01025	5.64	0.007	5.66/0.09	0.023/0.018
		CD01013	5.73	0.007		
		CD01032	5.73	0.043		
		CD01026	5.54	0.035		

TABLE B.1. TABULATION OF ALL S-BAND CAVITY MEASUREMENTS
FOR SAI MATERIALS (CONTINUED)

SAI Sample #	Material Identification	Run #	Dielectric Constant (ϵ_r)	Loss Tangent ($\tan\delta$)	Dielectric Constant ($\overline{\epsilon_r}/\sigma_{\epsilon_r}$)	Loss Tangent ($\overline{\tan\delta}/\sigma_{\tan\delta}$)
202	ZrO ₂ - Y ₂ O ₃	CD12088 CD12098	28.01 28.19	0.223 0.008	28.10	0.116
333	Al ₂ O ₃ - TiO ₂	CD12089 CD12099	23.17 26.53	0.062 0.172	24.85	0.117

TABLE B.3. CERAMIC SAMPLE THICKNESSES*

Sample	SAI Sample #	Frequency Band	D ₁	D ₂
ZrO ₂ - M _g O	2	S	0.056	0.053
ZrO ₂ - 12%Y ₂ O ₃	3	S	0.060	0.053
Al ₂ O ₃ - 2% CaO ₂	4	S	0.059	0.054
ZrO ₂	5	S	0.058	0.056
Spinel	6	S	0.058	0.057
ZrO ₂ - CaO ₂	201	S	0.082	0.041
ZrO ₂ M _g O	210	S	0.069	0.051
Spinel	356	S	0.084	0.040
ZrO ₂ - CaO ₂	201	X	0.059	0.054
ZrO ₂ -Y ₂ O ₃	202	X	0.064	0.051
ZrO ₂ - M _g O	210	X	0.065	0.052
Al ₂ O ₃ - TiO ₂	333	X	0.065	0.052
Al ₂ O ₃ -TiO ₂ burned	333	X	0.056	0.052
ZrO ₂ - Y ₂ O ₃ burned	202	X	0.052	0.010

* The parameters D₁ and D₂ are indicated in Figure B-1.
 Dimenions are in inches.

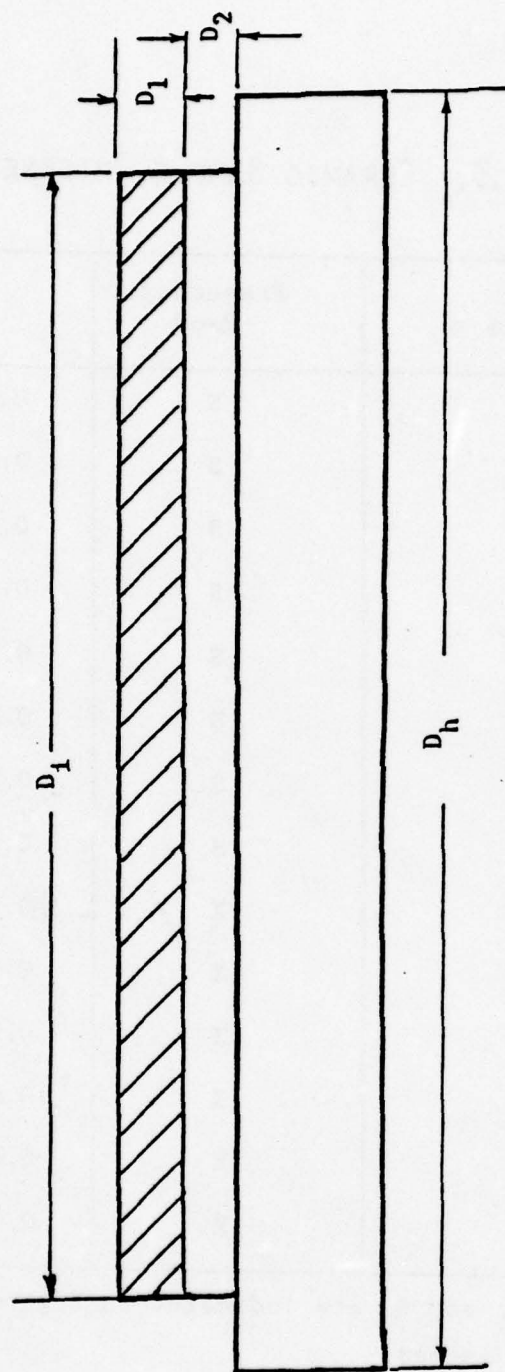


FIGURE B.1. A CROSS-SECTION OF THE CERAMIC-COATED ENDPLATE.

APPENDIX C

ANALYSIS OF A CYLINDRICAL CAVITY MEASUREMENT
PROCEDURE FOR THE DETERMINATION OF THE DIELECTRIC
CONSTANT AND THE LOSS TANGENT OF A
THIN DIELECTRIC SLAB MOUNTED ON A METAL DISC

1.0 INTRODUCTION AND SUMMARY

The process for producing the plasma-sprayed ceramic materials required the use of a metal support or backing plate. In addition, it was desired to keep the ceramic materials as thin as possible so as to minimize deleterious effects on the array performance. At X-band (9 GHz), for example, the ceramic thicknesses were expected to be less than one-eighth of a wavelength. Hence, conventional bulk measurement techniques were not applicable.

The Engineering Experiment Station of The Georgia Institute of Technology, acting as a subcontractor to SAI for the electrical properties measurement tasks, suggested that a microwave resonant cavity approach could prove useful. EES further suggested the use of a TM_{010} excitation mode. Although cavity techniques have been previously used for the measurement of electrical properties, no documented investigations could be found in the technical literature which exactly addressed the problem of measuring thin dielectrics mounted on metal facing-plates. Furthermore, the method had to be reliable and inexpensive. For these reasons, an analytical investigation of the cylindrical cavity measurement procedure was conducted. In this Appendix, we present the results of that analysis.

The conclusions can be briefly summarized as:

1. A TM cylindrical cavity measurement procedure is a reliable, cost-effective approach.
2. The theoretical precision of the dielectric constant and loss tangent measurements for the plasma-sprayed ceramic materials are as good with the TM cavity excitation mode as they are with the more common TE excitation mode.
3. The construction difficulties associated with a TM-excited cavity are significantly less than those associated with a TE-excited cavity.

In the remaining portions of this appendix, we examine in detail the cavity measurement technique for the determination of the electrical properties of thin, dielectric materials that are mounted on metal discs. The absolute precision of the TE and TM excitation modes is investigated. These results indicate that the suggestion by Georgia Tech of the TM_{010} mode for the cavity excitation was a reasonable choice. Based upon their recommendation as well as the analysis, it was agreed by SAI and Georgia Institute of Technology that the TM_{010} resonant cavity mode would be used in the measurement procedure.

A sensitivity analysis was performed for both the dielectric constant extraction process and the loss tangent extraction process, for a resonant cavity with a TM excitation mode. This analysis indicated that for measurement errors at about the level of those found in the experimental data collection process, a true dielectric constant of seven can be measured with a tolerance of ± 0.50 at the 95% confidence level. Similarly, loss tangents larger than 0.002 can be determined with a relative error less than 25%. True loss tangent values less than 0.002 cannot be determined with an error bound less than 0.002. The actual loss tangent error bounds are a function not only of the nominal loss tangent value, but also of the nominal dielectric constant value. The actual error sensitivities are given later in graphical form for some representative cases of interest.

2.0 GEOMETRY

The geometry of this problem is illustrated by Figure C.1. A right circular cylinder of radius "a" and height "d" is partially filled from the bottom to a height "b" with a material having a permittivity $\epsilon = \epsilon_r \epsilon_0$ and a conductivity σ . The dielectric-filled portion of the cylinder is called region 1, while the remaining free space portion is called region 2. The

coordinate system is oriented such that the z - axis is coincident with the longitudinal axis of the cylinder.

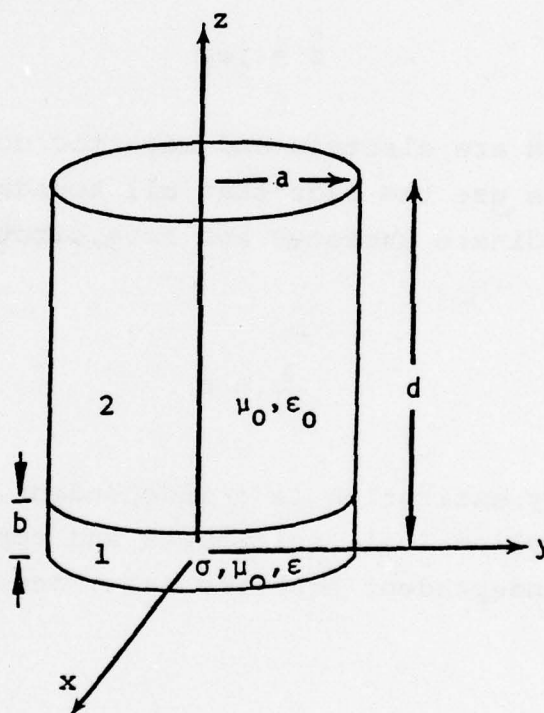


FIGURE C.1. CIRCULAR RESONATOR WITH DIELECTRIC SAMPLE FILLING REGION 1 ($0 < z \leq b$)

3.0 REVIEW OF CIRCULAR RESONATOR THEORY

We begin with Maxwell's curl equations

$$\nabla \times \vec{H} = \vec{J} + \hat{y} \vec{E} \quad (1)$$

$$\nabla \times \vec{E} = -\vec{M} - \hat{z} \vec{H} \quad (2)$$

where

$$\hat{y} = j\omega\epsilon + \sigma \quad (3)$$

$$\hat{z} = j\omega\mu \quad (4)$$

and where \vec{J} and \vec{M} are electric and magnetic current sources, respectively. We use the fact that all boundaries conform to cylindrical coordinate surfaces and have circular symmetry to conclude that

$$\frac{\partial}{\partial \phi} = 0 \quad (5)$$

provided that any excitation is ϕ -independent. Expansion of (1) and (2) in cylindrical coordinates and application of (5) results in two independent equation sets, one TE_z and one TM_z , viz:

$$TE \left\{ \begin{array}{l} \frac{\partial}{\partial r} \left[\frac{1}{r} \frac{\partial}{\partial r} (rE_\phi) \right] + \frac{\partial^2 E_\phi}{\partial z^2} + k^2 E_\phi = \hat{z} J_\phi + \frac{\partial M_r}{\partial z} - \frac{\partial M_z}{\partial r} \\ H_r = \frac{1}{\hat{z}} \left(-M_r + \frac{\partial E_\phi}{\partial z} \right) \\ H_z = \frac{1}{\hat{z}} \left[-M_z - \frac{1}{r} \frac{\partial}{\partial r} (rE_\phi) \right] \end{array} \right. \quad (6)$$

$$\text{TM} \left\{ \begin{array}{l} \frac{\partial}{\partial r} \left[\frac{1}{r} \frac{\partial}{\partial r} (r H_\phi) \right] + \frac{\partial^2 H_\phi}{\partial z^2} + k^2 H_\phi = \hat{y} M_\phi - \frac{\partial J_r}{\partial z} + \frac{\partial J_r}{\partial r} \\ E_r = \frac{1}{\hat{y}} \left(-J_r - \frac{\partial H_\phi}{\partial z} \right) \\ E_z = \frac{1}{\hat{y}} \left[-J_z + \frac{1}{r} \frac{\partial}{\partial r} (r H_\phi) \right] \end{array} \right. \quad (7)$$

where

$$\hat{k}^2 = -\hat{y} \hat{z} \quad (8)$$

4.0 TE EXCITATION MODES

Since the two mode sets do not cross-couple, we can analyze each set independently. We shall briefly consider the TE mode set. This approach has received considerable attention in the literature (see references C1 through C5). The modes which are excited are found by solving the homogeneous form of the differential equation in (6) to give

$$E_\phi = J_1(k_r r) \left[A \sin(k_z z) + B \cos(k_z z) \right] \quad (9)$$

$$H_r = \frac{k_z}{j\omega\mu} J_1(k_r r) \left[-A \sin(k_z z) + B \cos(k_z z) \right] \quad (10)$$

$$H_z = -\frac{1}{j\omega\mu r} \frac{\partial(r E_\phi)}{\partial r} \quad (11)$$

where

$$k_r = \frac{x'_{01}}{a}, \quad k_z = \frac{n\pi}{d} \quad (12)$$

and

$$k^2 = k_r^2 + k_z^2 \quad (13)$$

Note that x'_{01} is the first root of the Bessel function $J(k_r a) = 0$; namely $x'_{01} = 3.832$.

This mode set can be excited by J_ϕ , M_r and M_z . An application of the equivalence principle

$$\vec{n} \times \vec{H} = \vec{J} \quad (14)$$

for $H_z|_{r=a}$ leads to

$$\begin{aligned} J_\phi \vec{\phi} &= \vec{n} \times \left. H_z \right|_{r=a} \vec{z} \\ &= \left. H_z \right|_{r=a} \vec{\phi} \end{aligned} \quad (15)$$

Thus, the surface current density \vec{J} on the wall is azimuthal and excitation coupling could be obtained with an axially directed slot in the cylindrical cavity wall.

4.1 TE_{01n} Mode Set

The TE cavity is usually operated in the TE_{01n} mode.* For this mode, the cavity is above cutoff for many other modes. These

*For circular resonators, the modes are designated TE_{k,m,n} and TM_{k,m,n}. Integer k determines periodicity in ϕ , m denotes the number of electric-field zeros in the radial direction (not counting zero on axis), and n is the number of half-wavelengths in the axial direction.

other modes will obscure the electrical properties of the material under test if they are allowed to exist in the cavity. Figure C.2 provides a pictorial view of the modes which are physically excitable together with their relative cutoff frequencies.

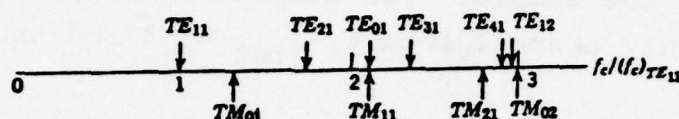


FIGURE C.2. RELATIVE CUTOFF FREQUENCIES OF WAVES IN A CYLINDRICAL RESONATOR

The multimode contamination of the cavity is the major problem associated with TE_{01n} excitation. Substantial efforts have been described in the literature which are directed at minimizing the excitation of unwanted modes. Unfortunately, the success of these approaches is directly related to mechanical tolerances which have finite limits.

4.2 Determination of the Dielectric Constant

The usual perturbation theory approach is valid for this situation. Consequently, for an empty cavity resonant frequency of $\omega_0/2\pi$ and a dielectrically-filled cavity resonant frequency of $\omega/2\pi$, the normalized shift in the resonant frequency of the filled cavity $(\omega - \omega_0)/\omega_0$ is

$$\frac{\omega - \omega_0}{\omega_0} = - \frac{\int_V \Delta\epsilon \vec{E}_{int} \cdot \vec{E}_0 dv}{2 \int_V \epsilon |\vec{E}_0|^2 dv} \quad (16)$$

where

$$\Delta\epsilon = \epsilon - \epsilon_0 \quad (17)$$

and the volume V is composed of both region 1 and region 2. The quantity \vec{E}_0 is the E-field in the empty cavity, while \vec{E}_{int} is the E-field in the sample. For samples which perturb the empty cavity field only a small amount, $\vec{E}_{int} \approx \vec{E}_0$ and thus

$$\frac{\omega - \omega_0}{\omega_0} \approx - \frac{\int_V \Delta\epsilon |\vec{E}_0|^2 dv}{2 \int_V \epsilon |\vec{E}_0|^2 dv} \quad (18)$$

The small perturbation assumption also allows us to approximate the permittivity ϵ associated with the energy lost by the free space permittivity ϵ_0 . Then,

$$\frac{\omega - \omega_0}{\omega_0} = - \frac{\int_{V_s} |\vec{E}_0|^2 dv_s}{2 \int_V |\vec{E}_0|^2 dv} \left(\frac{\epsilon - \epsilon_0}{\epsilon_0} \right) \quad (19)$$

where " V_s " is the volume of the material sample and " V " is the total volume of the empty cavity. But

$$\frac{\Delta f}{f_0} = \frac{f - f_0}{f_0} = \frac{\omega - \omega_0}{\omega_0}$$

and hence,

$$\frac{\Delta f}{f_0} = - (\epsilon_r - 1) \frac{\int_{V_s} |\vec{E}_0|^2 dv_s}{2 \int_V |\vec{E}_0|^2 dv} \quad (20)$$

Consequently, we are left with the job of computing the integral of $|\vec{E}_0|^2$ over two different volumes. From equation (9), we know that $\vec{E}_0 = \vec{E}_\phi \vec{\phi}$. That is, the unperturbed E-field in the cavity has only an azimuthal component, viz:

$$\vec{E}_0 = J_1(k_r r) B \sin(k_z z) \vec{\phi} \quad (21)$$

and as before

$$k_z = n\pi/d$$

$$k^2 = k_r^2 + k_z^2$$

Then,

$$\begin{aligned} \frac{\Delta f}{f_0} &= - \frac{(\epsilon_r - 1)}{2} \frac{2\pi B^2 \int_0^b \int_0^a J_1^2(k_r r) \sin^2(k_z z) r dr dz}{2\pi B^2 \int_0^b \int_0^a J_1^2(k_r r) \sin^2(k_z z) r dr dz} \\ &= - \left(\frac{\epsilon_r - 1}{2} \right) \frac{\int_0^b \sin^2 \frac{n\pi z}{d} dz}{\int_0^d \sin^2 \frac{n\pi z}{d} dz} \end{aligned}$$

and finally,

$$\frac{\Delta f}{f_0} = - \left(\frac{\epsilon_r - 1}{2} \right) \left(\frac{b}{d} \right) \left[1 - \frac{\sin(2n\pi b/d)}{(2n\pi b/d)} \right] \quad (22)$$

4.3 Sensitivity in the Determination of the Dielectric Constant Value

It is easily seen that the dielectric constant value may be found from the normalized resonant frequency shift of the cavity. To illustrate the precision of the extraction process, the normalized resonant frequency shift is plotted as a function of the relative dielectric constant ϵ_r in Figure C.3. Variation of the cavity fill factor b/d produces the family of curves shown. The value of n has been set to 1 for simplicity. Hence, the mode of operation is TE_{011} . Note that the curves are linear with a slope s , viz:

$$s = \frac{1}{2} \left(\frac{b}{d} \right) \left[1 - \text{sinc} (2n\pi b/d) \right] \quad (23)$$

4.4 Fill Factor

In order to interpret Figure C.3 correctly, one must know the fill factor, which is a function of the sample thickness b , as well as the cavity height d . As an example, we consider two representative values of b ; these are 0.050 inches and 0.125 inches. The cavity height can be found from

$$k^2 = k_r^2 + k_z^2$$

or

$$\omega^2 \mu_0 \epsilon_0 = \left(\frac{3.832}{a} \right)^2 + \left(\frac{n\pi}{d} \right)^2 \quad (24)$$

CAVITY SENSITIVITY

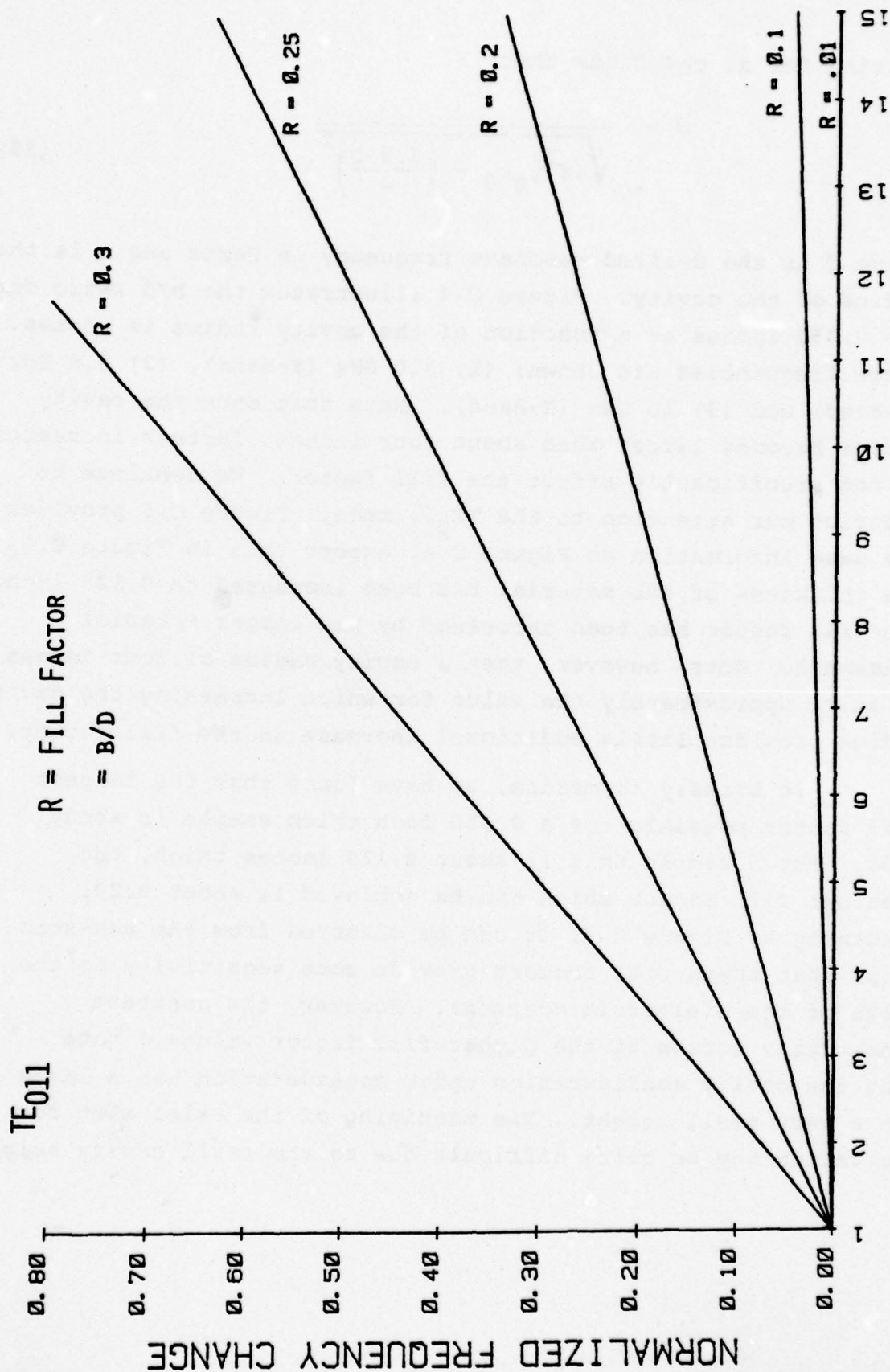


FIGURE C.3. NORMALIZED RESONANT FREQUENCY CHANGE AS A FUNCTION OF DIELECTRIC CONSTANT FOR TE₀₁₁ CAVITY

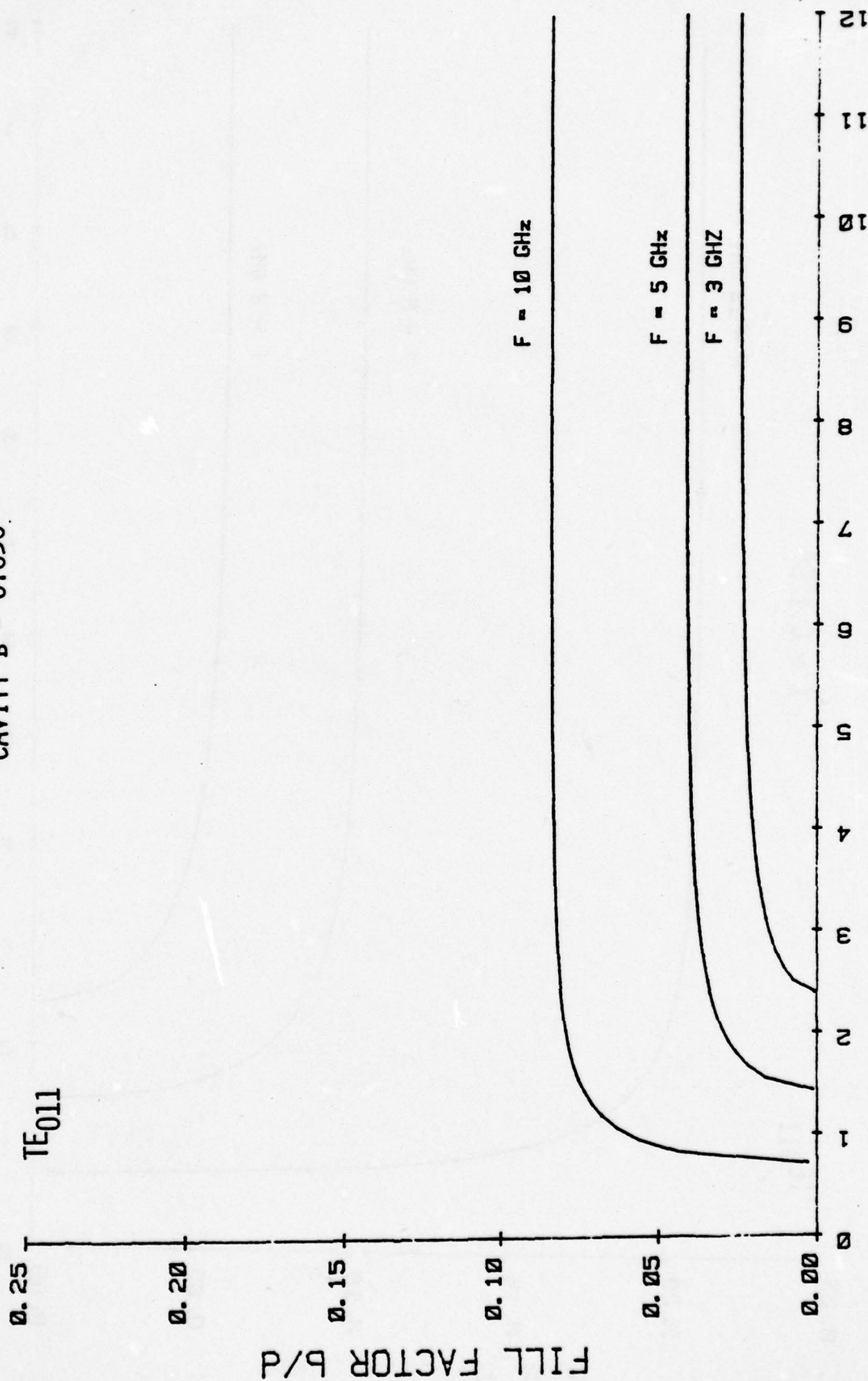
Solving for d, one finds that

$$d = \frac{1}{\sqrt{4f^2 \mu_0 \epsilon_0 - \left(\frac{3.832}{a}\right)^2}} \quad (25)$$

where f is the desired resonant frequency in Hertz and a is the radius of the cavity. Figure C.4 illustrates the b/d ratio for b = 0.050 inches as a function of the cavity radius in inches. Three frequencies are shown; (1) 3.0 GHz (S-Band), (2) 5.0 GHz (C-Band) and (3) 10 GHz (X-Band). Note that once the cavity radius becomes larger than about four inches, further increases do not significantly affect the fill factor. We continue to restrict our attention to the TE₀₁₁ mode. Figure C.5 provides the same information as Figure C.4, except that in Figure C.5 the thickness of the material has been increased to 0.125 inches. The fill factor has been increased by the larger material thickness. Note, however, that a cavity radius of four inches is still approximately the value for which increasing the cavity radius provides little additional increase in the fill factor.

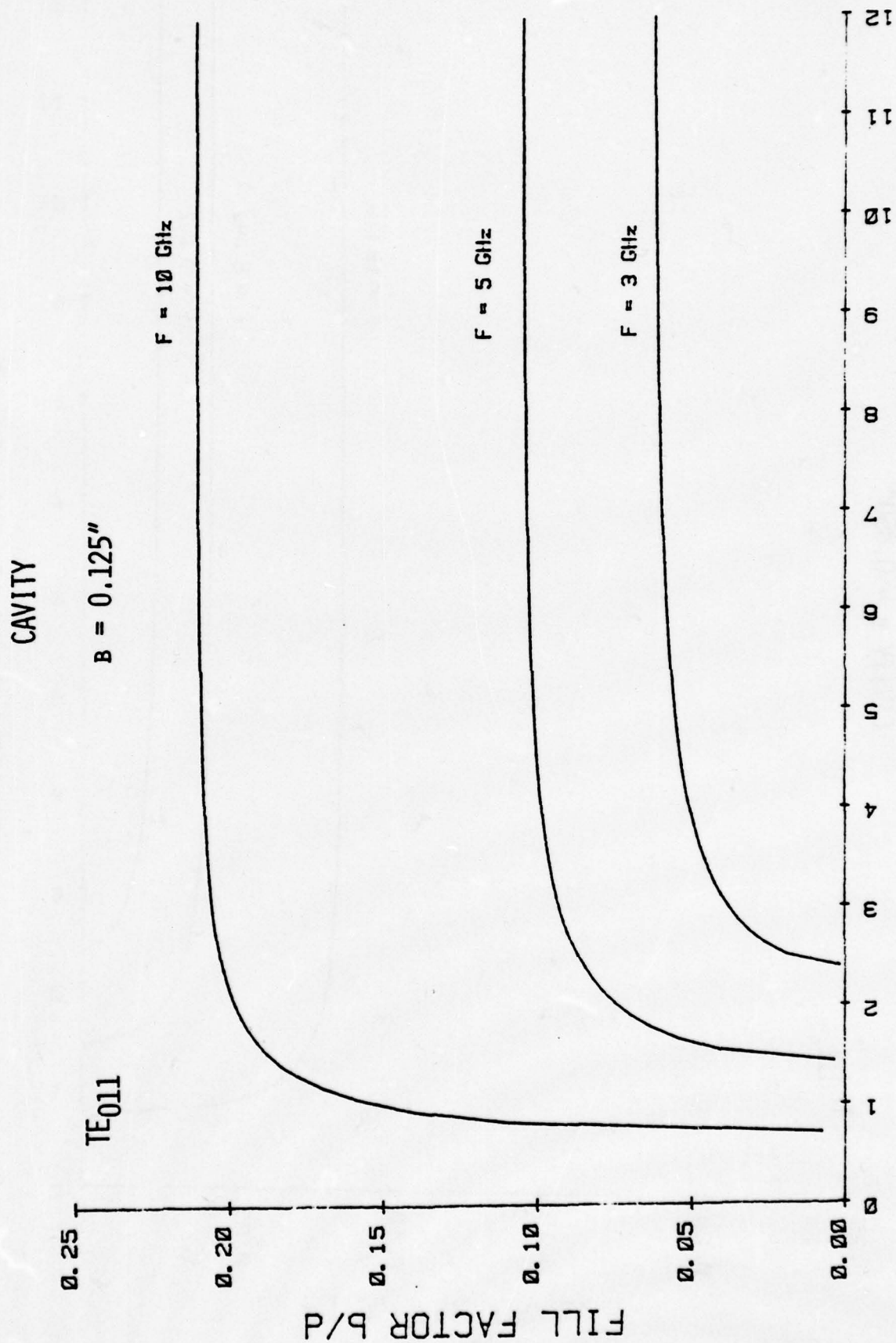
To briefly summarize, we have found that the largest fill factor possible for a 0.050 inch thick sample is about 0.08. For a sample that is about 0.125 inches thick, the greatest fill factor which can be achieved is about 0.20. Returning to Figure C.3, it can be observed from the non-zero slope that these fill factors provide some sensitivity to the value of the dielectric constant. However, the greatest sensitivity occurs at the higher fill factor values. Note that the cavity configuration under consideration has a large radius but a very small height. The machining of the axial slot for excitation may be quite difficult due to the small cavity height.

CAVITY B = 0.050"



CAVITY RADIUS (a) [in.]

FIGURE C.4. FILL FACTOR AS A FUNCTION OF CAVITY RADIUS FOR TE₀₁₁ MODE AND MATERIAL THICKNESS OF 0.050 INCHES



CAVITY RADIUS (a) [in.]

FIGURE C.5. FILL FACTOR AS A FUNCTION OF CAVITY RADIUS FOR TE_{011} MODE AND MATERIAL THICKNESS OF 0.125 INCHES

In the next sections, we will determine the relationships for the TM_{01n} mode corresponding to those we have just presented for the TE_{011} mode. Thus, comparisons between the two excitation modes may be made and the appropriate one selected for further investigation.

5.0 TM EXCITATION MODES

The TM excitation modes will be considered in the same manner as the TE mode set. That is, we shall investigate the cavity fields and determine the effects of placing a material sample at one end of the cavity. Although the analysis is straightforward, it is more complicated than that for the TE excitation mode. This is due to the fact that the perturbation approach is no longer valid, and a more complete treatment must be undertaken.

We begin by referring to the TM set of equations (7). This set can be excited by sources M_ϕ , J_r , or J_z , provided that circular symmetry is preserved. Note that J_r and J_z are a continuous current that flows between the cylinder walls and the endplates. An application of the equivalence principle

$$-\vec{n} \times \vec{E} = \vec{M} \quad (26)$$

at the endplate at $z = d$ results in

$$E_r \Big|_{z=d} = -M_\phi \quad (27)$$

which shows that an annular slot in the endplate is a possible excitation method. To determine the modes excited we may solve the homogeneous form of the differential equation in (7) to give

$$H_\phi = J_1(k_r r) \begin{Bmatrix} \cos k_z z \\ \sin k_z z \end{Bmatrix} \quad (28)$$

$$E_r = - \frac{1}{\hat{y}} \frac{\partial H_\phi}{\partial z} \quad (29)$$

$$E_z = \frac{1}{\hat{y}} \frac{1}{r} \frac{\partial}{\partial r} (r H_\phi) \quad (30)$$

where

$$\hat{k}^2 = k_r^2 + k_z^2 \quad (31)$$

Equations (27) through (31) form the basis for the consideration of both the unloaded and loaded resonator.

5.1 Unloaded Resonator

In the unloaded resonator, the boundary conditions are

$$E_r \Big|_{z=0} = E_r \Big|_{z=d} = 0 \quad (32)$$

$$E_z \Big|_{r=a} = 0 \quad (33)$$

Application of these conditions in (28) through (31) results in

$$H_\phi = A J_1 (k_r r) \cos k_z z \quad (34)$$

$$E_r = \frac{k_z}{\hat{y}} A J_1 (k_r r) \sin k_z z \quad (35)$$

$$E_z = \frac{k_r}{\hat{y}} A J_0 (k_r r) \cos k_z z \quad (36)$$

where

$$\hat{k}^2 = \omega^2 \mu_0 \epsilon_0 \quad (37)$$

$$k_r^2 = \left(\frac{2.405}{a} \right)^2 \quad (38)$$

$$k_z^2 = \left(\frac{n\pi}{d} \right)^2 \quad (39)$$

Consideration of the resonance conditions in expressions (31) and (37) through (39) shows that the dominant mode occurs for $n = 0$, and gives $E_r = 0$ and

$$H_\phi = A J_1(k_r r) \quad (40)$$

$$E_z = \frac{k_r}{\hat{y}} A J_0(k_r r) \quad (41)$$

with (31) we obtain

$$f_0 = \frac{2.405c}{2\pi a} \quad (42)$$

where f_0 is the resonant frequency of the dominant mode and c is the velocity of light in free space.

The Q of the unloaded resonator can be obtained from the basic definition

$$Q = \frac{\omega W}{P} \quad (43)$$

where W is the energy stored in the resonator and P is the power dissipated in the walls. The derivation follows classical lines^(C6) and will not be repeated here. The result is

$$Q_u = \frac{1.202 \eta_0}{R_s (1 + \frac{a}{b})} \quad (44)$$

where Q_u is the unloaded Q , η_0 is the intrinsic impedance of free space, and R_s is the resistivity of the walls.

5.2 Loaded Resonator

In the case of the resonator with dielectric loading from $z = 0$ to $z = b$ (Figure C.1), Equations (28) through (31) are written for $0 < z < b$ (region 1) and for $b < z < d$ (Region 2), viz:

$$\left. \begin{aligned} H_{\phi 1} &= C J_1 (k_r r) \cos k_{z1} z \\ E_{r1} &= \frac{k_{z1}}{\hat{Y}_1} C J_1 (k_r r) \sin k_{z1} z \\ E_{z1} &= \frac{k_r}{\hat{Y}_1} C J_0 (k_r r) \cos k_{z1} z \end{aligned} \right\} 0 < z < b \quad (45)$$

$$\left. \begin{aligned} H_{\phi 2} &= B J_1 (k_r r) \cos k_{z2} (d - z) \\ E_{r2} &= - \frac{k_{z2}}{\hat{Y}_2} B J_1 (k_r r) \sin k_{z2} (d - z) \\ E_{z2} &= \frac{k_r}{\hat{Y}_2} B J_0 (k_r r) \cos k_{z2} (d - z) \end{aligned} \right\} b < z < d \quad (46)$$

where

$$k_r^2 + k_{z1}^2 = \hat{k}_1^2 \quad (47)$$

$$k_r^2 + k_{z2}^2 = \hat{k}_2^2 \quad (48)$$

and

$$\hat{k}_1^2 = \omega^2 \mu_0 \left(\epsilon + \frac{\sigma}{i\omega} \right) \quad (49)$$

$$\hat{k}_2^2 = \omega^2 \mu_0 \epsilon_0 \quad (50)$$

In (47) and (48), k_r is given by (38) but k_{z1} and k_{z2} must be determined in conjunction with the boundary conditions at $z = b$. Equations (45) and (46) contain the boundary conditions at $z = 0$ and $z = d$. Application of the requirement for continuity of the tangential E and H fields at $z = b$ yields the additional relations

$$C \cos k_{z1} b = B \cos k_{z2} (d - b) \quad (51)$$

$$\frac{k_{z1}}{\hat{y}_1} C \sin k_{z1} b = - \frac{k_{z2}}{\hat{y}_2} B \sin k_{z2} (d - b) \quad (52)$$

$$\frac{k_{z1}}{\hat{y}_1} \tan k_{z1} b = - \frac{k_{z2}}{\hat{y}_2} \tan k_{z2} (d - b) \quad (53)$$

The Q of the loaded resonator can be obtained from equation (43), viz:

$$Q_L = \frac{\omega(W_1 + W_2)}{P_D + P_W} \quad (54)$$

where W_1 and W_2 are the energy stored in the dielectric and free space regions, respectively; also, P_D is the power loss in the dielectric and P_W is the power loss in the resonator walls. By inverting (54), we may obtain

$$\frac{1}{Q_L} = \frac{1}{Q_D} + \frac{1}{Q_W} \quad (55)$$

where Q_D and Q_W are the Q's due to the dielectric loss and wall loss, respectively, Explicitly,

$$Q_D = \frac{\omega(W_1 + W_2)}{P_D} \quad (56)$$

and

$$Q_W = \frac{\omega(W_1 + W_2)}{P_W} \quad (57)$$

where

$$W_1 = \frac{1}{2} \int_0^b \int_0^{2\pi} \int_0^a \epsilon (|E_{r1}|^2 + |E_{z1}|^2) r dr d\phi dz \quad (58)$$

$$W_2 = \frac{1}{2} \int_b^d \int_0^{2\pi} \int_0^a \epsilon_0 (|E_{r2}|^2 + |E_{z2}|^2) r dr d\phi dz \quad (59)$$

$$P_D = \frac{1}{2} \int_0^b \int_0^{2\pi} \int_0^a \sigma (|E_r|^2 + |E_z|^2) r dr d\phi dz \quad (60)$$

$$P_W = \frac{R_s}{2} \int_0^{2\pi} \left[\int_0^b a |H_{\phi 1}|^2_{r=a} dz + \int_b^d a |H_{\phi 2}|^2_{r=a} dz \right. \\ \left. + \int_0^a |H_{\phi 1}|^2_{z=0} r dr + \int_0^a |H_{\phi 2}|^2_{z=d} r dr \right] d\phi \quad (61)$$

In (58) through (61), the various field components are given by (45) and (46).

5.3 Determination of the Dielectric Constant

Expression (53) can be solved to give a relationship among the resonant frequency f of the loaded resonator, the unloaded resonant frequency f_0 , the dielectric constant ϵ_r , the loss tangent ($\tan \delta$) and the resonator dimensions. Since the equation is transcendental and has complex roots, numerical methods are required for its solution. Fortunately, for the cases of present interest in the Georgia Tech experimental program, the cavity dimensions are small enough so that the tangents can be replaced by their arguments with the result

$$k_{z1}^2 b \cong - \frac{\hat{Y}_1}{\hat{Y}_2} k_{z2}^2 (d - b) \quad (62)$$

where from (47) through (50) and (3),

$$k_{z1}^2 = k^2 \epsilon_r (1 - j \tan \delta) - k_r^2 \quad (63)$$

$$k_{z2}^2 = k^2 - k_r^2 \quad (64)$$

$$\frac{\hat{y}_1}{\hat{y}_2} = \epsilon_r (1 - j \tan \delta) \quad (65)$$

and where

$$k^2 = \omega^2 \mu_0 \epsilon_0 \quad (66)$$

$$\tan \delta = \frac{\sigma}{\omega \epsilon} \quad (67)$$

Substitution of (63) through (67) into (62) yields a complex algebraic equation, the real part of which produces

$$\frac{k_2^2}{k_r^2} = 1 - \frac{b}{d} \left(\frac{\epsilon_r - 1}{\epsilon_r} \right) \quad (68)$$

or

$$\frac{f}{f_0} = \left[1 - \frac{b}{d} \left(\frac{\epsilon_r - 1}{\epsilon_r} \right) \right]^{\frac{1}{2}} \quad (69)$$

To compare these results with those from perturbation theory, we subtract unity from both sides to give

$$\frac{\Delta f}{f_0} = \left[1 - \frac{b}{d} \left(\frac{\epsilon_r - 1}{\epsilon_r} \right) \right]^{\frac{1}{2}} - 1 \quad (70)$$

where

$$\Delta f = f - f_0 \quad (71)$$

If the second term in brackets in (70) is small enough, a Taylor series expansion gives the approximation

$$\frac{\Delta f}{f_0} \approx -\frac{1}{2} \left(\frac{\epsilon_r - 1}{\epsilon_r} \right) \frac{b}{d} \quad (72)$$

which is the perturbation theory result⁽⁸⁾, with quasi-static modification.

5.4 Determination of the Loss Tangent

The loss tangent can be related to the Q of the dielectric by consideration of Equation (56). Substitution of (45) and (46) into (58) through (60) followed by substitution of the result into (56) yields

$$Q_D = \frac{1}{\tan \delta} \left\{ 1 + \frac{1}{\epsilon_r} \left| \frac{\hat{y}_1}{\hat{y}_2} \right|^2 \left| \frac{B}{C} \right|^2 \frac{\int_b^d \left[k_{z2}^2 \sin^2 k_{z2} (d-z) + k_r^2 \cos^2 k_{z2} (d-z) \right] dz}{\int_0^b \left(\left| k_{z1} \sin k_{z1} z \right|^2 + k_r^2 \left| \cos k_{z1} z \right|^2 \right) dz} \right\} \quad (73)$$

Again, we shall assume that the cavity dimensions are small enough so that the trigonometric functions in (73) may be replaced by the first terms in their Taylor series expansions. In this case, the dominant contribution from both integrals is

the leading (unity) term in the cosine and we obtain

$$Q_D = \frac{1}{\tan \delta} \left[1 + \epsilon_r \left(\frac{1 - \frac{b}{d}}{\frac{b}{d}} \right) \right] \quad (74)$$

where we have used

$$\left| \frac{\hat{y}_1}{\hat{y}_2} \right|^2 = \epsilon_r^2 \left[1 + (\tan \delta)^2 \right] \cong \epsilon_r^2 \quad (75)$$

and

$$\left| \frac{B}{C} \right|^2 = \left| \frac{\cos k_{z1} b}{\cos k_{z2} (d - b)} \right|^2 \cong 1 \quad (76)$$

Since Q_D is not an observable, we also require a calculation of Q_W in (57). Substitution of (45) and (46) into (58), (59), and (61) and subsequent substitution of that result into (57) gives

$$Q_W = \frac{\omega \epsilon a}{R_s} \left\{ \frac{\left| \frac{C}{\hat{y}_1} \right|^2 \int_0^b \left(\left| k_{z1} \sin k_{z1} z \right|^2 + k_r^2 \left| \cos k_{z1} z \right|^2 \right) dz}{\left| C \right|^2 \left[a + 2 \int_0^b \left| \cos k_{z1} z \right|^2 dz \right] + \left| B \right|^2 \left[a + 2 \int_b^d \cos^2 k_{z2} (d - z) dz \right]} + \frac{\frac{1}{\epsilon_r} \left| \frac{B}{\hat{y}_2} \right|^2 \int_b^d \left[k_{z2}^2 \sin^2 k_{z2} (d - z) + k_r^2 \cos^2 k_{z2} (d - z) \right] dz}{\left| C \right|^2 \left[a + 2 \int_0^b \left| \cos k_{z1} z \right|^2 dz \right] + \left| B \right|^2 \left[a + 2 \int_b^d \cos^2 k_{z2} (d - z) dz \right]} \right\} \quad (77)$$

If the same approximations are made in (77) as were made in (73), the result is simply

$$Q_W = Q_u \left(\frac{f}{f_o} \right) \quad (78)$$

where Q_u is given by (44). Therefore, we have in Equation (55)

$$\frac{1}{Q_L} = \frac{1}{Q_D} + \frac{1}{Q_u \left(\frac{f}{f_o} \right)} \quad (79)$$

where Q_L is an observable and Q_D and Q_u are given in (68) and (44), respectively.

5.5 Sensitivity in the Determination of the Dielectric Constant

An indication of the sensitivity in the dielectric constant determination is given by Equation (70). We note that the b/d ratio is set by the resonator design and that the normalized frequency change $\Delta f/f_o$ is an observable in the experiment. We plot normalized frequency change versus dielectric constant with the b/d ratio as a parameter (Figure C.6). Note that any errors in the measurement of $\Delta f/f_o$, while relatively unimportant in the determination of low dielectric constants, become increasingly significant as the dielectric constant increases. Also, the smaller the b/d ratio, the more difficult the task.

5.6 Sensitivity in the Determination of the Loss Tangent

Equation (79) is used to plot Q_L , which is an observable in the experiment, as a function of the logarithm of the loss tangent, with dielectric constant as a parameter

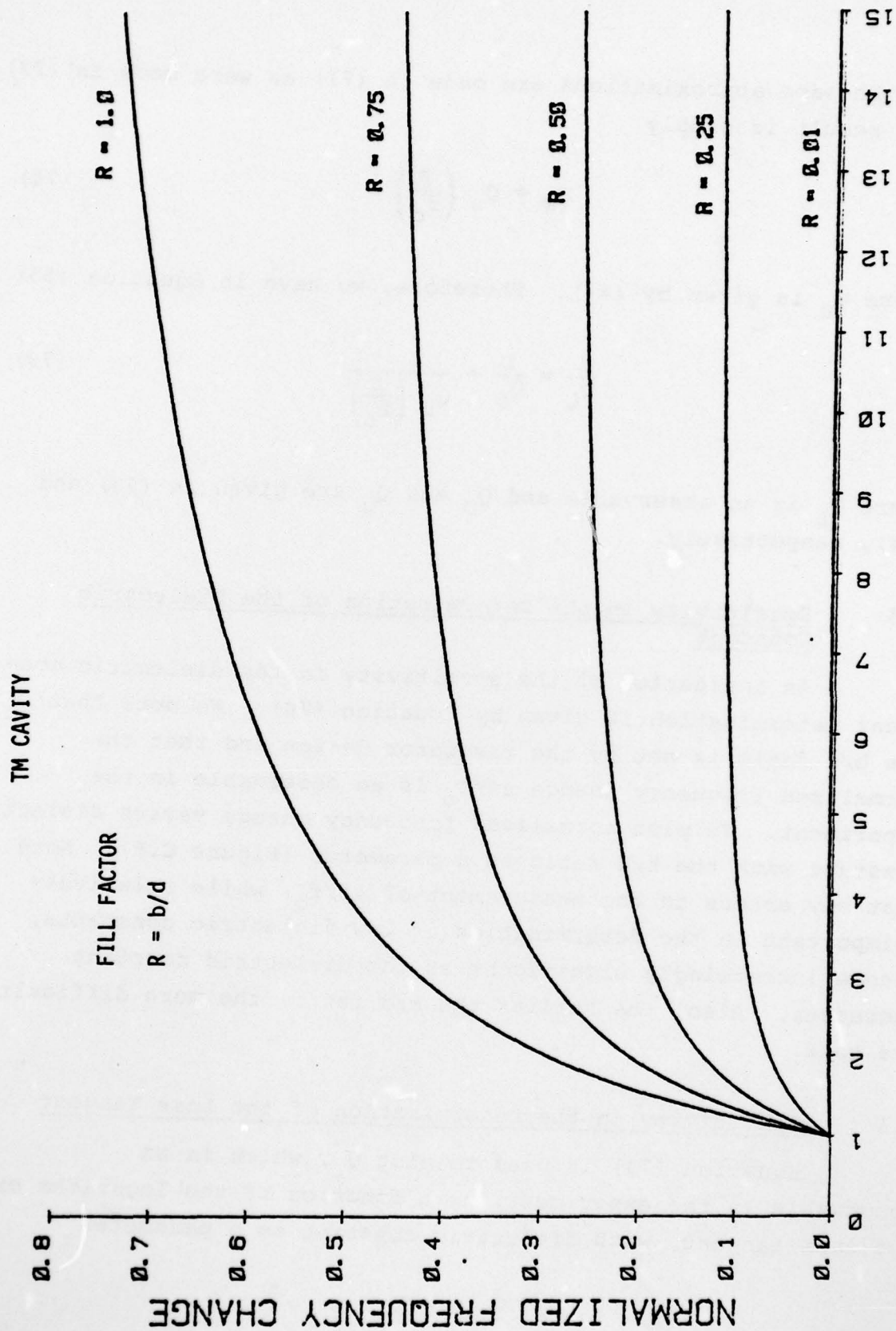


FIGURE C.6. NORMALIZED FREQUENCY SHIFT VS. DIELECTRIC CONSTANT

(Figure C.7, Figure C.8, and Figure C.9). In all three figures, the b/d ratio is 0.25. In Figure C.7, for a conductivity equal to that of brass ($\sigma_{\text{brass}} = 1.57 \times 10^7$ mhos/meter), we note that accurate determination of the loss tangent becomes difficult for $\tan \delta < 10^{-3}$. This limitation becomes more stringent in Figure C.8 and Figure C.9, which give the results for conductivities one-half and one-quarter that of brass, respectively.

5.7 Analysis of the Approximations in a Typical Case

Consider the Georgia Tech resonator, viz:

$$a = 1.5''$$

$$d = 0.2''$$

$$b = 0.050''$$

$$b/d = 0.250$$

For this case, expression (42) yields

$$f_o = 3.014 \text{ GHz}$$

For a dielectric constant of 10, Equation (69) gives

$$\frac{f}{f_o} = 0.8803$$

and thus

$$f = 2.653$$

we obtain

$$k_{z1} b = 0.2083$$

$$k_{z2} (d - b) = j 0.1141$$

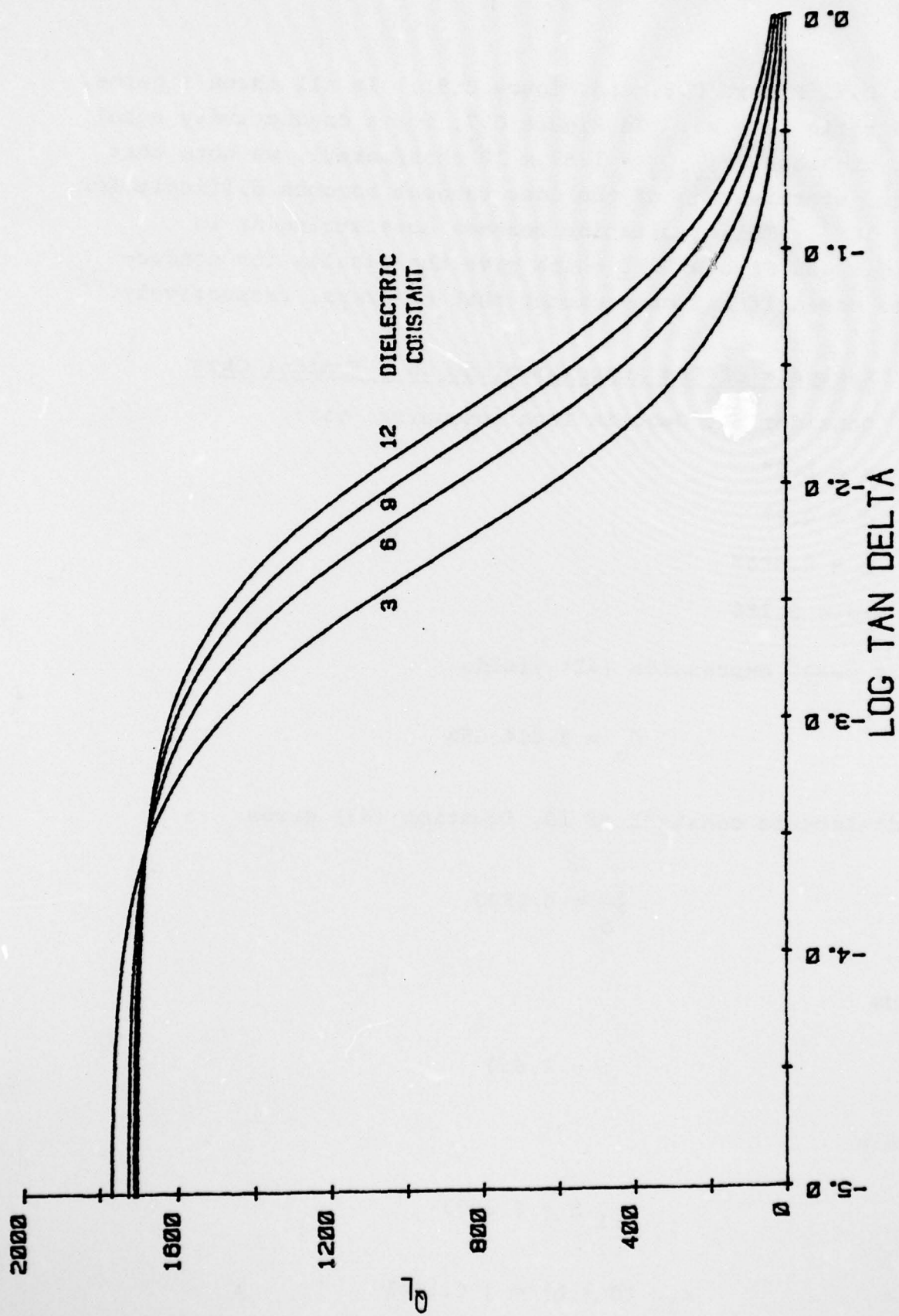


FIGURE C.7. LOADED Q VERSUS LOSS TANGENT, $\sigma = \text{BRASS}$

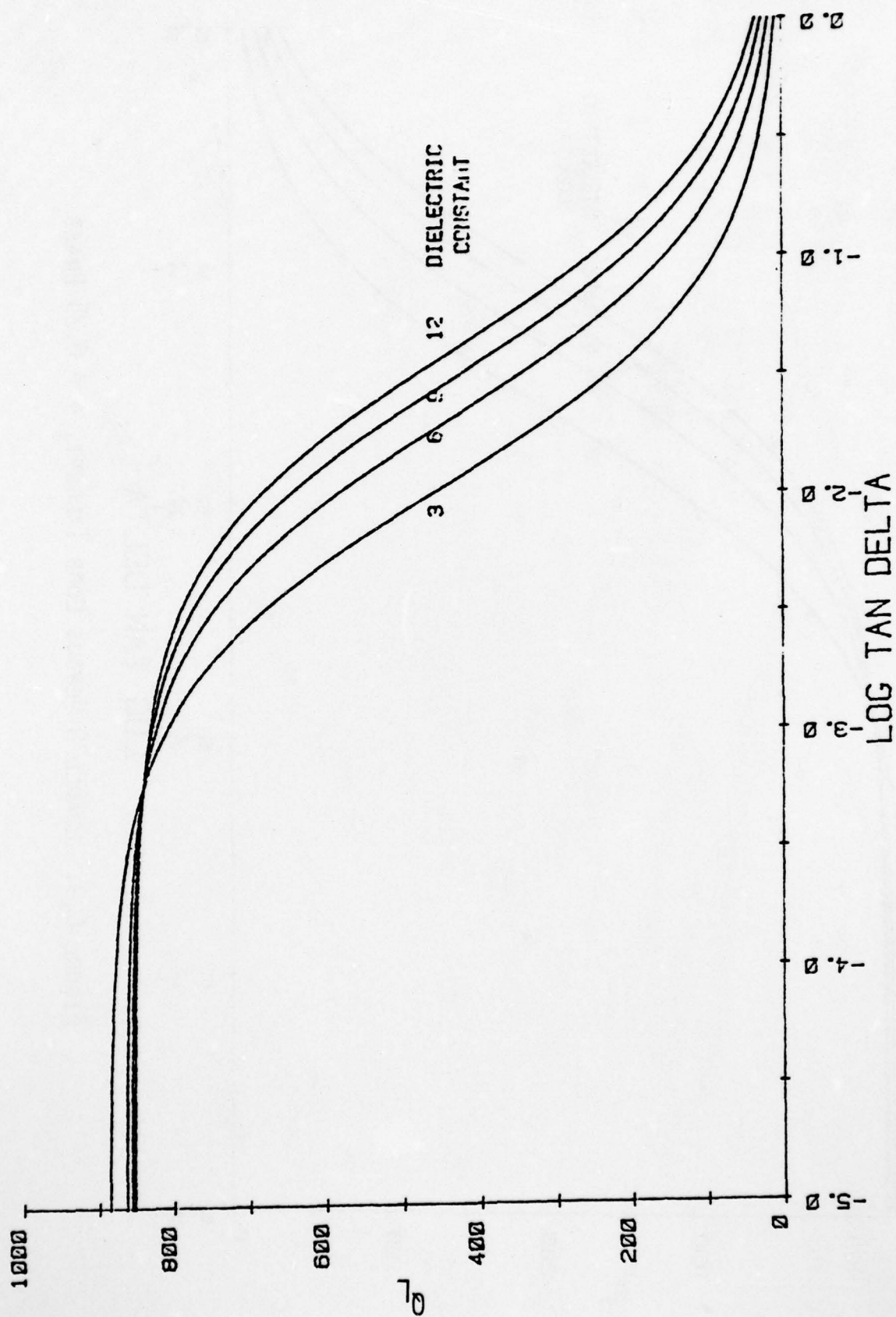


FIGURE C.8. LOADED Q VERSUS LOSS TANGENT, $\sigma = 0.5$ BRASS

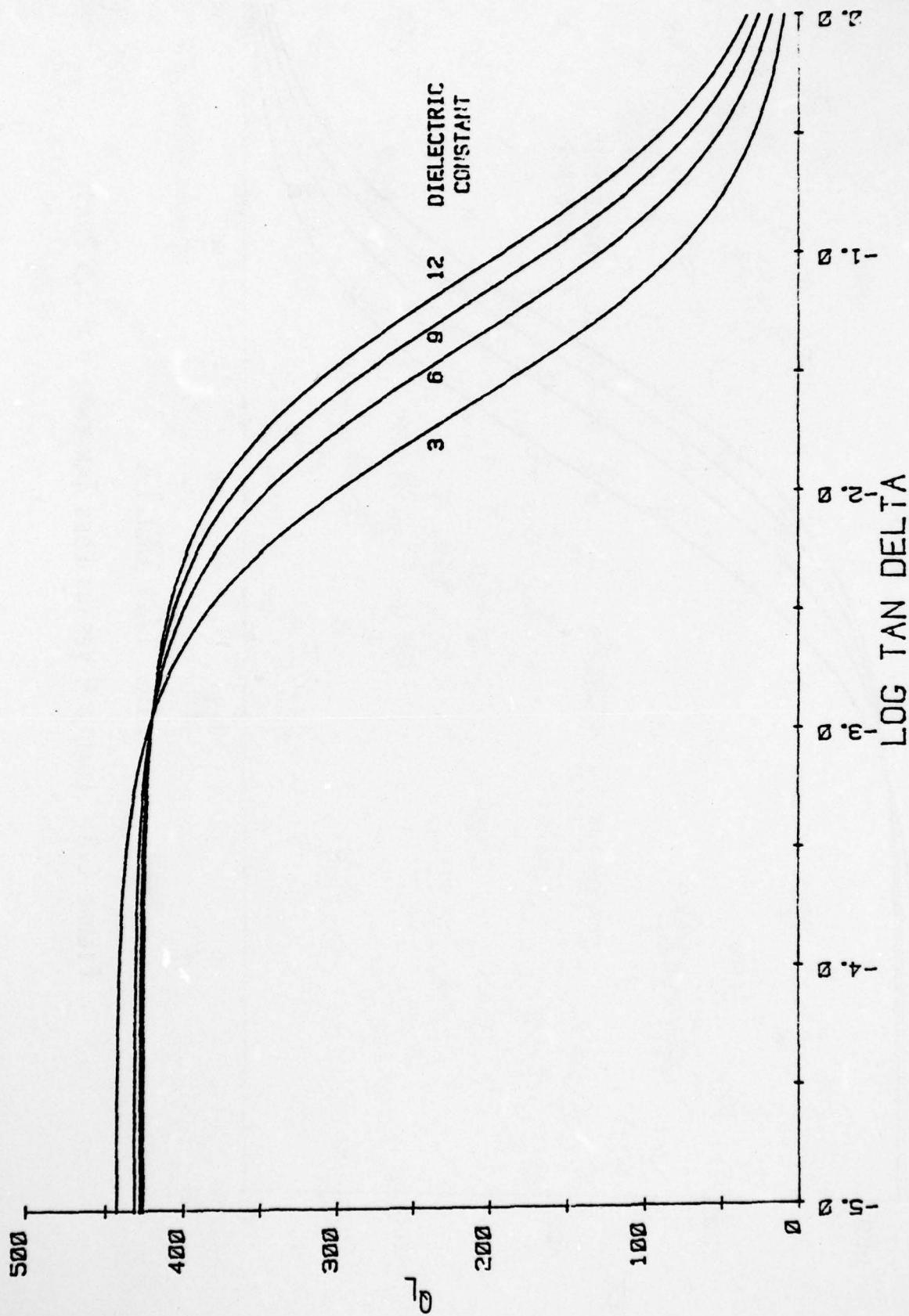


FIGURE C.9. LOADED Q VERSUS LOSS TANGENT, $\sigma = 0.25$ BRASS

AD-A077 805

SCIENCE APPLICATIONS INC EL SEGUNDO CALIF
HARDENED RADAR COMPONENT MATERIALS DEVELOPMENT STUDY. (U)
MAY 79 I OSOFSKY, R SEMELSBERGER, T DUNCAN

F/G 17/9

DAAG46-78-C-0052

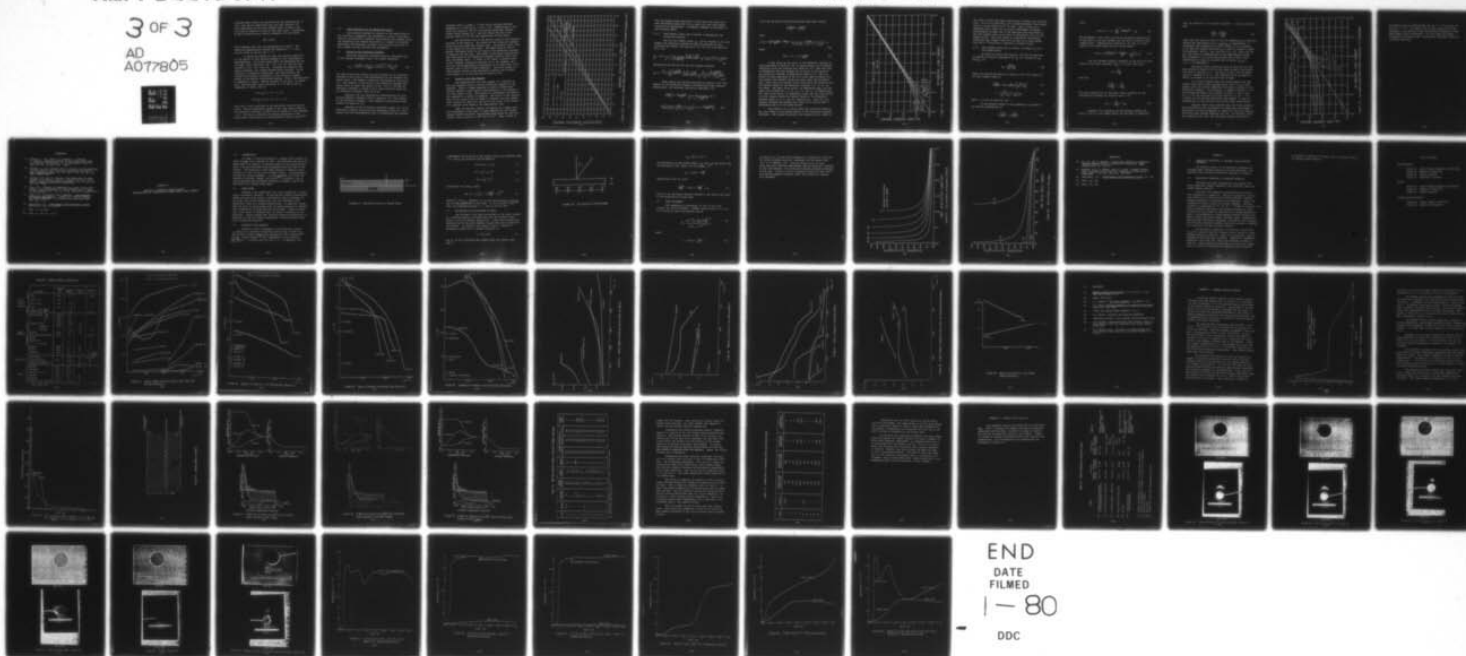
UNCLASSIFIED

AMMRC-TR-79-34

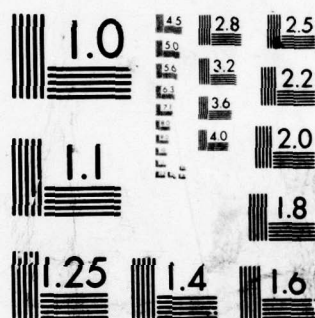
NL

3 OF 3

AD
A077805



END
DATE
FILMED
1-80
DDC



MICROCOPY RESOLUTION TEST CHART
NATIONAL BUREAU OF STANDARDS-1963-A

Although these results are obtained from the approximation in (62), they may be substituted into the exact Equation (53) with consistency to the third decimal place (0.3466 on the left side of equation; 0.3403 on the right side). Furthermore, we may calculate the B/C ratio in Equation (51) and obtain

$$\frac{B}{C} = 0.9720$$

which compares well with our approximation of unity. The remaining approximations involve the expression $1 - j \tan \delta$ and are valid as long as $\tan \delta \ll 1$.

It should be pointed out that the relative simplicity of the results of this analysis depends on the trigonometric approximations. For cavity sizes where the approximations are no longer valid, Equations (53), (73), and (77) must be used instead of (61), (74), and (78). Although the integrals are easily evaluated, the algebra becomes quite unwieldy. As the resonator is presently constructed, the field patterns are altered only slightly by addition of the dielectric sample except in one readily recognizable fashion. First, the additional E_r component is small. Second, because of the small "d" dimension, the additional cosine variation in z in the H_ϕ and E_z components is small; that is

$$\cos k_{z1} z \approx 1 \quad (0 < z \leq b)$$

$$\cos k_{z2} (d - z) \approx 1 \quad (b \leq z < d)$$

This fact is also reflected in the near-unity value of the B/C ratio. The one significant change is the jump (nearly equal to the dielectric constant) in the value of normal E at the boundary $z = b$. But this is precisely the change postulated in the quasi-static modification to the perturbation theory results^(C8).

6.0 Error Analysis for the TM-Excited Cavity

This section provides an analysis of the sensitivity of the electrical properties test procedure to errors in the estimates of the dielectric constant value and the loss tangent value. The expressions are complex functions of a number of variables, among them the dielectric constant, the Q of the cavity due to wall losses, and the various error parameters.

6.1 Errors in the Dielectric Constant

Since the dielectric constant value is influenced only by the resonant frequency shift, the simple expression

$$\Delta\epsilon_r = \frac{2\epsilon_r^2 [1 - b/d (1 - 1/\epsilon_r)]^{1/2}}{b/d} \frac{\Delta(f_0 - f)}{f_0} \quad (80)$$

has been found which relates the error bounds of the dielectric constant to the error in the determination of the resonant frequency shift. The symbol Δ should be interpreted as "the error in." For example, if the error in the normalized resonant frequency shift is about one percent [$\Delta(f_0 - f)/f_0 \approx 1\%$] and the dielectric constant is found to be 8, then the error bound for the dielectric constant value is ± 0.50 .

Equation (80) was obtained by differentiating the normalized resonant frequency shift of Equation (70) with respect to the dielectric constant. Some algebraic manipulation leads directly to Equation (80).

Analysis of the 95 percent confidence bounds (3 σ) on the dielectric constant values from the experiments leads to a conclusion that the corresponding error in determining the resonant

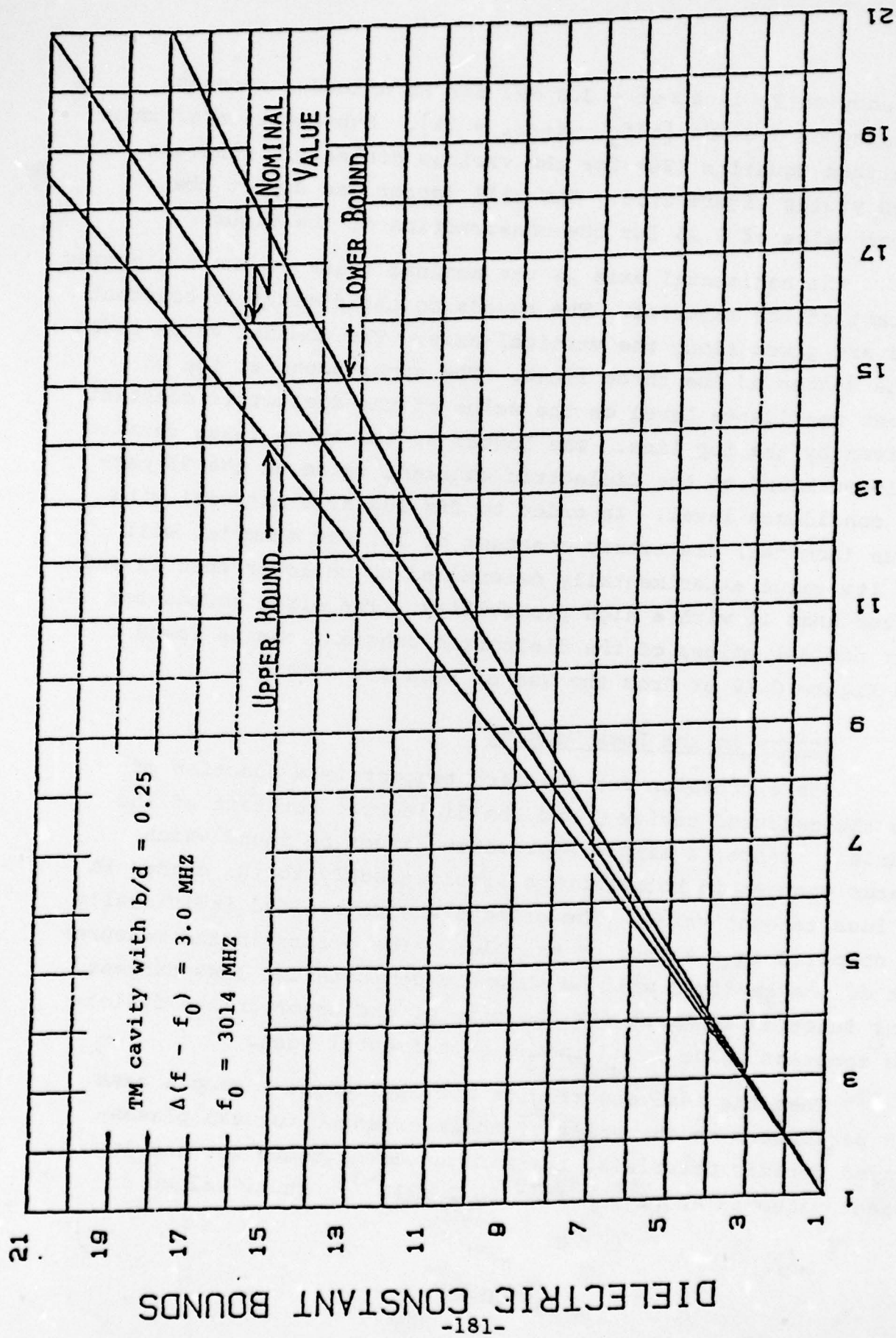
frequency shift is about ± 3.0 MHz for an unloaded resonant frequency of 3.0 GHz [$\Delta(f_0 - f)/f_0 = 1\%$]. Substitution of this value into Equation (80) for the various dielectric constant values yields Figure C.10. The fill factor was set at the typical value of 0.25 for the construction of the figure.

The horizontal axis is the nominal value of the dielectric constant of the material. The bounds on the dielectric constant value are given along the vertical axis. The nominal value trace is the center of the three lines. The upper bound at the 95 percent confidence level on the value of the dielectric constant is given by the top line. The lowest of the three lines details the lower bound on the dielectric constant value at the 95 percent confidence level. In order to fix ideas, a material with a true (nominal) dielectric constant of 12, for example, will have its value experimentally determined to be lower than 13 and greater than 11 with a high probability. The error bounds for other nominal values of the dielectric constant can be found from Figure C.10 or from the use of Equation (80).

6.2 Errors in the Loss Tangent

The expression for the loss tangent is a function of both the measured cavity Q and the dielectric constant of the material. Hence, a simple expression cannot be found which relates changes in both factors simultaneously to the change in the loss tangent value. The effects are determined individually and compared in a series of examples. The errors in the measurement of the cavity Q will be shown to dominate the loss tangent error function at least for the size of the error in the dielectric constant value found in the experimental work.

When the analysis results are applied to a sample case with parameters on the order of those expected for the plasma-sprayed ceramic materials, the minimum error bound for the loss tangent value is about 1×10^{-3} to 2×10^{-3} . Thus, values of



NOMINAL DIELECTRIC CONTANT

FIGURE C.10. DIELECTRIC CONSTANT ERROR BOUNDS CAUSED BY UNCERTAINTY IN RESONANT FREQUENCY SHIFT

the loss tangent whose magnitude is less than this figure will have confidence bounds that are so great that the loss tangent value will be meaningless. A complete treatment is provided in the following pages.

6.2.1 Loss Tangent Errors Due to Errors in Determining the Dielectric Constant

The Q of the loaded cavity, Q_L , can be related to the loss tangent and dielectric constant of the test material by substituting the results from Equations (56) and (57) into Equation (55), viz:

$$\frac{1}{Q_L} = \tan \delta \left[\frac{1}{1 + \epsilon_r \left(\frac{1 - b/d}{b/d} \right)} \right] + \frac{R_s [1 + a/d]}{1.202 (120\pi)} \frac{1}{[1 - b/d (1 - 1/\epsilon_r)]^{1/2}} \quad (81)$$

Rearranging and solving for the loss tangent produces

$$\tan \delta = \frac{[1 + \epsilon_r \left(\frac{1 - b/d}{b/d} \right)]}{Q_L} - \frac{R_s [1 + a/d]}{1.202 (120\pi)} \frac{[1 + \epsilon_r \left(\frac{1 - b/d}{b/d} \right)]}{[1 - b/d (1 - 1/\epsilon_r)]^{1/2}} \quad (82)$$

After taking the partial derivative of Equation (82) with respect to the dielectric constant and performing some algebraic manipulation, the following form can be generated, viz:

$$\begin{aligned} \frac{\partial \tan \delta}{\partial \epsilon_r} &= \frac{(1 - b/d)}{(b/d)} \frac{1}{[1 + \epsilon_r \left(\frac{1 - b/d}{b/d} \right)]} \tan \delta \\ &+ \frac{1}{Q_L} \left\{ \frac{b/d}{2\epsilon_r^2 [1 - b/d (1 - 1/\epsilon_r)]} \left[1 + \epsilon_r \left(\frac{1 - b/d}{b/d} \right) \right] \right\} \end{aligned} \quad (83)$$

If we let the partial derivatives become some small change,

$$\frac{\partial \tan \delta}{\partial \epsilon_r} \approx \frac{\Delta \tan \delta}{\Delta \epsilon_r}$$

then,

$$\Delta \tan \delta = \left[\frac{(1 - b/d)}{b/d} \frac{\tan \delta}{\tau} + \frac{\tau}{Q_W} \frac{(b/d)}{2\epsilon_r^2 [1 - b/d (1 - 1/\epsilon_r)]} \right] \Delta \epsilon_r \quad (84)$$

where

$$\tan \tau = 1 + \epsilon_r \frac{1 - b/d}{b/d} \quad (85)$$

If the value for the error in the dielectric constant is found according to Equation (80) at approximately the 95 percent confidence value and inserted into Equation (85), then the error in determining the loss tangent due to errors in the value of the dielectric constant is depicted by Figure C.11. The fill factor is again specified as the 0.25 value used in Figure C-10. The nominal loss tangent values are given along the horizontal axis, while the error bounds can be found along the vertical axis. The nominal values of the dielectric constant ($\epsilon_r = 8, 16, 24$) are shown. The upper three curves (in descending order) are the upper error bounds for $\epsilon_r = 24, \epsilon_r = 16$, and $\epsilon_r = 8$ respectively. The lower three curves (in descending order) are the lower bounds for loss tangent errors for nominal values of the dielectric constant equal to 8, 16, and 24, respectively. Note that this complete analysis has assumed that there are no errors made in determining the Q of the loaded cavity.

From Figure C.11 it can be seen that the error bounds on the loss tangent value become tighter as the dielectric constant decreases. The minimum detectable loss tangent can be viewed as

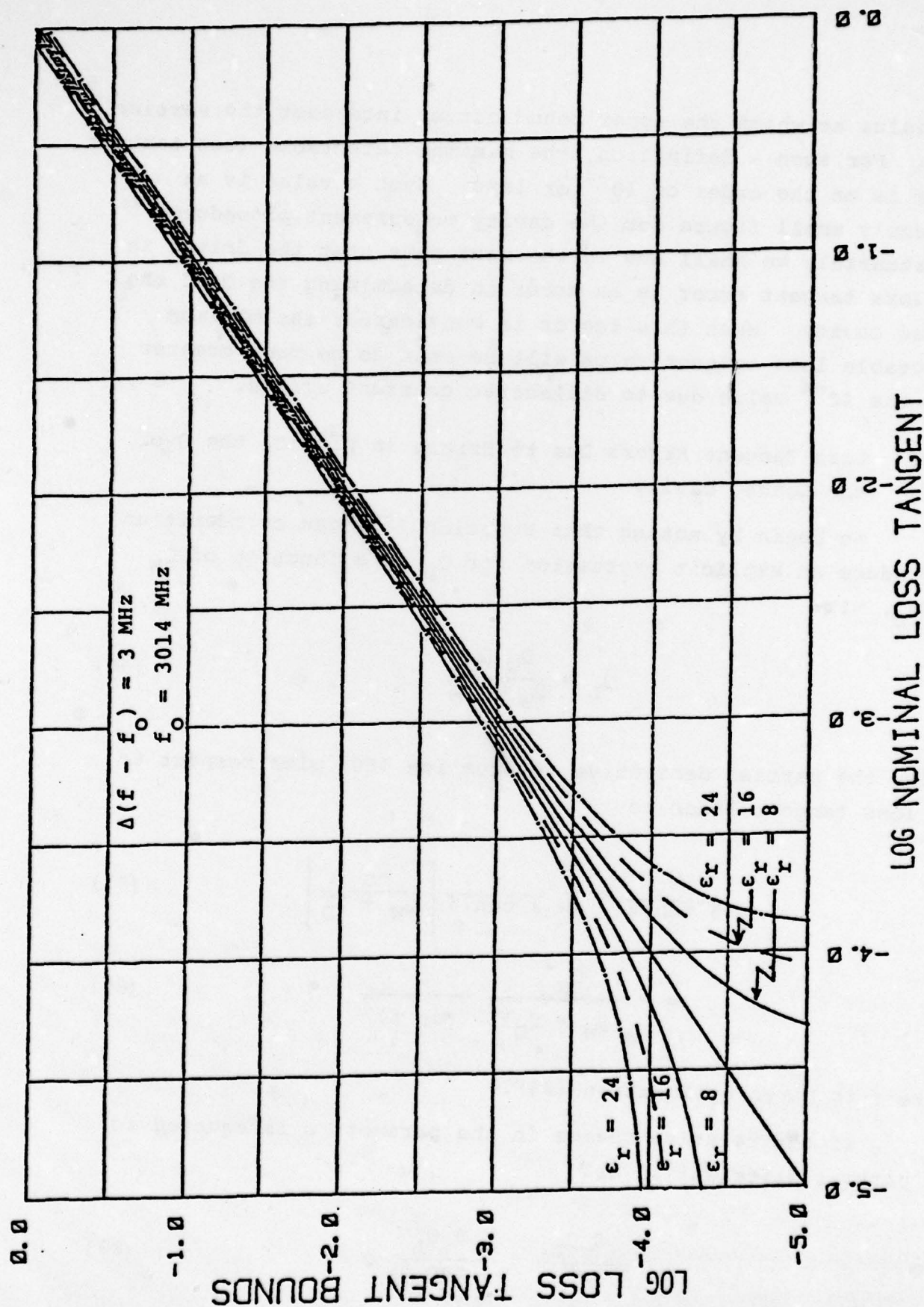


FIGURE C.11. LOSS TANGENT ERROR BOUNDS CAUSED BY UNCERTAINTY IN THE DIELECTRIC CONSTANT

the value at which the upper bound curves intersect the vertical axis. For such a definition, the minimum detectable loss tangent value is on the order of 10^{-4} or less. Such a value is an extremely small figure for the cavity measurement procedure. Unfortunately we shall see in the next part that the driver in the loss tangent error is an error in determining the Q of the loaded cavity. When this factor is considered, the minimum detectable loss tangent value will be seen to be much greater than the 10^{-4} value due to dielectric constant errors.

6.2.2 Loss Tangent Errors Due to Errors in Finding the Q of the Loaded Cavity

We begin by noting that Equation (55) can be rewritten to produce an explicit expression for Q_L as a function of Q_W and Q_D , viz:

$$Q_L = \frac{Q_W Q_D}{Q_W + Q_D} \quad (86)$$

Taking the partial derivative of Equation (86) with respect to the loss tangent leads to

$$\frac{\partial Q_L}{\partial \tan \delta} = Q_W \frac{\partial}{\partial \tan \delta} \left[\frac{Q_D}{Q_W + Q_D} \right] \quad (87)$$

$$= - \frac{Q_W^2}{(Q_W + Q_D)^2} \frac{\tau}{(\tan \delta)^2} \quad (88)$$

where τ is given by Equation (85).

If the relative change in the parameters is equated to the partial differential as

$$\frac{\partial Q_L}{\partial \tan \delta} \approx \frac{\Delta Q_L}{\Delta \tan \delta} \quad (89)$$

then,

$$\Delta \tan \delta = - \left(1 + \frac{Q_D}{Q_W} \right)^2 \frac{(\tan \delta)^2}{\tau} \Delta Q_L \quad (90)$$

The parameters $\Delta \tan \delta$ and ΔQ_L can be interpreted respectively as the error in the loss tangent and the error in the Q of the loaded cavity. Substitution of Equations (56) and (57) into Equation (90) above leads directly to the result

$$\Delta \tan \delta = \left[\frac{(\tan \delta)^2}{\tau} + \frac{2 \tan \delta}{Q_W} + \frac{\tau}{Q_W^2} \right] \Delta Q_L \quad (91)$$

For the unloaded resonant frequency f_0 and the 3 db bandwidth of the cavity resonance f_{3db} , it is well known that

$$Q_L = \frac{f_0}{f_{3db}} \quad (92)$$

and thus,

$$\frac{d Q_L}{d f_{3db}} = - \frac{Q_L}{f_{3db}} \quad (93)$$

The usual substitution of the small change notation for the differential produces the desired result, viz:

$$\Delta Q_L = - \frac{Q_L}{f_{3db}} \Delta f_{3db} \quad (94)$$

Equation (94) specifies the relationship between the error in the Q of the loaded cavity and the error in measuring

the 3 db bandwidth of the resonant response. A simple rearrangement

$$\frac{\Delta Q_L}{Q_L} = \frac{\Delta f_{3db}}{f_{3db}} \quad (95)$$

shows that the relative error of the two parameters are identical. Because the determination of $\Delta f_{3db}/f_{3db}$ is experimental, a reasonable error appears to be on the order of 5 to 6 percent. If we take the maximum value for Q_L in order to produce a worst-case estimate, then $Q_L \approx Q_W = 850$ and $\Delta Q_L \approx 50$. Note that the $Q_W = 850$ value is representative of the experimental results and corresponds to a cavity constructed from a metal whose conductivity is equal to one-half that of brass ($\sigma_{brass} = 1.57 \times 10^7$ mhos/meter).

The major result previously given as Equation (91) has been plotted in Figure C.12 for the three values of the dielectric used in section 6.2.1. The error in the Q of the loaded cavity is assumed to be 50. The conductivity of the metal in cavity is assumed to be one-half that of brass.

It is quite apparent that the minimum detectable loss tangent value due to this representative error in Q_L is much greater than the minimum detectable value due to errors in the dielectric constant. In particular, it appears that for $\epsilon_r = 8$ the minimum detectable loss tangent is about 2×10^{-3} , while for $\epsilon_r = 24$ the value may be on the order of 6×10^{-3} . The criteria for the minimum detectable loss tangent is again the intersection of the vertical axis and the upper bound curves.

Although these values indicate that the cavity measurement procedure is not as sensitive as some other measurement procedures, the cavity approach is usable for very thin samples while the other methods generally are not. In addition, since the samples are so thin, the calculated losses attributed to

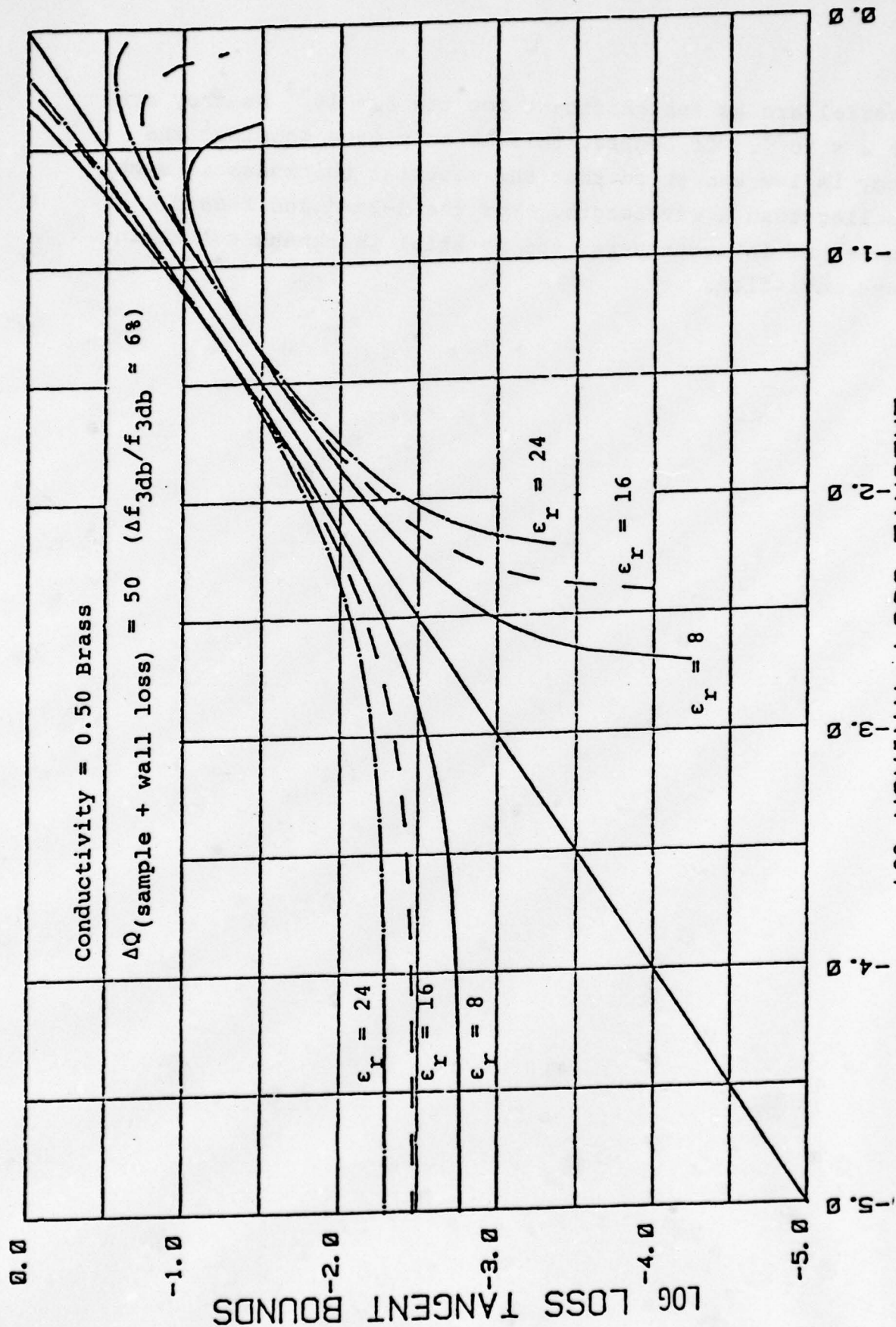


FIGURE C.12. LOSS TANGENT ERROR BOUNDS CAUSED BY UNCERTAINTY IN Q MEASUREMENT

the material are as insignificant for $\tan \delta = 10^{-3}$ as they are for $\tan \delta < 10^{-4}$. Of course, this is only true provided the frequency is low enough so that the material thickness is much, much smaller than a wavelength. For the S-Band and X-Band frequencies of interest here, the material thickness constraint is always satisfied.

REFERENCES

- C1. Horner, F., T.A. Taylor, R. Dunsmeir, J. Lamb and W. Jackson, "Resonance Methods of Dielectric Measurement at Centimeter Wavelengths," J. of IEE (London), Vol. 93, Part III, No. 21, pp. 53-68 (1946).
- C2. Bleaney, B., J.H. Loubser and R.P. Penrose, "Cavity Resonator for Measurements with Centimeter Electromagnetic Waves", Proc. Physical Society, Vol. 59, Part 2, No. 332, pp. 185-199 (1 March 1947).
- C3. Hotston, E.S. and J.E. Houldin, "The Measurement of Small Changes in Dielectric Constant by Means of a Cavity Wave-meter", Journ. of Scientific Instruments, Vol. 32, pp. 484-485 (Dec. 1955).
- C4. Aron, C.P., "Effects of Degenerate E_{11u} Mode in H_{01u} Mode Cavity on the Measurement of Complex Permittivity," Proc. of IEE (London), Vol. 114, No. 8, pp. 1030-1034 (August 1967).
- C5. Cook, R.J., "Microwave Cavity Methods," High Frequency Dielectric Measurement, J. Chamberlain and G.W. Chanty, ed. Surrey, England: IPC Science and Technology Press, 1973. pp. 12-27.
- C6. Harrington, R.F., Time-Harmonic Electromagnetic Fields, McGraw-Hill 1961, p. 213-216.
- C7. Ibid., p. 321-326.
- C8. Ibid., p. 324, eq. (7-14).

APPENDIX D

ANALYSIS OF HARDENING MATERIAL-ARRAY
INTERACTIONS FOR A DIELECTRIC COVERED PHASED ARRAY ANTENNA

1.0 INTRODUCTION

In order to provide protection, a phased array antenna is often covered with a dielectric slab. The resulting structure has been shown^(D1) to support, at certain angles in the radiation pattern, a surface wave mode which propagates along the face of the antenna. The existence of this mode produces a resonance which results in a null in the active element pattern. This phenomenon is known as "array blindness." In this appendix, we follow the analysis of Knittel, Hessel, and Oliner^(D2) to produce a set of curves relating slab thickness, dielectric constant, and blindness angle for a simple array model.

2.0 ARRAY MODEL

Consider a two dimensional slot array covered by a uniform slab of dielectric material. To analyze the surface guided waves, assume that the slots occupy a sufficiently small percentage of the total area of the antenna face that the dielectric slab essentially rests on a uniform ground plane. In addition, assume that the array is large enough that the great majority of elements "see" essentially the same physical environment. There is therefore little error in assuming that the array is infinite in surface area. Finally assume that the array aperture distribution is separable so that the scanning phenomena in each principal plane can be separately analyzed.

3.0 DIELECTRIC SLAB ANALYSIS

Consider a slab of thickness T and dielectric constant ϵ_r resting on a perfectly conducting ground plane (Figure D-1). The dominant surface guided mode supported by this structure^(D3) is TM₀. We may express^(D4) the x-dependence of the fields by $\begin{cases} \sin ux \\ \cos ux \end{cases}$ for $x < T$ and by $\exp(-vx)$ for $x > T$. In addition, the

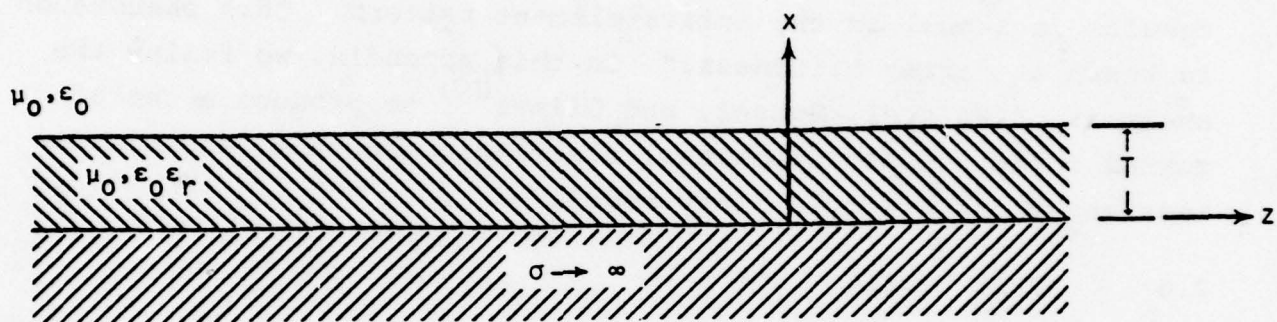


FIGURE D.1. DIELECTRIC SLAB ON A GROUND PLANE

z-dependence can be given by $\exp(+ik_z z)$ where the relations among u , v , and k_z are given for the TM modes by

$$uT \tan uT = \epsilon_r vT \quad (1)$$

$$u^2 + k_z^2 = \epsilon_r k^2 \quad (2)$$

$$-v^2 + k_z^2 = k^2 \quad (3)$$

Elimination of v and k_z gives

$$\tan uT = \epsilon_r \left[(\epsilon_r - 1) \left(\frac{kT}{uT} \right)^2 - 1 \right]^{1/2} \quad (4)$$

where $k^2 = \omega^2 \mu_0 \epsilon_0$. Equation (4) is the characteristic equation for TM mode propagation in the slab. It is not hard to show ^(D5) that, for propagating modes, u , v , and k_z are all real.

4.0 EXCITATION OF TM SLAB MODES BY ARRAY

The TM modes in the slab are excited by the slots located at a uniform spacing d and polarized with the electric field vector in the z -direction (Figure D.2). (Note that E-plane scan produces the TM slab modes whereas H-plane scan would produce TE slab modes). To produce a main beam at angle θ requires a progressive phase shift α between radiators of

$$\alpha = kd \sin \theta \quad (5)$$

Let k_{zA} be the z -directed wave number along the antenna face. Then,

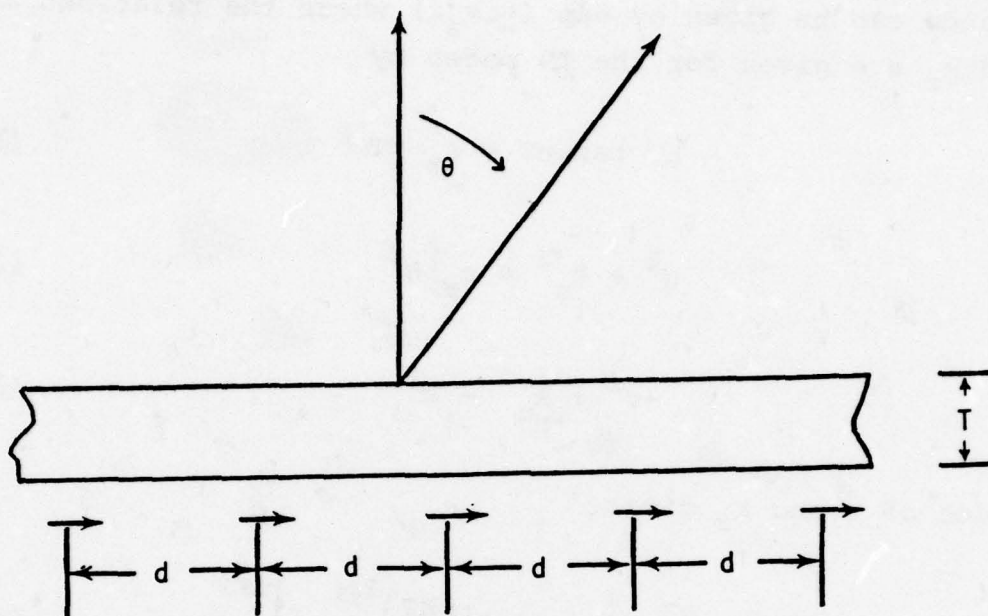


FIGURE D.2. EXCITATION OF TM SLAB MODES

$$k_{zA} = \frac{a}{d} = k \sin \theta \quad (6)$$

For excitation of the surface modes, $k_z d$ and $k_{zA} d$ may differ only by multiples of $2m\pi$, where m is an integer, or

$$k_z = k \sin \theta + \frac{2m\pi}{d} \quad (7)$$

Substitution into (2) gives

$$\left(\frac{uT}{kT}\right)^2 + \left(\sin \theta + \frac{2m\pi}{kd}\right)^2 = \epsilon_r \quad (8)$$

which is the constraint equation imposed on the slab by the array in the direction of E-plane scan.

5.0 ARRAY BLINDNESS

The combination of Equations (4) and (8) give the criteria for array blindness. Indeed, substitution of (8) into (4) followed by some rearrangement yields

$$\frac{T}{\lambda} = \frac{\tan^{-1} \left[\epsilon_r \left(\frac{\tau - 1}{\epsilon_r - \tau} \right) \right]^{1/2}}{2\pi(\epsilon_r - \tau)^{1/2}} \quad (9)$$

where

$$\tau = \left(\sin \theta + \frac{m}{d/\lambda} \right)^2 \quad (10)$$

In Figure D.3, we plot slab thickness as a function of $\sqrt{\epsilon_r}$ with the array blindness angle as a parameter for the lowest mode ($m = -1$ in Equation (10)). From the design point of view, given the array scanning requirements and the dielectric constant of the slab material, the curves give maximum allowable thickness of the slab. Figure D.4 as an alternative gives the slab thickness plotted against blindness angle with dielectric constant as a parameter.

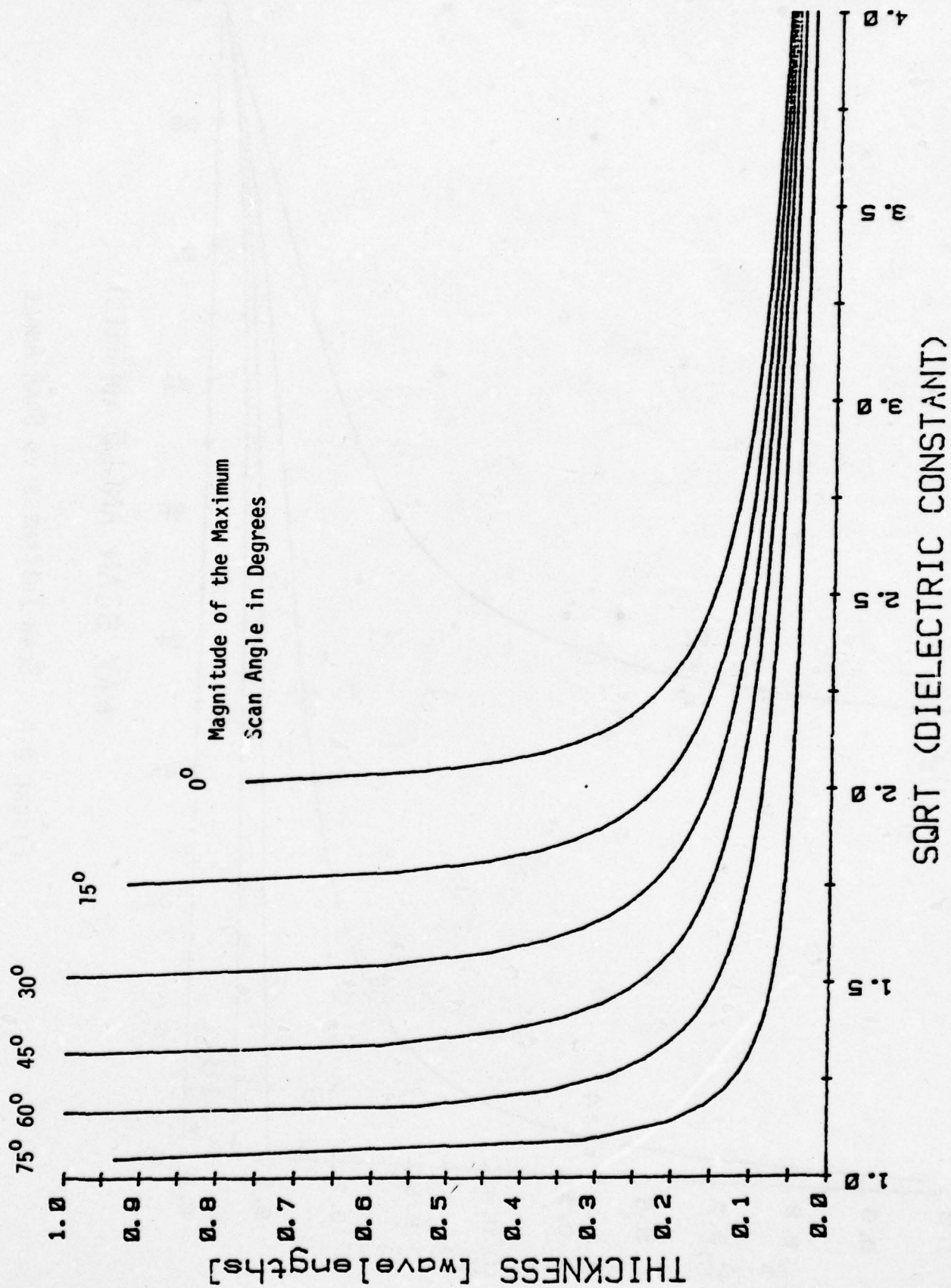


FIGURE D.3. SLAB THICKNESS VS DIELECTRIC CONSTANT

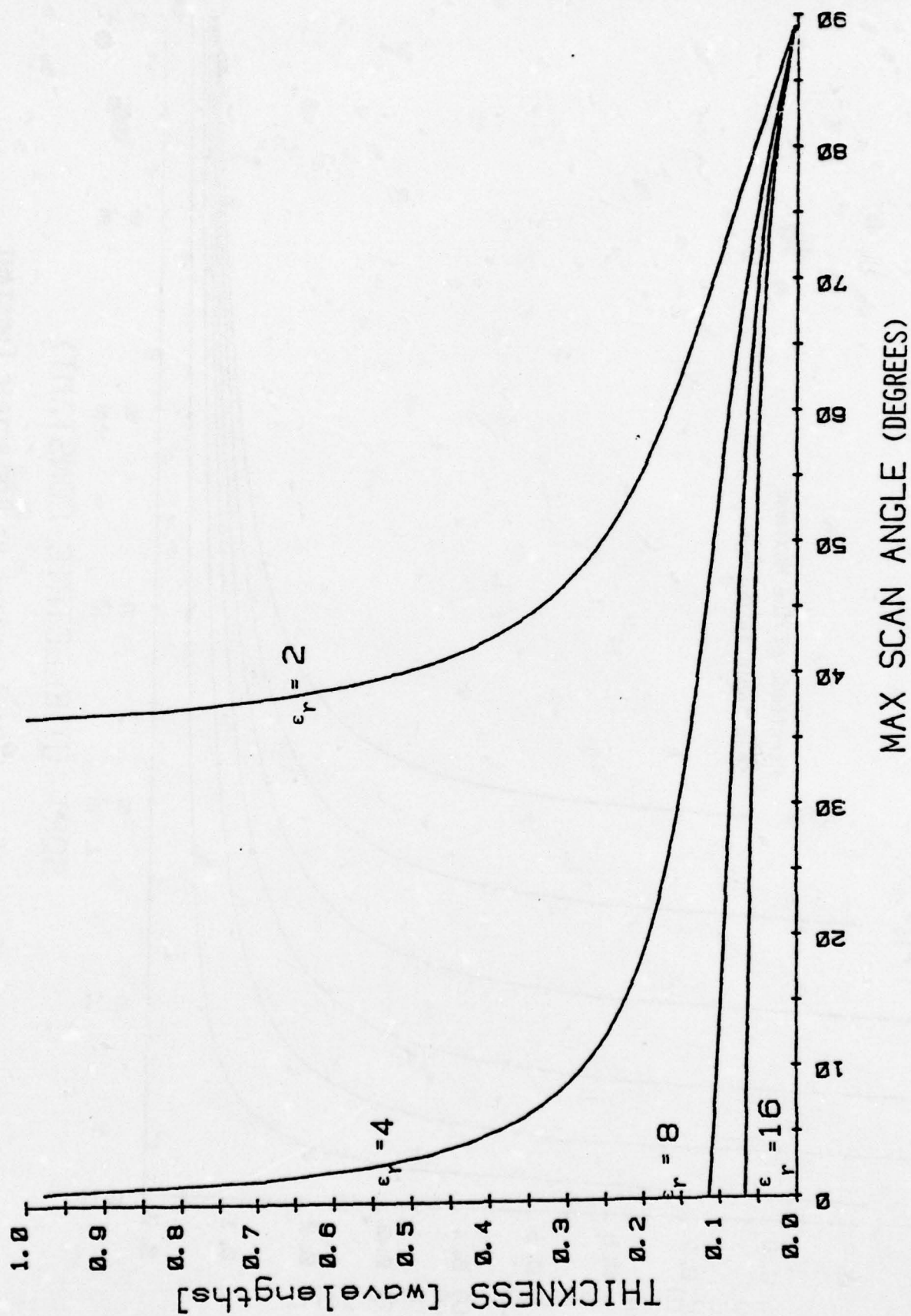


FIGURE D.4. SLAB THICKNESS VS SCAN ANGLE

REFERENCES

- D1. Wu, C.P. and V. Galindo, "Surface-Wave Effects on Dielectric Sheathed Phased Arrays of Rectangular Waveguides," BSTJ, January, 1968, pg. 117-142.
- D2. Knittel, G.H., A. Hessel, and A.A. Oliner, "Element Pattern Nulls in Phased Arrays and their Relation to Guided Waves," Proc. IEEE, V. 56, Nov., 1968, pg. 1822-1836.
- D3. Harrington, R.F., Time-Harmonic Electromagnetic Fields, pg. 168.
- D4. Ibid., pg. 164.
- D5. Ibid., pg. 166.

APPENDIX E

1.0 MECHANICAL PROPERTIES OF HARDENED RADAR CANDIDATE MATERIALS

An extensive search of the mechanical properties of Hardened Radar Candidate Materials has been performed. The available data has been reviewed and compiled as attached.

2.0 MECHANICAL PROPERTIES OF CANDIDATE MATERIALS

The materials under consideration are grouped into three categories, namely nonmetallic bulk material, metal and plasma sprayed ceramics.

Most data for nonmetallic bulk materials are found from references E1 through E5. Mechanical properties for some bulk materials are manufacturing process dependent; however, limited information is provided by the suppliers. Except for columbium the data for metal are rather complete. The main sources are references E1, E4, E6, E7). A number of technical articles furnished by the Metals and Ceramics Information Center provides the only source of information for plasma sprayed ceramics. The properties of plasma sprayed ceramics strongly depend on spray conditions (speed, distance, angle, temperature), particle size and coating thickness. Because so many variables are involved, mechanical property tests are required to complete and re-evaluate the data provided herewith.

The mechanical properties in the survey include melting point, specific gravity, Poisson's ratio, porosity, linear thermal expansion coefficient, modulus of elasticity, tensile, compressive and bond shear strengths. Temperature independent properties (the first four items) are tabulated as shown in Table E1. Other mechanical properties are plotted vs. temperature in Figures E1 through E4 for nonmetallic bulk materials,

in Figures E5 through E7 for metals and in Figures E8 and E9 for plasma sprayed ceramics.

LIST OF FIGURES

Bulk Materials

- Figure E1. Linear Thermal Expansion Coefficients
- Figure E2. Modulus of Elasticity
- Figure E3. Tensile Strength
- Figure E4. Compressive Strength

Metals

- Figure E5. Linear Thermal Expansion Coefficient
- Figure E6. Modulus of Elasticity
- Figure E7. Tensile Strength

Plasma Sprayed Ceramics

- Figure E8. Linear Thermal Coefficient
- Figure E9. Modulus of Elasticity

TABLE E1. GENERAL MATERIAL PROPERTIES

	Materials	Melting Point °F	Specific Gravity	Possion's Ratio	Porosity %
PLASMA SPRAYED CERAMICS	ZrO ₂	5010	5.3		11-12
	ZrO ₂ + MgO	3830			
	ZrO ₂ + Y ₂ O ₃	5010	5.88		14
	Al ₂ O ₃	3713	3.38		7
	Spinel (71% Al ₂ O ₃ 29% MgO)		3.47		1-5
BULK MATERIALS	Boron Nitride - NBR	3272*	1.9		
	- HP	5027*	1.9		
	- M	2552*	2.12		
	Alumina (99.5%)	3180*	3.89	.22	
	" - Durafrax	2900*	3.7	.22	0
	" - Monofrax		3.41	.22	1.9
	Beryllia	4660	2.1	.23	
	Slip Cast Fused Silicon	2012*	2.0		2.5-12
	AS-3DX				
	Teflon T7C		2.2		0
	" " (15% TiO ₂)				
	Steatite	1832*	2.7	.23	0
	Zircon	2012*	3.7	.25	0
	Corierite	2192*	2.3	.21	1% absorption
FIREBRICKS	Zircon SiO ₂		3.68	.25	16.3-19.2
	Alumina 90% Al ₂ O ₃	3390	2.96	.25	18
	Silfrax Fusil Foam 30		.51	.25	75
METALS	Tantalum	5425	16.6	.35	-
	Columbium	4474	8.58		-
	TZM (97% Mo, 3% Ti)	4760	10.24		-
	Tungsten	6200	19.3	.28	-
	Aluminum	1220	2.7	.33	-
	Stainless Steel AISI 303	2600	8.03	.29	-

*Max. usable temp.

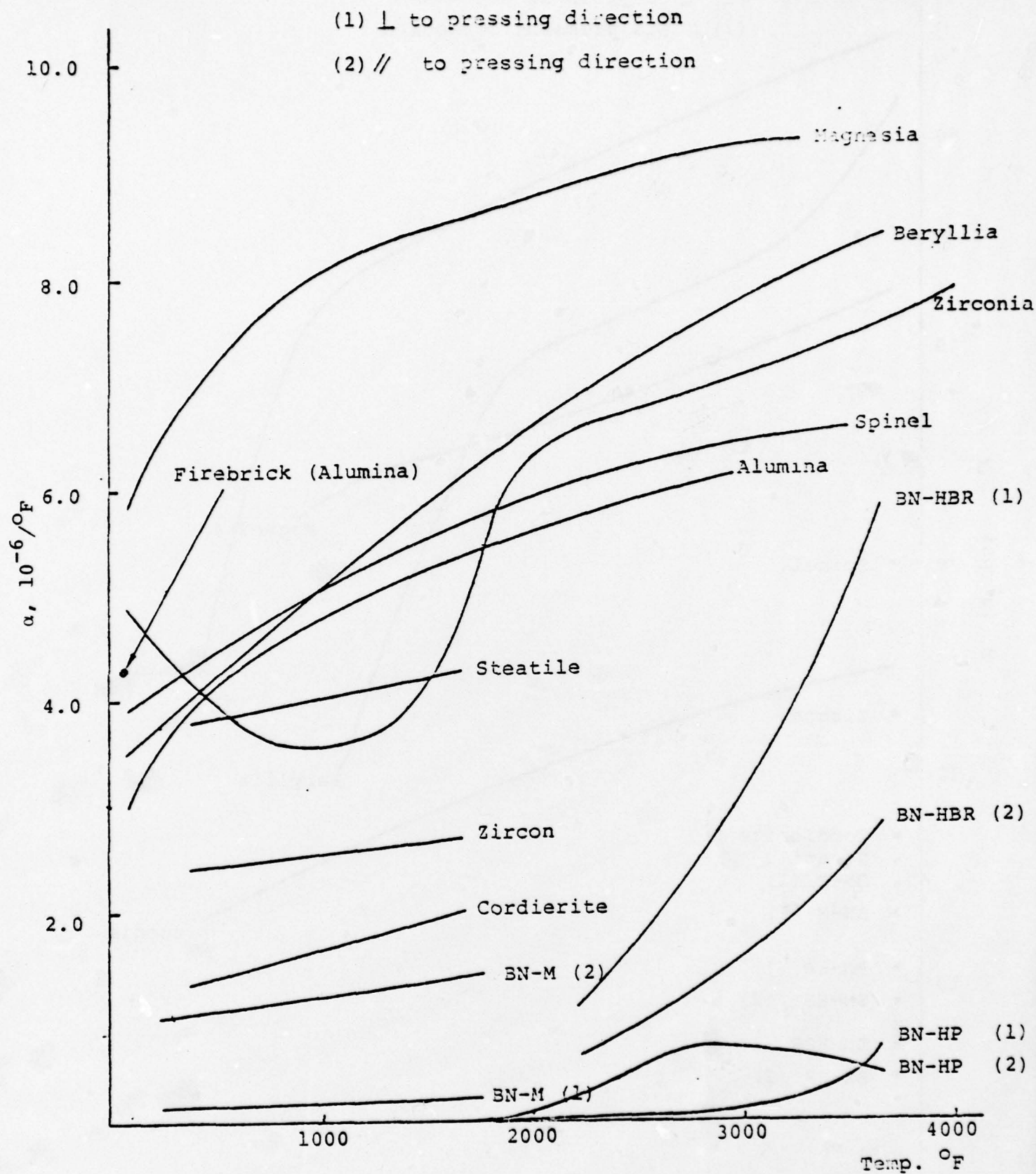


FIGURE E1. LINEAR THERMAL EXPANSION COEFFICIENT FROM 70°F
FOR BULK MATERIALS

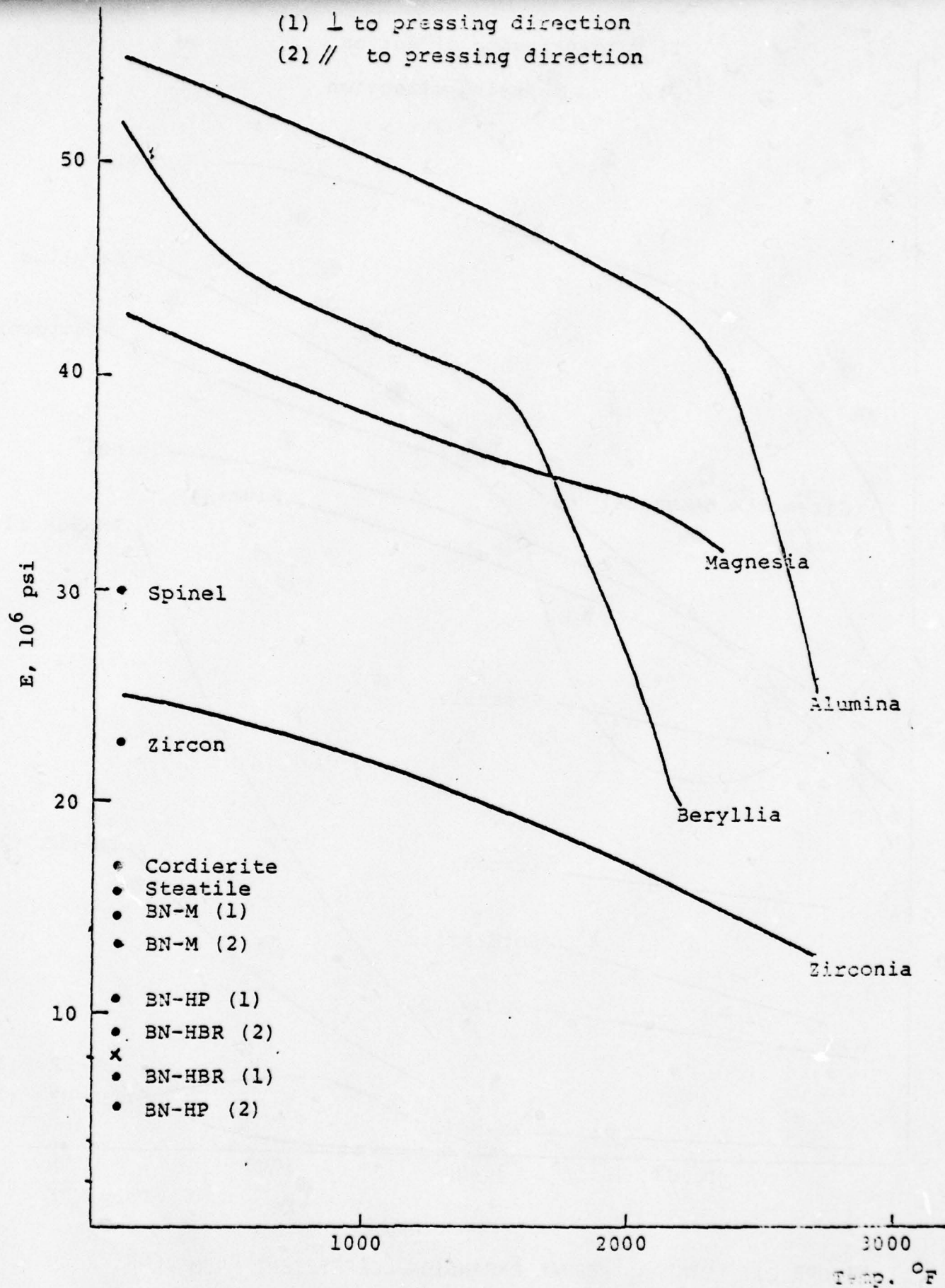


FIGURE E2. MODULUS OF ELASTICITY FOR VARIOUS BULK MATERIALS

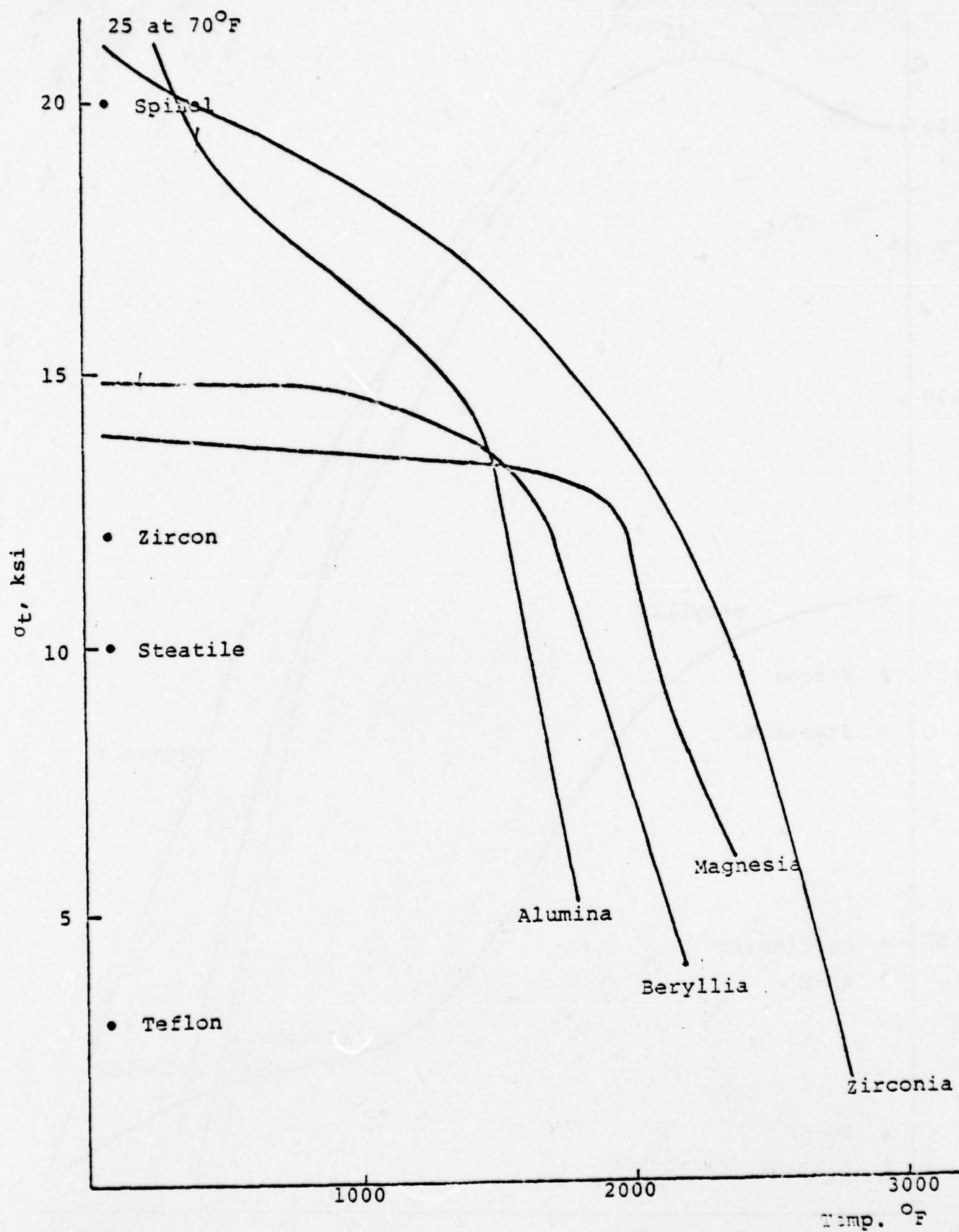


FIGURE E3. TENSILE STRENGTH FOR VARIOUS BULK MATERIALS

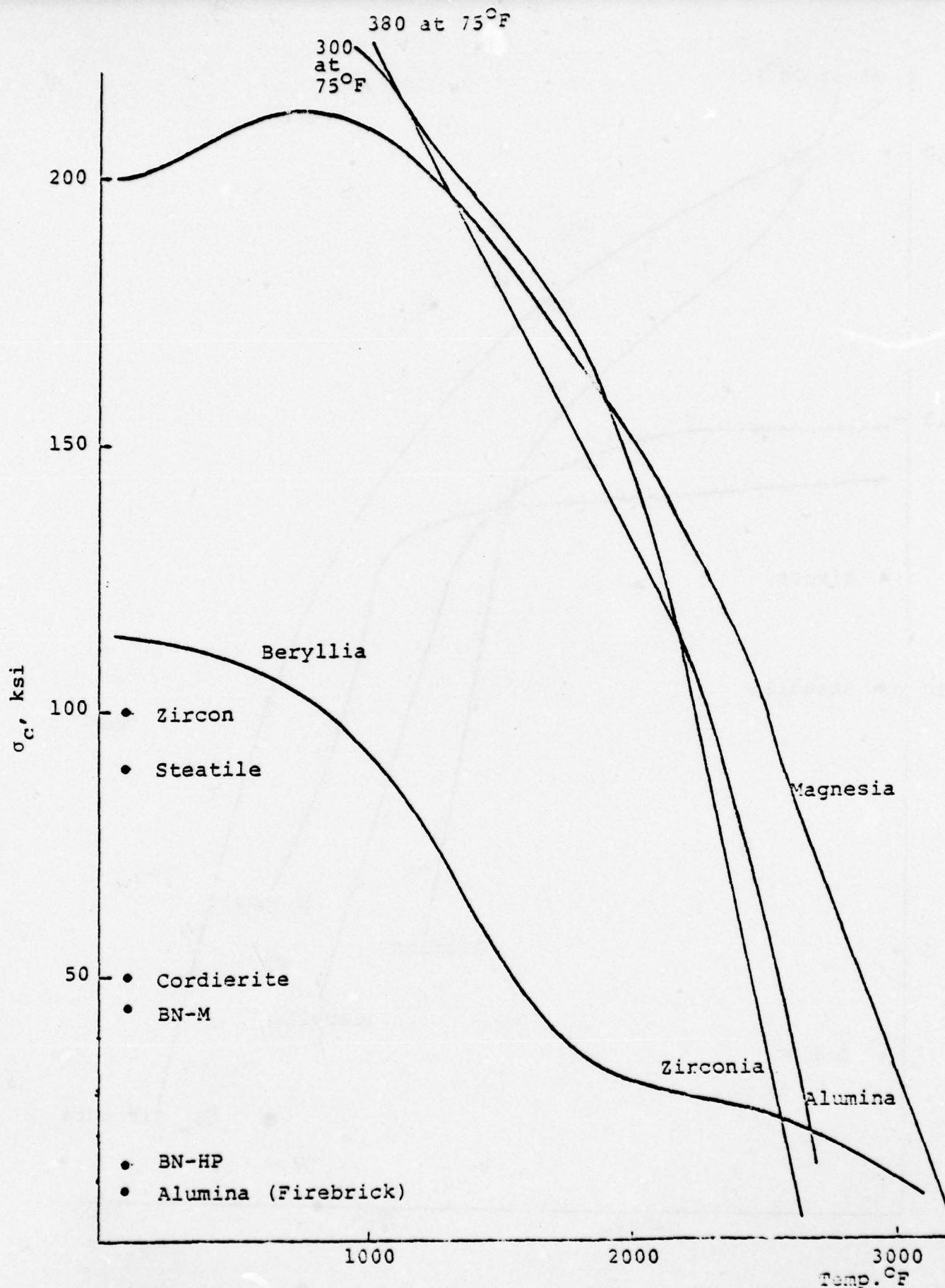


FIGURE E4. COMPRESSIVE STRENGTH FOR VARIOUS BULK MATERIALS

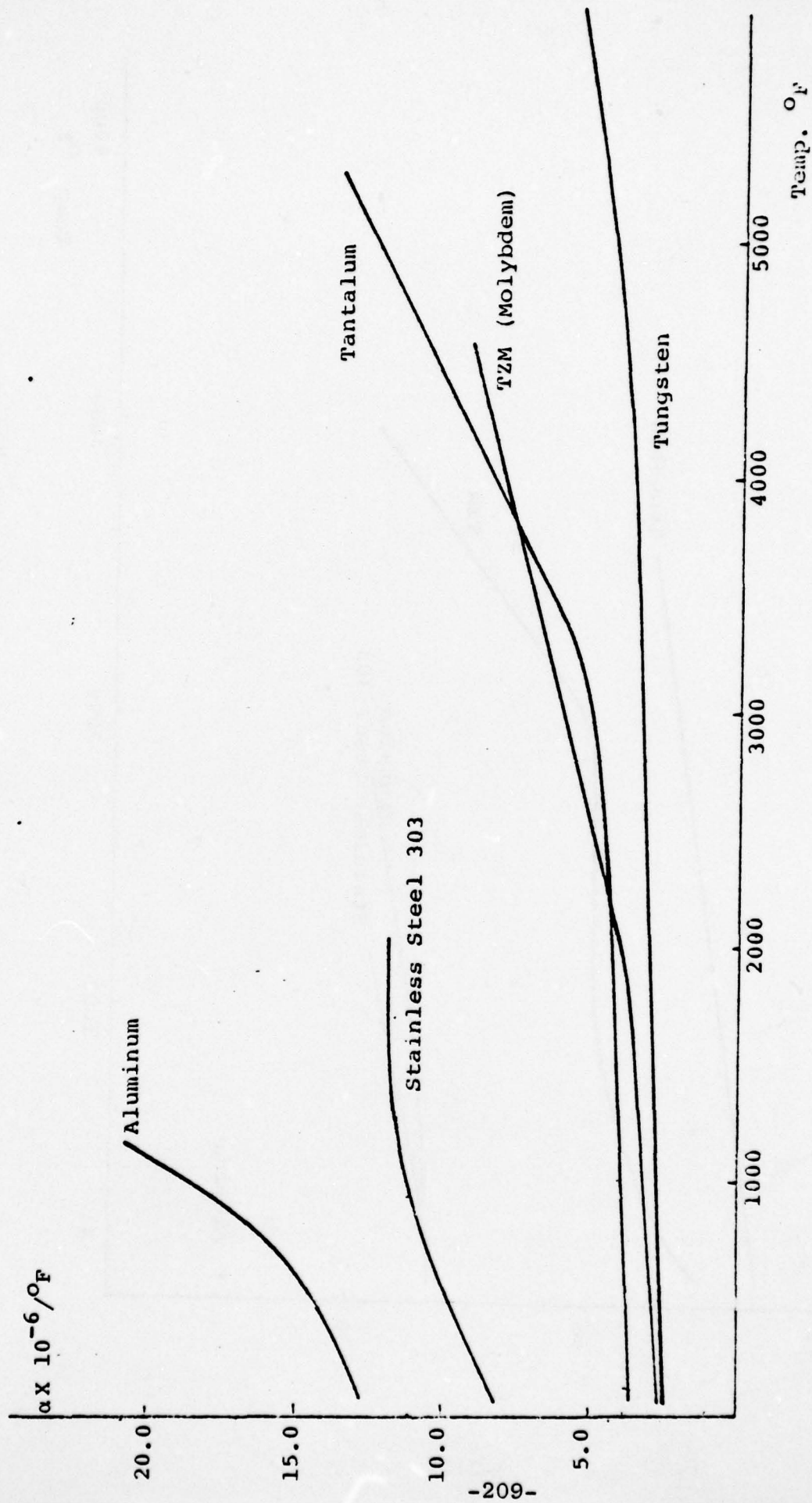


FIGURE E5. LINEAR THERMAL EXPANSION COEFFICIENTS FOR METALS

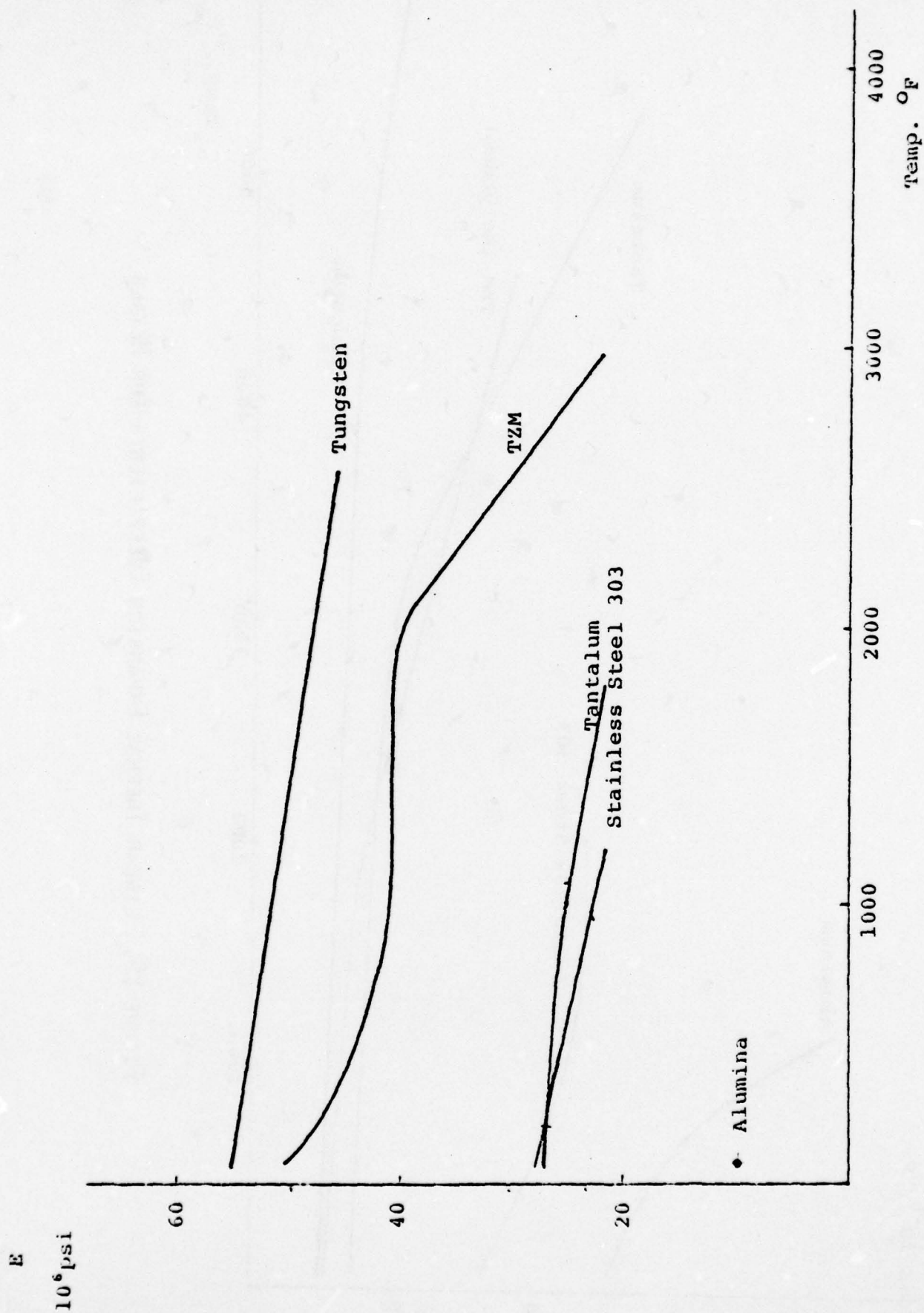


FIGURE E6. MODULUS OF ELASTICITY FOR VARIOUS METALS

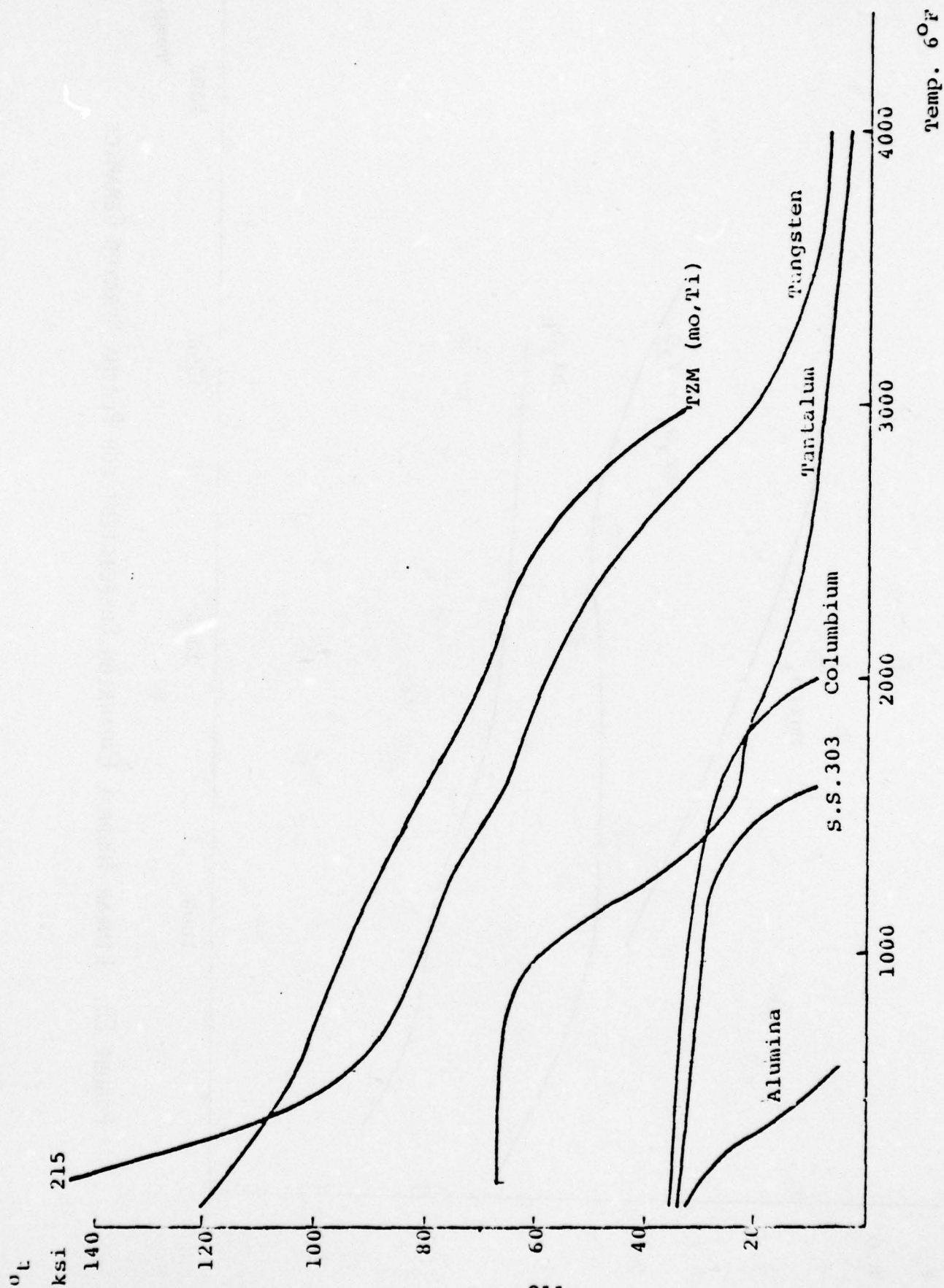


FIGURE E7. TENSILE STRENGTH FOR VARIOUS METALS

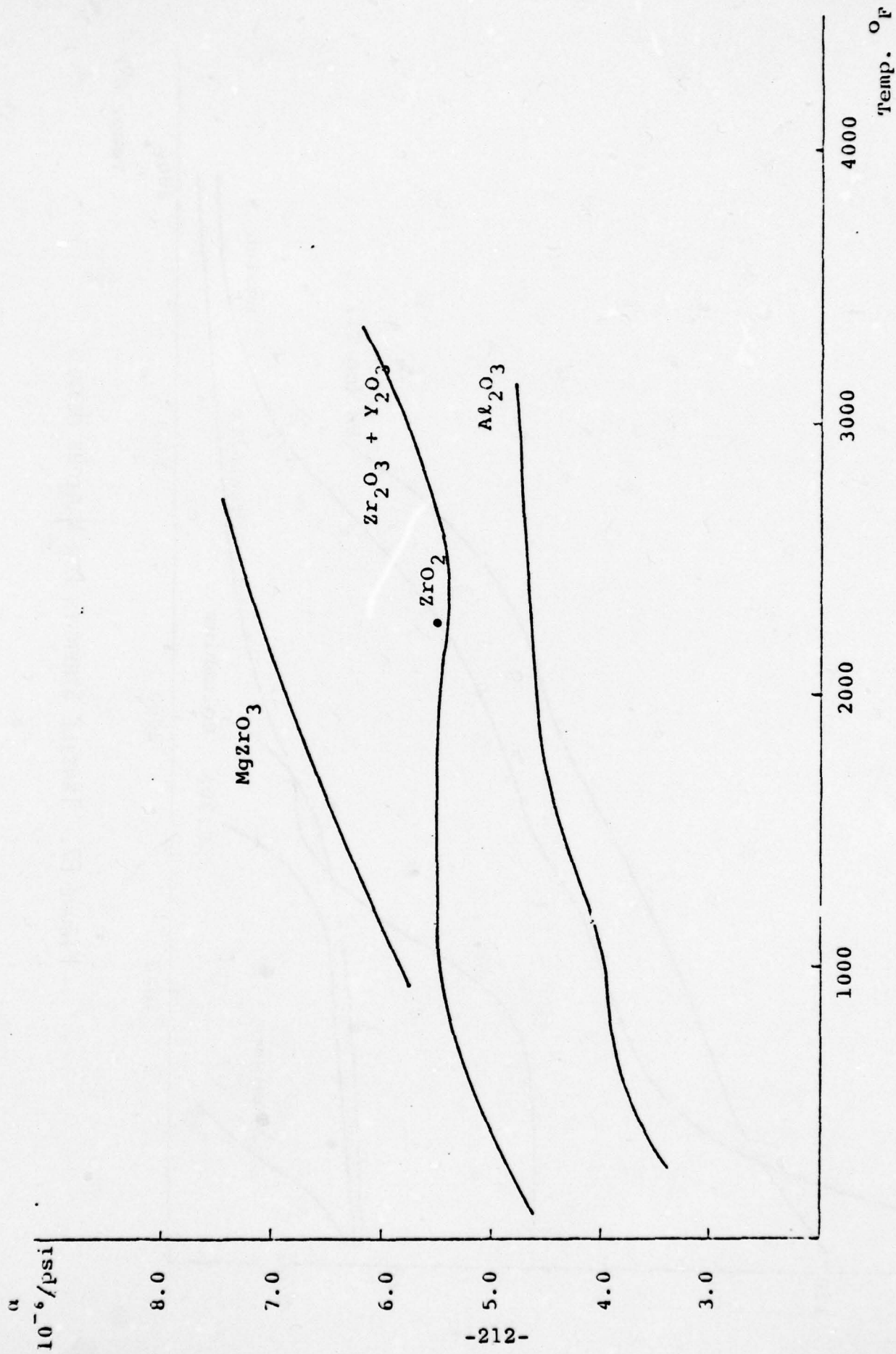


FIGURE E8. LINEAR THERMAL EXPANSION COEFFICIENT FOR PLASMA SPRAYED CERAMICS

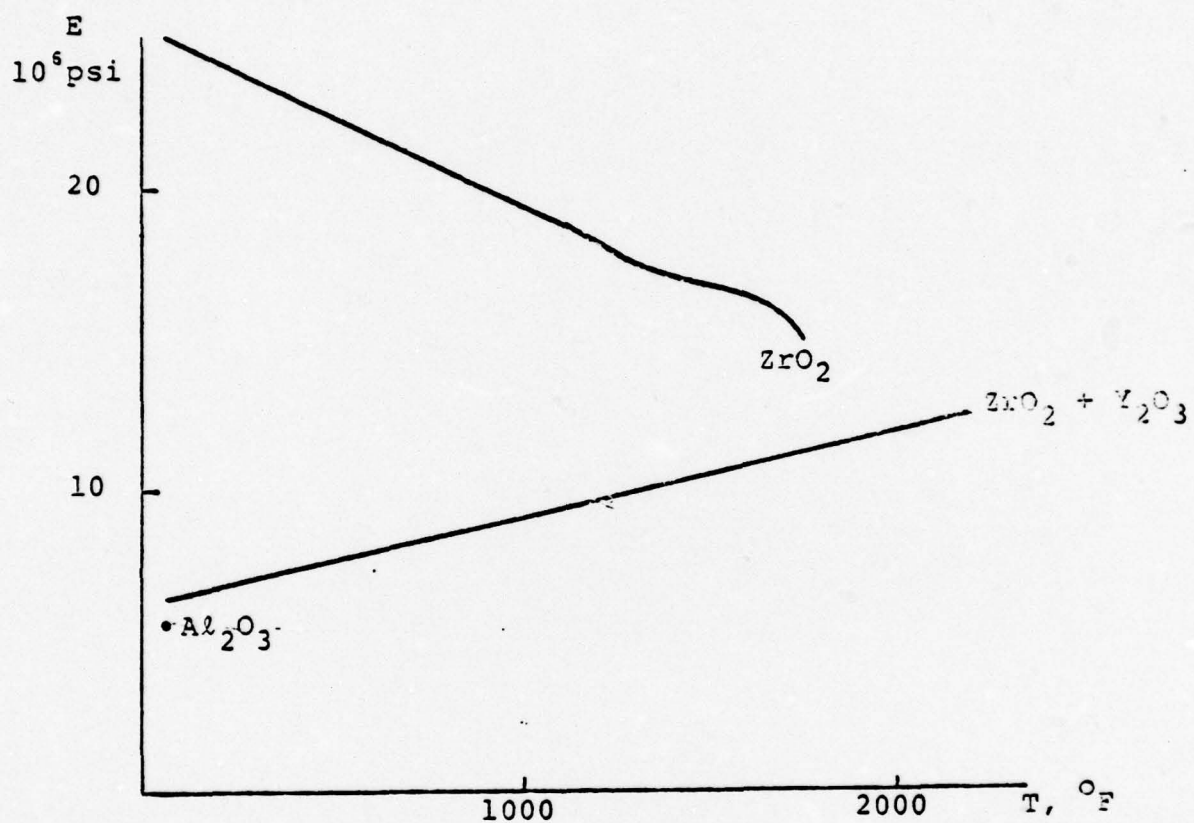


FIGURE E9. MODULUS OF ELASTICITY FOR PLASMA
SPRAYED MATERIALS

3.0 REFERENCES

- E1. Thermal Properties of Matter, Vol. 12 and 13. The TPRC Data Series, 1977.
- E2. Report FTD-78-181.
- E3. G.V. Samsonov, The Oxide Handbook, IFI/PHENUM, 1973
- E4. L.S. Marks, Standard Handbook for Mechanical Engineers, McGraw-Hill Co., 1967.
- E5. "Chart for ALSIMAG BRAND CERAMICS", 3M Co.
- E6. D.F. Taylor, "Tantalum and Tantalum Compounds"
- E7. "Refractory Metals", from Fansteel Metals/Torrance Plant.
- E8. P.W. Schilke, "Advanced Ceramic Seal Program (Phase 1)" Final Report, Naval Air Propulsion Test Center Report, AD-781-604.
- E9. D.B. Chevela, etc., "Porosity of Plasma-Sprayed Coatings" Soviet Powder Metallurgy and Metal Ceramics, No. 9, 1971.

APPENDIX F - THERMAL ANALYSIS RESULTS

A detailed thermal analysis of the ceramic coatings was made using the thermal model of Section 4.1, the material data of Appendix A, and the expected heating environment of the Thermal Radiation Simulator. The purpose of the analysis was to size the material specimens for the tests, to predict the materials expected performance in the tests, to provide temperature profiles for the structural analysis, and to parametrically investigate the effect of various material property and design variables.

The expected TRS environments used are shown in Figure F1. The radiation only environment has a maximum flux of $350 \text{ cal/cm}^2\text{-sec}$. When the specimen is exposed to the fireball, the maximum flux used is $1000 \text{ cal/cm}^2\text{-sec}$. Of this, $350 \text{ cal/cm}^2\text{-sec}$ is due to radiation, and the remainder is assumed to be due to a combination of convection and condensation of the gaseous aluminum oxide on the samples. Assuming a sample absorptivity of 0.2 the maximum flux input into the sample is then $0.2 \times 350 = 70 \text{ cal/cm}^2\text{-sec}$ radiation and $650 \text{ cal/cm}^2\text{-sec}$ convection/condensation. The fluence follows these same relationships.

The radiation only heating is what the samples protected by the pyrex glass should receive, while the total fireball heating is the maximum that the samples exposed to the fireball could receive. It was felt that these two heat profiles should define the lower and upper heating boundaries for sizing the samples and instrumentation. Also, the fireball heating is similar to the actual nuclear environment when the material has an absorptivity of 0.2 (80% of the nuclear heating would be reflected. This similarity is shown in

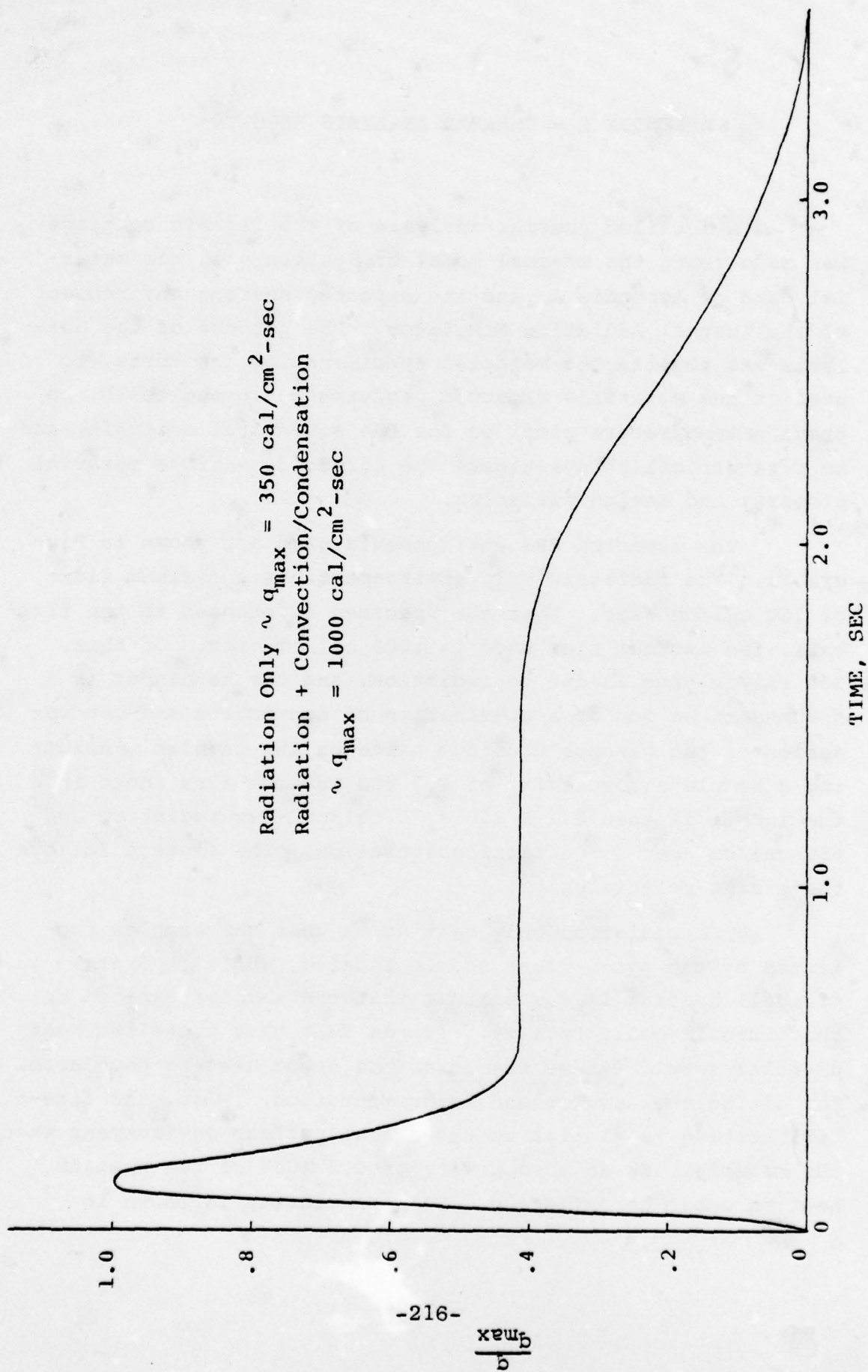


FIGURE F1. TRS HEAT FLUX ENVIRONMENT

in Figure F2 in which the heat received by the sample with an absorptivity of 0.2 is plotted for the two environments.

The thermal analysis was performed for both the alumina and zirconia coatings, with and without the silicone resin infiltrant. A schematic of the thermal model is shown in Figure F3. Parameters investigated include coating thickness, steel substrate thickness, and porosity. The effect of absorptivity was investigated using the nuclear environment (presented in Section 4.1.1.2) and using the solar furnace environment (presented in Section 4.4.3).

The maximum coating surface temperature, maximum interface temperature, and maximum substrate backface temperatures calculated are presented in Table A1 for the various models considered. All cases used a surface absorptivity and emissivity of 0.2.

Examples of the in-depth temperature profiles and surface recessions calculated are presented in Figures F4, F5, and F6 for .06 inch alumina, .09 inch alumina, and .06 inch zirconia coatings respectively, exposed to the fireball environment.

As indicated in Figures F4-F6, the ceramic coating surface heats to its melt temperature immediately and the surface begins to recede. The in-depth temperature profiles show the temperatures in the material as a function of time. As the surface recedes, the origin of the coordinate system follows the receding surface, so that the 0.0 on the abscissa is always at the new material surface.

The alumina and zirconia behave quite similarly thermally, except the zirconia has a higher melt temperature. Comparing cases 6 to 16 and 8 to 18, the recession for each is similar. The steel substrate temperature is a little

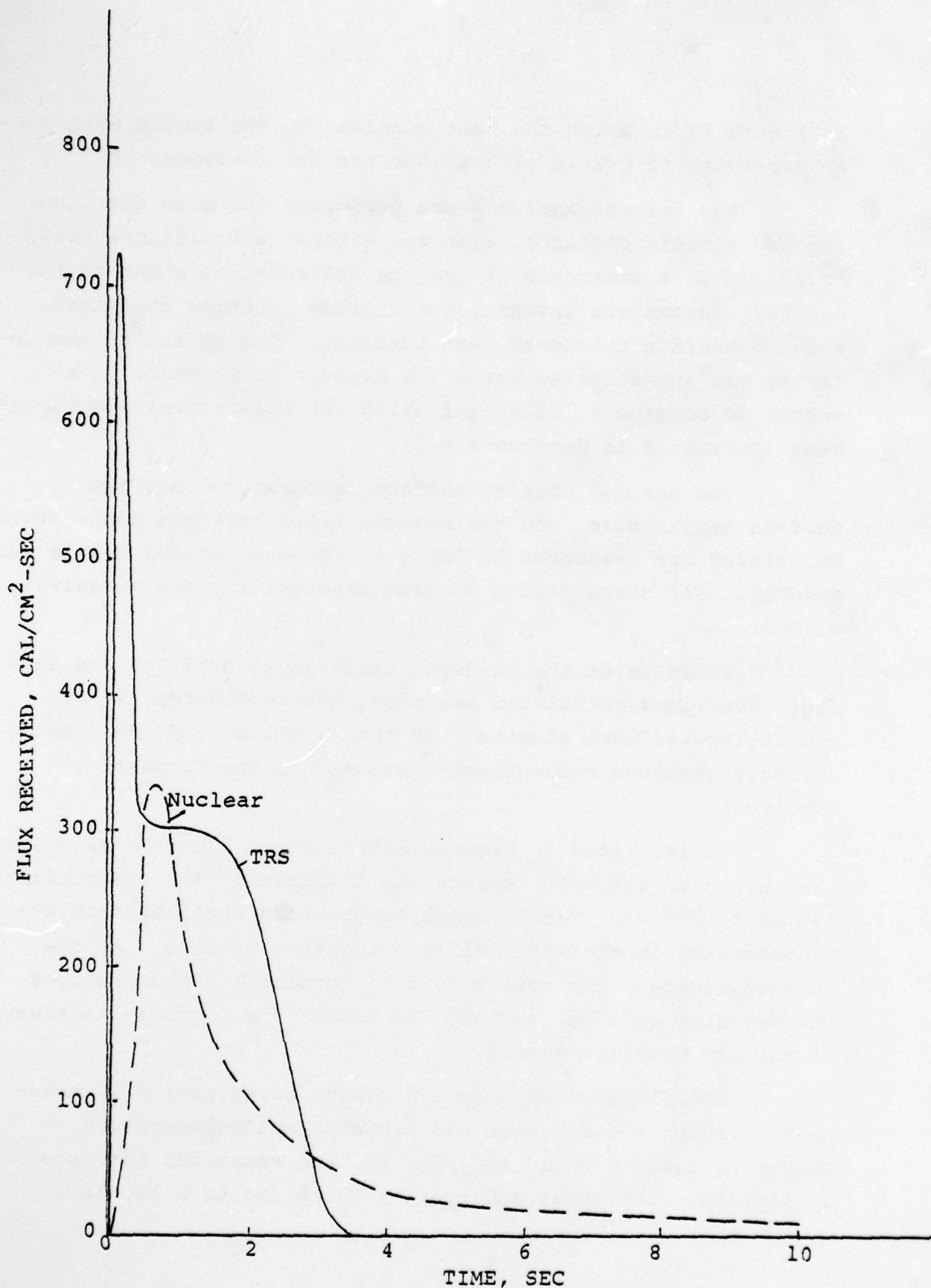


FIGURE F2. TRS vs NUCLEAR BURST THERMAL FLUX AS RECEIVED
BY A MATERIAL WITH AN ABSORPTIVITY OF 0.2

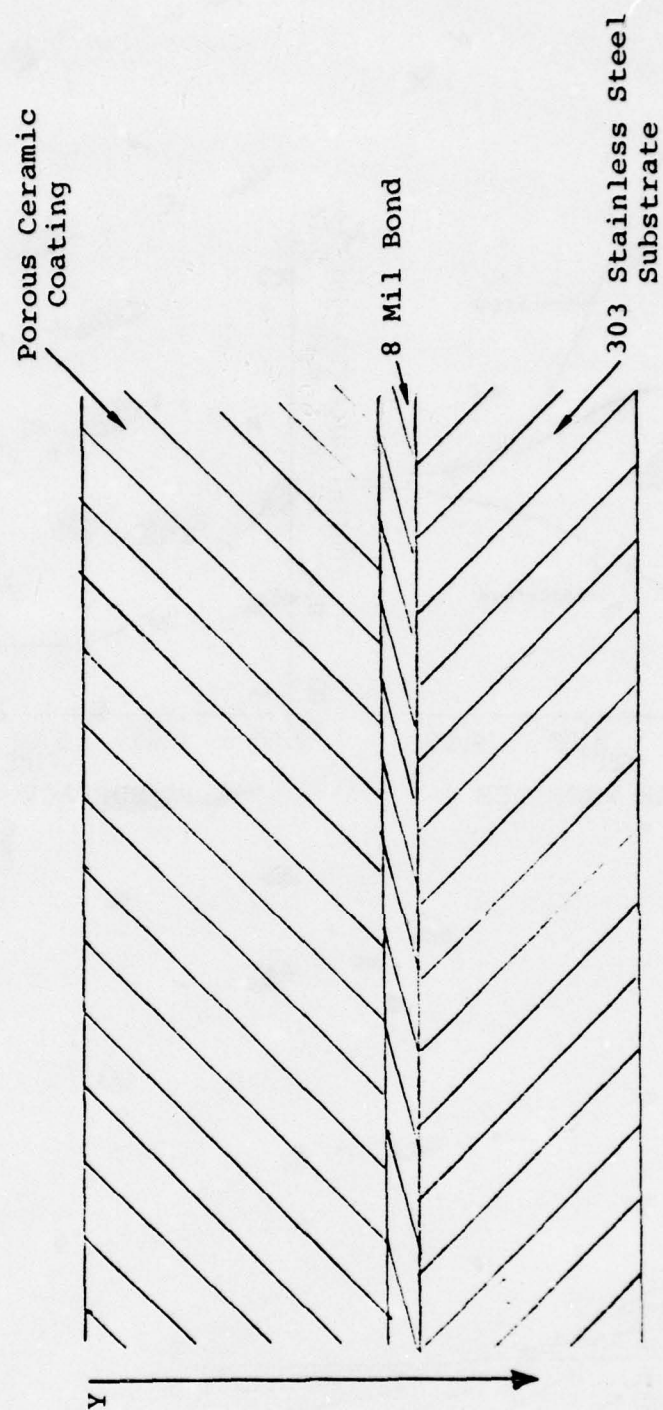


FIGURE F3. THERMAL MODEL SCHEMATIC

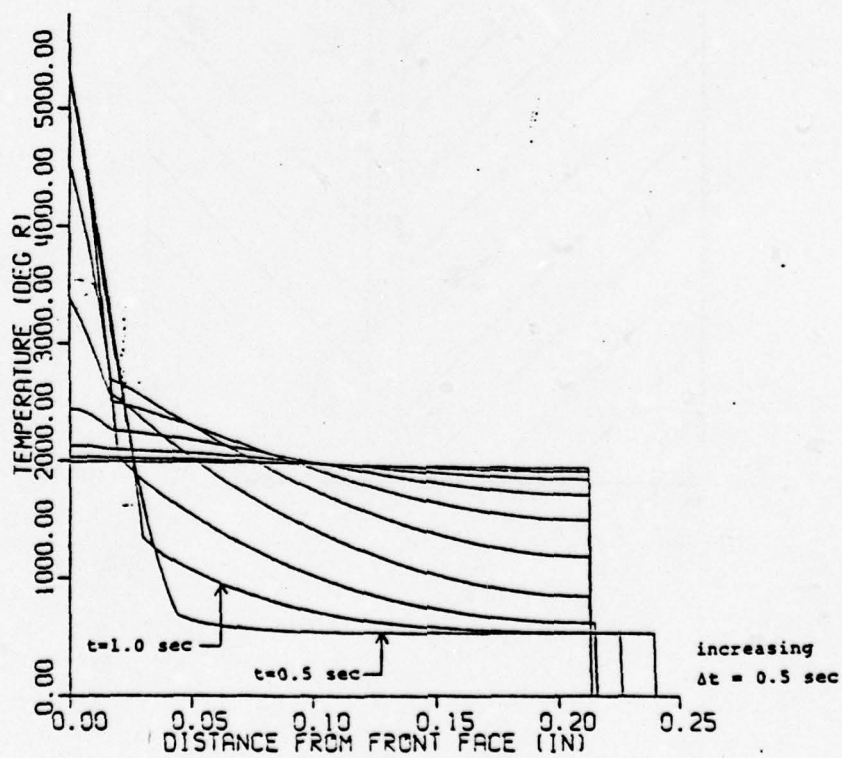
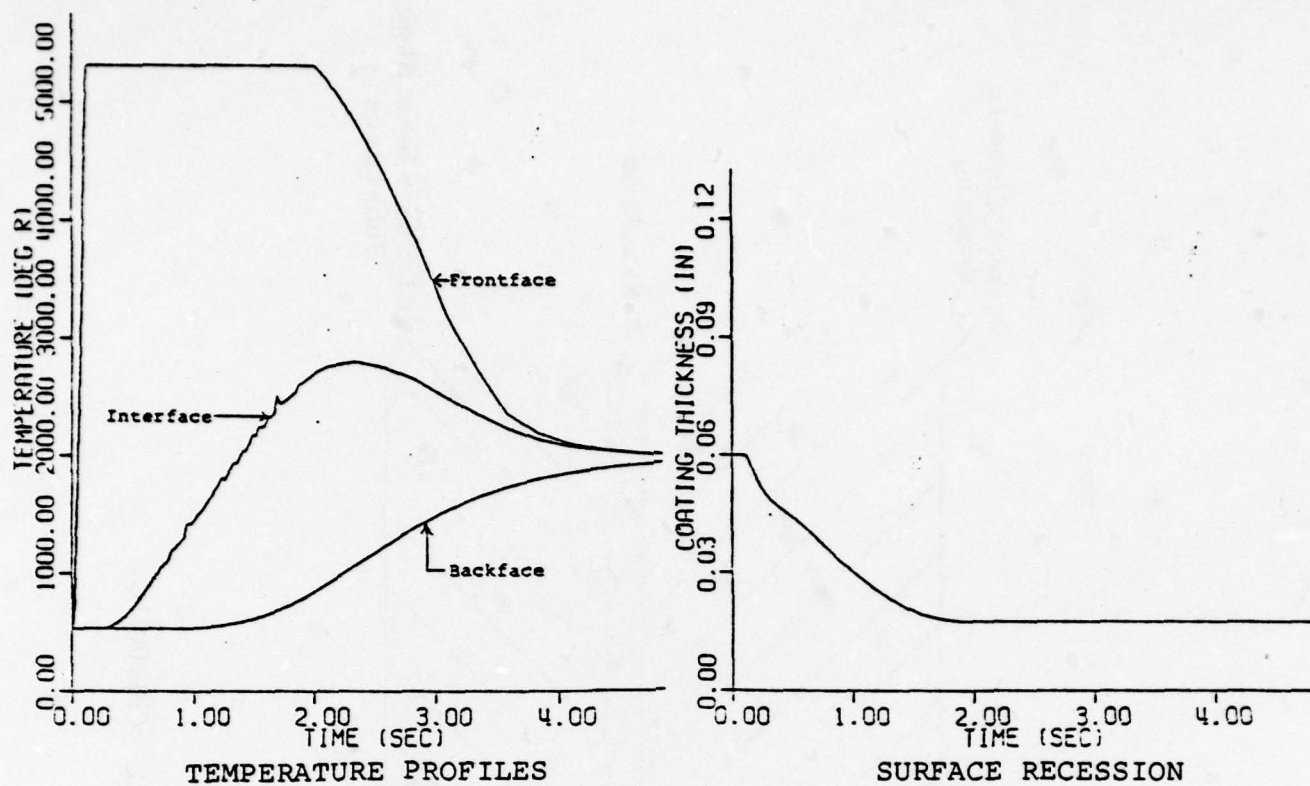


FIGURE F4, 0.060 INCH ALUMINA ON 0.1875 INCH STAINLESS
STEEL EXPOSED TO TRS FIREBALL

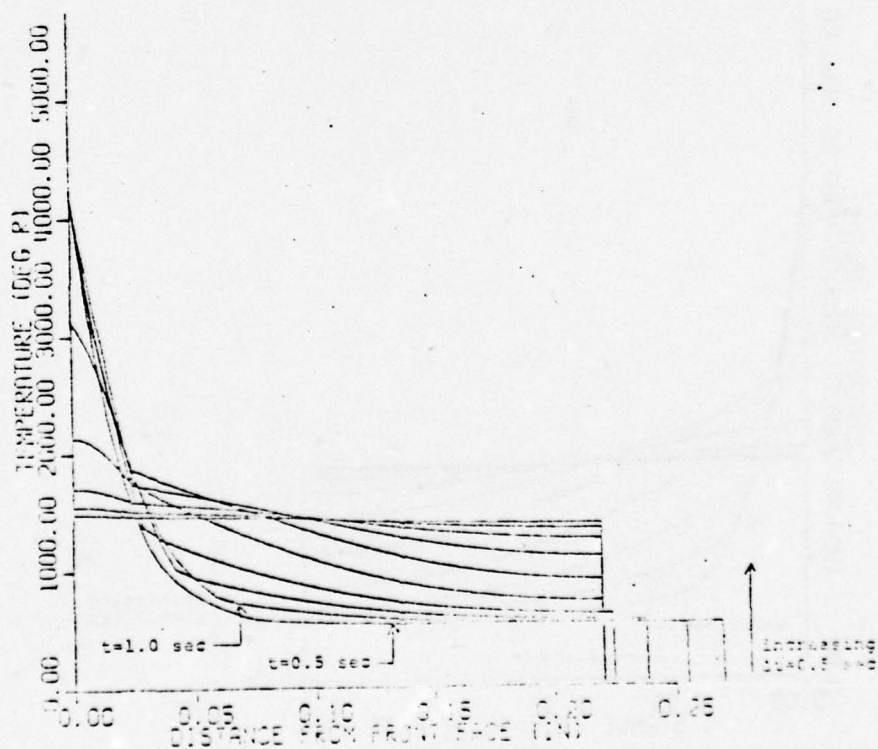
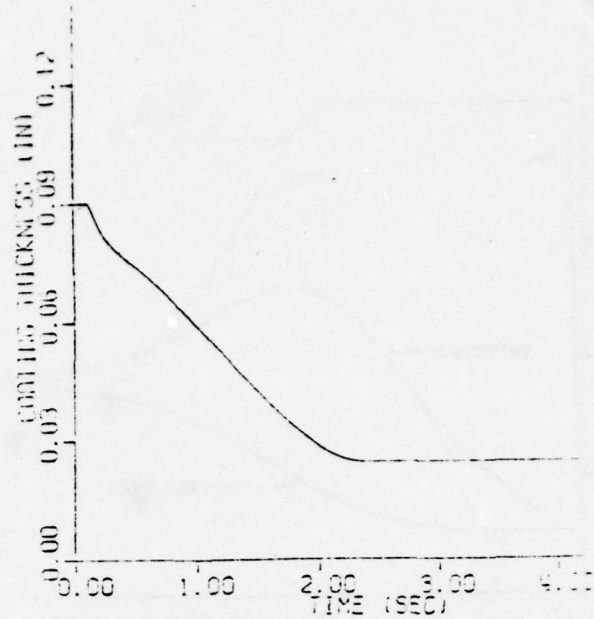
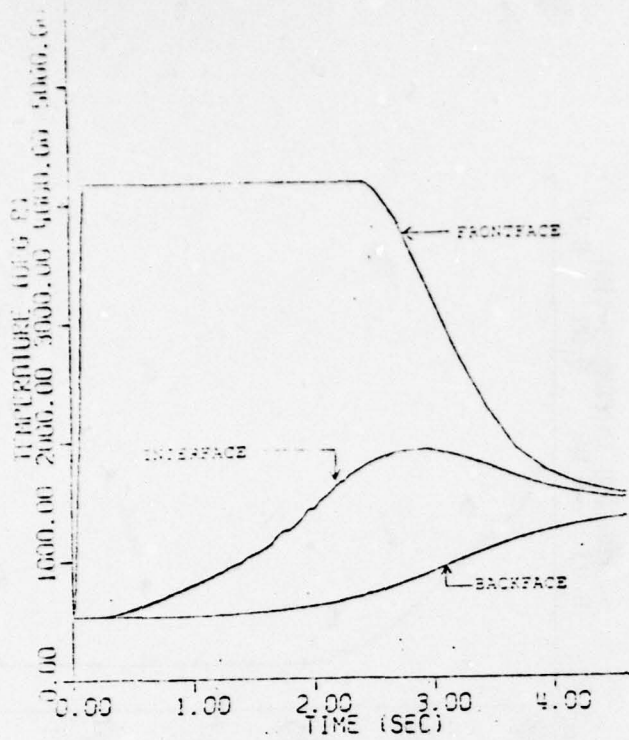
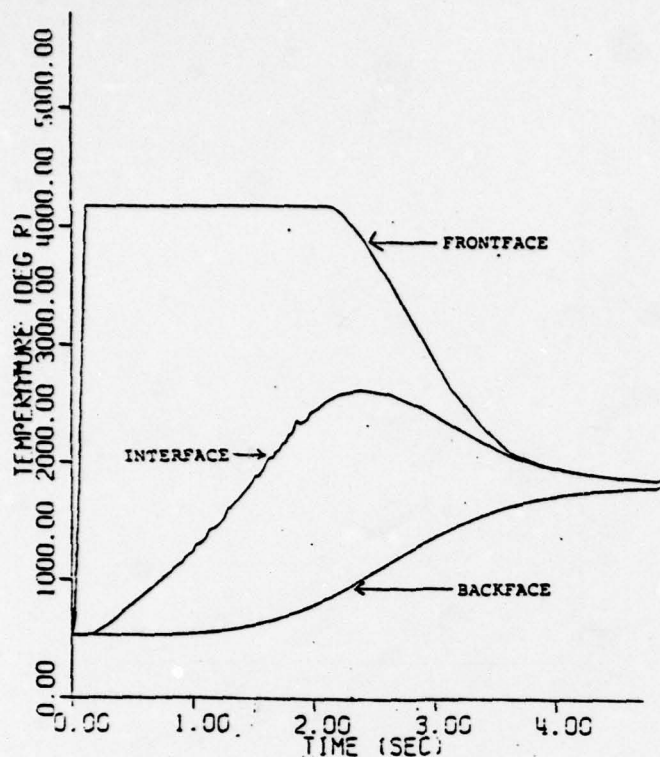
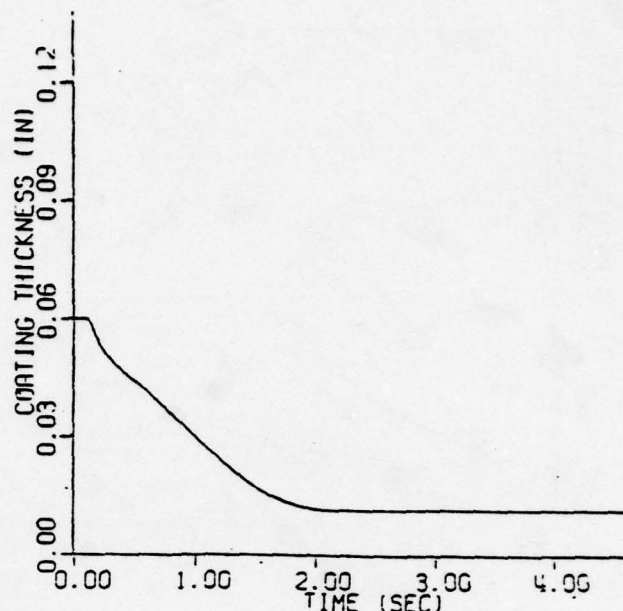


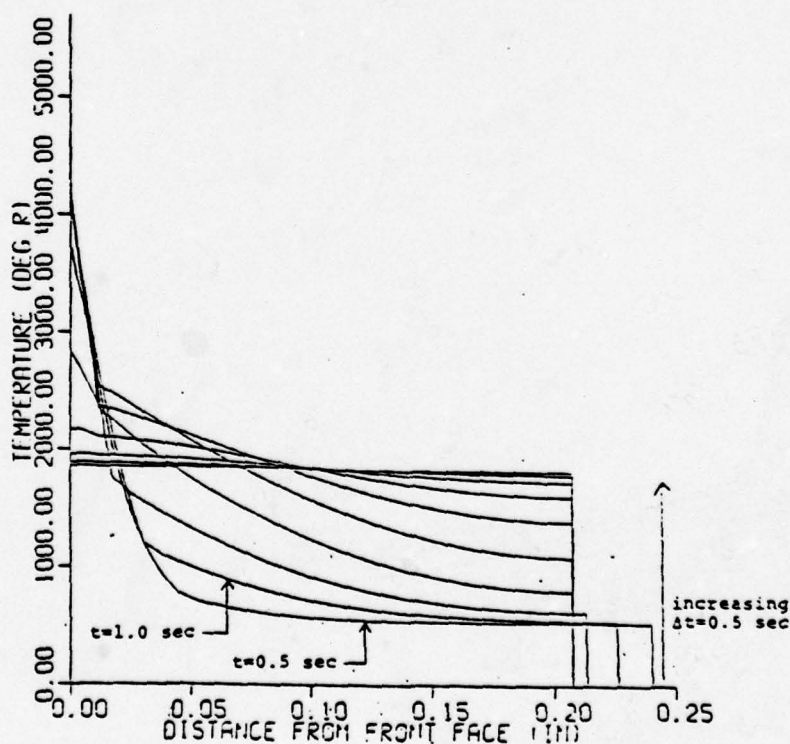
FIGURE F5. 0.090 INCH ALUMINA ON 0.1875 INCH STAINLESS STEEL EXPOSED TO THE TRS FIREBALL



TEMPERATURE PROFILES



SURFACE RECESSION



IN-DEPTH TEMPERATURE PROFILES

FIGURE F6. 0.060 INCH ZIRCONIA ON 0.1875 INCH STAINLESS STEEL
EXPOSED TO TRS FIREBALL

TABLE F1. NON-INFILTRATED CERAMIC COATINGS THERMAL RESPONSE

CASE	MATERIAL	HEAT FLUX ENVIRONMENT	CERAMIC THICKNESS (INCHES)	SS THICKNESS (INCHES)	POROSITY (PERCENT)	MAXIMUM TEMPERATURE (°R)			RECESSION DEPTH (INCHES)
						FRONTFACE	INTERFACE	BACKFACE	
1	Al ₂ O ₃	R (1)	.060	.1	15	1501	901	889	0
2	"	R	.060	.1875	15	1495	833	733	0
3	"	R	.060	.25	15	1496	829	660	0
4	"	R	.09	.1875	15	2563	769	674	0
5	"	R	.060	.1875	0 (bulk)	1052	856	752	0
6	"	R+C (2)	.060	.1875	15	4173	2612	1814	.0486
7	"	R+C	.060	.25	15	4173	2624	1466	.0486
8	"	R+C	.09	.1875	15	4173	1909	1377	.0656
9	"	R+C	.09	.25	15	4173	1909	1100	.0656
10	ZrO ₂	R	.060	.1	12	2075	896	861	0
11	"	R	.060	.1875	12	2081	814	702	0
12	"	R	.060	.25	12	2074	784	632	0
13	"	R	.06	.1875	12	3600	1135	921	0
14	"	R	.06	.1875	24	2254	820	705	0
15	"	R	.09	.1875	12	2116	732	620	0
16	"	R+C	.060	.1875	12	5310	2774	1940	.0424
17	"	R+C	.060	.25	12	5310	2778	1555	.0424
18	"	R+C	.09	.1875	12	5310	2126	1483	.0633
19	"	R+C	.09	.25	12	5310	2161	1182	.0633

(1) Radiation only environment, 350 cal/cm²-sec incident, 70 cal/cm²-sec absorbed

(2) Radiation plus convection/condensation

higher for the zirconia. Even though the zirconia would re-radiate away more heat, its lower thermal mass appears to amount for this higher substrate temperature.

Considering the coating thickness effects, comparing cases 6 to 8 and 16 to 18, the thicker coating exhibits more ablation. The thinner coating is less of an insulator and permits more of the heat to be conducted into the steel substrate during the ablation and the melting of the surface ceases at an earlier time during the exposure. Of course, even though the thicker material ablates more, it still has more material remaining after the exposure. Hence, the thicker coatings may be necessary.

Considering the steel substrate thickness, the steel acts as a thermal heat sink with a very low temperature gradient. The thicknesses considered, .1875 and 0.25 inches for the ablating cases, have sufficiently large thermal masses that the more resistive ceramic coating behaves independently of the steel substrate. This can be seen by comparing cases 6 to 7 and 8 to 9. The steel temperature varies according to its thermal mass.

The effect of changing the porosity in the non-infiltrated coatings effectively changes the conductivity and thermal mass. This is shown by comparing case 2 to case 5. In case 5 the higher conductivity of bulk material and its higher mass was used. Heat is conducted through the coating faster, and the coating absorbs more heat at a given temperature, resulting in a lower coating surface temperature. Case 5 has a slightly higher steel temperature, due to less heat being reradiated away at the ceramic surface.

Next, the effect of the silicone resin was investigated. The results are summarixed in Table F2 in which the case numbers correspond to the non-infiltrant cases discussed earlier.

TABLE F 2. COMPARISON OF PERFORMANCE WITH AND WITHOUT RESIN

CASE	MATERIAL	BACKFACE TEMP WITH RESIN	BACKFACE TEMP WITHOUT RESIN	RECESSION WITH RESIN	RECESSION WITHOUT RESIN
1	Al ₂ O ₃	874	889	0	0
2	"	723	733	0	0
4	"	663	674	0	0
6	"	1671	1814	.046	.0485
8	"	1246	1377	.057	.0656
10	ZrO ₂	850	861	0	0
11	"	687	702	0	0
15	"	609	620	0	0
16	"	1702	1940	.041	.0424
18	"	1324	1483	.056	.0633

Considering the low level heating of the TRS radiation only environment, the temperatures do not get high enough over a sufficient length of time to cause resin decomposition. The effects on temperature are negligible and only due to the resin's effect on conductivity and thermal mass.

At the high level heating environment, the resin decomposes and reduces the ceramic ablation and gives a somewhat reduced steel substrate temperature. By comparing Case 8 to 6, it can be seen that the thicker coating, .090 inch in Case 8, which thus contains more infiltrant, has a greater reduction in ablation. However, the resin effects are small as there is still significant ablation. The resin is much less effective in this radiation environment than in a convective environment, such as high speed flight, where blowing due to the decomposing resin aids the reduction in heat transfer.

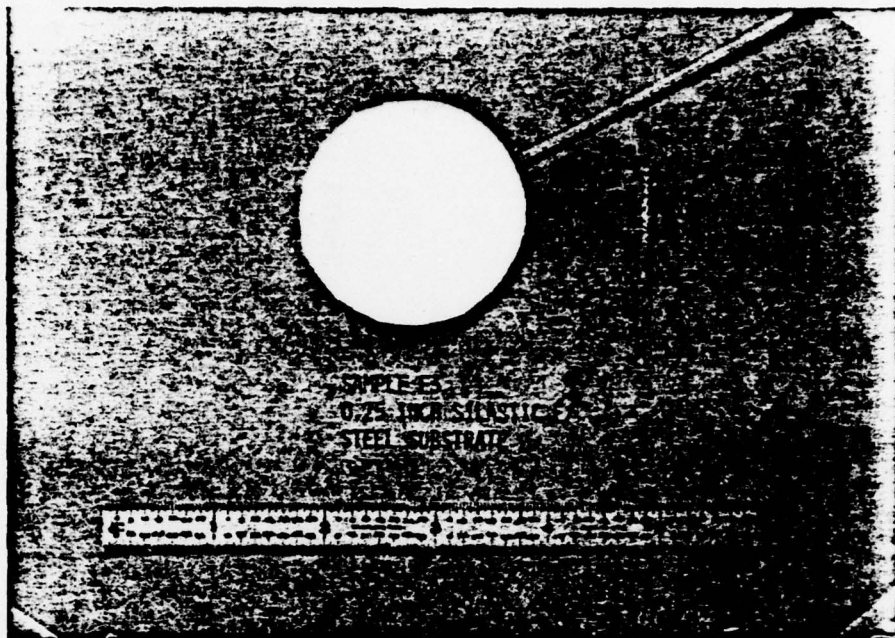
APPENDIX G - FRENCH SOLAR TEST DATA

This appendix contains the French Solar Furnace Test data. Table G1 presents the samples pre-test and post-test dimensional and mass data. Figures G1 through G6 present the pre-test and post-test photos of each sample. Figures G7 through G12 present the measured front face and back face temperatures. The instrumentation and temperatures are discussed in Section 4.4.

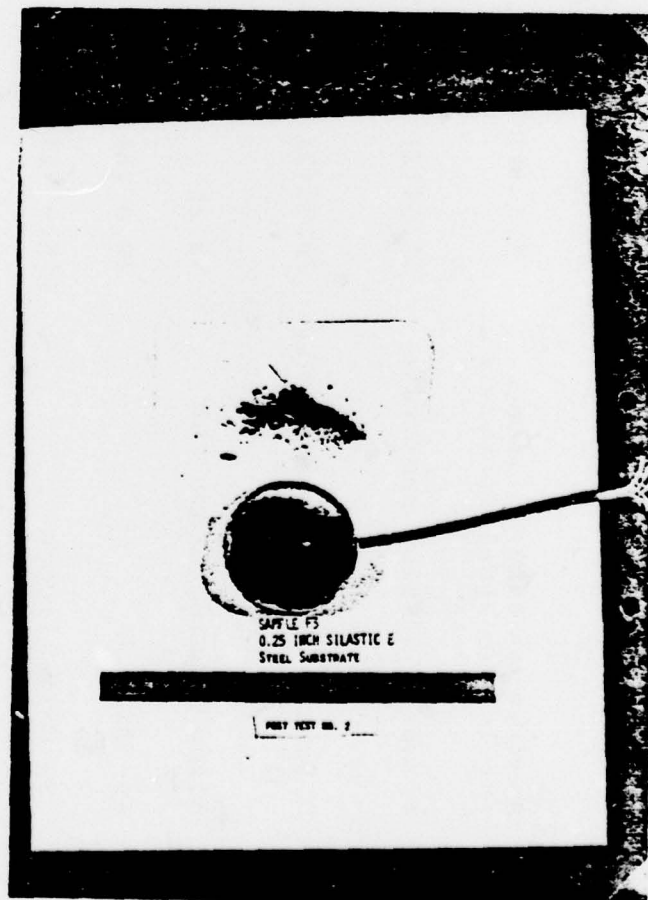
TABLE G1. SAMPLE DIMENSION AND WEIGHT DATA

Sample	Pre-test		Post-test		Remarks
	Weight (grams)	Thickness (inches)	Weight (gross)	Thickness (inches)	
F2 - Alumina coating/silicone infiltrant/steel substrate	117.9 (1)	0.118	96.5 (1)	-	Weight contains coating chips. Steel melted.
F3 - Silastic E/steel substrate	64.64 (2)	0.364	57.16 (2)	.24-.26 (2, 3)	
				.066 (4)	
F4 - Silastic E/steel substrate	79.55 (2)	0.643	71.5 (2)	.47-.49 (2, 3)	
				.09 (4)	
F8 - Boron Nitride, Grade HBR	52.21	0.500	46.3	0.510	Small pieces spalled off
F9 - AS-3DX	22.0 (5)	0.249	21.3	.03-.245	Melted nearly through on one side
F16 - Spinel/silicone infiltrant/steel	115.9 (1)	0.213	86.1 (1)	-	Weight contains coating chips. Steel melted

- (1) Weight and dimension includes .25 inch steel substrate
- (2) Weight and dimension includes .125 inch steel substrate
- (3) Char not included
- (4) Char layer
- (5) Weighed on scale with questionable accuracy

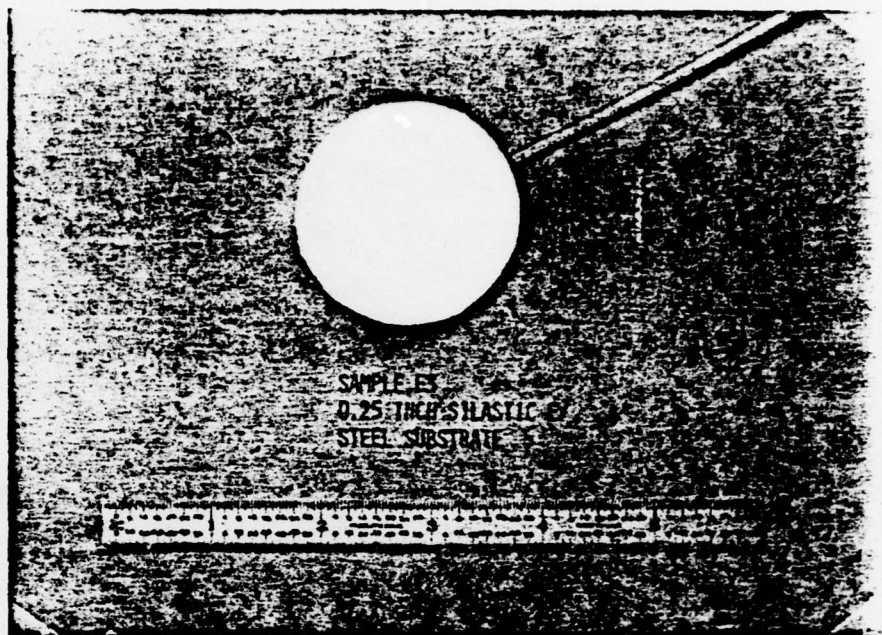


PRE-TEST

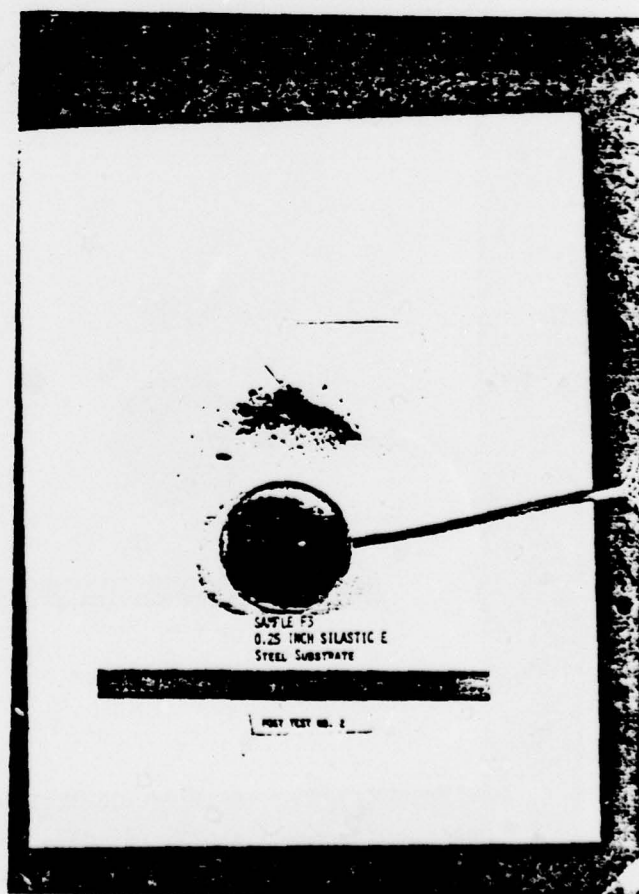


POST-TEST

FIGURE G1. ALUMINA COATING/SILICONE INFILTRANT, SAMPLE F2
-229-

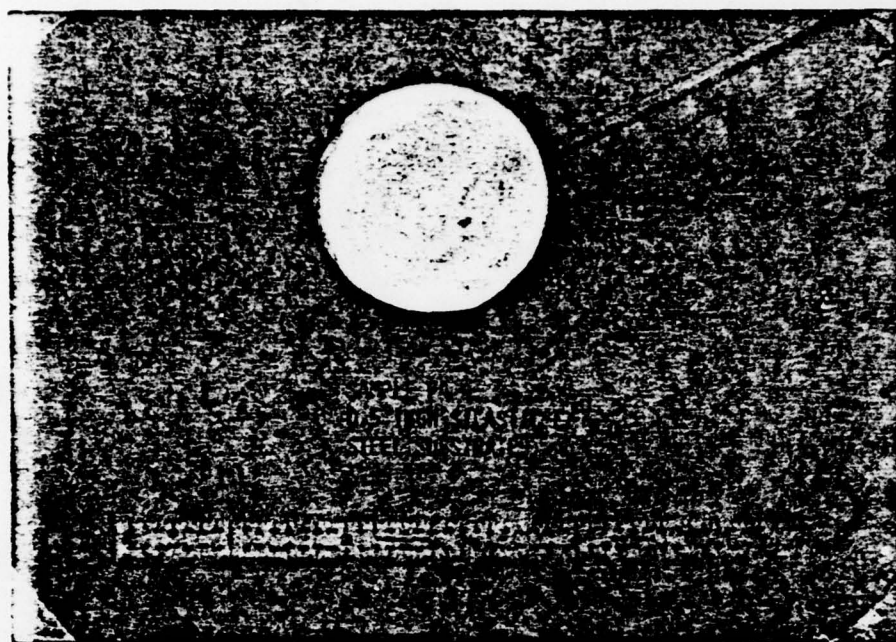


PRE-TEST

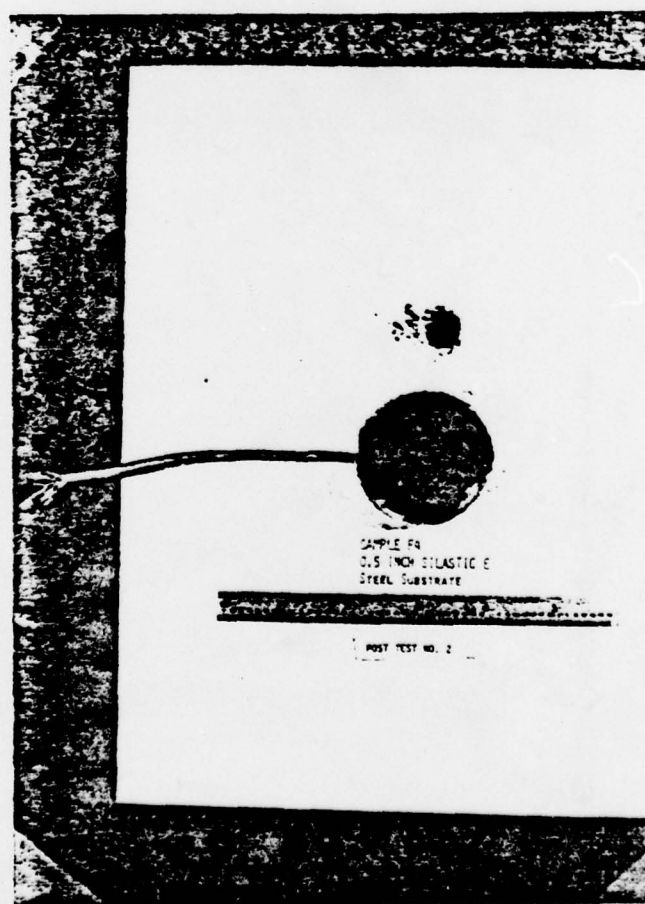


POST-TEST

FIGURE G2. 0.25 INCH SILASTIC E, SAMPLE F3
-230-

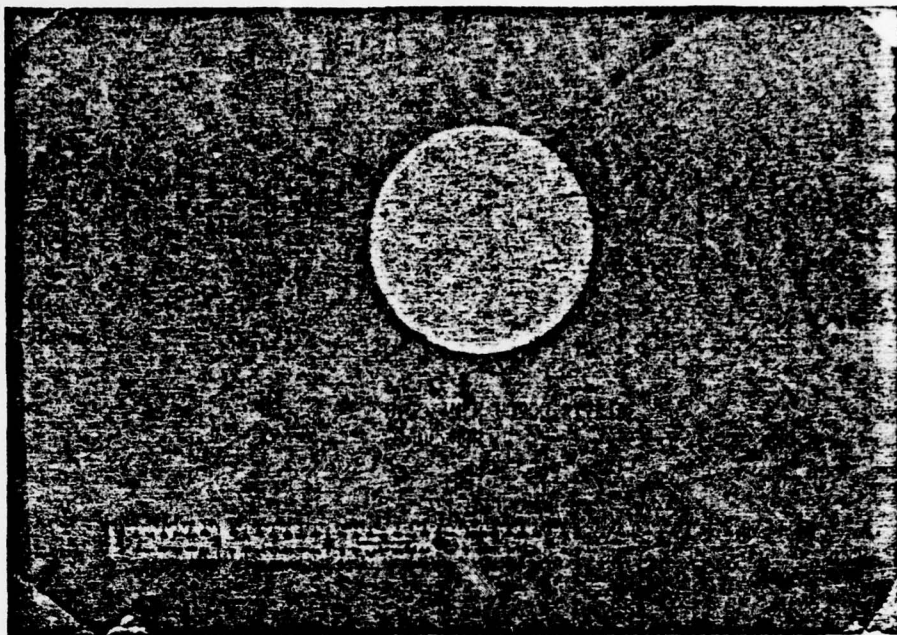


PRE-TEST

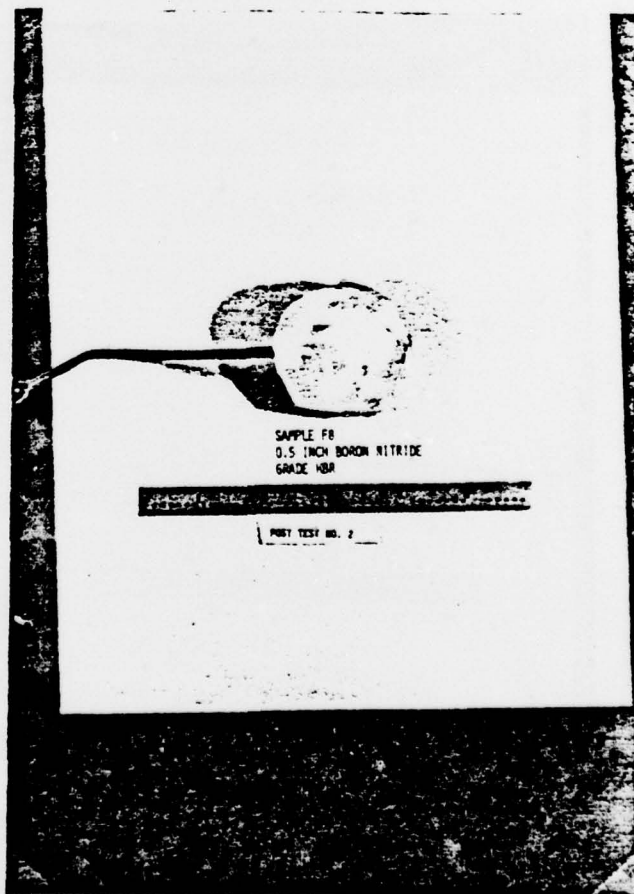


POST-TEST

FIGURE G3. 0.5 INCH SILASTIC E, SAMPLE F4
-231-

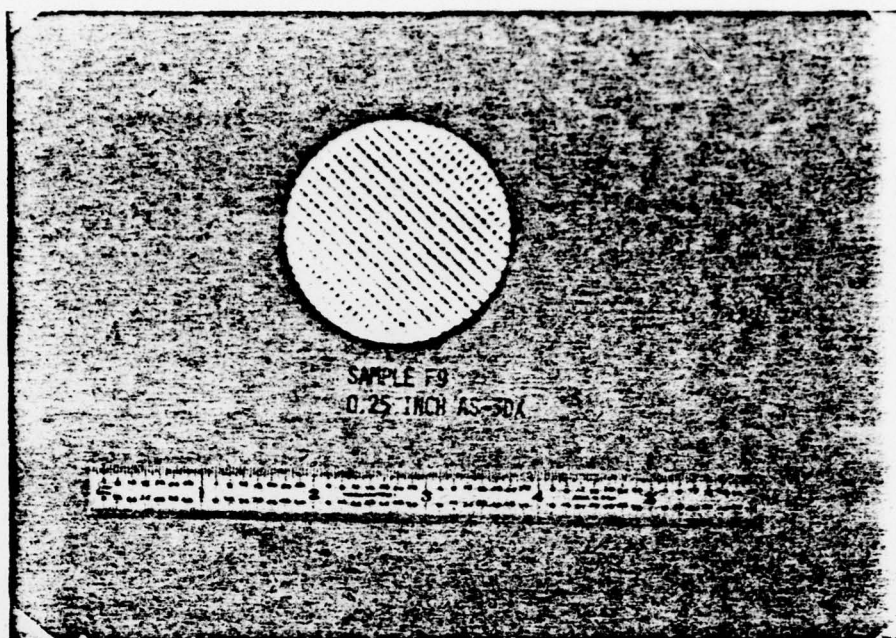


PRE-TEST

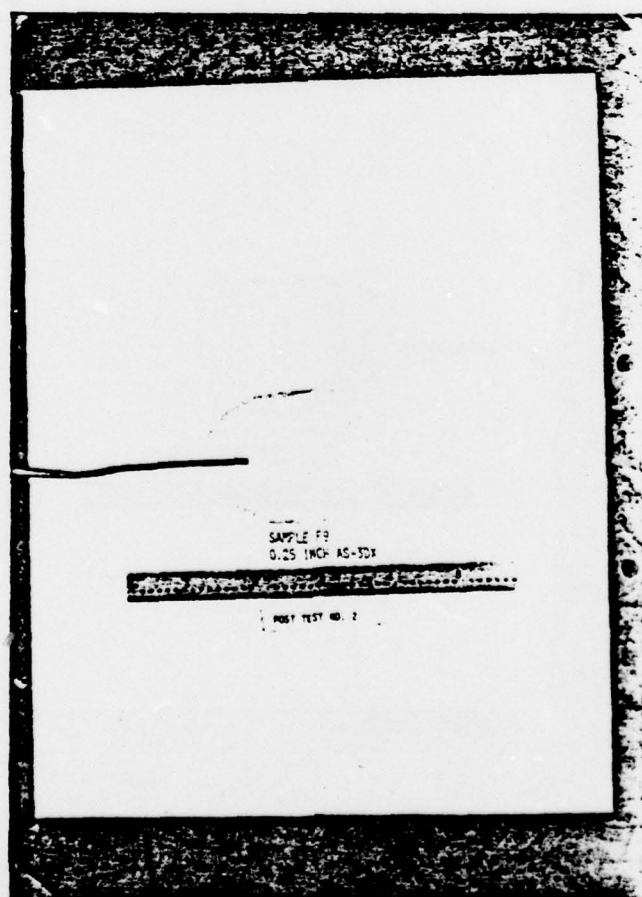


POST-TEST

FIGURE G4. BORON NITRIDE (HBR), SAMPLE F8
-232-

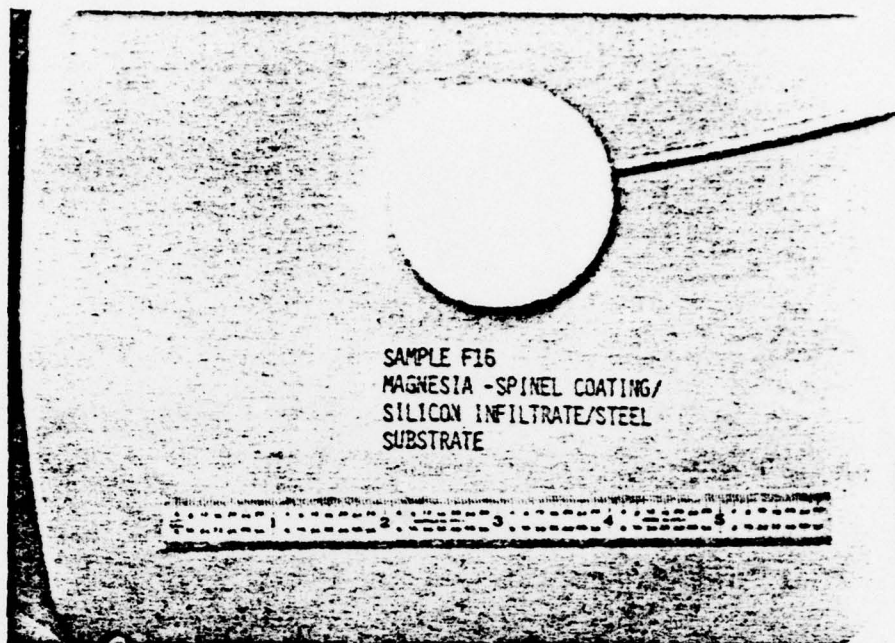


PRE-TEST

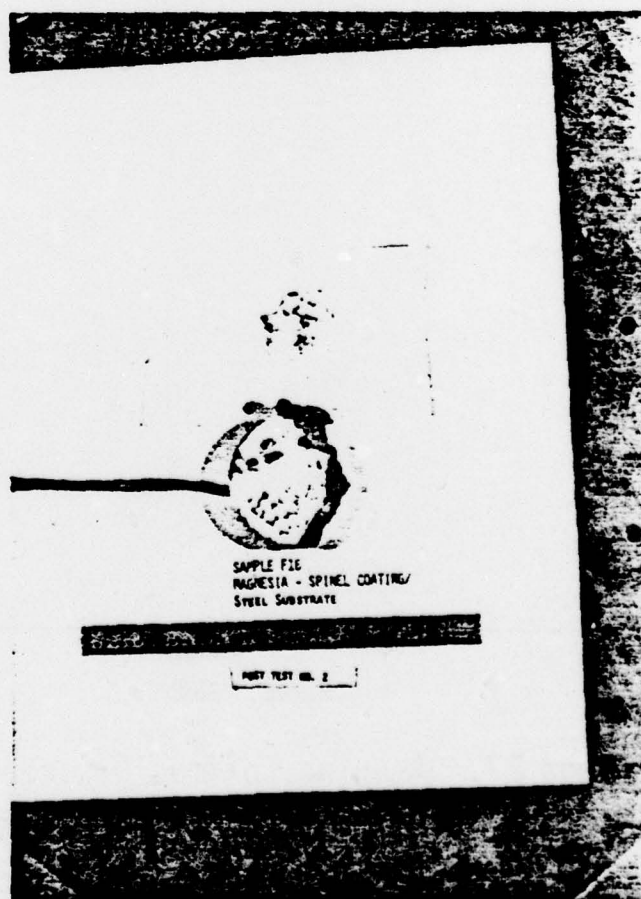


POST-TEST

FIGURE G5. AS-3DX, SAMPLE F9
-233-



PRE-TEST



POST-TEST

FIGURE G6. MAGNESIA-SPINEL COATING/SILICONE INFILTRANT, SAMPLE F16
-234-

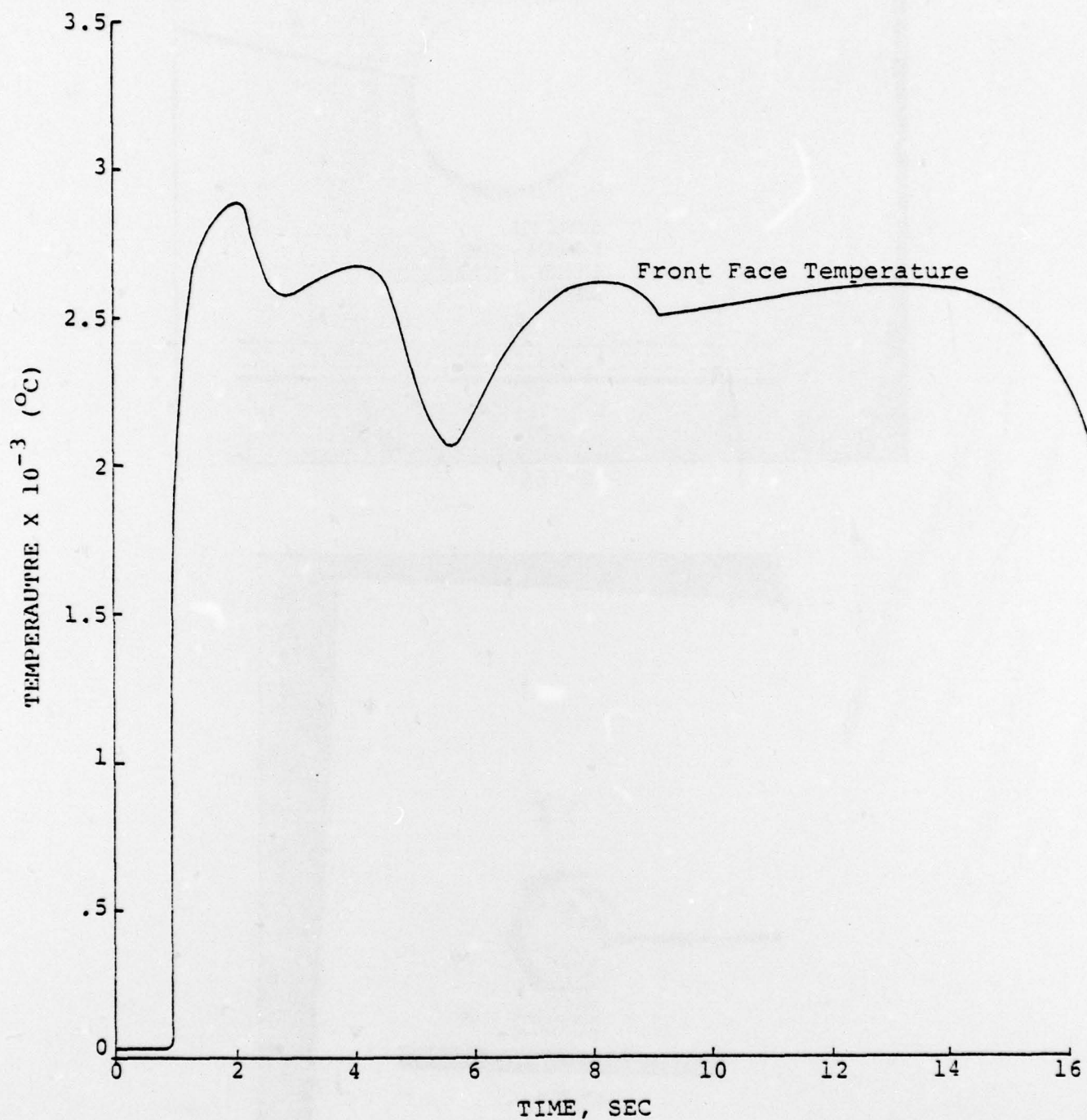


FIGURE G7. ALUMINA COATING/SILICONE INFILTRANT,
SAMPLE F2, TEMPERATURE RESPONSE

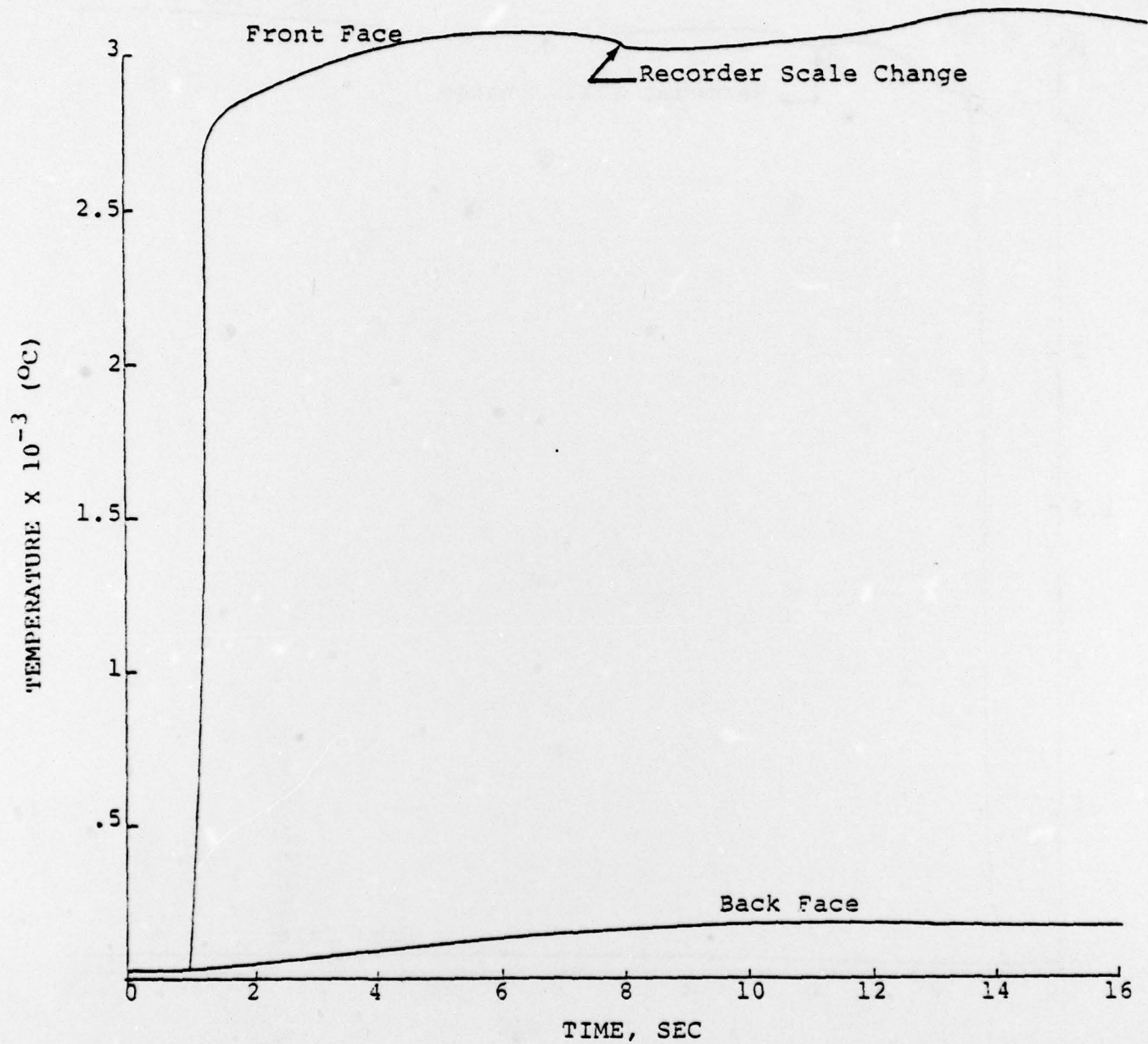


FIGURE G8. 0.25 INCH SILASTIC E/STEEL, SAMPLE F3,
TEMPERATURE RESPONSE

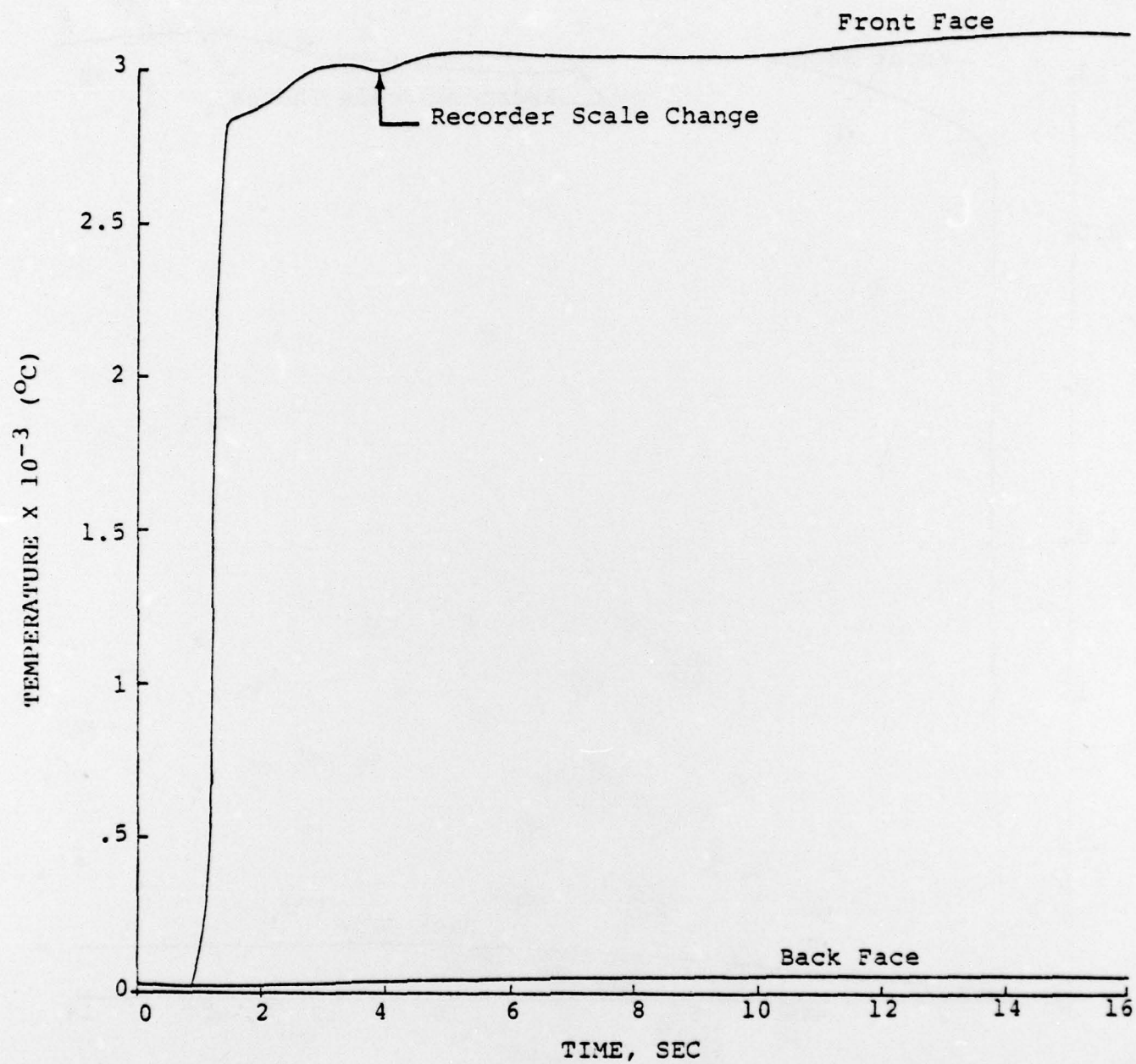


FIGURE G9. 0.5 INCH SILASTIC E/0.125 INCH STEEL, SAMPLE F4,
TEMPERATURE RESPONSE

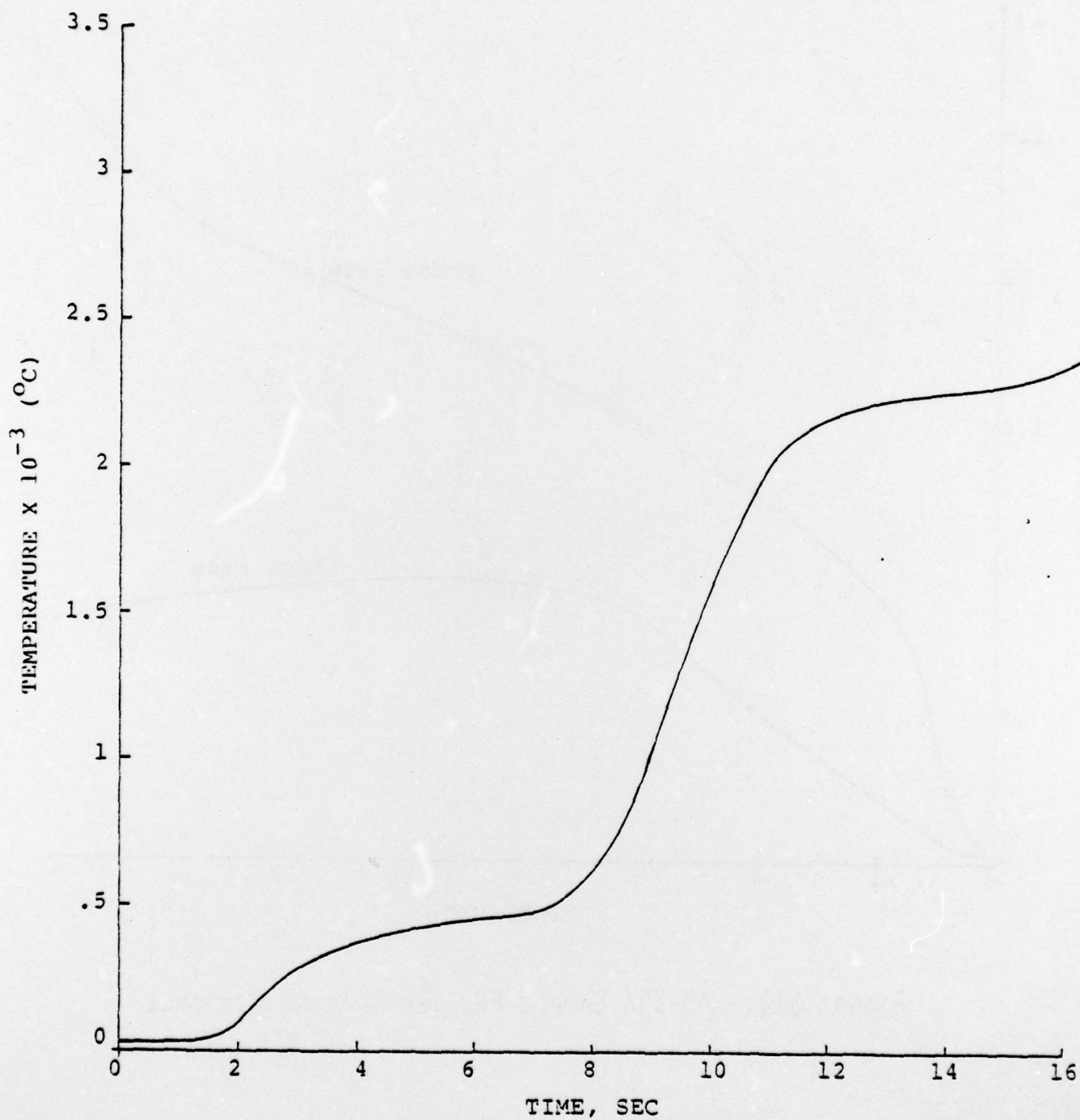


FIGURE G10. BORON NITRIDE, SAMPLE F8, TEMPERATURE RESPONSE

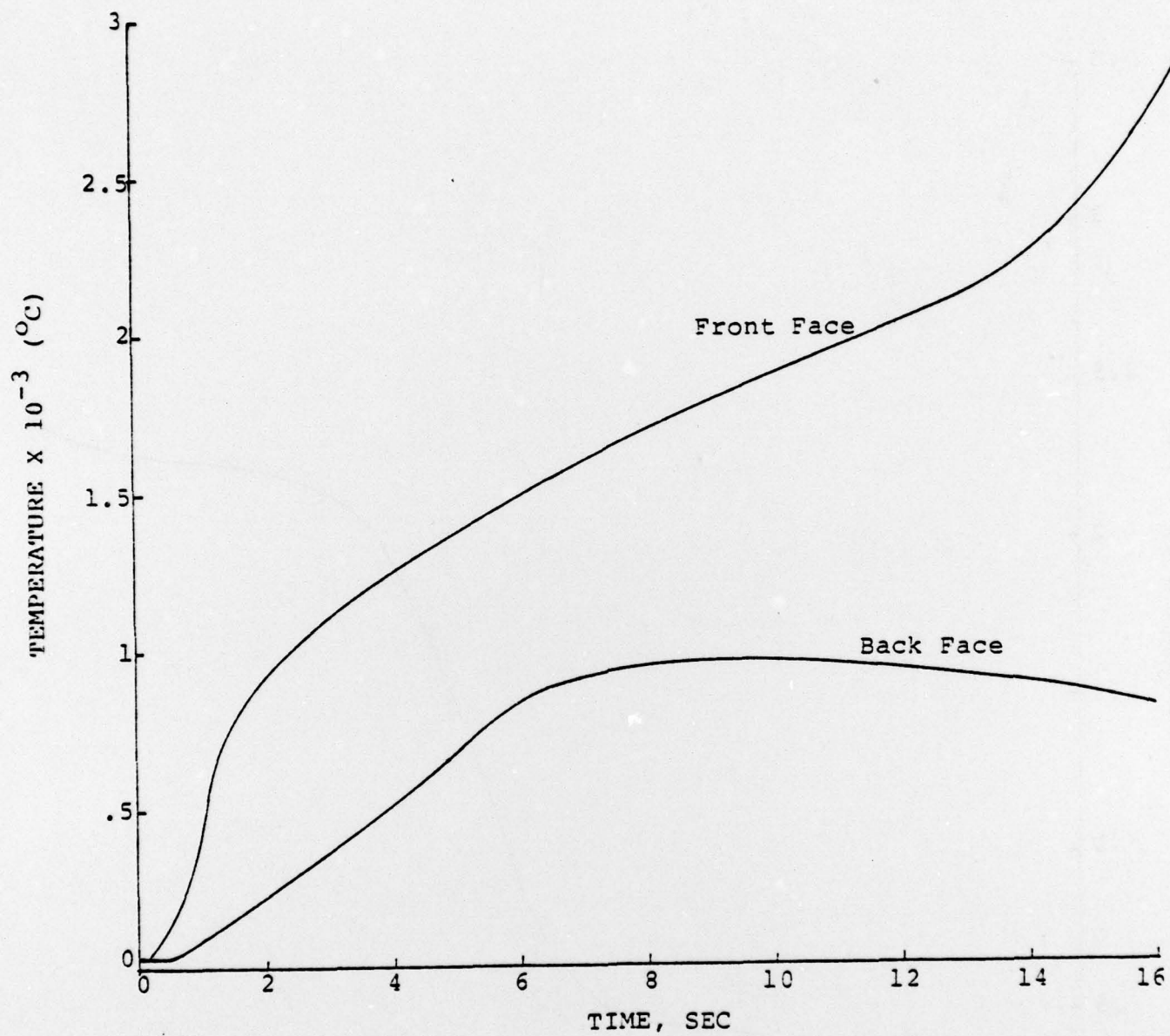


FIGURE G11. AS-3DX SAMPLE F9, TEMPERATURE RESPONSE

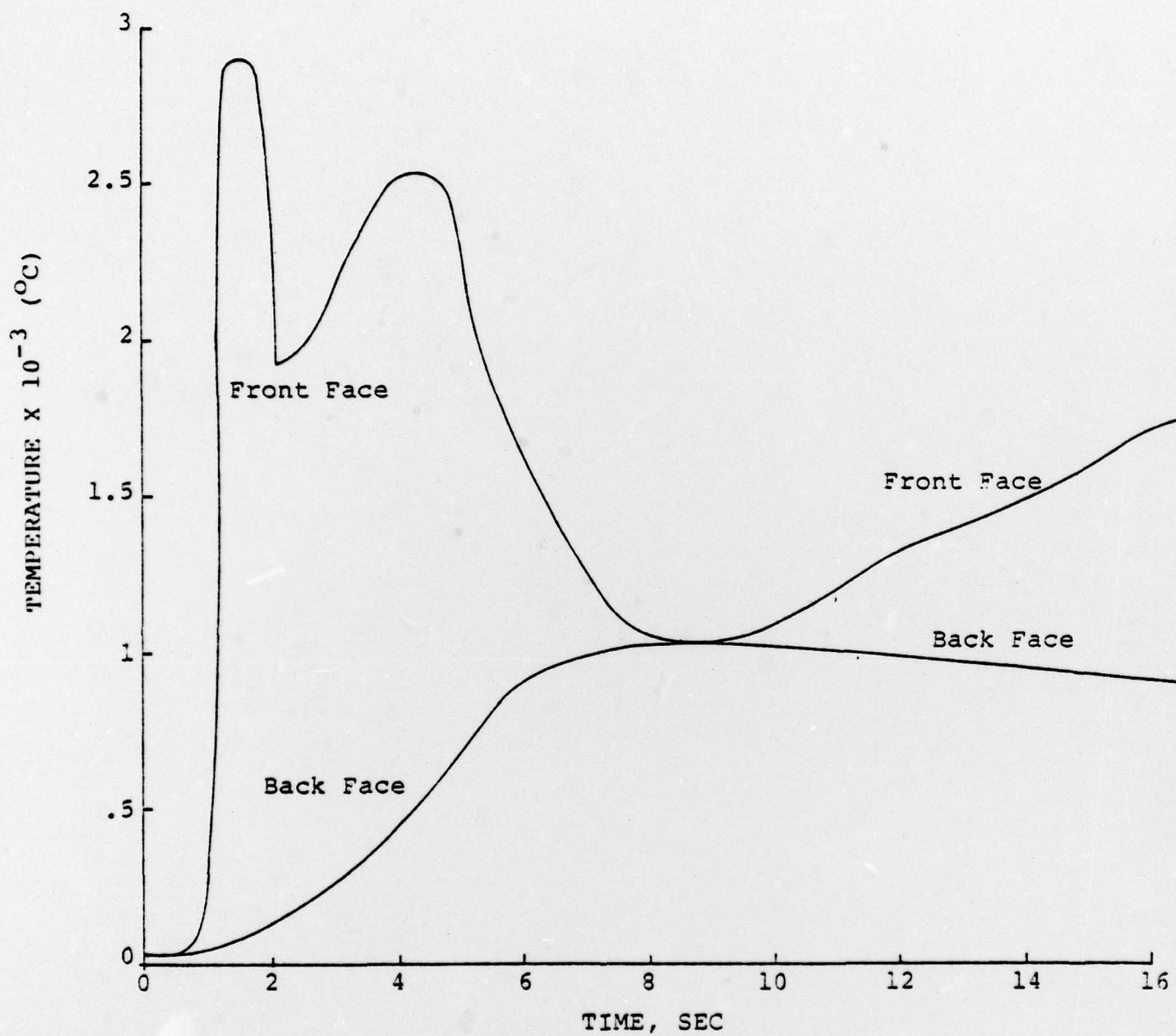


FIGURE G12. MAGNESIA SPINEL COATING/SILICONE INFILTRANT,
SAMPLE F16, TEMPERATURE RESPONSE